

General Disclaimer

One or more of the Following Statements may affect this Document

- This document has been reproduced from the best copy furnished by the organizational source. It is being released in the interest of making available as much information as possible.
- This document may contain data, which exceeds the sheet parameters. It was furnished in this condition by the organizational source and is the best copy available.
- This document may contain tone-on-tone or color graphs, charts and/or pictures, which have been reproduced in black and white.
- This document is paginated as submitted by the original source.
- Portions of this document are not fully legible due to the historical nature of some of the material. However, it is the best reproduction available from the original submission.

FR84-75-717
E1647

NASA CR-175272

FINAL REPORT

SPACECRAFT SYSTEM STUDY

A STUDY TO DEFINE THE IMPACT OF LASER
COMMUNICATION SYSTEMS
ON THEIR HOST SPACECRAFT

A STUDY UNDER CONTRACT NAS 5-27139

APRIL 1984

PREPARED FOR
NASA GODDARD SPACE FLIGHT CENTER
GREENBELT, MD



(NASA-CR-175272) SPACECRAFT SYSTEM STUDY:
A STUDY TO DEFINE THE IMPACT OF LASER
COMMUNICATION SYSTEMS ON THEIR HOST
SPACECRAFT Final Report (Hughes Aircraft
Co.) 261 p HC A12/MF A01

N85-16159

Unclassified
CSCL 20E G3/36 13828

FR84-75-717

FINAL REPORT

SPACECRAFT SYSTEM STUDY

**A STUDY TO DEFINE THE IMPACT OF LASER
COMMUNICATION SYSTEMS
ON THEIR HOST SPACECRAFT**

A STUDY UNDER CONTRACT NAS 5-27139

APRIL 1984

**PREPARED FOR
NASA GODDARD SPACE FLIGHT CENTER
GREENBELT, MD**



SPACECRAFT SYSTEM STUDY
A Study to Define the Impact of Laser Communication
Systems on their Host Spacecraft

A Study under Contract NAS 5-27139

FINAL REPORT

April 1984

Prepared For
NASA Goddard Space Flight Center
Greenbelt, Md.

HUGHES

TABLE OF CONTENTS

	<u>Page</u>
1.0 INTRODUCTION AND SUMMARY OF RESULTS	1-1
1.1 Introduction	1-1
1.2 Orbital Aspects	1-2
1.3 System Configuration	1-7
1.4 Burst Errors	1-12
1.5 Servo Analysis	1-16
1.6 Tracking and Beacon Link	1-18
1.7 Acquisition	1-19
1.8 System Weight and Power	1-21
2.0 REQUIREMENTS	2-1
2.1 Study Tasks	2-1
2.2 Link Requirements	2-1
3.0 ORBITAL ASPECTS	3-1
3.1 Introduction	3-1
3.2 CrossLink Parameters	3-4
3.3 Influence by the Sun and Moon	3-9
4.0 SYSTEM CONFIGURATION	4-1
4.1 Concept	4-1
4.2 Terminal Design Features	4-10
4.3 Acquisition Configuration	4-10
5.0 BURST ERROR	5-1
5.1 Introduction	5-1
5.2 System Configuration	5-2
5.3 Pointing Errors	5-4
5.4 System Example	5-10
5.5 System Implications	5-15
5.6 References	5-19
6.0 SERVO ELECTRONICS	6-1
6.1 Introduction	6-1
6.1.1 Servo Design Requirements	6-1
6.1.2 System Baseline Design and Assumptions	6-1

TABLE OF CONTENTS (CONT'D)

	<u>Page</u>
6.2 Servo System Configurations	6-4
6.2.1 Servo Configurations and Their Design Philosophies ...	6-5
6.2.2 Servo Block Diagram	6-10
6.3 Error Analysis	6-13
6.3.1 Sensor Noise	6-13
6.3.2 Spacecraft Motion Disturbances	6-16
6.3.3 Friction Torque Disturbances	6-22
6.3.4 Other Error Sources	6-27
6.4 Servo Configuration Analysis Summary and Conclusions	6-31
6.4.1 Error Analysis Results	6-31
6.4.2 Reaction Torque Results	6-34
6.4.3 Comparative Summary and Recommendations	6-36
6.5 Appendices	6-39
6.5.1 Justification of Soft-Mounting the IMC Mirror	6-39
6.5.2 Derivation of Servo Control Equations	6-40
6.5.3 Interpretation of Statistical Coulomb Friction Model	6-43
6.5.4 Orbital Mechanics Equations to Compute Relative LOS Angular Accelerations	6-47
6.5.5 References	6-50
7.0 TRACKING AND BEACON LINK	7-1
7.1 Introduction	7-1
7.2 Noise Equivalent Angle of Quad Cell Tracking Sensor	7-1
7.3 Quad Cell Dead Zone Loss	7-8
7.4 Quad Cell Closed Loop Field of View	7-12
7.5 Photodetection Analysis	7-13
7.5.1 Means and Variances (Gaussian)	7-13
7.5.2 Minimization of Thermal Noise	7-18
7.5.3 Optimum APD Gain	7-19
7.6 Link Equation	7-20
7.7 PIN Quadrant Detector Tracking	7-22
7.8 Avalanche Photodiode Quadrant Detector Tracking	7-30
7.8.1 Quad APD Detector	7-30
7.8.2 Quad APD Tracking Performance	7-31
7.9 Beacon Link-Tracking Split	7-33
7.10 Tracking on Beacon PPM	7-36
7.11 Tracking with an Acquisition Array	7-38
7.12 Summary - Tracking and Beacon Link	7-41

TABLE OF CONTENTS (CONT'D)

	<u>Page</u>
8.0 ACQUISITION	8-1
8.1 Introduction	8-1
8.2 Acquisition Sensors	8-4
8.2.1 Arrays	8-4
8.2.2 Quadrant Detectors	8-11
8.3 Acquisition Sources	8-13
8.4 Quadrant Detector Acquisition	8-18
8.4.1 Field of View Reduction	8-18
8.4.2 Servo Angular Step Reduction	8-19
8.4.3 Detection and False Alarm Probabilities	8-21
8.4.4 CW Integrating Approach	8-22
8.4.5 Sinusoidal Intensity Modulation Approach	8-38
8.4.6 Time-Gated Acquisition for LDL Array	8-49
8.4.7 Quadrant Detector Acquisition Sequence	8-52
8.5 Array Acquisition	8-55
8.5.1 Field of View Reduction	8-55
8.5.2 Detection and False Alarm Probabilities	8-55
8.5.3 Array Acquisition Performance	8-57
8.5.4 Array Acquisition Sequence	8-62
8.6 Issues for Acquisition Beam Scanning	8-65
8.6.1 Beamwidth	8-65
8.6.2 Beam Overlap	8-66
8.6.3 Beam Scan	8-67
8.6.4 Spacecraft Induced Errors	8-68
8.7 Recommended Acquisition/Tracking Configuration	8-70
8.8 Summary - Acquisition	8-72
9.0 SYSTEM WEIGHT AND POWER	9-1
9.1 Estimate Rationale	9-1
9.2 Weight and Power	9-6

LIST OF TABLES

<u>NUMBER</u>	<u>TITLE</u>	<u>PAGE</u>
1.1-1	Major Study Results	1-3
1.2-1	Summary of Gimbal Requirements (Maximum Values)	1-4
1.3-1	Terminal Concept Design Parameters	1-10
1.3-2	Concept Design Functions	1-11
1.4-1	Examples of System Requirements with Burst Error Probabilities	1-15
1.5-1	Two Axis Error Summary	1-17
1.8-1	Weight and Power Estimates	1-21
2.1-1	Study Tasks	2-2
2.2-1	System Link Requirements	2-3
3.1-1	Orbital Assumptions	3-1
3.2-1	Summary of Gimbal Requirements (Maximum Values) Determined by the LEO and GEO Orbits	3-4
3.3-1	Percent Time Loss Due to Orbital Geometry	3-14
3.3-2	Time Loss Due to Orbital Geometry	3-15
4.2-1	Terminal Concept Design Parameters	4-11
4.2-2	Concept Design Function Definitions	4-12
5.4-1	Example System Requirements Under Burst Error Limitations	5-12
5.5-1	Communication Link Budget Summary	5-18
7.6-1	Assumed Link Parameters	7-21
7.7-1	Astronomical Background Sources ($\lambda = 0.83 \mu\text{m}$)	7-25

LIST OF TABLES

<u>NUMBER</u>	<u>TITLE</u>	<u>PAGE</u>
8.2-1	Commercially Available Imaging Arrays	8-10
8.2-2	Commercially Available Quadrant Detectors	8-12
8.3-1	Commercially Available Single Transverse Mode Laser Diodes	8-14
8.4-1	HPIN 444Q Quadrant Detector Acquisition Performance	8-27
8.4-2	Acquisition with Sinusoidal Intensity Modulation (Hughes HPIN 444Q)	8-43
8.4-3	Acquisition with Sinusoidal Intensity Modulation (RCA Quadrant APD)	8-48
8.5-1	CCD Array - Acquisition Performance	8-60
8.7-1	Recommended Acquisition/Tracking Configuration	8-71
9.1-1	Terminal Concept Design Parameters	9-4
9.2-1	LEO Weight Estimate	9-7
9.2-2	Geosync Weight Estimate	9-8
9.2-3	LEO Power Estimate	9-9
9.2-4	Geosync Power Estimate	9-10

LIST OF FIGURES

<u>NUMBER</u>	<u>TITLE</u>	<u>PAGE</u>
1.2-1	Pointing Angles, S/C to S/C (September)	1-5
1.2-2	Outage Due to Sun in FO4 (4 degrees)	1-6
1.3-1	Baseline Configuration (LEO and GEO)	1-8
1.4-1	Antenna Diameter as Influenced by Burst Error	1-14
1.3-2	Basic System Block Diagram	1-9
3.1-1	Laser Crosslink Configuration	3-2
3.1-2	Spacecraft Gimbal Coordinate System	3-3
3.2-1	Pointing Angles, S/C to S/C (September)	3-5
3.2-2	Pointing Rates, S/C to S/C (September)	3-6
3.2-3	Pointing acceleration, S/C to S/C (September)	3-7
3.2-4	Point Ahead, GEO To LEO (September)	3-8
3.3-1	Sun and Moon Orientation to S/C (September)	3-10
3.3-2	Sun and Moon Orientation to S/C (December)	3-11
3.3-3	Time with Sun in Field of View (100 μ rad and 1 degree) ...	3-12
3.3-4	Outage Due to Sun in FOV (4 Degree)	3-14
4.1-1	Basic Optical Communication System Block Diagram	4-2
4.1-2	Baseline Configuration (LEO and GEO)	4-4
4.1-3	Basic System Block Diagram (LEO)	4-5
4.1-4	Optical Schematic - Data Transmitter	4-6
4.1-5	Basic System Block Diagram (GEO)	4-7

LIST OF FIGURES (CONT'D)

<u>NUMBER</u>	<u>TITLE</u>	<u>PAGE</u>
4.1-6	Optical Schematic - Data Receiver	4-8
4.1-7	Two Axis IMC	4-9
4.3-1	Acquisition/Tracking Basic Block Diagram	4-13
5.2-1	Simplified Servo Control Block Diagram Indicating the Major Functions and the Major Noise Sources Leading to Mistracking and Mispointing	5-5
5.3-1	Mispoint Factor (Loss) as a Function of the Ratio of the Pointing Error to the Beamwidth	5-9
5.4-1	Variation of the Probability of Burst Error as a Function of the Ratio of the Radial RMS Standard Deviation σ to the Optical Beamwidth a	5-11
5.4-2	The Diameter of the Optical Antenna Used to Provide the Optimum Beamwidth in the Pointing Error Environment Described by the Standard Deviation σ , is Noted for Several Selected Values of the Burst Error	5-14
5.4-3	A Limit to the Signal to Noise Ratio in the Tracking Servo control Loop is Defined by the Ratio of the Tracking Error to the Pointing Error for Several Values of the Receive Antenna Diameter	5-16
6.1-1	Transmitter/Receiver Functional Block Diagram	6-2
6.1-2	Receiver Telescope Schematic Diagram	6-3
6.2-1A	Gyro-Stabilized Functional Block Diagram	6-6
6.2-1B	Mass-Stabilized Functional Block Diagram	6-6
6.2-1C	Complementary Filter Functional Block Diagram	6-6
6.2-2	AABISM Steering Mechanism and Open Loop Response	6-8
6.2-3	Gyro-Stabilized Two-Axis Servo Block Diagram	6-11

LIST OF FIGURES (CONT'D)

<u>NUMBER</u>	<u>TITLE</u>	<u>PAGE</u>
6.2-4	Mass-Stabilized Two-Axis Servo Block Diagram	6-11
6.2-5	Complementary Filter Two-Axis Servo Block Diagram	6-12
6.3-1	Track Loop Model for Sensor Noise Analysis	6-14
6.3-2	Sensor Noise Results	6-16
6.3-3	Spacecraft Base Motion Disturbance PSD	6-17
6.3-4	Two Axis Gimbal Rate Piogram	6-18
6.3-5	Four Axis Gimbal Rate Piogram	6-19
6.3-6	Servo Configuration Comparisons of Base Motion Error Rejection	6-21
6.3-7	LOS Error vs IMC Loop Bandwidth	6-22
6.3-8	Friction Torque Disturbance Input to Servo Loops	6-23
6.3-9	Friction Acceleration Effects to Servo Configuration LOS Errors	6-24
6.3-10	Friction Disturbance Angular Acceleration Transfer Function	6-25
6.3-11	Friction Disturbance Angular Displacement Transfer Function	6-25
6.3-12	Friction LOS Error Summary	6-26
6.3-13	Track Loop Block Diagram for Following Error	6-28
6.4-1	Two Axis Error Analysis Results	6-32
6.4-2	Error Analysis Summary	6-31
6.4-3	Reaction Torque Summary	6-34
6.4-4	Spacecraft Reaction Acceleration PSD	6-35
6.4-5	Servo Configuration Summary Comparison	6-37

LIST OF FIGURES (CONT'D)

<u>NUMBER</u>	<u>TITLE</u>	<u>PAGE</u>
6.5.1-1	IMC Servo Block Diagram with Soft-Mounting Dynamics	6-39
6.5.2-1	Simplified Complementary Filter Configuration Servo Block Diagram	6-42
6.5.2-2	Complementary Filter Configuration Servo Block Diagram ...	6-44
6.5.3-1	Friction Acceleration Model	6-43
6.5.3-2	Base Motion Rate and Friction Acceleration vs. Time	6-45
6.5.3-3	Poisson Distribution for $\mu T = 3$ to 5	6-46
6.5.3-4	Friction Acceleration Autocorrelation Function	6-46
6.5.3-5	Friction Acceleration PSQ Variations with μ	6-47
6.5.4-1	Orbital Geometry	6-48
6.5.4-2	In-Plane Polar Coordinate System	6-48
7.2-1	Noise Equivalent Angle Focal Plane Geometry	7-5
7.3-1	Geometry for Determination of Intensity Loss Due to Quadrant Dead Zone	7-9
7.3-2	Fraction of Intensity Lost Due to Quadrant Gap (n) versus $\gamma = (d/f)/\lambda/(D_p)$	7-11
7.5-1	Direct Detection Receiver Circuit Model	7-14
7.7-1	Data Sheet for Hughes Industrial Products Division Quadrant Detectors	7-23
7.7-2	Block Diagram of Tracking Detection Circuit	7-26
7.7-3	Probability Densities for Gaussian Threshold Detection ...	7-27
7.7-4	AC-Coupled, Low Pass Filter Tracking Circuit	7-28
7.9-1	Pulse Position Modulation Format	7-34
8.2-1	Schematic Diagram of CCD Readout Technique	8-5

LIST OF FIGURES (CONT'D)

<u>NUMBER</u>	<u>TITLE</u>	<u>PAGE</u>
8.2-2	Schematic Diagram of CID and Photodiode Array Readout Technique	8-7
8.2-3	Hitachi 384 x 485 Element MOS Photodiode Array	8-9
8.3-1(a)	Laser Diode Labs High Pulsed Power Array	8-15
8.3-1(b)	Laser Diode Labs High Pulsed Power Array Data Sheet	8-16
8.4-1	Required Power (P_T) versus the Inverse of Acquisition Time ($1/T_{ACQ}$) for Integration Time $T = 0.1$ msec	8-30
8.4-2	Required Power (P_T) versus the Inverse of Acquisition Time ($1/T_{ACQ}$) for Integration Time $T = 1.0$ msec	8-31
8.4-3	Required Power (P_T) versus the Inverse of Acquisition Time ($1/T_{ACQ}$) for Integration Time $T = 10.0$ msec	8-32
8.4-4	Required Power (P_T) versus the Inverse of Acquisition Time ($1/T_{ACQ}$) for Integration Time $T = 100$ msec	8-33
8.4-5	Required Power (P_T) versus the Inverse of Acquisition Time ($1/T_{ACQ}$) for Integration Time $T = 1000$ msec	8-34
8.4-6	Required Power (P_T) versus Integration Time (T) for Acquisition Time $T_{ACQ} = 2500$ Seconds	8-35
8.4-7	Required Power (P_T) versus Integration Time (T) for Acquisition Time $T_{ACQ} = 250$ Seconds	8-36
8.4-8	Quadrant Detector Demodulator for Acquisition with Sinusoidal Intensity Modulation	8-39
8.4-9	Required Power (P_{CW}) versus the Inverse of the Acquisition Time ($1/T_{ACQ}$) for the HPIN 44Q Quadrant Detector with Sinusoidal Intensity Modulation	8-45

LIST OF FIGURES (CONT'D)

<u>NUMBER</u>	<u>TITLE</u>	<u>PAGE</u>
8.4-10	Required Power (P_{CW}) versus the Inverse of Acquisition Time ($1/T_{ACQ}$) for an RCA Quadrant APD with Sinusoidal Intensity Modulation	8-47
9.1-1	Baseline Configuration and Rationale for Weight Estimate	9-2
9.1-2	Basic Optical Layout	9-3
9.1-3	Telescope Weight Scaling with Size for Be and Cervit Material	9-5

Electro-Optical and Data Systems Group
J.D. Barry
K.J. Held
G.S. Mecherle
Space and Communications Group
A.J. Einhorn

1.0 INTRODUCTION AND SUMMARY OF RESULTS

1.1 INTRODUCTION

This report discusses the results of a study completed by personnel of the Electro-Optical and Data Systems Group, Hughes Aircraft Company in El Segundo, CA for NASA/GSFC in Greenbelt, Md under contract NAS 5-27139. The intent of the study was to determine the mutual influence of a laser communication system and its host spacecraft and to what degree the mutual influence limited the acquisition, tracking and pointing processes so important to a laser communication link between the two spacecraft. The study used as a baseline a laser link between a low earth orbiting (LEO) satellite and a geosynchronous earth orbiting (GEO) satellite. The LEO satellite was modeled as a LANDSAT satellite and the GEO as a TDRSS satellite. Vibrational and disturbance data from the LANDSAT satellite was used to model the baseframe noise environments for the study.

The laser link between satellites was a generic channel transferring 500 Mbps data from the LEO to GEO using the GaAlAs laser as the laser light source. The LEO optical subsystem was fashioned as a 6 inch diameter optical telescope for transmit and the GEO used a 20 inch diameter optical telescope for receive functions. The probability of bit error was specified as 1×10^{-6} . The bit probability of burst error due to mispointing was not specified but was shown by the study to be of basic concern. Burst errors arise when the realtime mispoint angle is greater than the nominal mispoint angle. The occurrence of such mispoint is described by a probability function and has been evaluated herein.

The major aspects of pointing and tracking with a satellite-borne optical system have been evaluated. We have evaluated the major influencing areas, including: (1) orbital aspects such as spacecraft relative motions, point ahead, and sun and moon optical noise, (2) burst errors introduced by the electronic and optical noise levels, (3) servo system design and configurations, and the noise sources such as, sensor noise, base motion disturbances,

gimbal friction torque noise, (4) an evaluation of the tracking and beacon link and the type of sensors used, (5) the function of the acquisition procedure and an evaluation of the sensors employed, and (6) an estimate of the size, weight and power needed for the satellite system. The system was evaluated as a two axis gimballed configuration with all optical, electro-optical, laser and receiver components borne on-gimbal. Support electronics such as servo control electronics, communication electronics, power supply and thermal control were placed off-gimbal. The laser source was a GaAlAs laser diode operating at about 8300 Å. An avalanche photodiode communication sensor was assumed.

The major study results are briefly summarized in Table 1.1-1. The study indicated that 1 µrad rms pointing may be achieved on a satellite with base-frame motion disturbances as measured on the LANDSAT satellite. The design of the servo control subsystem is critical and those aspects have been identified. The system weight and power values have been estimated for a non-redundant configuration and for redundant electro-optical and electronic components. The redundant system weight for a LEO satellite is about 175.2 lb and that for a GEO satellite system is 211.5 lb. The associated electrical power requirements are 137.8 watt and 143.1 watt, respectively. Since the system incorporates moving electro-optical and optomechanical elements, the torque imparted to the satellite is of concern. We estimate that the torque will be 0.03 ft lb. Spatial acquisition between the LEO and GEO with an angular uncertainty of 0.5 degree may be accomplished within 20 minutes if a solid state array sensor is employed.

In general, we find that the pointing/tracking and acquisition requirements can be met with an appropriately design system, and with components that are currently commercially available.

1.2 ORBITAL ASPECTS

The orbital aspects of the two satellite configuration was evaluated with respect to the influence upon the operation of the laser communication system. The laser system was modeled as a two axis gimballed configuration and it was determined that the gimbal would have requirements as summarized in Table 1.2-1.

TABLE 1.1-1. MAJOR STUDY RESULTS

Parameter	Study Result
• Pointing Accuracy	• 1 μ rad rms possible with properly designed servo control subsystem, with LANDSAT type base motion disturbances
• Weight (with redundancy)	• LEO = 175.2 lb • GEO = 211.5 lb • Redundant components assumed
• Power	• LEO = 137.8 • GEO = 143.1
• Torque imparted to spacecraft by moving optomechanical elements	• 0.03 ft-lb
• Acquisition time	• 2 minutes, with area array sensor

TABLE 1.2-1. SUMMARY OF GIMBAL REQUIREMENTS (MAXIMUM VALUES)
DETERMINED BY THE LEO AND GEO ORBITS.

Pointing Error			Angular Velocity		Angular Acceleration	
Spacecraft	Az	E1	Az	EL	Az	E1
LEO	$\pm 175^\circ$	$\pm 140^\circ$	200 μrad sec	200 μrad sec	1 μrad sec^2	0.5 μrad sec^2
GEO	$\pm 20^\circ$	$\pm 20^\circ$	1 μrad sec	200 μrad sec	1 μrad sec^2	1 μrad sec^2

The various parameters associated with pointing and tracking from one terminal to the other were graphically illustrated. These parameters included; the pointing angles in azimuth (Az) and elevation (E1), the pointing angle rates (Az-dot and EL-dot), the angular acceleration (Az-double dot and E1-double dot), and point ahead angles. One example of this type of orbital calculation is shown in Figure 1.2-1.

The influence of the sun and moon as inhibiting agents to maintenance of the satellite to satellite link due to being high background optical noise sources was also evaluated. The angular position of the sun and moon relative to the line of sight between the two satellites was determined with the orbital program. The amount of operational time lost per month when the sun and moon were within a small angle of the line of sight was evaluated. The angles were 4° , 1° and 100 μrad . The system outage was noted graphically and in tabular form in hours per month over the year. An example is shown in Figure 1.2-2.

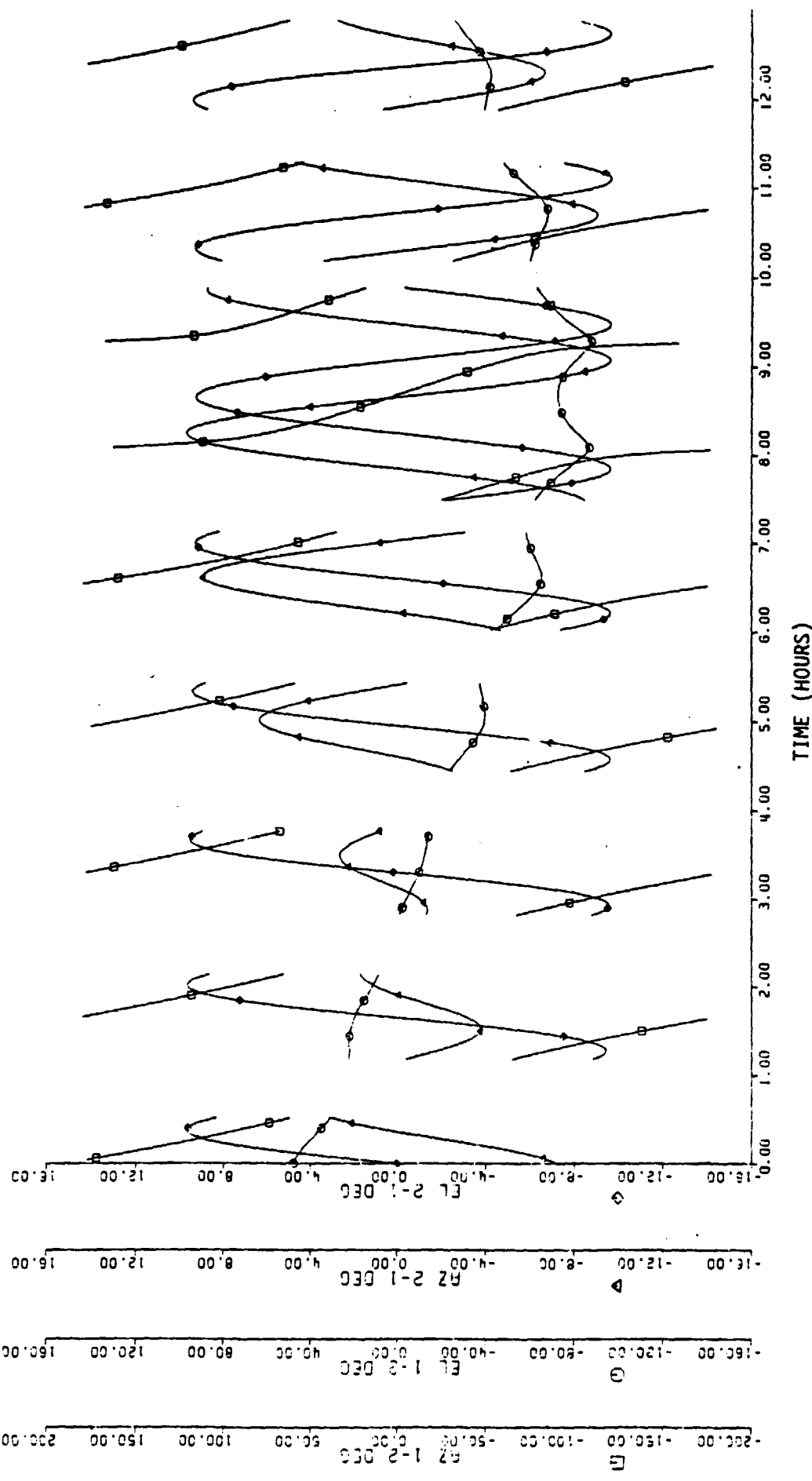


Figure 1.2-1. Pointing Angles, S/C to S/C (September)

ORIGINAL PAGE IS
OF POOR QUALITY

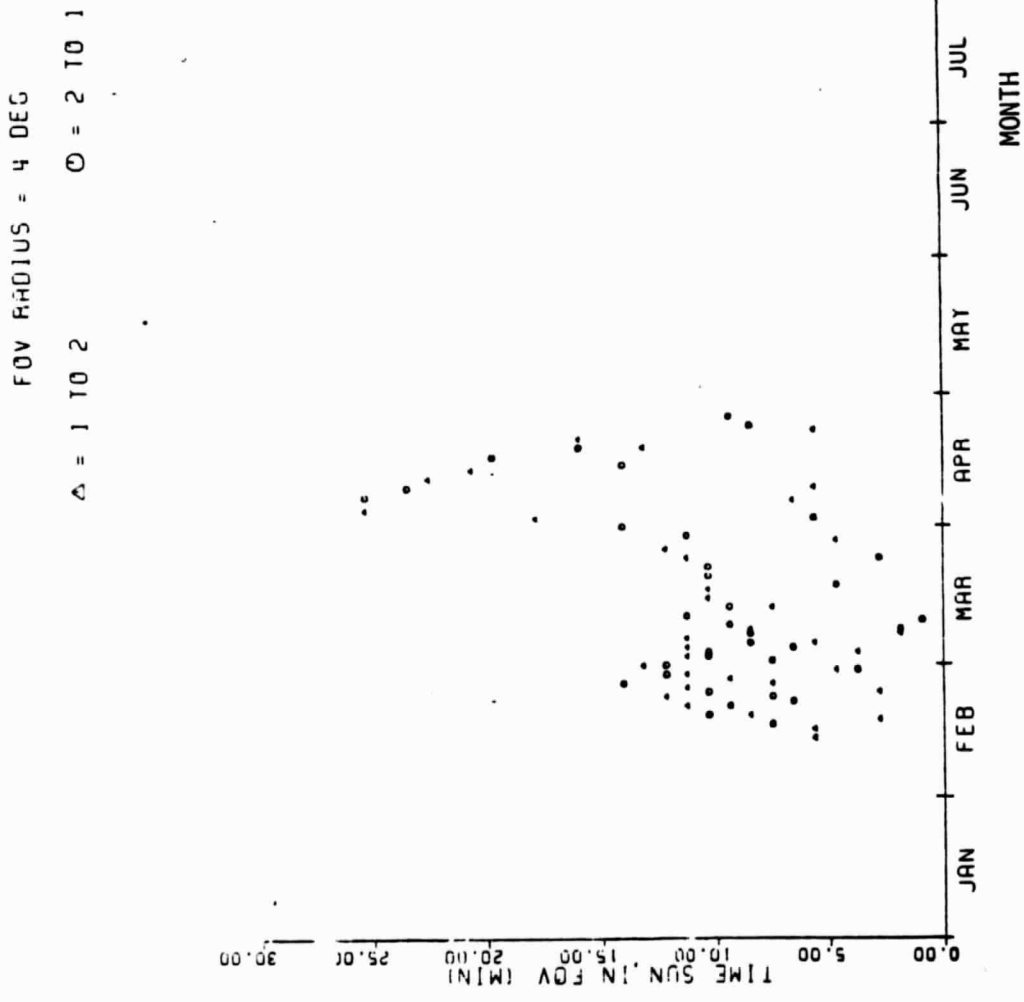


Figure 1.2-2. Outage Due to Sun in FOV (4-degrees).

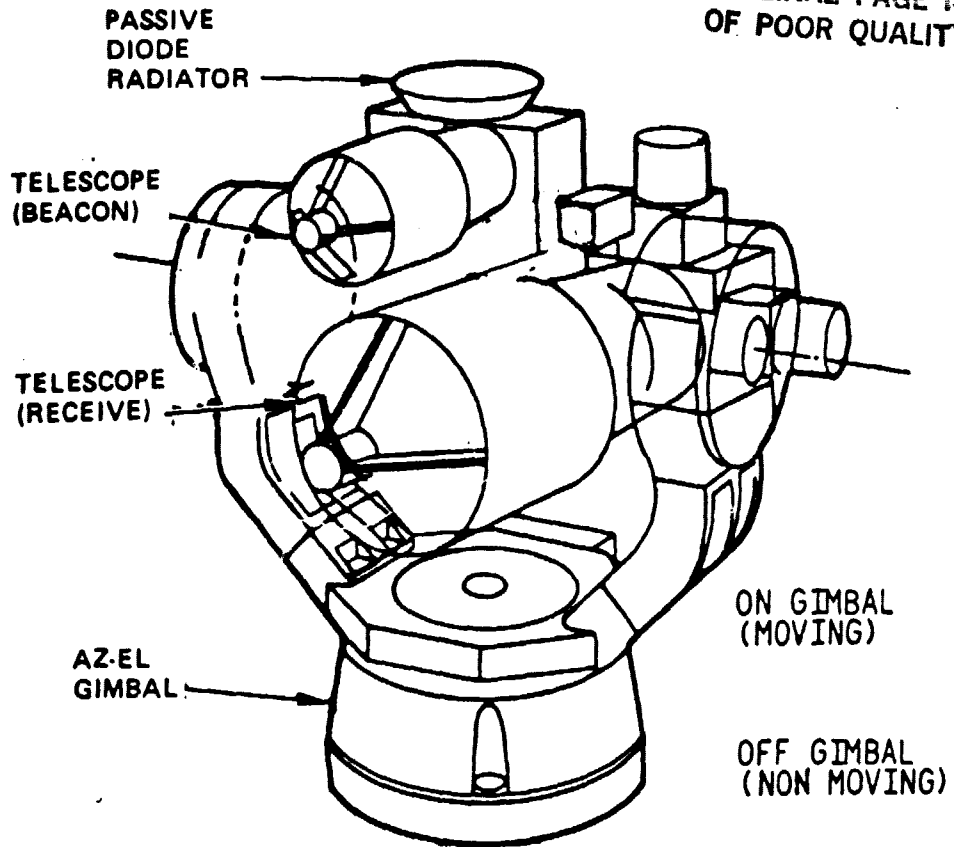
The clear line of sight between satellites was determined to be about 71 percent of the time as about 29 percent of the time the LEO satellite is obscured by the earth from the GEO satellite. The amount of time loss per month due to gimbal lock was also determined. This is principally due to gimbal lock in the LANDSAT satellite. It was found, for example, that the maximum amount of time lost due to the sun vs moon in 4° field of view along the line of sight is less than a maximum of about 166 minutes per month with an average of only about 60 minutes per month. The maximum time lost per month due to gimbal dock was about 3300 minutes and the average was about 2600 minutes.

1.3 SYSTEM CONFIGURATION

The optical and mechanical configuration of the optical communication terminal for the LEO and GEO satellites was developed. Two concepts were evaluated. One used a flat scan mirror to direct the laser light to the distant receiver. Common transmit and receive optics were assumed. The second used separate transmit and receive optics to avoid the complexity of dichroic elements. All optics and laser related components are borne on a two axis gimbal. This latter approach is the baseline concept. The selected configuration is noted in Figure 1.3-1.

The basic system block diagram (transmitter) is noted in Figure 1.3-2. The figure notes at the laser transmitted, receiver, associated electronics and all optics are borne on-gimbal. The large scale, low frequency pointing and tracking errors are corrected by the two axis gimbal. The small, high frequency angular disturbances are correct by the small image motion compensation (IMC) mirrors. The normal processing and support electronics are placed off gimbal. A bifurcating mirror is used to provide the separation between the large acquisition field of view and the smaller tracking field of view. A 6 inch telescope is used in the transmitter and a 20 inch telescope is used in the receiver.

ORIGINAL PAGE IS
OF POOR QUALITY



DESIGN FEATURE	REASON
<ul style="list-style-type: none">• SEPARATE TRANSMIT & RECEIVE OPTICS	<ul style="list-style-type: none">• TRANSMIT & RECEIVE AT SAME λ• NEED TO QUALE ONLY ONE DIODE TYPE• DO NOT REQUIRE COMPLEX DICHROIC COATINGS• EASILY ACHIEVE THE REQUIRED 90 dB + TRANSMIT AND RECEIVE ISOLATION• FEWER OPTICAL COATINGS TO QUALE• MODULAR DESIGN• SIMPLICITY• NO OFF GIMBAL OPTICAL ROUTING
<ul style="list-style-type: none">• ALL OPTICS ON GIMBAL	

Figure 1.3-1. Baseline Configuration (LEO and GEO).

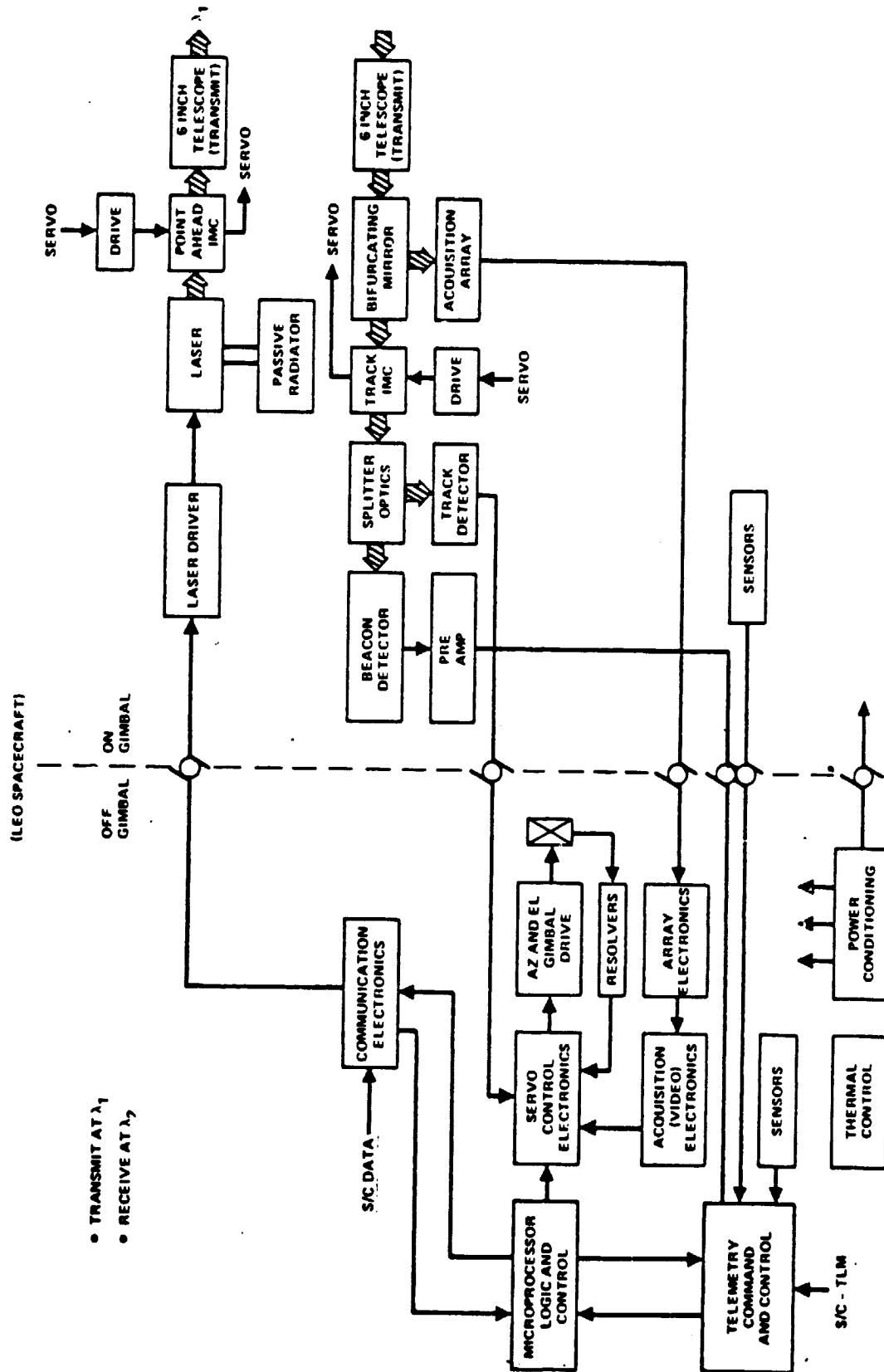


Figure 1.3-2. Basic System Block Diagram (transmitter).

The design parameters of the baseline approach are noted in Table 1.3-1 and the concept design functions are noted in Table 1.3-2. The size, weight and power summary for the LEO terminal is a 6 inch diameter telescope, 175.2 pounds and 137.8 watts. The associated factors for the GEO terminal is a 20 inch diameter telescope, 211.5 pounds and 143.1 watts.

TABLE 1.3-1. TERMINAL CONCEPT DESIGN PARAMETERS

Property	GEO	LEO
• Concept	• Separate Transmit and Receive Optics	• Separate Transmit and Receive Optics
• Transmit Optics	• 2.3 Inch Diameter	• 6 Inch Diameter
• Receive Optics	• 20 Inch Diameter	• 6 Inch Diameter
• Primary Material	• Beryllium	• Beryllium
• Acq Sensor	• Si-Quad	• Si-Array
• Track Sensor	• Si-Quad (APD)	• Si-Quad (APD)
• Comm Sensor	• Si-APD	• SI-APD
• Laser Source	• GaAlAs	• GaAlAs
• Transmit Wavelength	• Beacon (LDR) = 0.85 μm	• Comm (HDR) = 0.83 μm
• Receive Wavelength	• Comm (HDR) = 0.83 μm	• Beacon (LDR) = 0.85 μm
• Gimbal	• Two Axis-Optics on Gimbal	• Two Axis - Optics on Gimbal
• Az Range	• $\pm 20^\circ$	• $\pm 175^\circ$
• El Range	• $\pm 20^\circ$	• $\pm 140^\circ$
• Weight (with redundancy)	211.5 lb	175.2 lb
• Power	• 143.1 watt	• 137.8 watt

TABLE 1.3-2. CONCEPT DESIGN FUNCTION DEFINITIONS

Function	Design	Parameter
Acquisition	<ul style="list-style-type: none"> ● Concept ● Field-of-Regard ● Angular Scan Rate ● Laser Wavelength ● Laser Power ● Beamwidth ● Acquisition Sensor ● Acquisition Time 	<ul style="list-style-type: none"> ● Initiated by GEO ● 0.5 deg Cone for GEO and LEO ● 1.6 deg/sec ● 0.85 μm ● 50 mW - cw ● 130 μrad (full Airy Lobe) ● Nominal 400 x 500 area array on LEO ● Quad Cell on GEO ● \leq 2 minutes
Tracking	<ul style="list-style-type: none"> ● Concept ● Field-of-View ● T C Wavelength ● T C Data Rate ● GEO Beacon Power ● GEO Beacon Beamwidth ● GEO and LEO Sensor 	<ul style="list-style-type: none"> ● GEO Tracks on Data Uplink ● LEO Tracks on T C Downlink ● 140 μrad full Sensor, 13.7 μrad Closed Loop ● 0.81 μm ● 10 Kbps ● 20 mW - cw ● 35 μrad (full Airy Lobe) ● APD - Quad Cell
Communications	<ul style="list-style-type: none"> ● Concept ● Power ● Beamwidth ● Data Rate ● Wavelength 	<ul style="list-style-type: none"> ● Multisource Summing Device ● 200 mW - Average ● 10 μrad ($1/E^2$)* ● 500 MBPS ● 0.8 - 0.9 μm
Point Ahead	<ul style="list-style-type: none"> ● Concept 	<ul style="list-style-type: none"> ● Closed Loop Update via T & C Link for LEO Uplink ● Minor Update for GEO Downlink

* Not consistent with burst error requirements and 1 μrad pointing capability

1.4 BURST ERRORS

The performance of a free space, satellite-borne optical communication system is described by two major parameters: the probability of bit error and the probability of burst error. The probability of bit error is normally specified as a system requirement. It determines the nominal signal intensity required to recover the signal from the communication channel with its contributory noises. The nominal probability of bit error is proportional to the signal and noise counts received during the bit time interval. The probability of burst error on the other hand, is frequently ignored as it is not directly dependent upon the optical signal and noise levels. The probability of burst error establishes the percent of time that the servo system will maintain pointing within some error limit. Should the pointing error ϵ become greater than some value ϵ^* , the signal intensity at the distant receiver would be decreased, and the system performance described by the probability of bit error would be degraded. Many data bits could be lost since the pointing servo response time is much longer than the bit time.

The single axis probability distribution for mispointing (P_ϵ^*) is described as a gaussian function. It is shown that the gaussian assumption is reasonable for the complementary filter servo approach as sensor noise (gaussian in form) dominates the servo control system performance. The probability of burst error is defined as

$$P_\epsilon^* = \int_{\epsilon^*}^{\infty} P(\epsilon) d\epsilon$$

where the required pointing error must be maintained at $\epsilon < \epsilon^*$.

The resulting equation for the burst error is related to the laser beamwidth by the standard range equations. The nominal mispoint loss which should be included in the link budget is shown to be about -4 dB. The resulting equation may be manipulated to show that the diameter of the optical antenna is limited by the burst error. This is given by

$$D = \frac{\lambda}{2.4 \sigma \sqrt{-\ln P_e^*}}$$

where λ is the laser wavelength and σ is the standard deviation of the single axis gaussian probability distribution.

The diameter of the optical antenna used to provide the optimum beam-width in the pointing error environment described by the standard deviation σ is related to the probability of burst error as shown in Figure 1.4-1. Examples of the system requirements under burst error limitations are noted in Table 1.4-1.

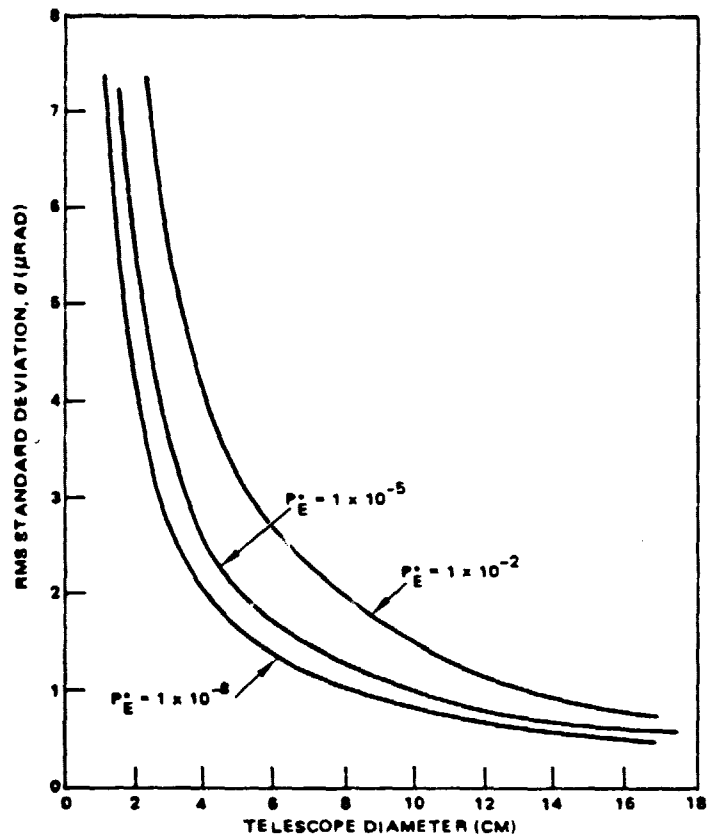


Figure 1.4-1 Antenna Diameter as Influenced by Burst Error.

Table 1.4-1. EXAMPLE SYSTEM REQUIREMENTS UNDER BURST ERROR LIMITATIONS.

System Availability (percent)	PBE	ϵ/σ	a/σ	Optimum Antenna Diameter for $\sigma = 1 \mu\text{rad}$ and $\lambda = 0.83 \mu\text{m}$ (inch)	Relative Power Required (dB)
90	10^{-1}	2.13	8.86	22.8	0.0
99	10^{-2}	3.03	12.60	16.1	3.1
99.9	10^{-3}	3.70	15.39	13.2	4.8
99.99	10^{-4}	4.28	17.80	11.4	6.1
99.999	10^{-5}	4.79	19.93	10.2	7.0
99.9999	10^{-6}	5.25	21.84	9.3	7.8

1.5 SERVO ANALYSIS

A servo analysis of the baseline system configuration was completed. Both azimuth and elevation axes were represented by a single axis analysis. All error sources were assumed identical for both axes except for base motion. Spacecraft base motion coupling was in accordance with the LANDSAT satellite disturbance data provided by NASA/GSFC. The worst case envelope of all the spacecraft disturbances were used for the study.

Three servo configurations were considered for the study and included; (a) gyro-stabilized, (b) mass stabilized and (c) complementary filter. The gyro stabilized configuration has an outer low bandwidth track loop with two higher bandwidth inner loops. The mass stabilized design replaces the two gyros with a reference platform that points along the desired LOS. The complementary filter configuration closes a single wide bandwidth loop about the track sensor with no inner loops. Two bandwidths were evaluated; 1 Hz for the gyro stabilized servo and 400 Hz for the complementary filter servo.

These were the contributing noise sources from the servo analysis; base motion, gimbal friction and track sensor noise. Other noise sources were shown to be negligible or may be removed by appropriate calibration. Sensor noise was represented as white gaussian noise and its contribution to the residual pointing error evaluated for each servo configuration. Similarly, the contribution by base motion disturbances was evaluated. The measured satellite LANDSAT base motion disturbance provided by NASA/GSFC were used for the evaluation. The measured disturbances from 0 to 125 Hz were converted to a power spectral density (PSD) curve by squaring the amplitude at each frequency and a 1 Hz bandwidth was assumed.

The friction disturbance was modeled as a Coulomb friction torque acting at the gimbal bearings. Friction and motor hysteresis were not addressed as they will be dependent upon the particular devices selected for the satellite system. A PSD for the friction disturbance was developed from a probability density function (PDF) which was derived from modeling the Coulomb friction as a random process. The PSD was applied to the three configurations and the effect documented.

A summary of the contributions due to the three main error sources is noted in Table 1.5-1. The contributions due to four other error sources were also evaluated but noted to be less significant. These included; point ahead error, dynamic following error, linear variable displacement transformer (LVDT) non-linearity error and gyro noise errors. The resulting data were included with the other results for the single axis evaluation and evaluated for a two axis (Az, El) configuration.

TABLE 1.5-1. TWO AXIS ERROR SUMMARY

Servo Configuration	Aperture Diameter	Mean LOS Error (μ rad)	1σ LOS Error (μ rad)	Total LOS Error (μ rad)
Gyro Stab	6 inch	0.078	0.63	0.71
	20 inch	0.078	0.49	0.57
Mass Stab	6 inch	0.078	11.65	11.73
	20 inch	0.078	11.65	11.73
Compl. Filter	6 inch	0.066	0.93	1.0
	20 inch	0.066	0.52	0.59

Two conclusions were reached as a result of the servo analysis. First, it was determined that a 1- μ rad pointing and tracking accuracy could be maintained with either the gyro-stabilized or complementary filter approaches. Although the gyro-stabilized approach had better tracking performance and lower sample rates from the optical sensor, a space-qualified gyro and greater number of control loops are required. The second conclusion is to recommend the complementary filter approach since it is the simplest design that meets the pointing requirements.

1.6 TRACKING AND BEACON LINK

The tracking and beacon link between the LEO satellite and the GEO satellite was evaluated. The pointing accuracy required for the LEO satellite is more severe than that required for the GEO link since the LEO terminal has a narrower beamwidth and is the high data rate transmitter. The study focused on the LEO link, recognizing that if it may be accomplished, the GEO return link could easily be maintained.

This analysis focused on the problem of tracking a data beacon from the GEO satellite to less than one microradian rms accuracy in order to derive pointing commands for a high data rate LEO transmitter. The noise equivalent angle of a quadrant tracking detector was derived explicitly stating the assumed signal and noise parameters per element. The tracking detector quadrant gap has been identified as an area needing further technology development, but which does not preclude operational systems with currently available devices. The angular dynamic range over which closed loop tracking can be maintained was shown to be proportional to the rms SNR in an element of the quadrant detector.

Photodetection analysis and link equations were presented to allow calculation of tracking (and acquisition) link budgets. It was shown that a PIN quadrant detector was not sensitive enough to close the tracking link budget to 1.0 μ rad rms accuracy unless a gyro-stabilized tracking servo is used or laser of 200 mW or greater are available. The quadrant APD detector is about 19 dB more sensitive than the PIN, which allows 1.0 μ rad tracking accuracy with the complementary filter servo approach, 35 μ rad GEO beamwidth, a commercial 20 mW laser diode, and 6 dB link margin.

For tracking a GEO 10 Kbps beacon data link three different configurations were shown to be viable. A 50-50 optical beamsplit between an APD quadrant tracking detector and single element APD data detector satisfied both functions (with adequate margin) with a commercial 20 mW laser. Or the quadrant APD tracking detector may also provide the data detection by summing the four outputs. This may be necessary if the tracking sample rate has significant spectral overlap with the beacon data, as would be the case with a

4.0 KHz complementary filter sample rate and 10 Kbps beacon data. Finally, it was shown that if an array were selected as the acquisition detector, it could also perform the tracking function. A CCD (or CID) array with standard video frame rates is compatible with the gyro-stabilized tracking servo. A CID array with a circuit to create a 40 x 40 pixel tracking gate could provide updates at the 4.0 KHz complementary filter servo sample rate.

1.7 ACQUISITION

Acquisition for optical communications is the process by which two terminals initially locate one another and progress to mutual fine tracking and two way communication. Each satellite terminal has some knowledge of the distant location of the other in terms of angular data relative to an inertial coordinate system. Its position is then an uncertainty solid angle which must be interrogated to solicit response from the opposite terminal.

Several desirable features of an acquisition system were early established. These included: (1) minimum number of acquisition peculiar components and complexity, (2) reliable acquisition within several minutes of acquisition start, (3) single stage transfer from wide field of view (FOV) acquisition to narrow field of view tracking and (4) avoidance of mechanically moving elements in the optical path to accomplish the FOV reduction.

Spatial acquisition between the LEO and GEO is critical as it must be accomplished first before communications may begin. Additionally, it must be accomplished periodically as the LEO to GEO line of sight is broken as the LEO passes behind the earth in its orbit. In general, the positional uncertainty of one satellite from the other is dependent upon several factors. These include: (1) the altitude uncertainty of the satellite itself, (2) orbital ephemeris uncertainties of the position and velocity of the other satellite from the first, (3) relative timing errors and point ahead errors. The relative significance of these errors was evaluated with the use of actual TDRSS satellite data. It was found that satellite attitude errors dominate and could be as large as about ± 0.23 deg, 3 axis, rms. We therefore used a value of 0.5 degree diameter for the angular uncertainty cone from one satellite to the other at the beginning of acquisition.

The key parameters associated with acquisition performance, once the angular uncertainty is known, is the acquisition time (the time from initiation to fine tracking), the laser power required to accomplish acquisition, and the probability that successful acquisition takes place. The acquisition sensors and modulation/detection alternatives were evaluated with emphasis on these parameters.

Acquisition sensors were investigated, including CCD, CID and photodiode arrays, as well as PIN and APD quadrant detectors. Commercially available arrays seem to be compatible with acquisition requirements, while quadrant detectors may require development in the areas of smaller quadrant gap, and smaller device size to reduce capacitance and dark current.

Acquisition sources were evaluated, including the single mode cw lasers and the high peak power Laser Diode Labs incoherent array. Although the 1.0 kW peak power of the LDL array was appealing, it was found that its large source size and divergence made it difficult to collect and collimate its emission. Single mode cw lasers (or coherent multi-stripe arrays, if they become available) are recommended as the choice for acquisition source.

Issues for quadrant detector acquisition were examined, including field of view reduction and servo angular step reduction. The probability of successful acquisition was derived based on detection probability when illuminated by the transmitter, and false alarm probabilities while not illuminated. Three different modulation/detection approaches for acquisition were evaluated for quadrant detector acquisition. These are the cw integrating (CWI) approach, sinusoidal intensity modulation (SIM), and time-gated acquisition (TGA). The CWI approach was found to yield the best shot noise performance for quadrant detector acquisition, but is seriously limited by the DC component of optical background in a practical system. SIM avoids the DC background problem, but is about 4.5 dB worse in shot noise performance than CWI. Acquisition times for SIM exceed ten minutes with a quadrant APD detector and a 100 mW source, with no power margin. The TGA scheme was found to have no advantage over SIM. The quadrant detector acquisition sequence was identified.

The field of view reduction for array acquisition was derived, as well as the probability of a successful acquisition. Commercially available CCD arrays were found to allow acquisition times under two minutes, with a 50 mW source and 6.0 dB power margin. The acquisition sequence using an array was described.

Acquisition times were found to be directly proportional to the uncertainty solid angle, and inversely proportional to laser power, for both array and quadrant detector acquisition.

Issues for scanning the acquisition transmitter beam were identified, including optimum beamwidth, beam overlap, scanning with a pulsed laser, and spacecraft uncompensated drift.

A recommended acquisition/tracking configuration was proposed, which used an acquisition array on the LEO, and a quadrant APD for both tracking and beacon data demodulation on the LEO. Further investigation is recommended to evaluate performing the tracking function with the acquisition array and a video tracker.

1.8 SYSTEM WEIGHT AND POWERS

Weight and power estimates were made for the baseline concept - the two axis gimballed optical assembly. The estimate rationale was based on the use of beryllium as well as light weighted cervit for the material for the main optical elements. Beryllium optics is baseline. The weight and power estimates were made for both the LEO and GEO satellites. Redundancy of the electronic, electro-optical and some optical components was considered as necessary for a reliable system. A summary of the results are noted in Table 1.8-1.

TABLE 1.8-1. WEIGHT AND POWER ESTIMATE

Satellite	Weight (lb) with Reduncancy	Power (watt)
LEO	175.2	137.8
GEO	211.5	143.1

2.0 REQUIREMENTS

2.1 STUDY TASKS

The study tasks were three fold. Task 1 - determine the influence of the spacecraft on the communication system. The Spacecraft can introduce link degradation due to the influence of attitude and ephemeris errors on the LEO to GEO and GEO to LEO pointing accuracy. Additionally, the spacecraft can influence the link acquisition time and the complexity of the acquisition and tracking subsystems by introducing pointing or tracking errors. Task 2 - determine the influence of the communication system on the spacecraft. Torques will be generated by moving optical elements and the torques must be recognized to allow proper design of the spacecraft control system. Task 3 - develop a concept design for the LEO and GEO terminals.

The task requirements are summarized in Table 2.1-1.

2.2 LINK REQUIREMENTS

The communication system link requirements are summarized in Table 2.2-1. The system is configured as a 500 megabit per second (Mbps) channel originating at the LEO (Landsat) satellite and relayed to the GEO (TDRSS) satellite. The laser source is a GaAlAs laser diode operating at a nominal wavelength of $0.8 \mu\text{m}$. The probability of bit error was specified as 1×10^{-6} . Burst error was not specified but its influence is discussed in section 4.0. A 6 inch diameter telescope is specified for the LEO and a 20 inch diameter telescope is specified for the GEO. It is shown in section 4.0 that these diameters are consistent with a pointing error of $1 \mu\text{rad}$.

TABLE 2.1-1. STUDY TASKS

Task	Title	Specifics
1	<u>Spacecraft Impact on the Communication System</u>	<p>(a) Determine the influence on the performance or the communication link due to spacecraft related errors:</p> <ul style="list-style-type: none"> • Attitude errors • Attitude instabilities • Ephemeris errors • Attitude commands uplinked from ground control <p>(b) Determine the influence on the system performance due to spacecraft related errors:</p> <ul style="list-style-type: none"> • Acquisition time • Tracking accuracy • Pointing accuracy <p>(c) Determine the system configuration and complexity due to spacecraft related errors:</p> <ul style="list-style-type: none"> • Number of acquisition stages • Number of track stages
2	<u>System Impact on the Spacecraft</u>	<p>(a) Determine the influence on the spacecraft due to the operation of the communication system during acquisition, tracking, pointing and communication:</p> <ul style="list-style-type: none"> • Moving optical elements • Moving mechanical elements <p>(b) Determine the feedback to the communication system from the spacecraft originally influenced by the operation of the system.</p>
3	<u>System Concept Design</u>	<p>(a) Develop concept designs for the LEO and GEO terminals</p> <ul style="list-style-type: none"> • Configuration • Block diagram • Weight • Size • Power

TABLE 2.2-1. SYSTEM LINK REQUIREMENTS

ITEM	REQUIREMENT
• LEO	• LANDSAT
• GEO	• TDRSS
• DATA RATE	• 500 MPBS
• PBE	• 1×10^{-6}
• DT	• 6 INCH
• DR	• 20 INCH
• WAVELENGTH	• 0.80 μm

3.0 ORBITAL ASPECTS

3.1 INTRODUCTION

The optical communication system spacecraft architecture under evaluation is a Landsat to TDRSS link. The primary high data rate communication terminal is assumed to be borne on the low earth orbiting (LEO) LANDSAT spacecraft and the high data rate receiver borne in the geosynchronous earth orbiting (GEO) TDRSS spacecraft. The orbital parameters for the two spacecraft are noted in Table 3.1-1 and the orbital configuration noted in Figure 3.1-1.

TABLE 3.1-1. ORBITAL ASSUMPTIONS

SPACECRAFT	PRIMARY TERMINAL	ORBIT
Landsat	Transmitter	<ul style="list-style-type: none">• low earth orbit• circular orbit• 705.3 Km altitude• 98.2° inclination• sun-synchronous
TDRSS	Receiver	<ul style="list-style-type: none">• geosynchronous orbit• 43,900 Km altitude• 41° W position

The spacecraft gimbal coordinate system is defined in Figure 3.1-2. The coordinate system is applicable to both the low earth orbit (LEO) and geosynchronous earth orbit (GEO) satellites. The X axis is nadir pointing, Y is opposite the velocity vector in the orbital plane, and Z is perpendicular to the orbit plane following a right hand rule.

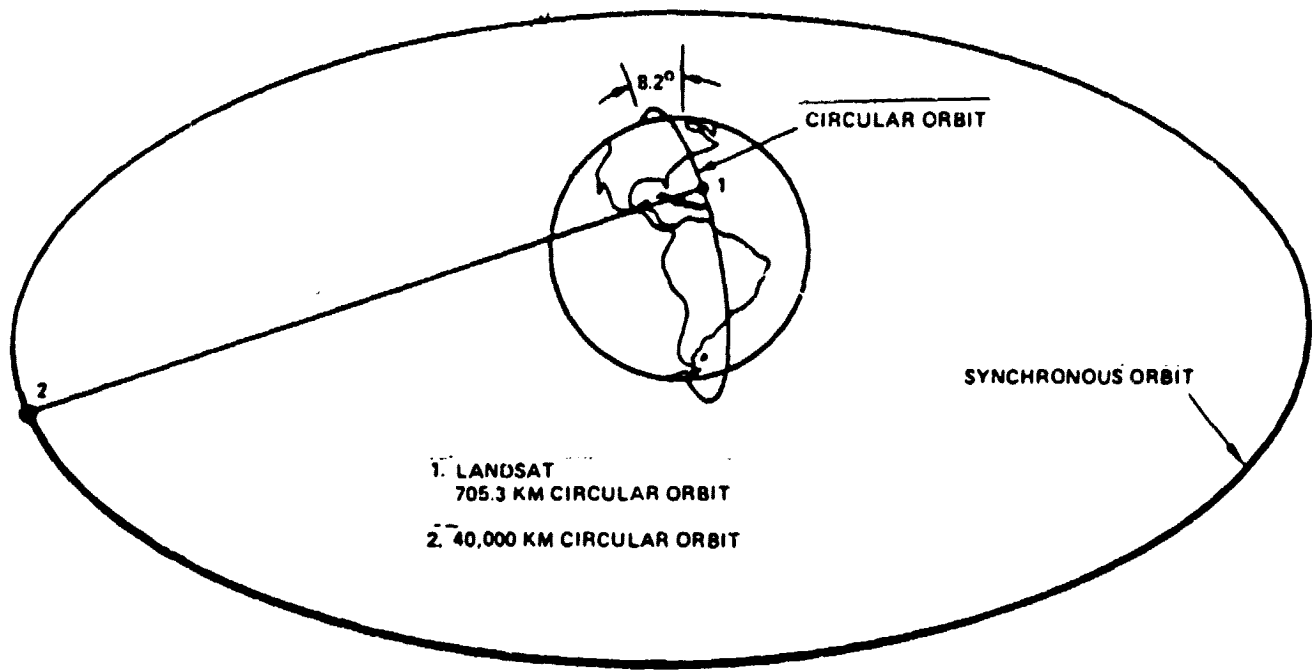
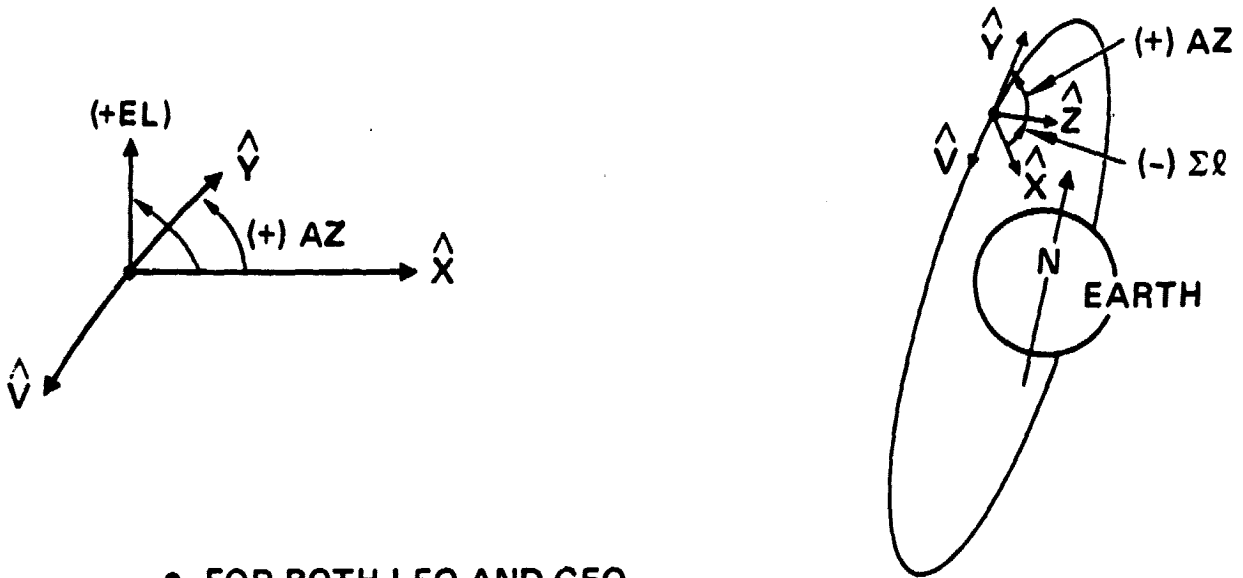


Figure 3.1-1. Laser Crosslink Configuration.



- FOR BOTH LEO AND GEO

AXIS	DEFINITION
\hat{X}	NADIR POINTING
\hat{Y}	OPPOSITE VELOCITY VECTOR
\hat{Z}	PERPENDICULAR TO \hat{X} AND \hat{Y} , RH-RULE
AZ	IN ORBITAL PLANE, POSITIVE FROM \hat{X} TO \hat{Y}
EL	OUT OF ORBITAL PLANE NEGATIVE FROM \hat{X} TO \hat{Z}

Figure 3.1-2. Spacecraft Gimbal Coordinate System.

3.2 CROSS LINK PARAMETERS

The applicable link parameters have been defined for the LEO (Landsat) to GEO (TDRSS) and GEO (TDRSS) to LEO (Landsat) configuration using an orbital program previously developed. The program determines the pointing angles for azimuth (Az) and elevation (El) for each satellite terminal, the pointing angle rates for Az and El, pointing angle accelerations for Az and El, and point ahead angles in Az and El. An example of the expected Az and El pointing angles (with the GEO designated as 1 and the LEO designated as 2) for the month of September are shown in Figure 3.2-1. In general, the Az gimbal coverage required for the GEO satellite is about $\pm 20^\circ$ Az and about $\pm 20^\circ$ El. That required for the LEO satellite is about $\pm 175^\circ$ Az and $\pm 140^\circ$ El.

The results of the orbital program are summarized in Table 3.2-1. Plots for the angular velocity for September are shown in Figure 3.2-2, plots for the angular acceleration for September are shown in Figure 3.2-4. The resulting point ahead is shown in Figure 3.2-4.

TABLE 3.2-1. SUMMARY OF GIMBAL REQUIREMENTS (MAXIMUM VALUES)
DETERMINED BY THE LEO AND GEO ORBITS.

Pointing Error			Angular Velocity		Angular Acceleration	
Spacecraft	Az	El	Az	El	Az	El
LEO	$\pm 175^\circ$	$\pm 140^\circ$	200 μrad sec	200 μrad sec	1 μrad sec^2	0.5 μrad sec^2
GEO	$\pm 20^\circ$	$\pm 20^\circ$	1 μrad sec	200 μrad sec	1 μrad sec^2	1 μrad sec^2

ORIGINAL PAGE IS
OF POOR QUALITY

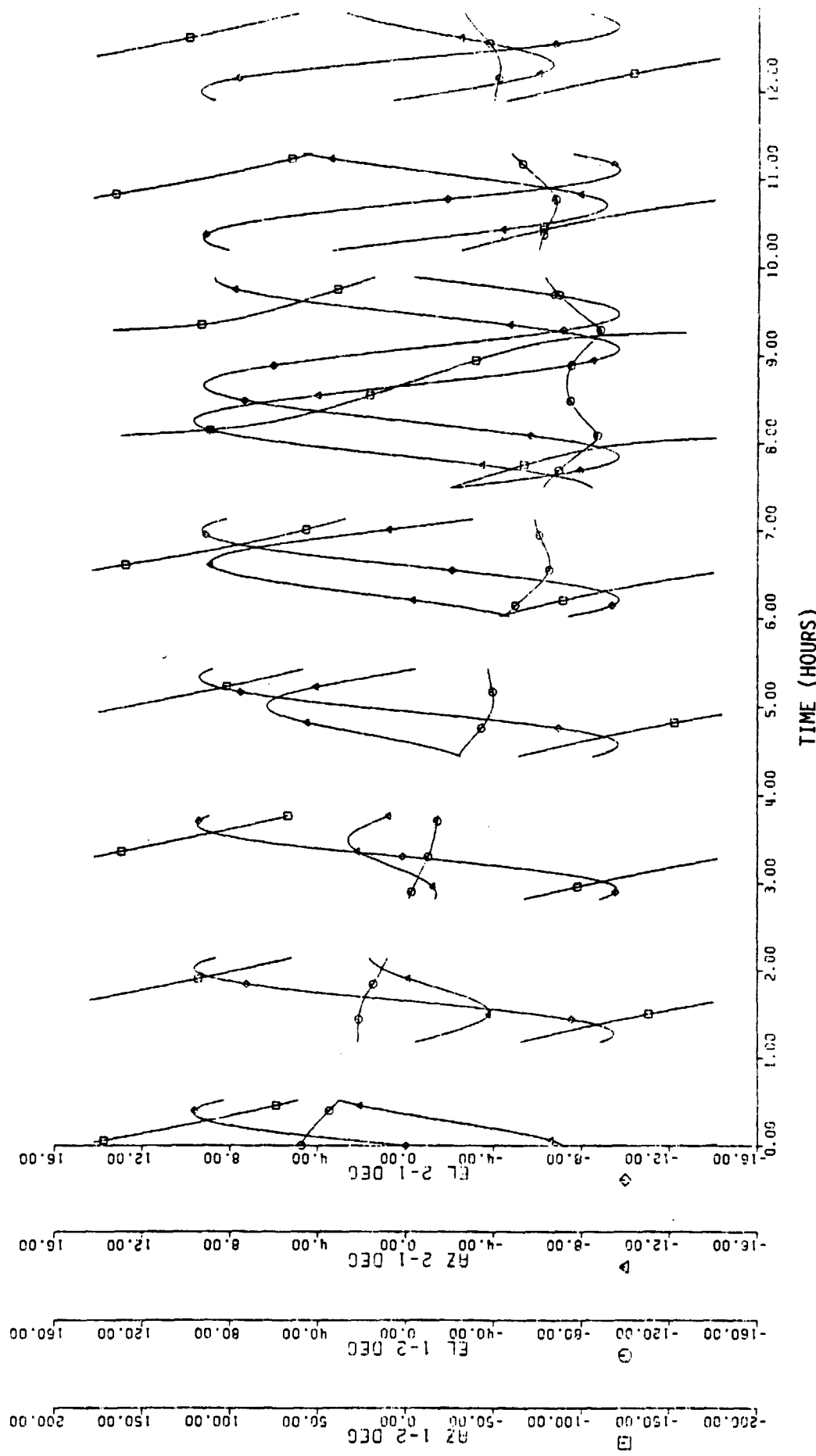


Figure 3.2-1. Pointing Angles, S/C to S/C (September)

ORIGINAL PAGE NO.
OF POOR QUALITY

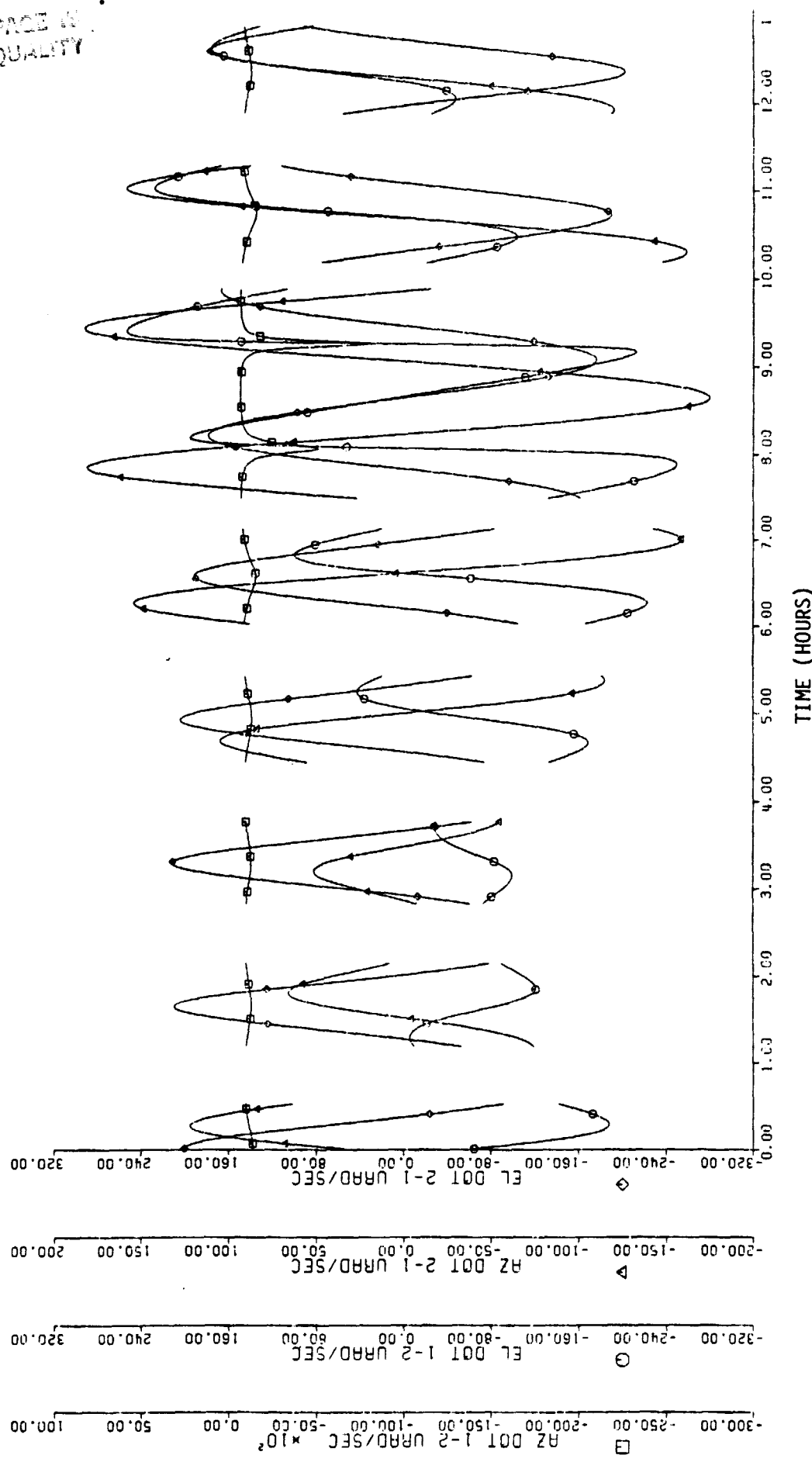


Figure 3.2-2. Pointing Rates, S/C to S/C (September)

ORIGINAL PAGE
OF POOR QUALITY

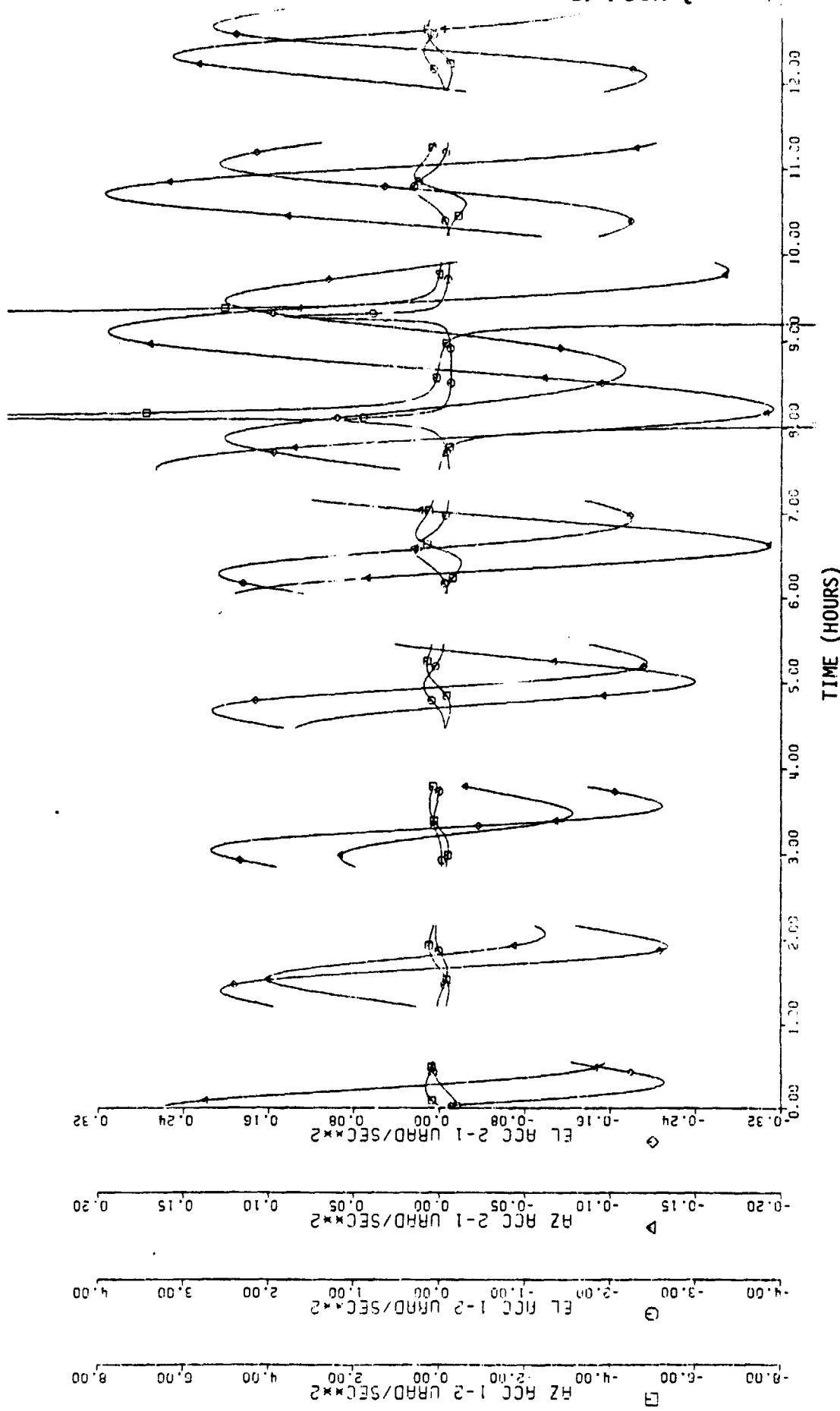


Figure 3.2-3. Pointing Acceleration, S/C to S/C (September)

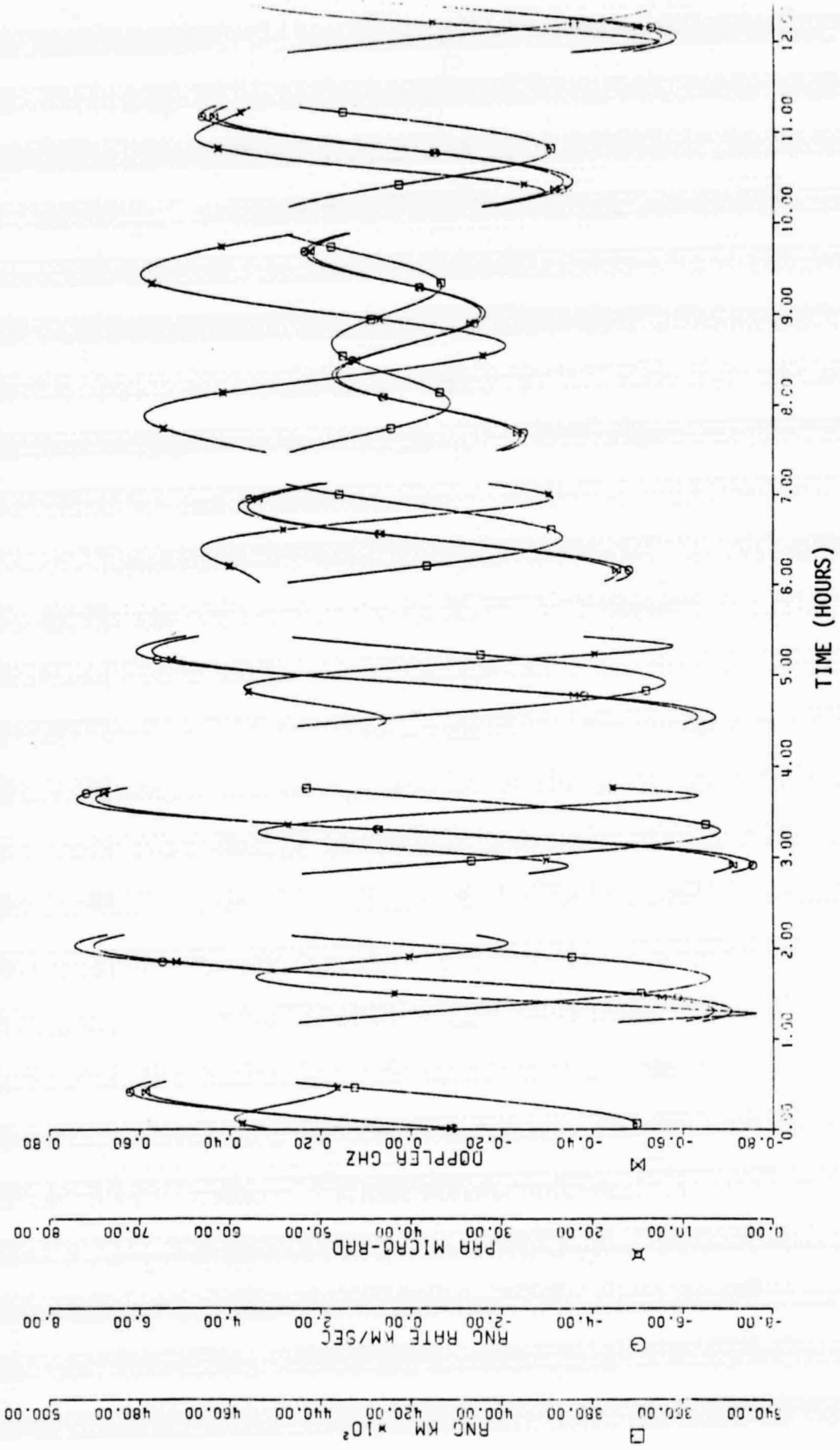


Figure 3.2-4. Point Ahead, GEO to LEO (September)

3.3 INFLUENCE BY THE SUN AND MOON

The position of the sun and moon relative to the line of sight between the LEO and GEO spacecraft are of concern. If either is within a few degrees, link outage could occur due to increased background noise on the data channel or due to link disruption caused by automatic sensor surge current protection mechanisms. The position of the sun and moon relative to the line of sight may be calculated with the orbital program. Their orientation for September, for example, is shown in Figure 3.3-1 and that for December is shown in Figure 3.3-2.

We can use this orbital information to determine the disruption periods to the communication link due to the sun or moon in the field of view. We show in Figure 3.3-3, for example, the total time that the sun is within 1° of the line of sight between the LEO and GEO. The link outage for the sun in a 4° field-of-view of the line of sight is shown in Figure 3.3-4.

Link disruption due to the sun in the field-of-view is not the only cause for link outage. The link will be disrupted when the LEO is eclipsed by the earth and also when the gimbal is within gimbal-lock range. We assume the two axis (Az, El) gimbal configuration as it is less complex than a 3 axis gimbal which would have zero time loss due to gimbal lock. We have tabulated these effects in Tables 3.3-1 and 3.3-2 for each month of the year. In Table 3.3-1, we show the percent of the time that the link is available from geometry (not earth eclipsed), time loss due to gimbal-lock and time loss for the sun within 4° of the line of sight. The associated times in time counts (1 count = 0.9375 min) are noted in Table 3.3-2. In general, link outage due to gimbal lock is less than about 33000 seconds per month (< 2.8 percent per month). Outage due to the sun within 4° of the line-of-sight is less than 180 sec per month (< 0.55 percent of the month).

Orbital constraints will not preclude operation of the link but will cause some outage. Once the actual orbits are known, the outage may be predicted.

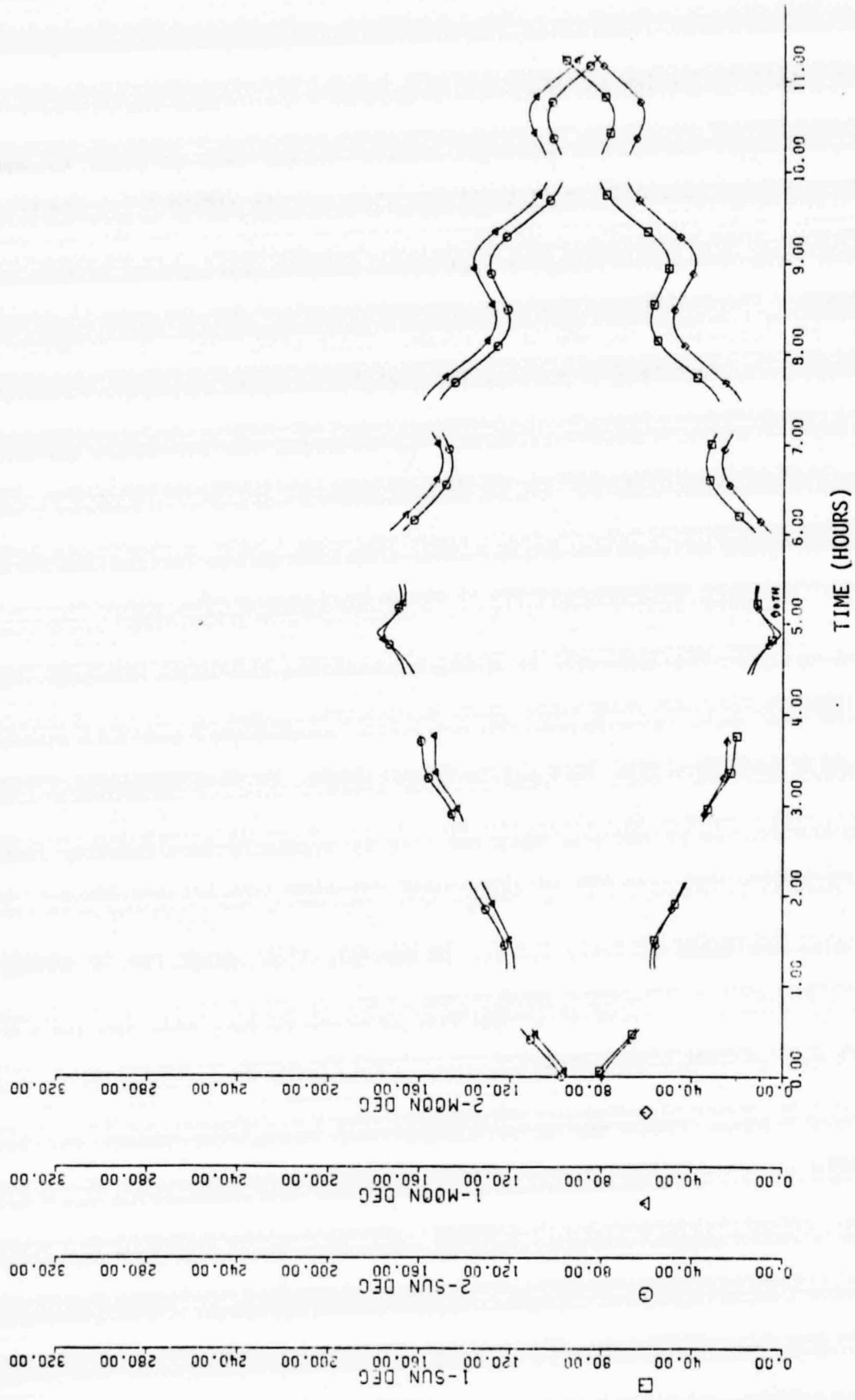


Figure 3.3-1. Sun and Moon Orientation to S/C (September)

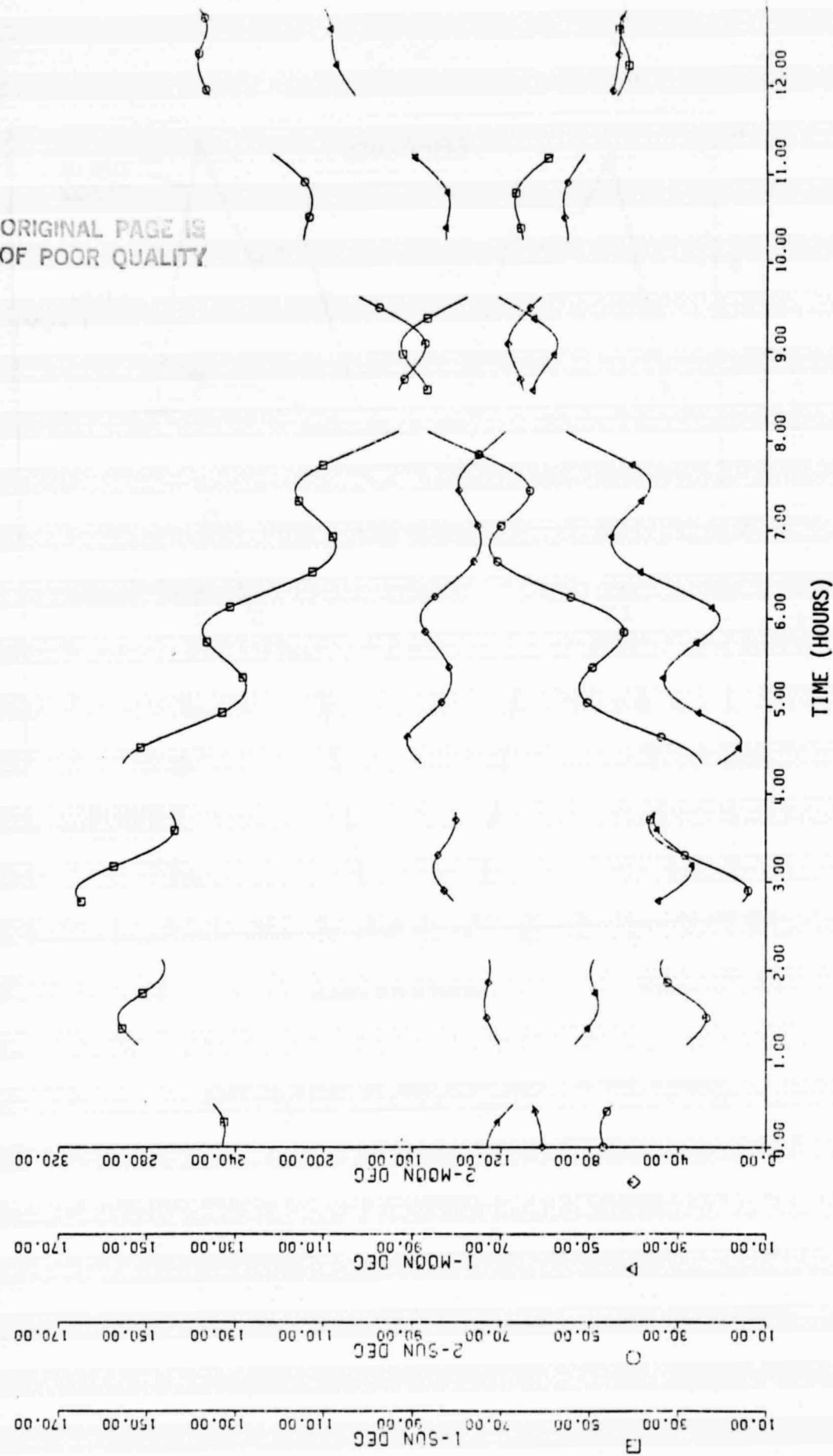


Figure 3.3-2. Sun and Moon Orientation to S/C (December)

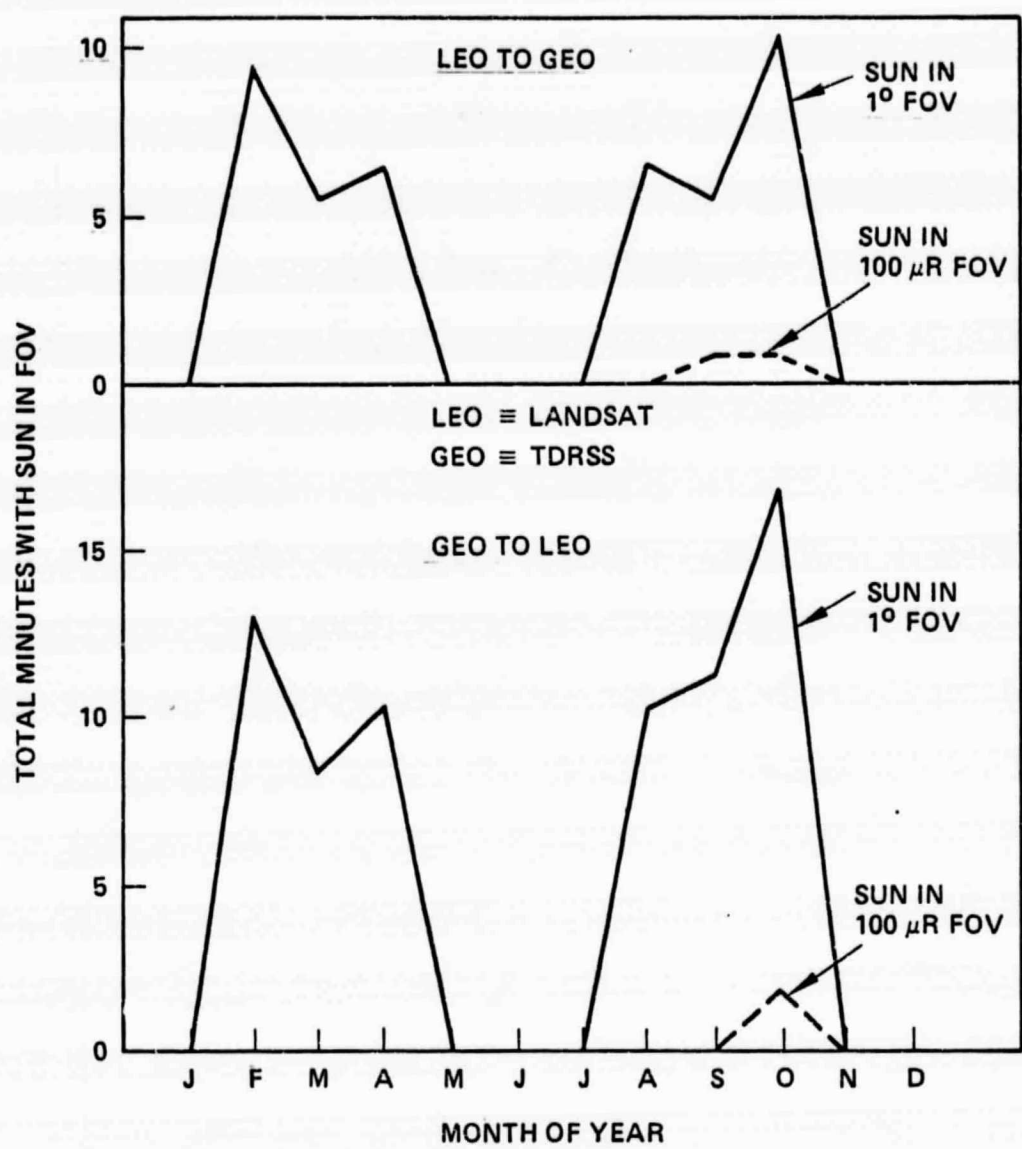


Figure 3.3-3. Time with Sun in Field of View
(100 μ rad and 1 degree)

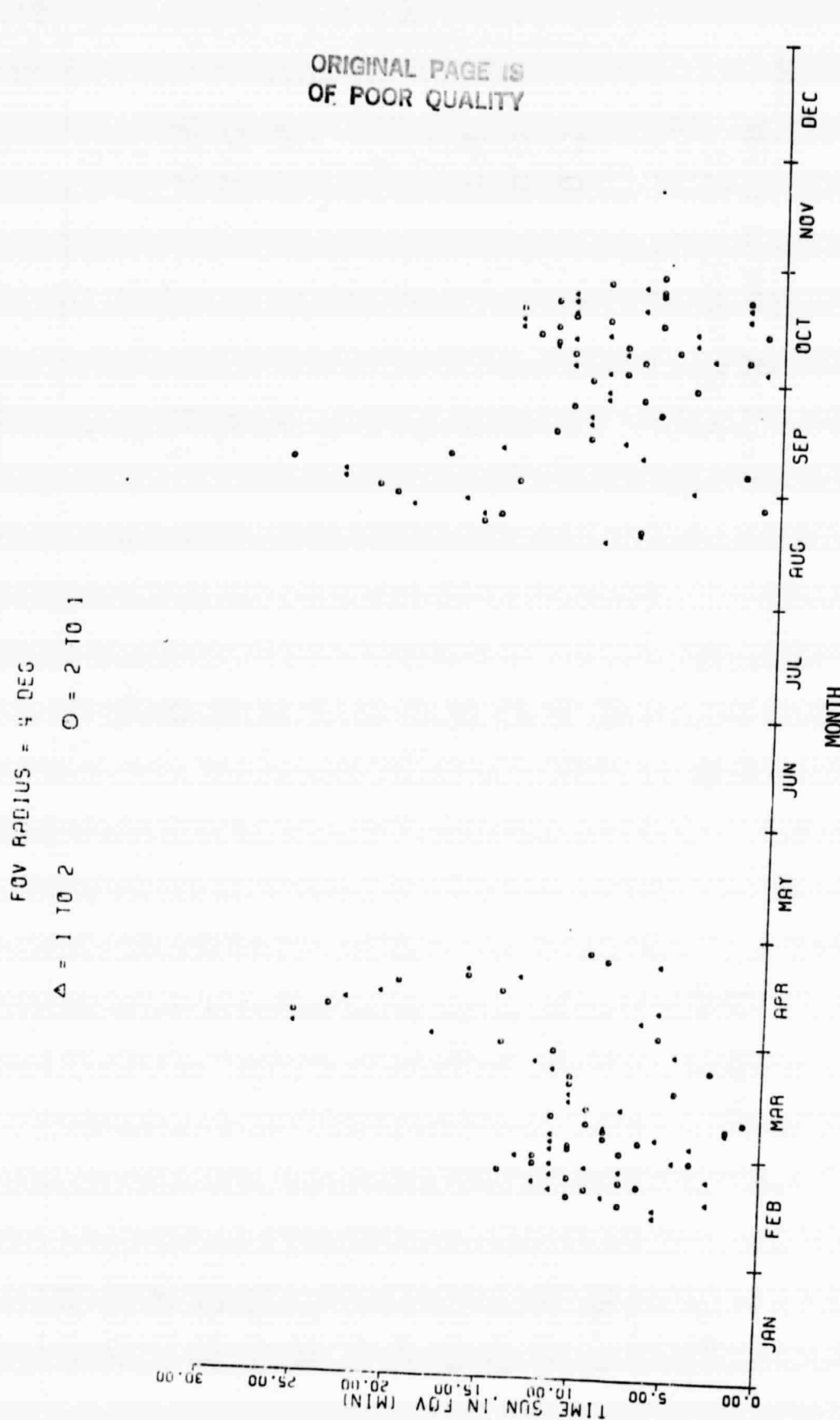


Figure 3.3.4. Outage Due to Sun in FOV (4 degree)

MONTH	AVAILABILITY - CLEAR LOS	TIME LOSS GIMBAL LOCK	TIME LOSS - SUN IN 4° FOV	
			LEO TO GEO	GEO TO LEO
JANUARY	71.0	2.693	0	0
FEBRUARY	70.9	2.745	0.37	0.33
MARCH	71.0	2.722	0.36	0.45
APRIL	70.9	2.735	0.45	0.41
MAY	71.0	2.714	0	0
JUNE	70.9	2.717	0	0
JULY	70.9	2.708	0	0
AUGUST	71.0	2.671	0.24	0.26
SEPTEMBER	70.9	2.705	0.39	0.41
OCTOBER	70.9	2.688	0.51	0.54
NOVEMBER	71.0	2.695	0	0
DECEMBER	70.9	2.719	0	0

TABLE 3.3-1. PERCENT TIME LOSS DUE TO ORBITAL GEOMETRY

(IN COUNTS, 1 COUNT = 0.9375 MIN)

MONTH	AVAILABILITY - CLEAR LOS	TIME LOSS - GIMBAL LOCK	TIME LOSS - SUN IN 4° FOV AND NOT GIMBAL LOCKED	
			LEO TO GEO	GEO TO LEO
JANUARY	33792	32882	0	0
FEBRUARY	31579	30712	113	100
MARCH	33804	32884	117	147
APRIL	32682	31788	142	130
MAY	33785	32868	0	0
JUNE	32689	31801	0	0
JULY	33758	32844	0	0
AUGUST	33805	32902	79	87
SEPTEMBER	32684	31800	125	131
OCTOBER	33775	32867	167	177
NOVEMBER	32696	31815	0	0
DECEMBER	33758	32840	0	0

TABLE 3.3-2. TIME LOSS DUE TO ORBITAL GEOMETRY

4.0 SYSTEM CONFIGURATION

4.1 CONCEPT

The configuration concept for the optical communication terminal on the LEO (Landsat) and GEO (TDRSS) satellites is needed to complete the task requirement. The configuration and design, for example, will influence the way in which the system responds to spacecraft related disturbances. In a like manner, the design will influence the response of the spacecraft to moving elements in the terminal. Similarity, size, weight and power estimates will be directly influenced by the design concept.

An optical communication system has two major subsystems; one electro-optical in nature and the other mechanical and electrical in nature. A basic block diagram is shown in Figure 4.1-1. The implementation and configuration of the system can take several forms. Since the main concern for future systems is accurate acquisition, pointing and tracking, the concepts for the system configuration were primarily based on the consideration.

Two basic concepts were evaluated. One has all optics and electro-optics, such as the laser source, receiver and associated electronics borne on-gimbal. The laser light is directed to the distant target by moving the two axis gimbal which points the electro-optical portion of the terminal. The second has only a gimbal-borne flat mirror and the electro-optical components are mounted on a nearby baseplate. The laser light is reflected and directed by the flat mirror to the distant receiver. Two axis gimballing is required as a general feature due to the orbits associated with the LEO (Landsat) and GEO (TDRSS) spacecraft.

The gimbal range for the LEO spacecraft was found by orbital analysis in section 2.0 to be $\pm 175^\circ$ Az and $\pm 140^\circ$ El. Such a range would preclude a 2 axis gimballed flat mirror concept for the LEO spacecraft. The gimbal range for the GEO spacecraft was only $\pm 20^\circ$ in Az and El and a gimballed flat mirror could be used.

ORIGINAL PAGE IS
OF POOR QUALITY

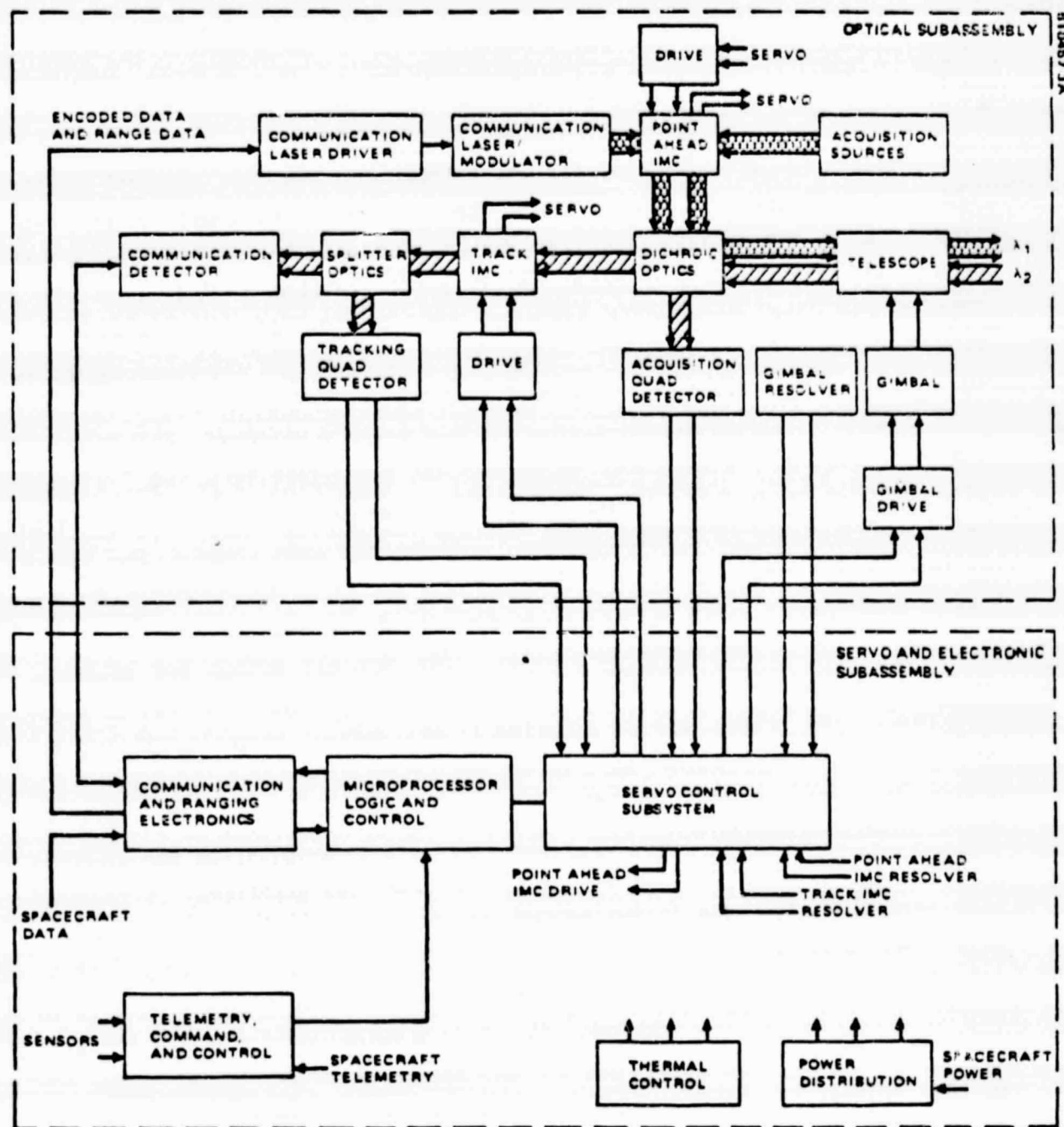


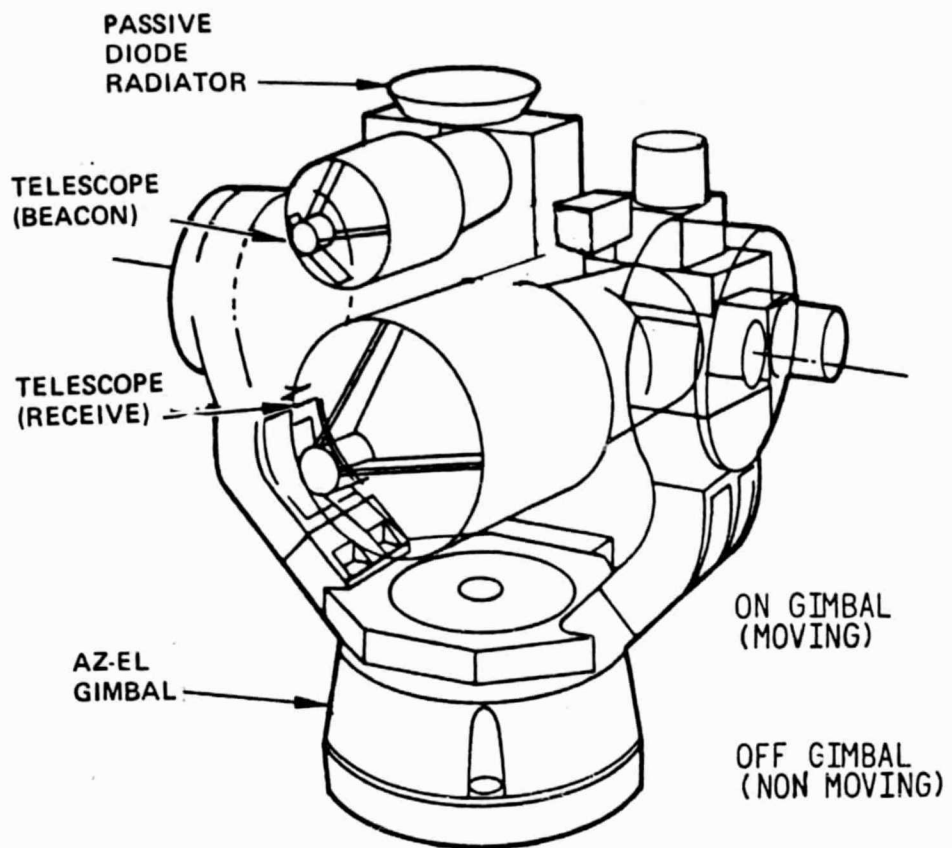
Figure 4.1-1. Basic Optical Communication System Block Diagram.

The gimballed flat mirror must be larger than the primary telescope diameter (20 inches) by at least a factor of $\sqrt{2}$. Similarly, the mirror support structure and gimbal mechanism must all be larger and more massive. As a result, the weight of either approach is the same to first order. We selected the two axis gimballed optics approach as our baseline design. In this way, the design and some subsystems and components would be identical in the LEO and GEO terminals. Recurring and non-recurring costs would be minimized.

In order to complete the baseline concept design, we evaluated the use of common versus separate optics for transmit and receive. Common optics requires dichroic elements to separate the transmit and receive wavelengths to avoid self jamming. The required isolation is of order 90 dB. Our experience with dichroic elements intended for space applications and long life has not indicated that a 90 dB isolation can be achieved and maintained. Consequently, the baseline configuration is a gimballed electro-optical system employing separate transmit and receive optics. An added benefit is that only one wavelength is required for both data link and return beacon.

The baseline configuration is noted in Figure 4.1-2. The block diagram and optical schematic of the transmitter are shown in Figure 4.1-3 and 4.1-4, respectively, and that of the receiver are shown in Figures 4.1-5 and Figure 4.1-6, respectively. The use of separate transmit and receive optics allows a rather simple optics layout as shown in the optical schematics. The point ahead optics in the transmitter and the tracking optics in the receiver are similar moveable electro-optical elements. A two axis image motion compensation (IMC) mirror assembly is used. The unit has been developed at the Hughes Electro-Optical facility. An exploded view of the two axis IMC is shown in Figure 4.1-7.

The basic block diagram for the components of the LEO spacecraft noted in Figure 4.1-3 and that for the GEO spacecraft noted in Figure 4.1-5 are similar in nature, indicating the gimballed electro-optical components approach. All support electronics are shown off-gimbal. The various electronic units required are identified. The servo control electronics are used to determine



DESIGN FEATURE	REASON
• SEPARATE TRANSMIT & RECEIVE OPTICS	<ul style="list-style-type: none"> • TRANSMIT & RECEIVE AT SAME λ • NEED TO QUAL ONLY ONE DIODE TYPE • DO NOT REQUIRE COMPLEX DICHROIC COATINGS • EASILY ACHIEVE THE REQUIRED 90 dB + TRANSMIT AND RECEIVE ISOLATION • FEWER OPTICAL COATINGS TO QUALIFY • MODULAR DESIGN • SIMPLICITY • NO OFF GIMBAL OPTICAL ROUTING
• ALL OPTICS ON GIMBAL	

Figure 4.1-2. Baseline Configuration (LEO and GEO)

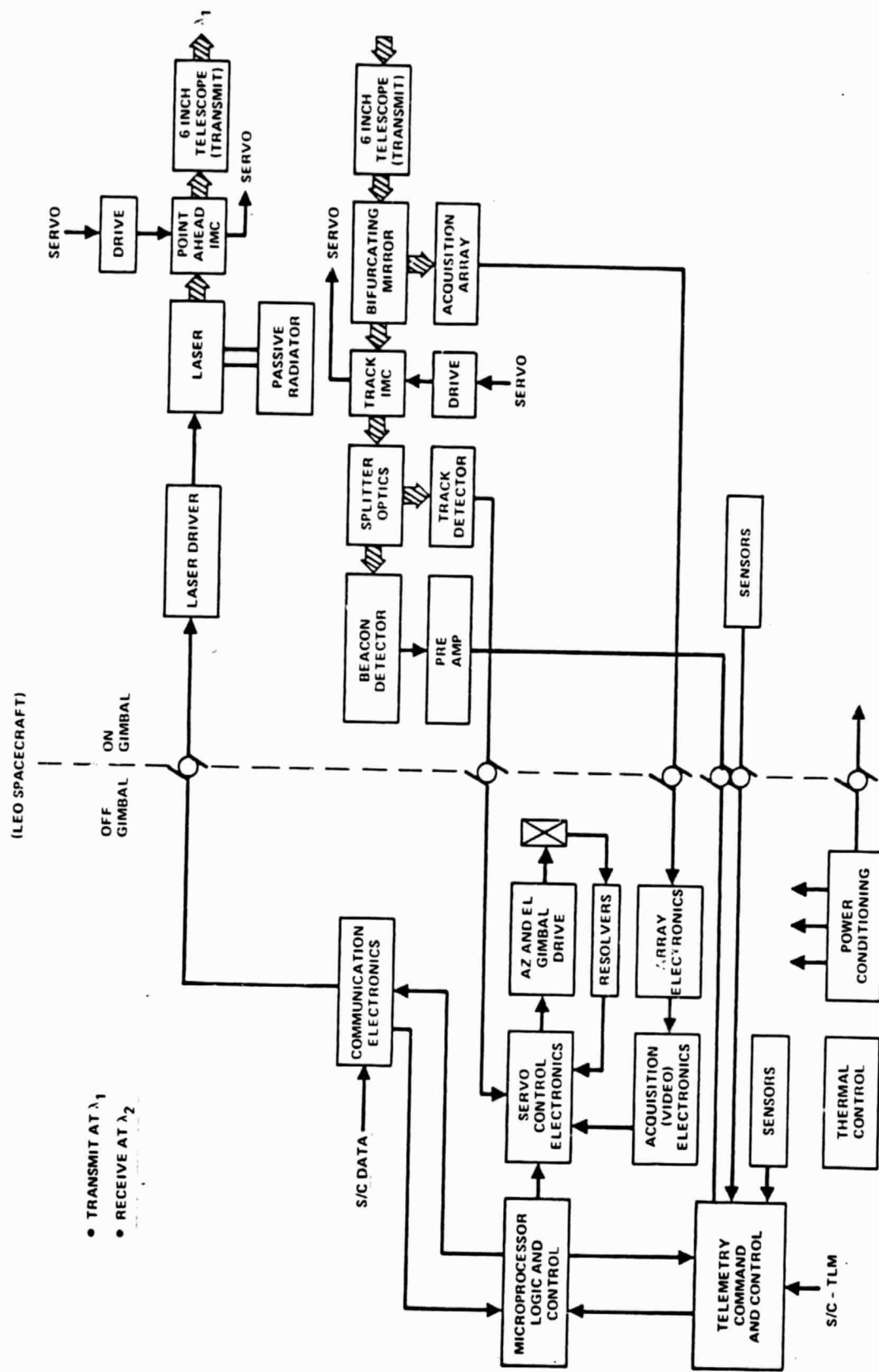


Figure 4.1-3. Basic System Block Diagram (HFO)

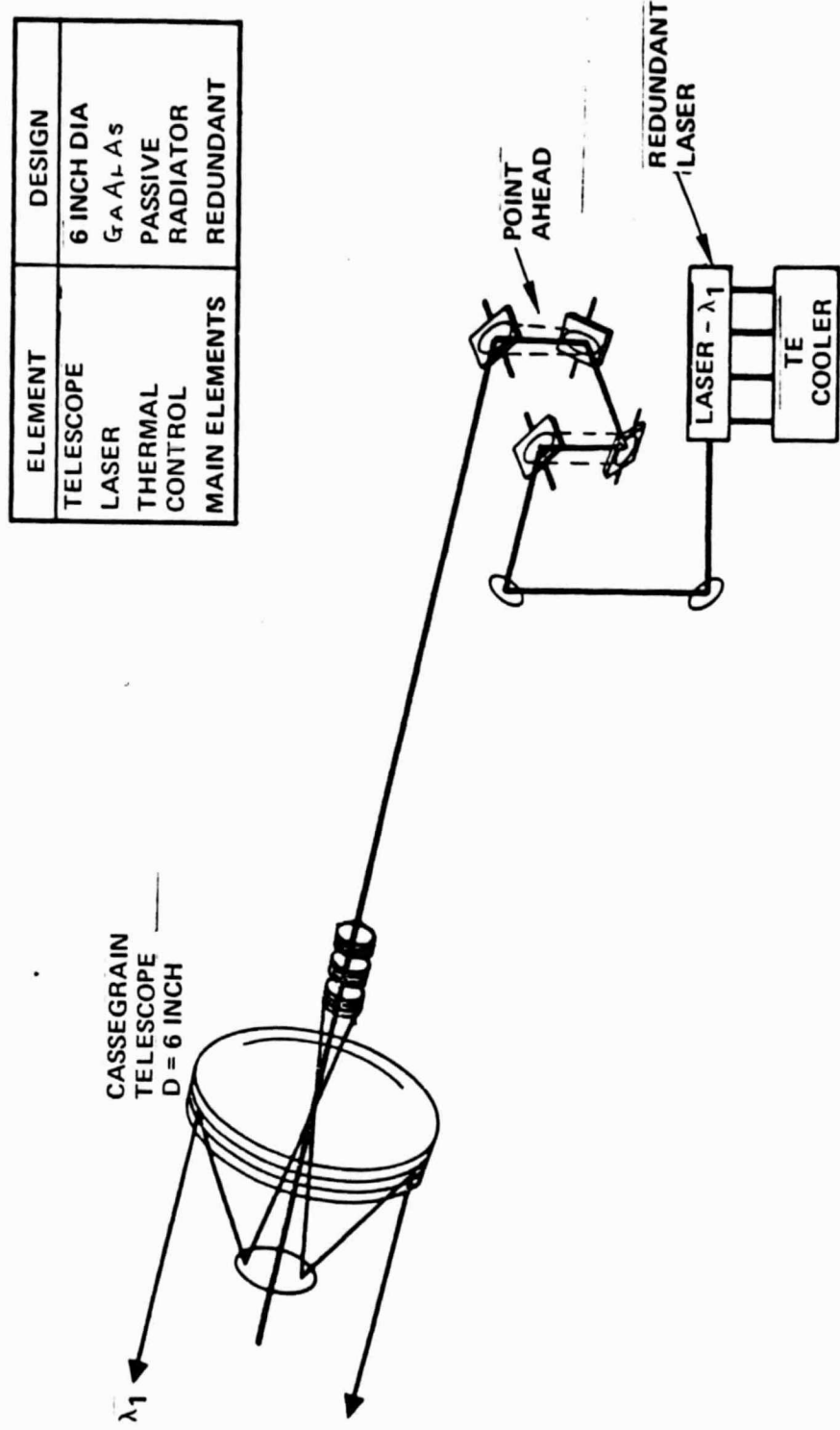


Figure 4.1-4. Optical Schematic-Data Transmitter.

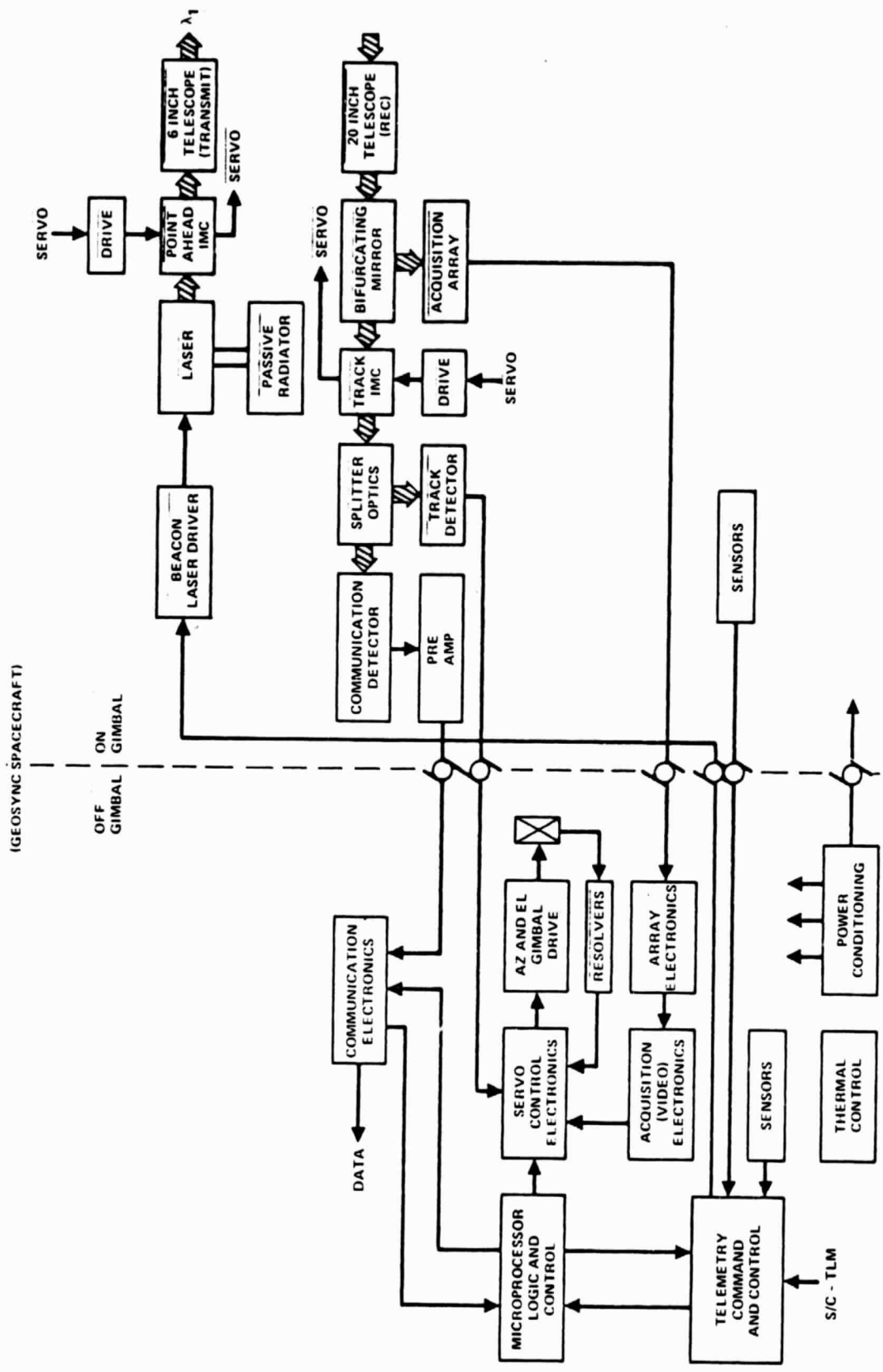


Figure 4.1-5. Basic System Block Diagram (GEO)

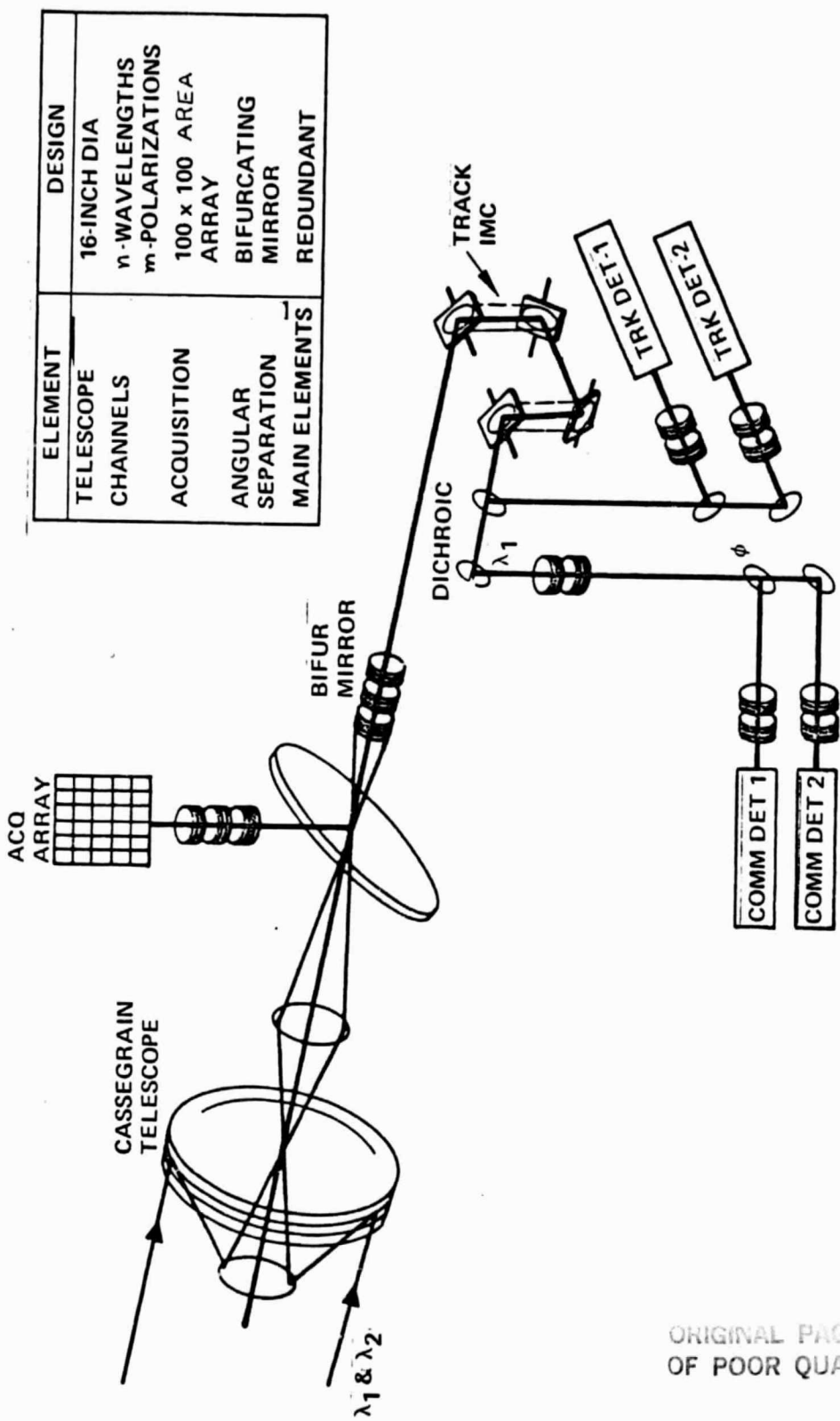
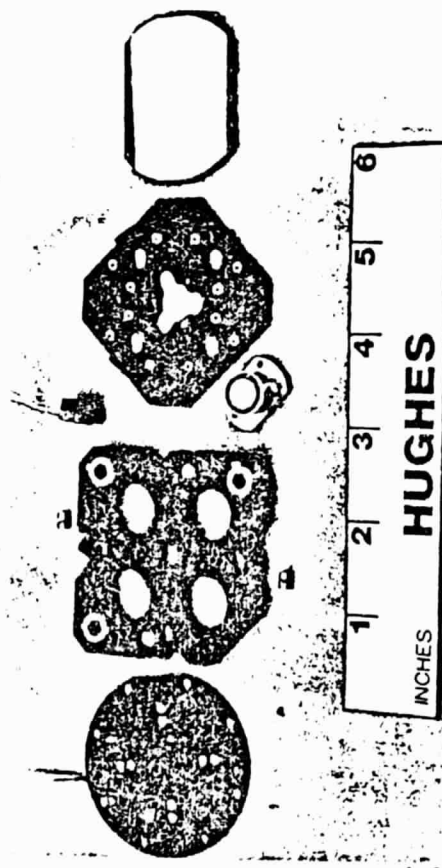
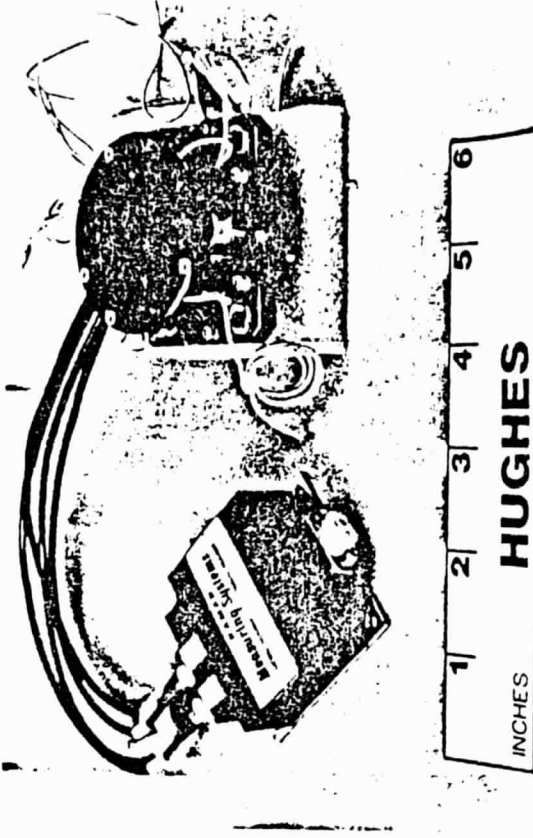


Figure 4.1-6. Optical Schematic - Data Receiver.

ORIGINAL PICTURES
OF POOR QUALITY

- A/C FLIGHT QUALIFIED
- S/C DESIGN UNDER CONSIDERATION



4-9

- MIRROR ASSEMBLY = 0.85 LB
- DRIVER = 0.5 LB
- POWER = 6 WATT

Figure 4.1-7. Two Axis IMC

the gimbal pointing and remove baseframe angular jitter from the line-of-sight. The acquisition electronics are used to deduce the angular position of the distant terminal within the large field-of-view of the acquisition sensor. Telemetry and command electronics, thermal control and power conditioning are included as required for any space terminal.

4.2 TERMINAL DESIGN FEATURES

The evaluation of terminal acquisition are described in Section 8.0. The evaluations of terminal tracking are described in Section 7.0. As a result of these evaluations, specific features of the terminal design have been identified. Other features have been identified after evalution of the requirements and orbital constraints. The resulting terminal design parameters are summarized in Table 4.2-1. Th concept design function definitions are summarized in Table 4.2-2.

It is instructive to note two features of the parameters noted in Table 4.2-1. As a result of the pointing error and burst error evaluations in Section 5.0, a maximum transmit optical diameter of 6 inches is associated with a $1-\mu\text{rad}$ (1σ) pointing error. A lesser pointing error cannot be easily maintained wiht the error baseframe vibrational noise inherent on the LANDSAT spacecraft. Smaller optics may be used for transmission of the acquisition and beacon beam from the GEO spacecraft. We use two 6 inch optical antennas in the LEO for commonality of design; one for transmit, one fore receive.

4.3 ACQUISITION CONFIGURATION

A block diagram of the acquisition/tracking function is noted in Figure 4.3-1. Note that an area array has been selected as the acquisition sensor. A bifurcating mirror provides the field-of-view reduction between acquisition and tracking. Silicon sensors are assumed since GaAlAs laser wavelengths (about $0.8 \mu\text{m}$) are used. The component selection for the acquisition and tracking functions are identified in Sections 7.0 and 8.0.

TABLE 4.2-1. TERMINAL CONCEPT DESIGN PARAMETERS

Property	GEO	LEO
• Concept	• Separate Transmit and Receive Optics	• Separate Transmit and Receive Optics
• Transmit Optics	• 2.3 Inch Diameter	• 6 Inch Diameter
• Receive Optics	• 20 Inch Diameter	• 6 Inch Diameter
• Primary Material	• Beryllium	• Beryllium
• Acq Sensor	• Si-Quad	• Si-Array
• Track Sensor	• Si-Quad (APD)	• Si-Quad (APD)
• Comm Sensor	• Si-APD	• SI-APD
• Laser Source	• GaAlAs	• GaAlAs
• Transmit Wavelength	• Beacon (LDR) = 0.85 μm	• Comm (HDR) = 0.83 μm
• Receive Wavelength	• Comm (HDR) = 0.83 μm	• Beacon (LDR) = 0.85 μm
• Gimbal	• Two Axis-Optics on Gimbal	• Two Axis - Optics on Gimbal
• Az Range	• $\pm 20^\circ$	• $\pm 175^\circ$
• El Range	• $\pm 20^\circ$	• $\pm 140^\circ$
• Weight (with redundancy)	211.5 lb	175.2 lb
• Power	• 143.1 watt	• 137.8 watt

TABLE 4.2-2. CONCEPT DESIGN FUNCTION DEFINITIONS

Function	Design	Parameter
Acquisition	<ul style="list-style-type: none"> ● Concept ● Field-of-Regard ● Angular Scan Rate ● Laser Wavelength ● Laser Power ● Beamwidth ● Acquisition Sensor ● Acquisition Time 	<ul style="list-style-type: none"> ● Initiated by GEO ● 0.5 deg Cone for GEO and LEO ● 1.6 deg/sec ● 0.85 μm ● 50 mW - CW ● 130 μrad (full Airy Lobe) ● Nominal 400 x 500 area array on LEO Quad Cell on GEO ● <u>< 2 minutes</u>
Tracking	<ul style="list-style-type: none"> ● Concept ● Field-of-View ● T C Wavelength ● T C Data Rate ● GEO Beacon Power ● GEO Beacon Beamwidth ● GEO and LEO Sensor 	<ul style="list-style-type: none"> ● GEO Tracks on Data Uplink ● LEO Tracks on T C Downlink ● 140 μrad full Sensor, 13.7 μrad Closed Loop ● 0.81 μm ● 10 Kbps ● 20 mW - CW ● 35 μrad (full Airy Lobe) ● APD - Quad Cell
Communications	<ul style="list-style-type: none"> ● Concept ● Power ● Beamwidth ● Data Rate ● Wavelength 	<ul style="list-style-type: none"> ● Multisource Summing Device ● 200 mW - Average ● 10 μrad ($1/E^2$)* ● 500 MBPS ● 0.8 - 0.9 μm
Point Ahead	<ul style="list-style-type: none"> ● Concept 	<ul style="list-style-type: none"> ● Closed Loop Update via T & C Link for LEO Uplink ● Minor Update for GEO Downlink

* Not consistent with burst error requirements and 1 μ rad pointing capability

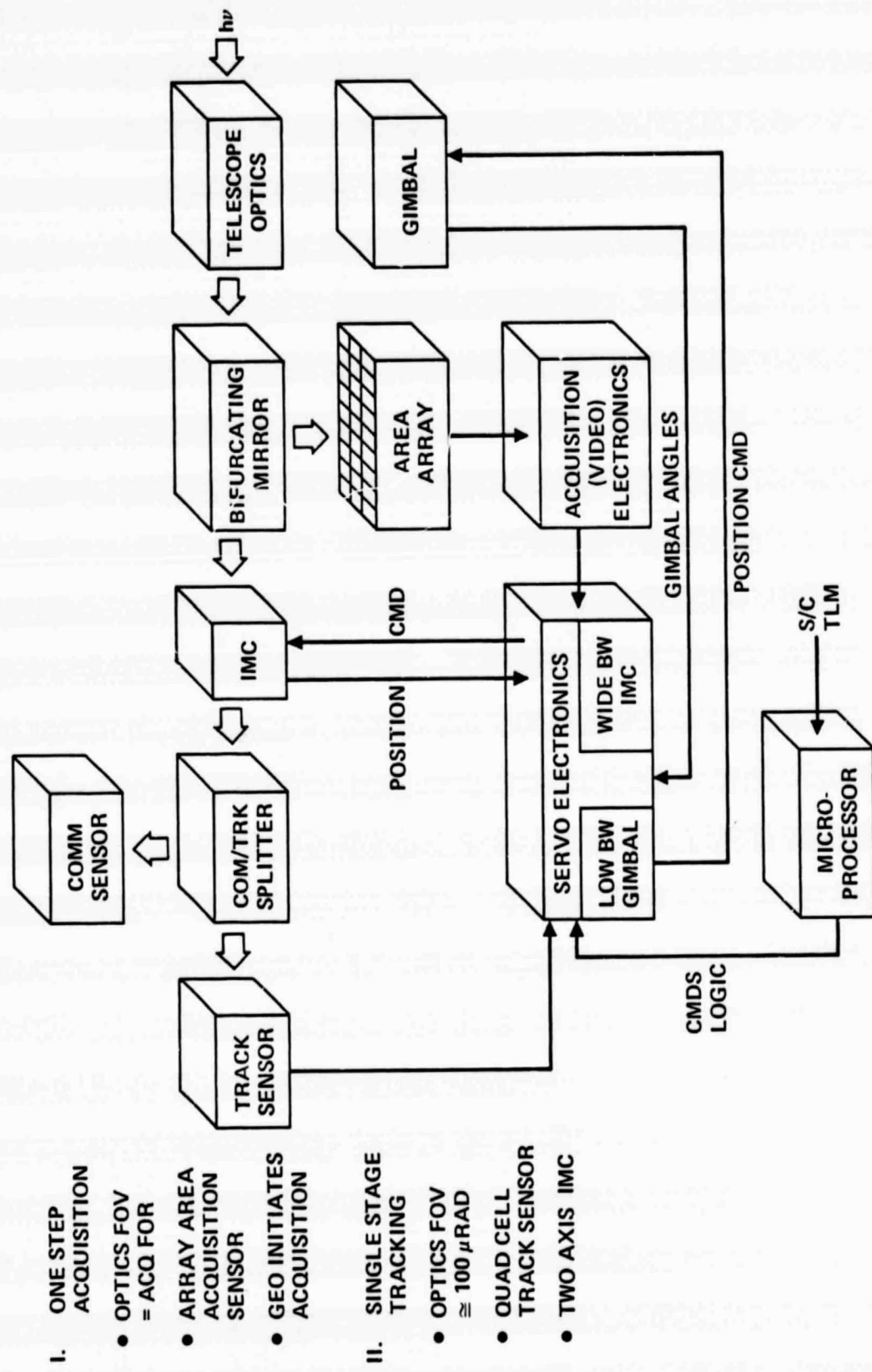


Figure 4.3-1. Acquisition/Tracking Basic Block Diagram

5.0 BURST ERROR

5.1 INTRODUCTION

Free space optical communications between satellites can be considered to involve three major system control functions: a) the laser aided acquisition of one satellite with the other leading to the fine pointing of the communication beam to the receiver, b) the maintenance of the cooperative tracking and tracking between opposite terminals and c) the continued operation of the data transfer channel. These system functions are interrelated, involving many of the same electro-optical components.

The data transfer channel and its electro-optical components have been extensively developed and tested in the laboratory over the last decade [1-16]. The pointing and tracking features have also received attention, but with not as much emphasis [17-23]. The lack of detailed attention, in comparison to that given to the communication subsystem, is apparently the result of the opinion that the pointing and tracking function is limited more by engineering than by technology. The pointing and tracking subsystem uses gimbals, servo control electronics, optical sensors and beam motion mirror devices. Most of these components have been used in other systems, are not necessarily state-of-the-art, and their performance is predictable by appropriate analysis. However, although the subsystems have received some ground and aircraft study, little is known of the satellite environment. Information regarding satellite attitude control and platform stability at the appropriate accuracies and angular motion rates (μ rad and mrad/sec, respectively) have only recently become available.

As such, the pointing and tracking simulations in the terrestrial environment can be considered as only order of magnitude correct for any space application. We develop the relations which connect the main parameters of the pointing and tracking subsystem with those of the communication subsystem.

We also identify the pointing and tracking related constraints on the application of an optical communication system to space. The constraints lead to design limits for the optical communication terminal and associated restrictions in its successful implementation for space missions.

5.2 SYSTEM CONFIGURATION

Angular pointing and tracking between two satellite-borne optical communication terminals may be accomplished only by cooperative means as a result of the large distance and rather low laser power levels available. Each satellite terminal emits a laser signal which is a tracking beacon for the other terminal. Only after an accurate line-of-sight (LOS) is established and accurate pointing maintained, may successful data transfer occur. Mispointing between terminals leads to system performance degradations and continuous accurate pointing is required for optical communication systems as they employ rather narrow beam widths.

The accuracy of beam pointing is dependent upon many parameters, some of which are not specifically related to the optical communication system. Such parameters are inherent with the host satellite and include: a) satellite attitude instabilities, b) satellite ephemeris algorithm errors, and c) system baseframe vibrational noise. Accurate beam pointing is also dependent upon system related factors such as: a) the tracking sensor noise, b) signal timing errors, c) microprocessor computational errors and d) mechanical misalignments. These factors are normally combined in rms fashion to yield the system pointing error value. As a result, the accuracy of beam pointing will be recognized as a primary system design requirement rather than a parameter of choice.

Although the pointing and tracking control system is distinct from the communication system, the two are interrelated in defining the performance possible with a system operating in the disturbance environment of the host satellite. This interrelationship is best seen by considering the basic system block diagram shown earlier in Figure 4.1-1, and the basic optical layouts which were shown schematically in Figures 4.1-4 and 4.1-6 [20]. It is

shown in the figures that the system incorporates two functional parts: the opto-mechanical part responsible for transmission and reception of the laser light, and the electronic control part responsible for the dynamic control (that is, pointing and tracking) of the optomechanical part.

In Figure 4.1-4, the light path for tracking of the beacon light from a distant terminal is illustrated by the dark line and the reverse light path for data transmission is noted by the dark line in Figure 4.1-6. The basic optical, mechanical and opto-mechanical elements required for the two inter-related functions are noted in the figure.

Two opto-mechanical elements are especially important for accurate pointing. The first is the image motion mirrors which are used to orient and compensate for LOS angular jitter induced by mechanical and baseframe disturbances on the host satellite. The second is the point ahead mirrors which are used to provide the angular pointing angles required due to relative motion between the two satellites.

As shown in Figure 4.1-4 and Figure 4.1-6, portions of the optical path are common to the pointing and tracking functions while other portions are dedicated to only one function. Consequently, the errors associated with mistracking are different from those associated with mispointing. The pointing errors are greater than the tracking errors since the former are dependent upon the latter and must also incorporate the errors associated with additional opto-mechanical devices, such as the point ahead elements.

Point ahead error is basically a low frequency, almost static offset related to the angular bias from the LOS between the two satellites due to the range related time delay for light transfer from one terminal to the other. The point ahead error is associated with ephemeris errors, algorithm errors and alignment errors. Additionally, the point ahead device must also incorporate higher frequency compensation unless another such element is used to correct for satellite induced pointing errors associated with attitude instabilities and baseframe vibrations.

The manner in which the various noises contribute to the tracking error is indicated by the simplified servo control block diagram shown in Figure 5.2-1. The main noise contributions to the tracking function may be

summarized as: a) mechanical and thermal base motion disturbances to the coarse and fine track loops, b) electronic noise associated with process logic and basic electronic circuitry and c) sensor noise which includes dark current, excess noise due to gain, thermal noise and optical background noise. The sensor noise may be interpreted as a noise equivalent angle (NEA) thereby establishing a lower limit to the tracking and pointing error.

5.3 POINTING ERRORS

The performance of a free space, satellite-borne optical communication system is described by two major parameters: the probability of bit error and the probability of burst error. The probability of bit error is normally specified as a system requirement. It determines the nominal signal intensity required to recover the signal from the communication channel with its contributory noises. The nominal probability of bit error is proportional to the signal and noise counts received during the bit time interval [7, 8, 24]. The probability of burst error on the other hand, is frequently ignored as it is not directly dependent upon the optical signal and noise levels. The probability of burst error establishes the percent of time that the servo system will maintain pointing within some error limit. Should the pointing error ϵ become greater than some value ϵ^* , the signal intensity at the distant receiver would be decreased, and the system performance described by the probability of bit error would be degraded.

There are several parameters which are commonly used to describe the nature of mispointing. These include: a) the radial angular mispoint error denoted by ϵ and b) the rms standard deviation σ of the probability distribution for mispointing, $P(\epsilon)$. We will first determine the proper relationship between ϵ and the standard deviation σ . We will examine the relationship between the probability distribution $P(\epsilon)$ and the desired communication channel performance as measured by the probability of bit error. We will then determine the relationship between the radial pointing error and the beamwidth a .

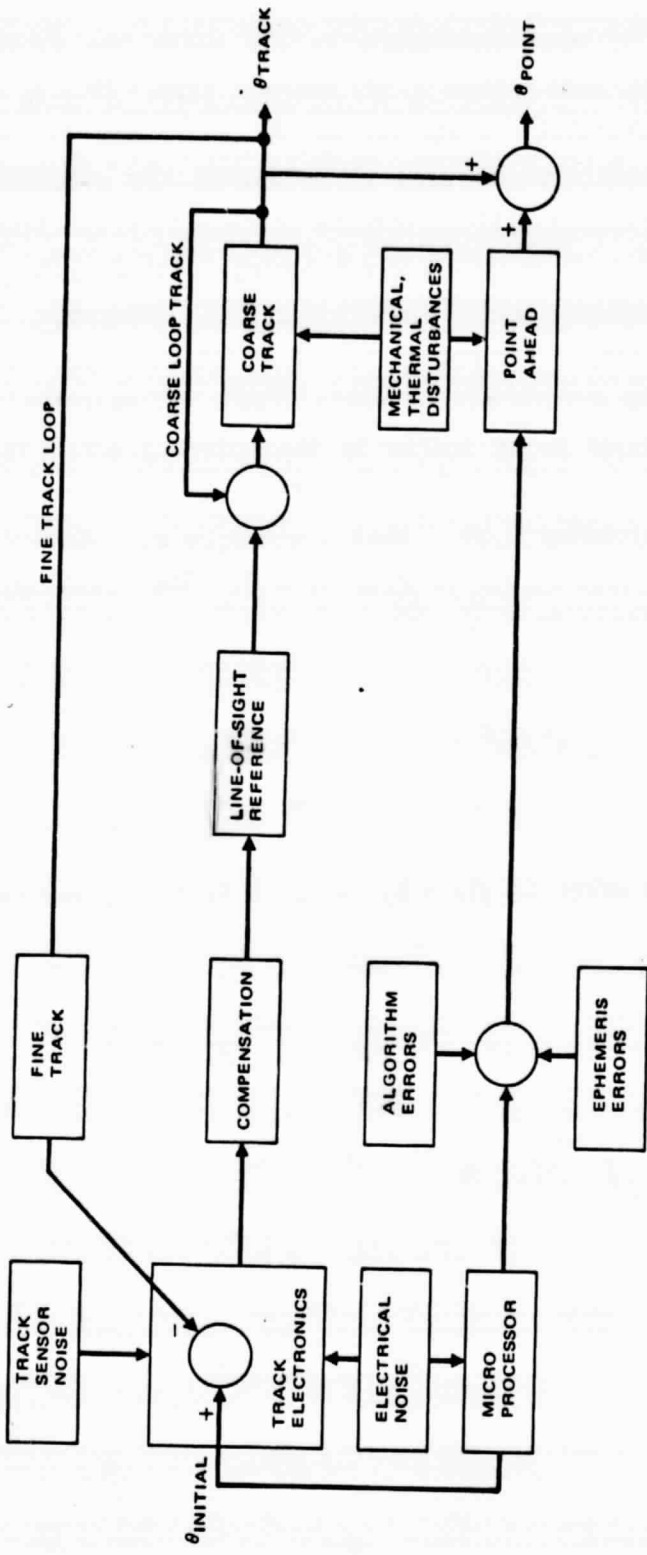


Figure 5.2-1. Simplified servo control block diagram indicating the major functions and the major noise sources leading to mistracking and mispointing.

The parameter is most importance is σ/α since the pointing error ϵ is normally defined as some value γ at the $N\sigma$ level ($N = 1, 2$ or 3). The pointing error probability distribution P_{ϵ}^* in terms of the ration σ/α . the parameter σ/α can also be used to establish the practical limit on the diameter D of the transmit optical antenna since α is proportional to $1/D$.

We assume a two axis pointing and tracking control system incorporating a quadrant tracking detector and a gimballed optical subsystem. We describe the single axis probability distribution for mispoint as a gaussian function with single axis pointing errors of ϵ_x and ϵ_y [22]. A gaussian distribution is assumed since the major noise source to the pointing error is usually sensor noise. The gaussian function has rms standard deviations σ_x and σ_y . We assume radial symmetry so that $\sigma = \sigma_x = \sigma_y$ and $\epsilon = (\epsilon_x^2 + \epsilon_y^2)^{1/2}$ and require a normalized $P(\epsilon)$; $\int_0^\infty P(\epsilon) d\epsilon = 1$. The radial probability distribution, in normalized form, may be recognized as the Rayleigh distribution,

$$P(\epsilon) = \frac{\epsilon}{\sigma^2} e^{-\epsilon^2/2\sigma^2} \quad (1)$$

The nominal pointing error is given by $\bar{\epsilon} = \int_0^\infty P(\epsilon) \epsilon d\epsilon$ and has the solution, $\bar{\epsilon}/\sigma = \sqrt{\pi/2}$.

The probability of burst error is of prime importance here and is given by,

$$P_E^* = \int_{\epsilon^*}^{\infty} P(\epsilon) d\epsilon \quad (2)$$

The solution of Equation 2 yields,

$$\epsilon^*/\alpha = \sqrt{\frac{2(-\ln P_E^*)}{E}} \quad (3)$$

which essentially establishes the probability of burst error possible given the single axis gaussian pointing error distribution inherent with a system operating within the limits imposed by the host satellite. In a like manner, one may specify P_E^* and given the pointing error probability distribution with its characteristics α , the required pointing error must be maintained at $\epsilon \leq \epsilon^*$.

The ratio ϵ^*/α can be related to the beamwidth α , and consequently, the system may be designed to operate at the desired performance level for all $\epsilon \leq n^*$. We remember that the bandwidth so defined will be consistent with the burst error probability. The intensity of the received beam power at $\epsilon = \epsilon^*$ must be sufficiently large enough to maintain the nominal probability of bit error at the desired level.

We determine the relationship between the pointing error $\epsilon = \epsilon^*$ and the basic system optical design parameter (the beamwidth α), by considering the optical power collected at the distant satellite receiver,

$$P(\epsilon, \alpha) = \frac{I(\epsilon, \alpha) L_0 A_R P_0}{\pi R^2 \alpha^2} \quad (4)$$

where L_0 represents the various optical losses in the transmitter and receiver ($L_0 \leq 1.0$), $A_R = D^2/4$ is the area of the receiver optical antenna, D is its diameter, R is the distance between satellites, P_0 is the laser power, and $I(\epsilon, \alpha)$ is the far field beam profile. We use the symbol ϵ here for the angular mispoint at its interpretation as ϵ or ϵ^* is not important. The far field beam profile is the Airy function given as

$$I(\epsilon, \alpha) = I_0 \left[\frac{2J_1(2.44\pi \epsilon/\alpha)}{2.44\pi \epsilon/\alpha} \right]^2 \quad (5)$$

where J_1 is the Bessel function of the first kind. The full Airy beamwidth to the first dark ring in the diffraction pattern is given by

$$\alpha = 2.44\lambda/D \quad (6)$$

It is frequently thought that by minimizing the pointing loss relative to the beamwidth selected to achieve the desired probability of bit error performance, the communication channel would be optimized. However, Equation 4 can be solved for the optimum value of the beamwidth relative to the pointing error which is inherent in the implementation of the system on the host satellite. It is optimized by setting,

$$\frac{dP(\epsilon, \alpha)}{d\alpha} = 0 \quad (7)$$

The solution to Equation 7 relates the channel beamwidth to the mispoint angle used in the link budget as,

$$\epsilon^*/\alpha = 0.24 \quad (8)$$

The point at which this falls on an Airy far field beam profile is shown in Figure 5.3-1. The nominal mispoint loss which should be used in link budget summarizes is about -4 dB.

The primary optical system design parameter was noted earlier as the ratio α/σ which defines the optical beamwidth needed to maintain system operation at the desired probability of bit error. Combining Equations 3 and 8, we find,

$$\frac{\alpha}{\sigma} = \sqrt{\frac{0.17}{(-\ln P_E^*)}} \quad (9)$$

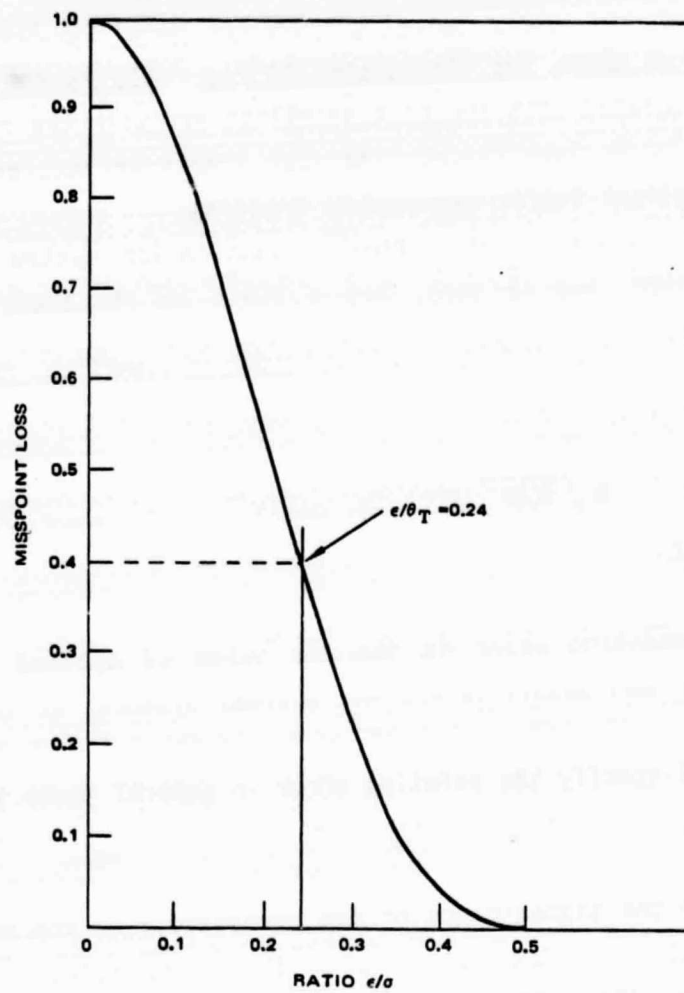


Figure 5.3-1. Mispoint factor (loss) as a function of the ratio of the pointing error to the beamwidth.

where it will be remembered that σ is the rms standard deviation of the pointing error distribution as determined by the dynamics of the host satellite and the operation of the optical system.

The degree of accurately pointing from one satellite-borne terminal to the other, as noted above and illustrated in Figure 3, is dominated by noise error sources associated with the host satellite and with the operation of the optical system. As we have placed practical limits on accurate pointing, we can establish practical limits on accurate tracking.

The tracking sensor in an optical communication system is normally a quadrant type sensor, and as such, has a limit to its tracking accuracy Δ given by [25],

$$\Delta = \frac{\pi \delta}{8\sqrt{S/N}} \quad (10)$$

5.4 SYSTEM EXAMPLE

The system pointing error is the rms value of various error sources contributed by the host satellite and the optical system. It is not possible here to provide an allocation to each noise source as such is application dependent. We will specify the pointing error in general terms as a value $\epsilon = \epsilon^*$ relative to the desired burst error P_E^* over a range of representative values.

We illustrate the significance of the probability of the burst error in terms of α/ϵ by plotting the relationship in Figure 5.4-1. We note that Equation 9 specifies the optimum power collected at the receiver. We have also summarized a number of the relevant example parameters in Table 5.4-1. We use a wavelength of $\lambda = 0.83 \mu m$ consistent with the Al(GaAs) laser diode optical source.

It may at first seem surprising that the ratio of the beamwidth to the standard deviation of the radial pointing error distribution is larger than about 5 to 1 as was assumed or implied by earlier evaluations [7,8]. The cause of this increase is that the communication system is directly influenced

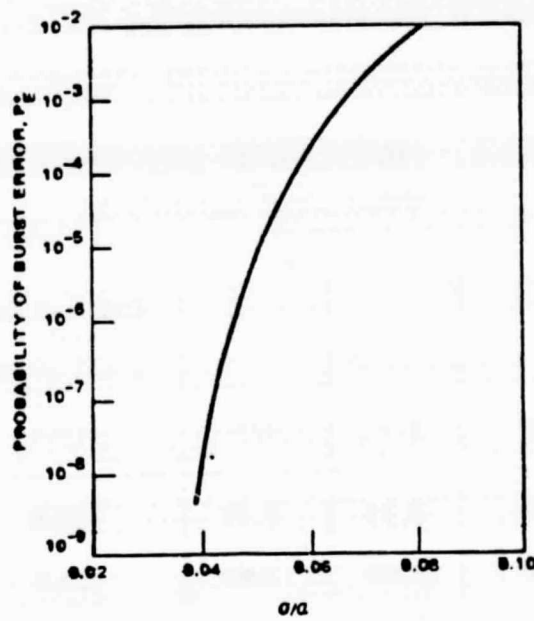


Figure 5.4-1. Variation of the probability of burst error as a function of the ratio of the radial rms standard deviation to the optical beam width.

by the probability of burst error and was not so considered in the earlier evaluations. A burst error of say, $P_E^* = 10^{-3}$, would require a beam-width $\alpha = 15.4 \mu\text{rad}$ when $\sigma = 1 \mu\text{rad}$, whereas a burst error of $P_E = 10^{-6}$ would require $\alpha = 22.1 \mu\text{rad}$ when $\sigma = 1 \mu\text{rad}$. A burst error of, say, $P_E^* = 10^{-3}$ means that a system initially configured to have a probability of bit error of, for example, $P_E = 1 \times 10^{-6}$, would have a temporal availability of only 0.999 as a result of the burst error. It would have degraded performance for 0.1 percent of the time and the probability of bit error would be $> 1 \times 10^{-6}$ since P_E is strongly dependent upon signal intensity [23,26]. Hence, operation of the system at the optimum beamwidth once σ and P_E^* are known is necessary to maximize performance.

TABLE 5.4-1. EXAMPLE SYSTEM REQUIREMENTS UNDER
BURST ERROR LIMITATIONS

System Availability (percent)	PBE	ϵ/σ	α/σ	Optimum Antenna Diameter for $\sigma = 1 \mu\text{rad}$ and $\lambda = 0.83 \mu\text{m}$ (inch)	Relative Power Required (dB)
90	10^{-1}	2.13	8.86	22.8	0.0
99	10^{-2}	3.03	12.60	16.1	3.1
99.9	10^{-3}	3.70	15.39	13.2	4.8
99.99	10^{-4}	4.28	17.80	11.4	6.1
99.999	10^{-5}	4.79	19.93	10.2	7.0
99.9999	10^{-6}	5.25	21.84	9.3	7.8

We also note that the correct pointing error loss which should be used in link budget and performance tabulations is not about -0.2 dB ([7,8] but rather about -4 dB. This results from the intensity decrease in the Airy profile as given by Equation 5 when the optimum ratio $\sigma/a = 0.24$ per Equation 8 is included. This -4 dB pointing error loss can significantly influence the long term performance of a communication system if ignored and insufficient power margin is allocated.

As an illustration of the influence of mispointing on the optical system design, we have combined Equations 6 and 9 to relate σ to the telescope diameter D , so that

$$\sigma D \approx \frac{\lambda}{2.4 \sqrt{(-\ln P_E^*)}} \quad (11)$$

We illustrate the result in Figure 5.4-2 for $\lambda = 0.83 \mu\text{m}$. We have included curves for several representative values of the burst error P_E^* . We note, for example, that for $P_E^* = 10^{-5}$ and $\sigma = 1 \mu\text{rad}$, the optimum transmit telescope diameter to maximize the power collected at the receiver is about 10 cm. The curious but inescapable conclusion is that once the 1σ value of the pointing error distribution has been determined for the optical communication system due to the environment on the host satellite and its performance in that environment, and the desired burst error selected, the optimum value of the transmit antenna is specified by Equation 11, and larger or smaller diameters only lead to degraded performance.

We can also evaluate the implications to the tracking sensor and its servo control loop by combining Equations 6 and 10

$$\Delta D = \frac{2\lambda}{\sqrt{S/N}} \quad (12)$$

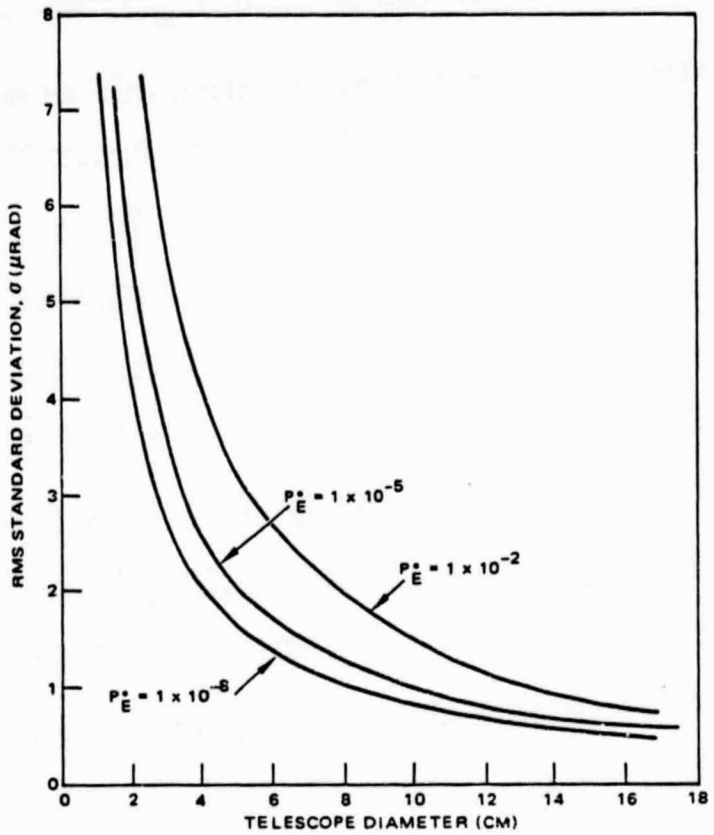


Figure 5.4-2. The diameter of the optical antenna used to provide the optimum beamwidth in the pointing error environment described by the standard deviation σ , is noted for several selected values of the burst error.

We illustrate the result in Figure 5.4-3 assuming a diffraction limited spot size for $\lambda = 0.83 \mu\text{m}$ on a quadrant type sensor. Curves for three selected values of the antenna diameter are shown. We note that it is required that $\Delta/\epsilon \leq 1.0$. As indicated by the curves in Figure 5.4-3 there is a lower limit to the S/N in the tracking sensor which must be maintained. The so determined value of the S/N in the tracking sensor will impact the design of the tracking channel per the normal range relation.

5.5 SYSTEM IMPLICATIONS

The mispointing of an optical communication beam from one host satellite to another has been evaluated. We have optimized the optical power collected at a distant receiver to show that an optimum ratio of the pointing error to beamwidth (ϵ/a) may be deduced. We find that the resulting pointing error loss is, in general, larger than that previously used in many system designs and a pointing error loss of about -4 dB must be allocated to the link budget.

We have modeled the single axis pointing error as having a gaussian distribution and deduced that the radial pointing error has a Rayleigh distribution. This radial pointing error distribution was used to define the probability of burst error which was shown to be dependent upon the ratio of the pointing error and the standard deviation of the pointing error distribution.

This relationship was combined with the earlier derived optimum ratio of ϵ/a to define the design parameter a/a as a function of the pointing error. Once a burst error probability is selected for the system operation and the 1σ value of the radial pointing error distribution of the host satellite known, the optimum beamwidth to maximize power collected at the receiver may be determined.

The design ratio a/a defines the appropriate transmit telescope diameter to optimize system performance. This result is in contrast to many who have erroneously assumed that a larger transmit antenna diameter and hence smaller beamwidth is beneficial to the system. We have also shown that deviations from the optimum a/a ratio will lead to an increase in the optical power needed to maintain the probability of burst error at the desired value. Additionally, the pointing requirements may be used to establish the design limits for the tracking channel.

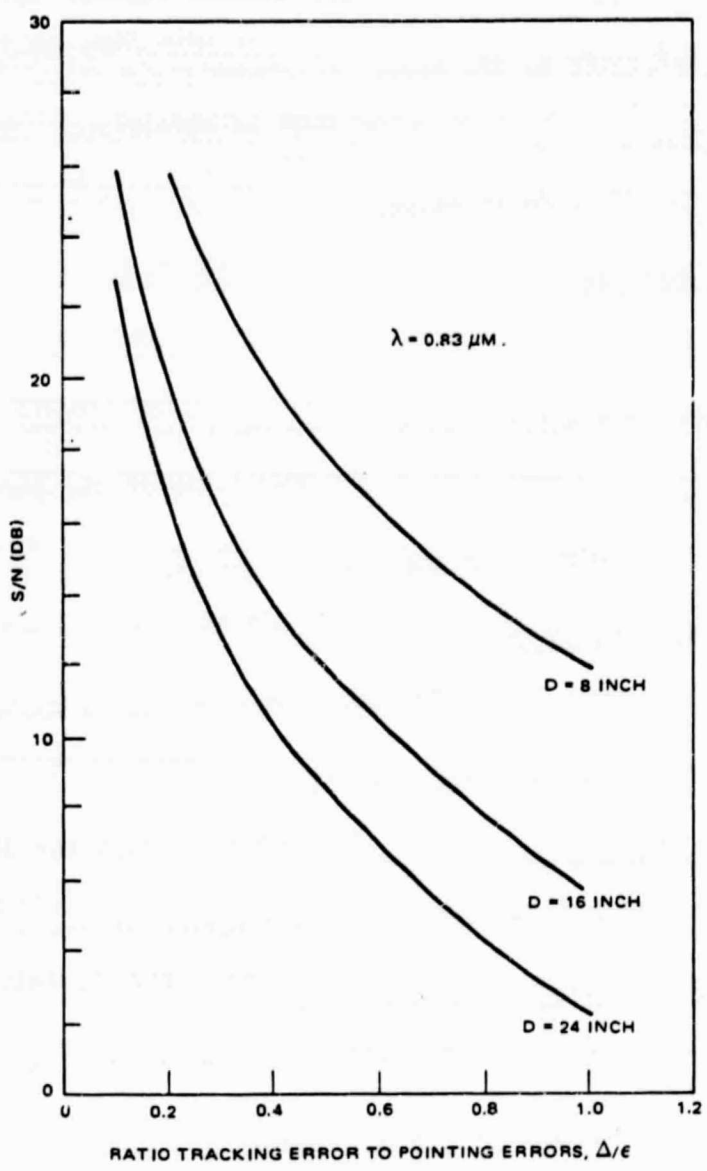


Figure 5.4-3. A limit to the signal to noise ratio in the tracking servo control loop is defined by the ratio of the tracking error to the pointing error for several values of the receive antenna diameter.

As an example, we show a link budget summary for a 500 Mpbs data channel at 0.8 μ m wavelength in Figure 5.5-1. The example assumes a low earth orbiting (LEO) satellite transmitting to a receiver on a geosynchronous earth orbiting (GEO) satellite. The LEO antenna is 15 cm (5.9 inches) in diameter. The calculations assume a pulse position modulation (PPM) format with $m = 4$, and a maximum a priori (MAP) receiver configuration. A link margin of only about 3 dB is available.

It has been determined that an optical communication system cannot be properly design without knowledge of the pointing error distribution associated with the host satellite and the operating system. We believe the dominant design parameter to be the probability of burst error and, hence, the a/a ratio. We believe that its influence is far reaching and can control the eventual application of otical communication systems for space mision.

TABLE 5.5-1. COMMUNICATION LINK BUDGET SUMMARY
(500 Mbps, PPM, m = 4, MAP DETECTION)

ITEM	FACTOR	dB
Peak Laser Power	0.8 watt	-0.97
LEO Optics/Combining	0.45	-3.47
LEO Antenna Gain	15 cm diameter	115.3
Pointing Loss	0.4	-3.98
Range	44,500 km	-296.36
GEO Antenna Gain	50 cm diameter	125.33
GEO Optics	0.32	-4.95
Received Peak Power	-	-69.16
Probability Bit Error	1×10^{-6}	-
Probability Burst Error	1×10^{-3}	-
Required Peak Power	-	-72.36
Margin	-	3.2 dB

5.6 REFERENCES

1. J.E. Geusic, E.V. Hoversten, S. Karp, and R.J. Kennedy, Editors, Special Issue on Optical Communications, Proc. IEEE, 58, October 1970.
2. D.C. Forster, F.E. Goodwin, and W.B. Bridges, "Wideband Laser Communications in Space", IEEE J. Quantum Electron, 8(2), 1972, pp. 263-272.
3. J. McElroy, "Carbon Dioxide Laser Space Data Relay Links", 1974 Optical Society Meeting, Washington, D.C., 21-25 April 1974, Digest, Paper MA2: pp 250.
4. M. Ross, "Optical Communications in Space", Optical Engineering, Vol. 13, 1974, pp. 374-382.
5. J.D. Barry, A. Darien, B.T. Dawkins, P. Freedman, J. M. Heitman, C.J. Kennedy, J.K. Lyon, G. Matassov, D.D. Matulka, C.E. Whited, and D.M. Zack, "1000 Megabits Per Second Intersatellite Laser Communications System Technology," IEEE Trans. Comm., Vol. 24, 1976, pp. 470-478.
6. J.D. Barry, "Laser Communications in Space: Nd:YAG Technology Status", Annals New York Academy of Science, Vol. 267, 1976, pp. 342-358.
7. J.H. McElroy, N. McAvoy, E.H. Johnson, J.J. Degnan, F.E. Goodwin, D.M. Henderson, T.A. Nussmeier, L.S. Stokes, B.J. Peyton, and T. Flattau, "CO₂ Laser Communications Systems for Near-Earth Space Application", Proc. IEEE, 65(2), 1977, pp. 221-251.
8. M. Ross, P. Freedman, J. Abernathy, G. Matassov, J. Wolf and J.D. Barry, "Space Optical Communications with the Nd:YAG Laser", Proc. IEEE, 66 (3), 1978, pp. 319-344.
9. J.D. Wolf, R.Z. Olshon, J. Pautler, and L.F. Eastwood, Jr., "System Design for Nd:YAG Laser Communications", International Telecommunications Conference, San Diego, California, November 1979.
10. M. Ross, J.D. Wolf, R.M.F. Linford, and J.L. Abernathy, "Space Laser Communications Systems for the Eighties", AIAA Communications Satellite Systems Conference Record, Orlando, Florida, April 1980.
11. R.S. Mason and G.M. Lanham, "Free Beam Laser Communications System Technology Development," Proc. Electro-Optics/Laser-80 Conference, Boston, Massachusetts, November 1980, pp. 278-294.
12. G.M. Lanham, "Air Force Laser Communications Space Measurement Unit", Proc. National Telecommunication Conference, Houston, Texas, December 1980, pp. 27.2-1-27.2.3.

13. J.L. Abernathy, H.D. Brixey, E.S. Clarke III, D.W. Dreisewerd and J.A. Maynard, "Laser Communications Acquisition and Tracking Flight Test", Abstract only, Proc. International Telemetering Conference (ITC/USA-80), Oct., 1980, pp. 643.
14. M. Katzman, "Laser Space Communication Technology Status", Proc. SPIE, Vol. 295, 1981, pp. 2-9.
15. G. Evans and J. Leary, "Issues Impacting the Application of Semiconductor Lasers in Space Communications", Proc. SPIE, Vol. 295, 1981 pp. 26-40.
16. R.F. Begley, D. Groux, D.W. Chen, and O. Giat, "Laser Beam Combiner: Applications to Space-Borne Laser Communications", Appl. Optics, Vol. 21 (17) 1982, pp. 3213-3220.
17. I.M. Teplyakov, "Acquisition and Tracking of Laser Beams in Space Communications", Acta Astronautica, 7, 1980, pp. 341-355.
18. E.S. Clarke and H. D. Brixley, "Acquisition and Tracking System for a Ground-Based Laser Communication Receiver Terminal", Proc. SPIE, Vol. 295, 1981, pp. 162-169.
19. J.M. Lopez and K. Long, "Acquisition, Tracking and Fine Pointing Control of Space-based Laser Communication Technology", PROC SPIE, Vol. 295, 1981 pp. 100-113.
20. V.A. Vilnrotter, "The Effects of Pointing Errors on the Performance of Optical Communication Systems", JPL-TDA Progress Report 42-63, 1981, pp. 136-146.
21. J.D. Barry, A.J. Einhorn, C.J. Kennedy, S.D. Kilstion and G.S. Mecherle, "Laser Aided Acquisition between Satellite-Borne Optical Communication Systems", submitted to IEEE Trans. Comm., 1983.
22. S.D. Kilstion, "Bit-Error Rate Dependence on Pointing Accuracy and Beam Diameter", Hughes Aircraft Company, Interdepartmental Correspondence, May 1981, unpublished.
23. G.S. Mecherle, "Optimization of Optical Transmitting Gain", Hughes Aircraft Company, Interdepartmental Correspondence, Dec. 1981, unpublished.
24. G.S. Mecherle and C.E. Farrell, "Optical m-ary PPM bit error rate analysis", unpublished, Hughes Aircraft Company report, SCG 810540R, November, 1981.
25. L. Stokes, K. L. Brinkman and F. Kali, "Reference Data for Advanced Space Communication and Tracking Systems", Final Report, NASA/GSFC Contract NAS S-9637, Oct. 1969, Vol. III, pp. 400-404.
26. R. Gagliardi and G. Prati, "On Gaussian Error Probabilities in Optical Receivers", IEEE Trans. Comm., Vol. 28, 1980, pp. 1742-1747.

6.0 SERVO ANALYSIS

6.1 Introduction

This section addresses all the servo requirements that were either well defined at the start of the study or evolved as the study progressed. It also defines a system baseline design and mentions those significant assumptions that qualify the results.

6.1.1 Servo Design Requirements

The primary purpose of this study was to establish a servo design configuration that would maintain a prescribed tracking accuracy between two earth orbiting satellites. Each satellite's servo system must track the other satellite's laser communication beam with an accuracy (2-axis) of 1 urad.

Of secondary concern was to design a servo that minimizes the reaction torque imparted to the spacecraft. This was accomplished by minimizing the 2-axis gimbal dynamics. The RMS reaction torques for the various servo designs were compared for base motion and friction disturbances.

Finally, a third requirement that evolved during the study emphasized design simplicity and reliability. The requirement for all components and devices to be space qualified, led toward a simplistic design which minimizes costs and boosts reliability while still meeting system performance goals.

6.1.2 System Baseline Design and Assumptions

The baseline system configuration is the same for both spacecraft trackers. It consists of two Cassegrain telescopes - one receiver and one transmitter - each mounted to the inner gimbal of a two gimbal set (outer azimuth and inner elevation). The optical train of each telescope contains a small (1 1/2 inch diameter) 2-axis IMC (image motion compensation) mirror which is capable of operating at high servo bandwidths (hundreds of hertz). The receiver's optical train also

contains a track sensor that generates a line-of-sight (LOS) error. This error is nulled by simultaneously torquing the azimuth and elevation gimbals, and the 2-axis IMC mirror.

Since both telescopes are mounted on the same gimbal set, the transmitter's LOS pointing error is very similar to the receiver's LOS tracking error. Therefore, an error analysis was performed on a receiver servo and then modified to reflect the transmitter's error sources (point ahead). Figure 6.1-1 shows a block diagram relating the receiver and transmitter functions.

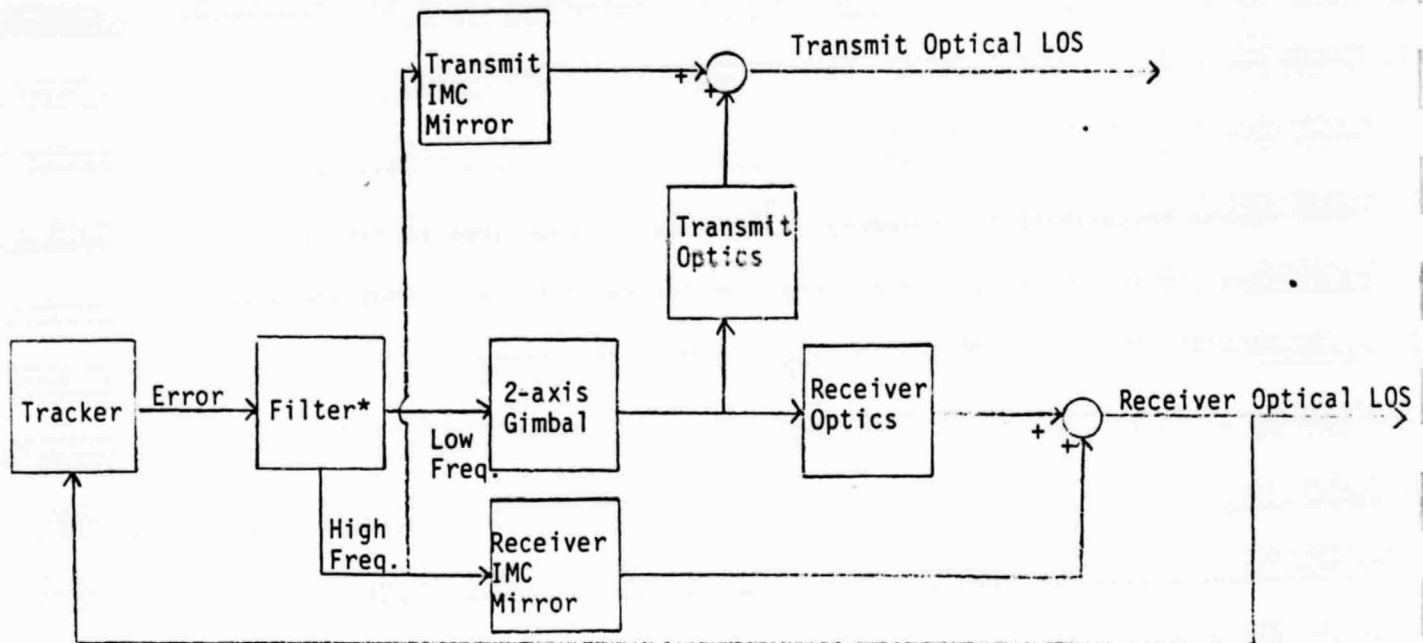


Figure 6.1-1: Transmitter/Receiver Functional Block Diagram

The schematic diagram for the baseline on-gimbal receiver configuration is presented in Figure 6.1-2. This diagram was used to generate the angular relationships of the optical LOS (output space) with respect to gimbal and IMC mirror positions (input space).

*This filter functionally represents the frequency splitting of the track error that occurs in each of the candidate servo configurations in Section 6.2

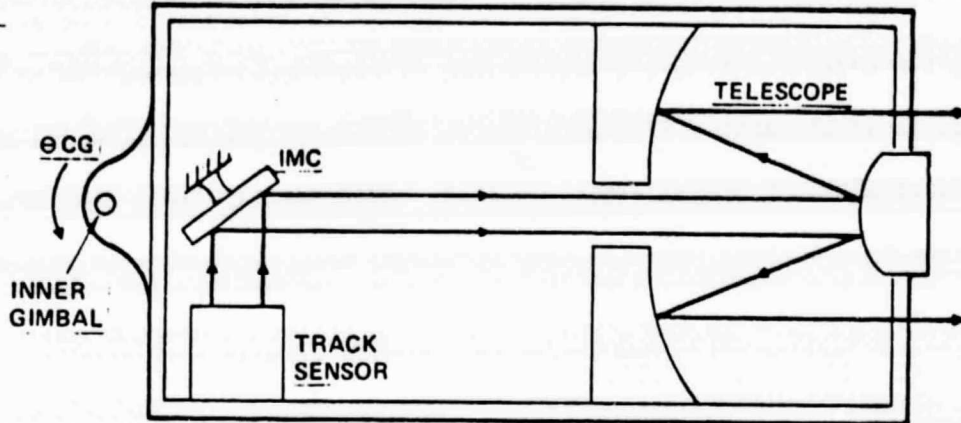


Figure 6.1-2: Receiver Telescope Schematic Diagram

The track sensor and telescope are rigidly mounted to the elevation fixture. Any gimbal motion directly transmits into track sensor and telescope motion. The IMC mirror, however, is shown to be soft-mounted to the fixture to minimize gimbal motion coupling to the mirror. A mathematical justification for soft-mounting the IMC mirror is discussed in Appendix 6A.1.

Both elevation and azimuth axes are represented by a single-axis analysis. All error sources were assumed identical for both axes except for base motion. Spacecraft base motion coupling into the optical LOS is discussed in Section 6.3.2. To simplify the analysis, azimuth and elevation angles were assumed to be small such that their cosine functions equal one and their sine functions equal the angle.

In performing the tracking analysis, various assumptions were made to bound the scope of this study and to account for the limited amount of satellite data available to us. NASA/GSFC provided HAC with base motion disturbance data measured on the LANDSAT spacecraft. To maintain a conservative approach, a worst case envelope was selected from this data to represent angular base motion disturbances about each of the three spacecraft axes - roll, pitch, and yaw.

Linear disturbances* were not considered in this analysis because of their negligible effect on tracking accuracies. Linear accelerations can be transformed to angular accelerations if the telescope centers-of-gravity (C.G.'s) are not coincident with the gimbal axes. This phenomenon called "mass-unbalance" is minimized by precisely balancing the on-gimbal weights about each of the gimbal axes.

6.2 Servo System Configurations

Three servo configurations were considered for this study - gyro-stabilized, mass-stabilized, and complementary filter. All three configurations control the system's inertial LOS angle such that the received laser beam is maintained near the tracker's center null position.

The gyro-stabilized configuration is a conventional design that has been implemented on many HAC built tracking systems (for ground, air, and space applications). It has an outer low bandwidth track loop with two higher bandwidth inner loops for attenuating base motion disturbances. It is a proven candidate design that can also be used as a baseline to compare to the two other configurations.

The mass-stabilized design was considered as a simplification to the gyro-stabilized design. It replaces the two rate-integrating gyros (RIG's) with a reference platform that points along the desired LOS. By replacing the gyros, this design improves reliability and reduces system weight and power requirements but, as pointed out in Section 6.3, it compromises tracking accuracy.

Finally, the complementary filter configuration was considered for its utmost simplicity of design. It differs from the other two by the fact it only closes a single wide bandwidth loop about the track sensor with no requirements for inner loops. Although its simplicity reduces the device count, its wide bandwidth allows more sensor noise to contaminate the track LOS.

*The angular accelerations induced by the relative satellite orbital dynamics are addressed in Section 6.3.4 with the dynamic equations derived in Appendix 6A.4.

The following sections discuss in detail each servo configuration and the philosophies behind their designs. A two-axis servo block diagram is presented for each design in Figures 6.2-3, 6.2-4, and 6.2-5. It illustrates the various servo loop dynamics and their interrelationships and is extremely helpful when discussing base motion coupling. Appendix 6A.2 derives the various servo control equations.

6.2.1 Servo Configurations and Their Design Philosophies

The gyro-stabilized configuration uses three Type II servo loops to control the azimuth and elevation LOS axes (see Figure 6.2.1a Single-Axis Functional Block Diagrams). The outermost track loop is low bandwidth and obtains its error signal from a centroid tracker. This LOS error is compensated by a lead-lag network and one electronic integrator as derived in Appendix 6A.2. The low bandwidth track loop minimizes sensor noise transmission to the LOS and is adequate for tracking targets having small angular accelerations (see Sections 6.3.1 and 6.3.4 for discussions of sensor noise and track following error).

The track loop compensates the track error to generate a rate command for the inner coarse gimbal (CG) rate loop. This rate command is manifested as a torque applied to the gyro's output axis. The angular displacement between the output axis and the gyro case establishes the inertial LOS error that is used by the rate loop to torque the azimuth and elevation gimbals. The gimbal motion about the gyro's input axis produces a torque about the output axis which nulls the position error. When this occurs, the gimbal (telescope) LOS is coincident with the desired track LOS.

The CG rate loop bandwidth has upper and lower bounds due to stability considerations. Because it is an inner loop, its bandwidth must exceed the outer track loop bandwidth by about a factor of 10 to achieve a stable track.* Otherwise,

*The CG loop bandwidth can probably be less than 10 times the track loop bandwidth because the IMC loop decouples it from the track loop.

ORIGINAL PAGE IS
OF POOR QUALITY

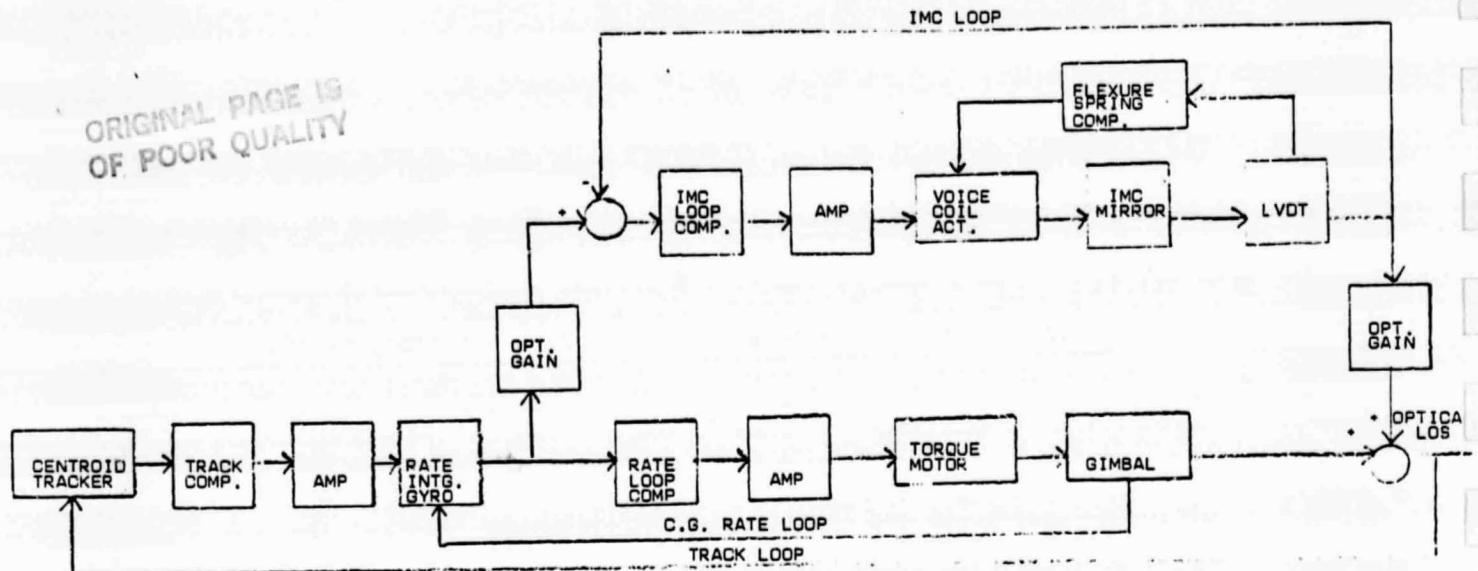


FIGURE 6.2-1A: GYRO-STABILIZED FUNCTIONAL BLOCK DIAGRAM

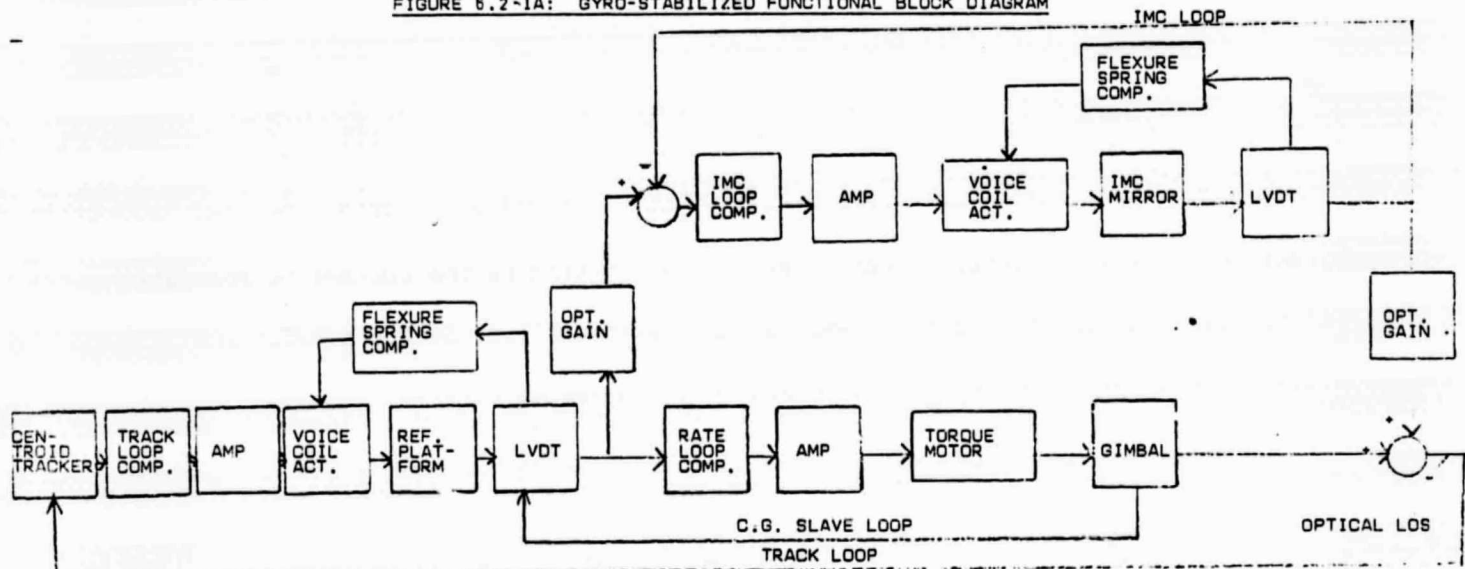


FIGURE 6.2-1B: MASS-STABILIZED FUNCTIONAL BLOCK DIAGRAM

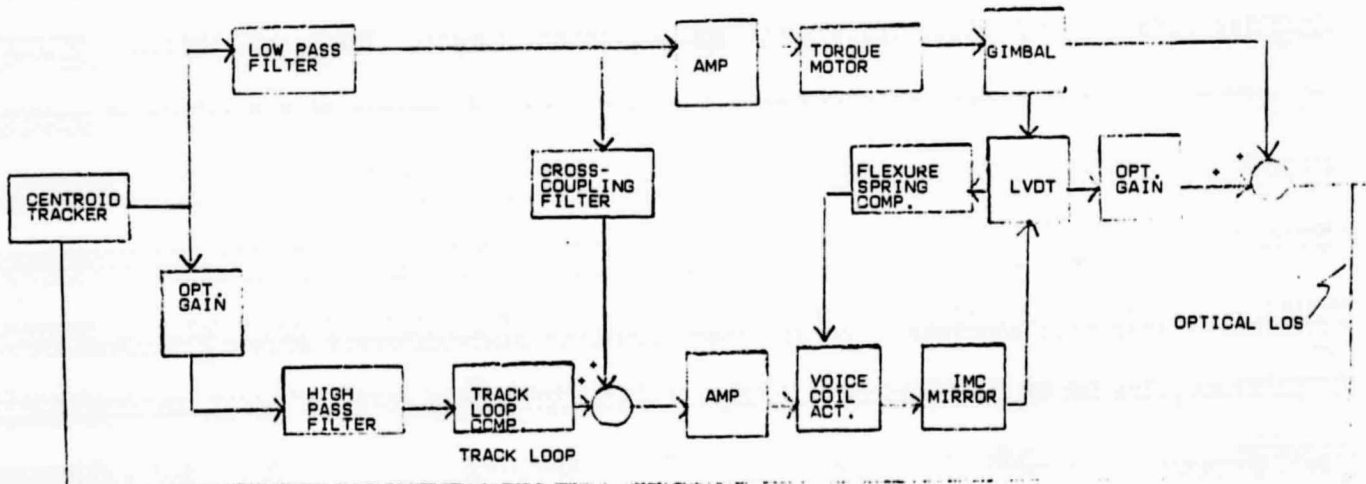


FIGURE 6.2-1C: COMPLEMENTARY FILTER FUNCTIONAL BLOCK DIAGRAM

the phase lag at the track loop crossover frequency will not satisfy minimum phase margin requirements (30 deg) for stability.

On the upper bound, the CG loop bandwidth must be less than five times the lowest structural resonant frequency of the gimbal. It must also be less than five times the RIG bandwidth. Both constraints satisfy CG loop stability requirements. Because of these upper constraints, a third inner loop is required to attenuate high frequency base motion disturbances.

The IMC loop is a very high bandwidth position loop (few hundred hertz) that is needed to attenuate high frequency disturbances. If a torque disturbance is applied to the gimbal base, the CG loop will remove that portion of the error that falls within its bandwidth. The remaining error appears in the gyro error signal that commands the IMC loop. This remaining error is the angular difference between the desired LOS and the gimbal's LOS. Because it is a correction to the gimbal LOS, the IMC loop error is formed by comparing the RIG error output to the relative angle between the IMC mirror and the coarse gimbal as measured by the LVDT (linear variable differentiating transducer). The IMC loop attenuates that portion of the error that does not exceed its bandwidth.

During the final presentation, there was some doubt expressed by NASA in building a 400 hertz IMC loop. An example of a wide bandwidth steering mirror built and tested by HAC is the AABISM used in the Air Force's Airborne Pointer Tracker (APT) alignment system.

The AABISM has a 21 cm diameter and an inertia of 0.2 in-lb-sec^2 and is water-cooled to align a high energy laser beam. The mirror is flexure-mounted and driven by voice coil actuators with a reactionless mass used to minimize torque coupling to the base.

The IMC mirror proposed by HAC for this study is 1 1/2 in. in diameter and has an inertia of $6.4 \times 10^{-3} \text{ in-oz-sec}^2$. The mirror is not water-cooled but is

flexure-mounted and driven by voice coil actuators. The necessity of using a reactionless mass to isolate the base (telescope) from torque disturbances is beyond the scope of this study. If required, the only limitation would be the volume constraints on the mirror.

Figure 6.2-2 shows a photograph of the AABISM steering mechanism along with the laboratory-measured open loop frequency response of the steering mirror loop. The crossover frequency (0 DB) in the plot occurs at 500 hertz with structural resonances measured at a few thousand hertz.

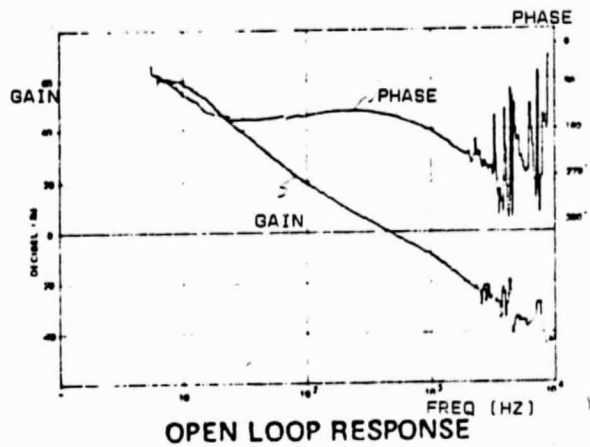
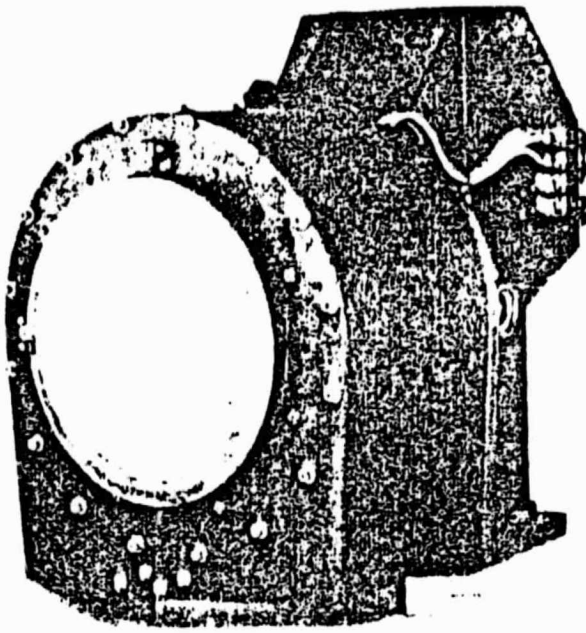


Figure 6.2-2: AABISM Steering Mechanism and Open Loop Response

The CG and IMC loops effectively split the LOS error into low and high frequency components, respectively. This feature is quite desirable when minimizing the reaction torque imparted to the spacecraft by the gimbal motion. Because the gimbal is considerably more massive than the IMC mirror, and the IMC mirror can use a reactionless drive, reducing the CG loop bandwidth effectively reduces the spacecraft reaction torque. However, the smallest attainable CG loop bandwidth is limited by the constraints mentioned above in addition to the travel limits of the IMC mirror (the less error removed by the coarse gimbal increases the amount of error to be removed by the IMC mirror).

Figure 6.2-1b shows the mass-stabilized functional block diagram. It is quite similar to the gyro-stabilized configuration since it closes an outer low bandwidth track loop and two inner high bandwidth position loops. The reference platform replaces the two RIG's as the LOS reference. The track loop now provides torque commands to voice coil actuators which reposition the soft-mounted reference platform to point along the desired LOS. The platform provides inertial dynamics to the track loop such that it eliminates the need for an electronic integrator that is required in the gyro-stabilized approach. The platform's relative angular position to the gimbal is measured by two LVDT's. This slave error drives the coarse gimbal position until it is aligned with the reference platform (and the slave error is nulled). The slave error output is used to command the IMC loop in the same manner as the gyro output was used in the gyro-stabilized configuration.

A shortcoming to the mass-stabilized approach is that any disturbance entering the inner CG loop is not totally isolated from the track loop. Gimbal base motion couples into the track loop through the single-post flexure at frequencies that are within the CG loop bandwidth. (It can be shown that the mass-stabilized LOS response to base motion approaches the gyro-stabilized response as the flexure spring rate approaches zero).

The complementary filter configuration is a simple servo design that closes a single wide bandwidth track loop with a minimal number of active devices (see Section 6.4.3 for component list). This design directly splits the track error signal into its low and high frequency components via a complementary filter (see Appendix 6A.2 for complementary filter derivation). The low frequency error component is removed by torquing the azimuth and elevation gimbals, and the high frequency component is removed by actuating the IMC mirror.

This approach has a number of advantages over the other configurations:

- 1) The only limit on splitting the error into high and low frequencies is the travel limit on the IMC mirror. Lowering the low pass filter (Figure 6.2-1C) corner frequency increases the error to be removed by the IMC mirror.
- 2) There are no inner loops or bandlimited devices other than the track sensor that must be considered for track loop stability.
- 3) Changing the error signal's frequency split only requires resetting the low pass filter corner frequency to the desired value. The multi-loop approach requires the CG loop gain and compensation to be redesigned and the overall track loop stability reverified.

A disadvantage to the complementary filter design is that it does not filter as much sensor noise from the loop as does a low bandwidth design. For this reason, a key tradeoff in this analysis centers around the sensor's noise-equivalent-angle, σ_{NEA} (derived in Section 7.2), and its effect on the optical LOS (Section 6.3.1).

6.2.2 Servo Block Diagrams

This section defines the variables that appear in the servo block diagrams in Figures 6.2-3 through 6.2-5. The loop bandwidth values were selected in Section 6.3 and were used to generate the error analysis results. The gain and compensation equations for each servo loop are derived in Appendix 6A.2 as a function of loop bandwidth.

The proposed IMC mirror for this study is being built by HAC for the HNVS program. Its flexure damping ratio and spring rate characteristics were taken from actual test data to be

$$\xi_m = \text{damping ratio} = .01$$

$$\omega_m = \text{spring rate} = 2\pi (1.25 \text{ hertz})$$

ORIGINAL PAGE IS
OF POOR QUALITY.

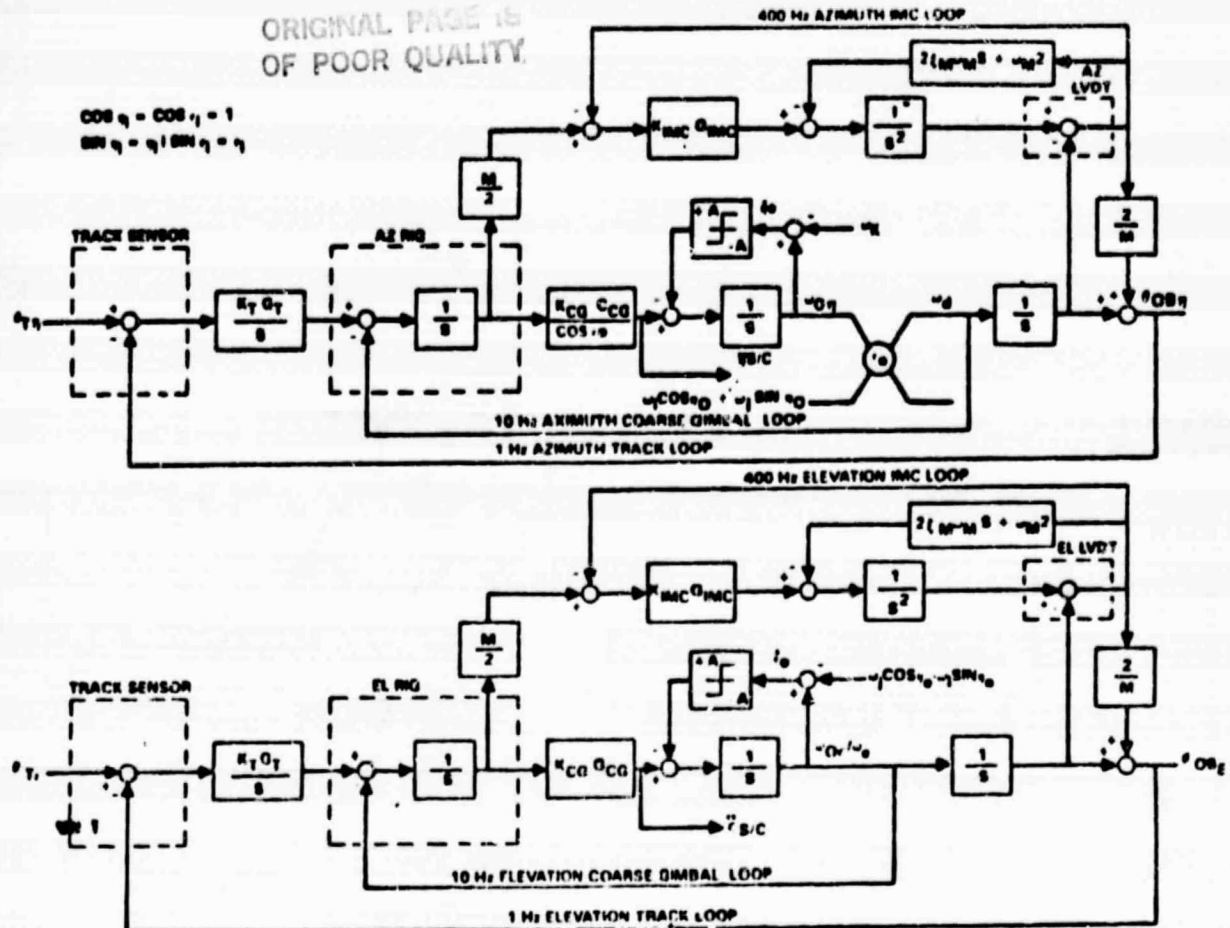


Figure 6.2-3: Gyro-Stabilized Two-Axis Servo Block Diagram

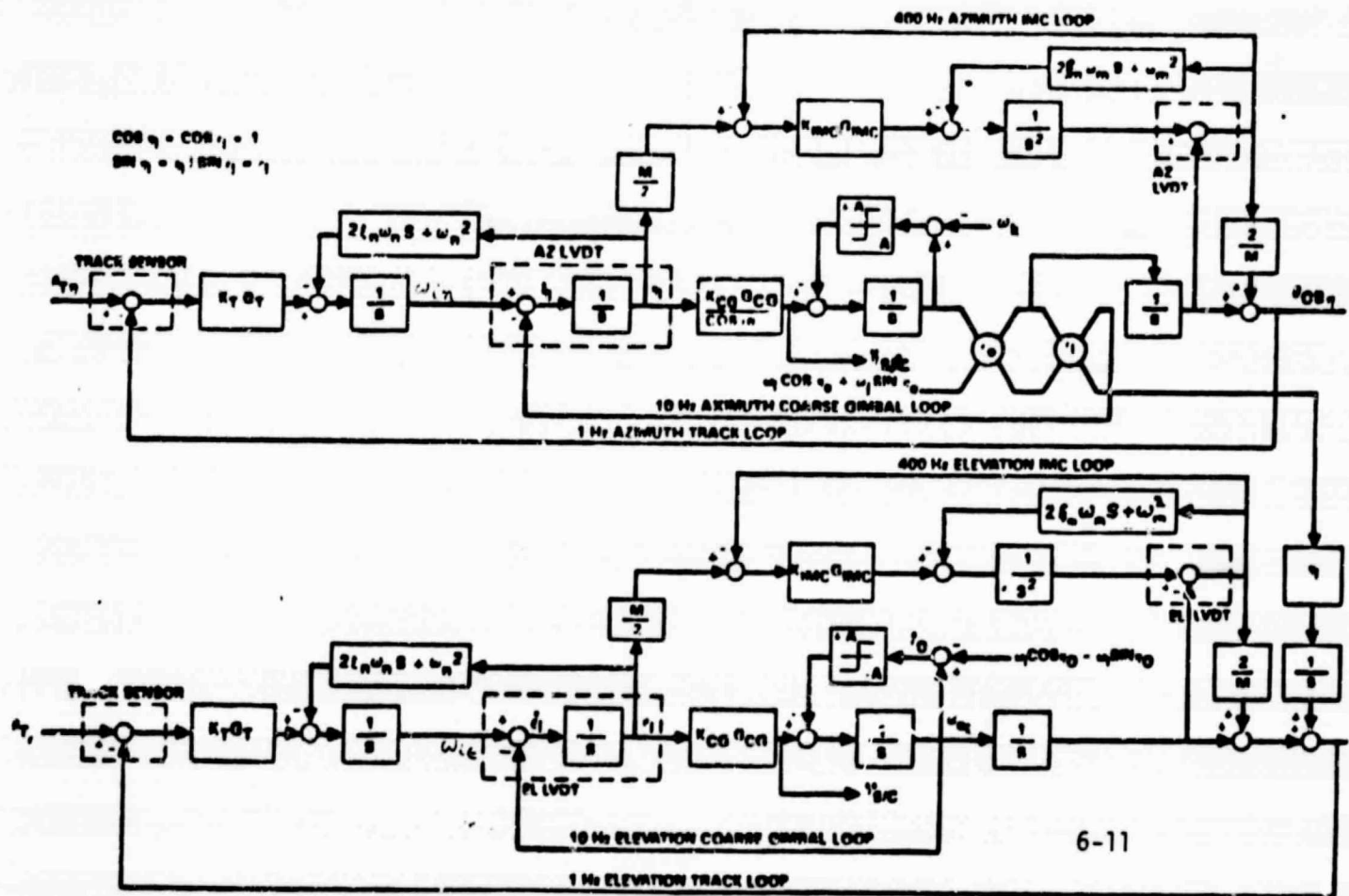


Figure 6.2-4: Mass-Stabilized Two-Axis Servo Block Diagram

ORIGINAL PAGE IS
OF POOR QUALITY

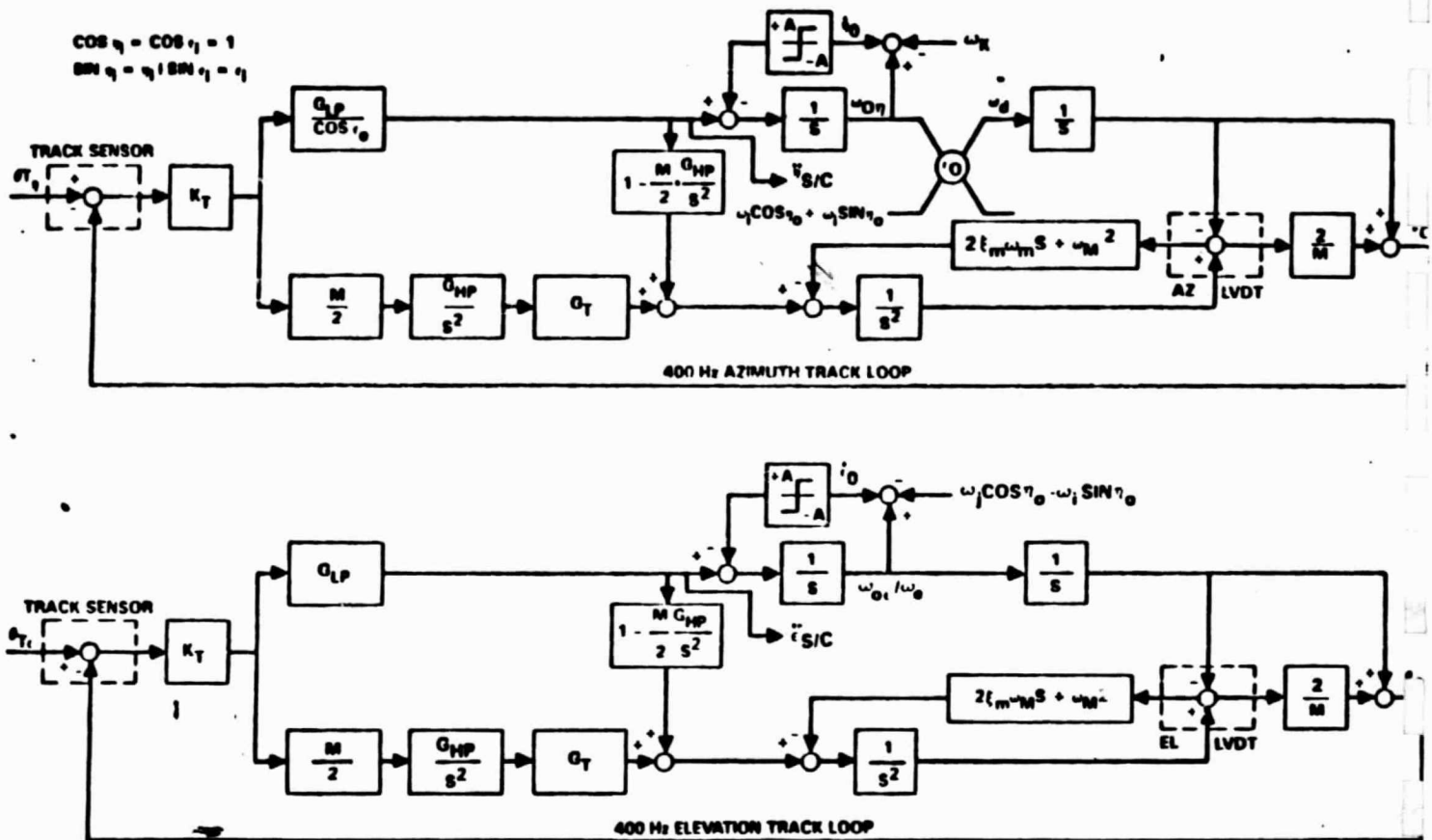


Figure 6.2-5: Complementary Filter Two-Axis Servo Block Diagram

For the azimuth channels in each block diagram, the coarse gimbal gain is adjusted by the term $\frac{1}{\cos \epsilon_0}$. This term transforms the CG error from LOS to gimbal coordinates so that the gimbal torque commands are in the proper coordinate system. The 2-axis gimbal piogram in Figure 6.3-4 shows this relationship as

$$\omega_d = \omega_{0n} \cos \epsilon_0 \quad (6.2.2.1)$$

In the same respect, the base motion disturbances that enter the loops through friction and kinematic coupling were derived from the respective 2-axis and 4-axis gimbal piograms.

6.3 Error Analysis

During the study, various error sources were investigated as to their effect on system performance. As a result, three sources dominated - base motion, friction, and sensor noise - while the others were considered negligible or assumed to be removable through calibration. The following sections examine base motion, friction, sensor noise, and other less significant sources to determine their contributions to the LOS error for our three candidate servo designs.

The error analyses also determined the required servo loop bandwidths that would satisfy the system error budget. The sensor noise and following error analyses determined an acceptable track loop bandwidth for the multi-loop servo designs and the base motion analysis determined the desired IMC loop bandwidth.

6.3.1 Sensor Noise

The amount of sensor noise the track loop responds to is a function of the track loop bandwidth. The track loop filters those frequency components of noise that exceed its bandwidth. This justifies why low bandwidth track loops are more desirable in systems where sensor noise is dominant. To determine appropriate track loop bandwidths for this study, an analytical model was used which determines the LOS RMS error output of the track loop due to sensor noise-equivalent-angle, σ_{NEA} .

The expression for the LOS RMS error due to sensor noise is derived in Reference 3. It assumes uncorrelated sensor error signals at the sampling outputs by bandlimiting the sensor noise to half the sampling frequency. The servo block diagram representing this analysis appears below.

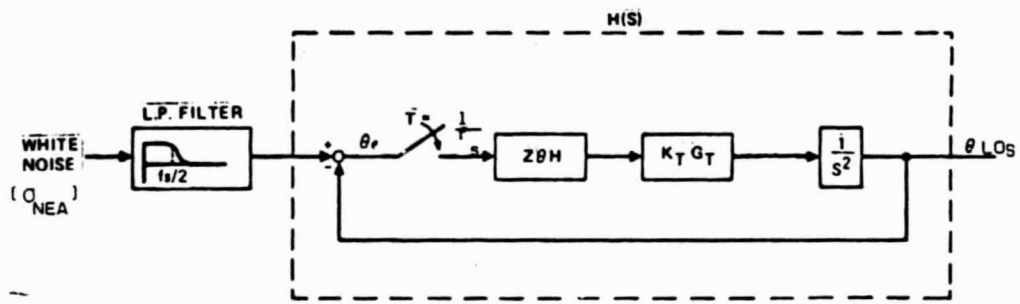


Figure 6.3-1: Track Loop Model for Sensor Noise Analysis

Sensor noise is represented by a white noise process with amplitude σ_{NEA} that is passed through a low pass filter with corner frequency $fs/2$ (half the sampling rate). The filtered noise enters the track loop (represented by $H(S)$) which samples the error signal at f_s hertz. The error is held constant for $1/f_s$ seconds with a zero-order-hold function. The loop gain and compensation are designed to achieve a desired bandwidth of f_c hertz with adequate phase margin for loop stability (see Appendix 6A.2 for derivation of servo control equations).

To solve for the RMS LOS error, θ_{RMS} , the white noise PSD is multiplied by the magnitude of $H(S)$ squared and integrated over all frequencies.

$$\theta_{RMS} = \frac{1}{2\pi j} \int_{-\frac{f_s}{2}}^{\frac{f_s}{2}} S_N(f) |H(2\pi jf) H(-2\pi jf)| d\omega^{1/2} \quad (6.3.1.1)$$

$$\text{where } S_n(f) = \sigma_{NEA}^2, -\frac{f_s}{2} \leq f \leq \frac{f_s}{2}$$

Substituting the closed loop transfer function for $H(S)$ into 6.3.1.1 yields,

$$\theta_{RMS} = \sigma_{NEA} \left[\frac{(1 + 2\xi)}{(1 + 2\xi)(1 - \frac{\pi f_c}{f_s}) - 1} \left(\frac{f_c}{f_s} \right) \right]^{1/2} \quad (6.3.1.2)$$

where, f_c = track loop bandwidth (hertz)

f_s = sampling rate (hertz)

ξ = track loop damping ratio

σ_{NEA} = sensor noise-equivalent-angle (urad)

Equation 6.3.1.2 shows θ_{RMS} to be a function of the ratio of track loop bandwidth to sampling rate, f_c/f_s . For this report, it was decided to fix this ratio at 1/10* and determine the effect on σ_{NEA} as the sensor sampling rate varies with track loop bandwidth.

σ_{NEA} is derived in Section 7.2 to be

$$\sigma_{NEA} = \frac{\pi}{8} \frac{1.22 \lambda}{D} \frac{1}{SNR} \quad (6.3.1.3)$$

where λ = laser beam wavelength (um)

D = aperture diameter (in)

SNR = signal-to-noise ratio

If we assume that we maintain a fixed average laser power for all choices of sampling rate, then

$$SNR \propto \frac{1}{f_s^{1/2}} \quad (6.3.1.4)$$

But since $f_c = \frac{1}{10} f_s$, then

$$SNR \propto \frac{1}{f_c^{1/2}} \quad (6.3.1.5)$$

Because of the proportionality relationship in 6.3.1.5, a value for SNR must be assumed for a given value of f_c . It was assumed that the sensor SNR equals 5 for a track loop bandwidth of 400 hertz and a sample rate of 4 kilohertz. With these initial conditions and

*In Section 6.2.1, it was stated that for track loop stability, the track loop sampling rate must be about 10 times the bandwidth.

$$\lambda = 0.9 \text{ um}$$

$$\text{and } \xi = .725$$

$$\text{Equation 6.3.1.2 reduces to } \theta_{\text{RMS}} = \frac{.17 f_c}{D}^{1/2} \quad (6.3.1.6)$$

This equation was applied to the three configurations for the 6 inch and 20 inch diameter apertures yielding the following results.

Configuration	Track Loop BW (Hz)	Sample Rate (Hz)	SNR	Aperature Diameter (in.)	RMS (urad)
Mass- and Gyro- Stabilized	1	10	100	6	.028
				20	.009
Complementary Filter	400	4000	5	6	.567
				20	.170

Figure 6.3-2: Sensor Noise Results

6.3.2 Spacecraft Base Motion Disturbances

As previously stated, LANDSAT base motion disturbance data was provided to HAC by NASA/GSFC. On board disturbances were measured by rate integrating gyros and angular displacement sensors. Together, they measured spacecraft roll, pitch, and yaw angular displacements over a bandwidth of 0 to 125 hertz. This data was converted by HAC to power spectral densities (PSD's) by squaring the angular amplitudes.

A worst case envelope of all the data was selected to represent the angular disturbances about each spacecraft axis - roll, pitch, and yaw - which appears in Figure 6.3-3.

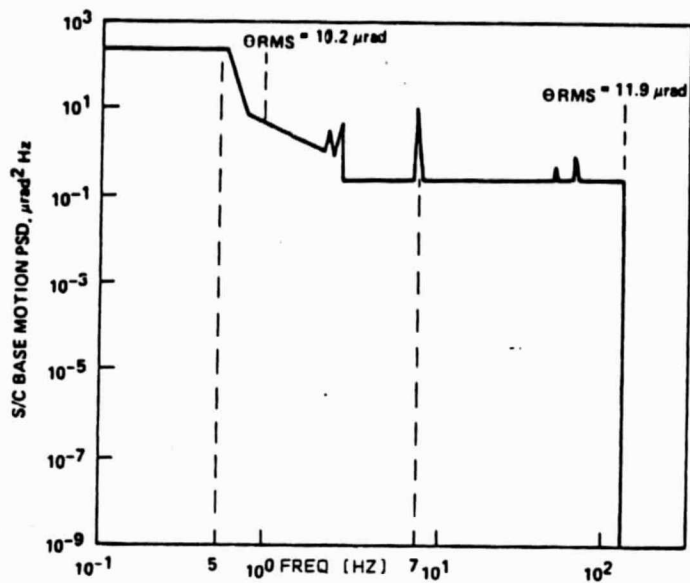


Figure 6.3-3: Spacecraft Base Motion Disturbance PSD

Figure 6.3-3 shows the measured data abruptly terminating at 125 hertz whereas the true data may extend beyond this frequency. However, the plot suggests that most of the power resides at the lower frequencies since the RMS error at 1 hertz equals 86% of the total RMS error at 125 hertz. Because of the uncertainty of disturbances beyond 125 hertz, the IMC loop bandwidth was chosen to exceed the highest base motion frequencies.

The base motion disturbance enters the tracking system at the base of the 2-axis gimbal. These disturbances take the form of roll, pitch, and yaw rates and are related to the gimbal's LOS rates by means of a piogram which appears in Figure 6.3-4.

The spacecraft base motion couples into the gimbal LOS through friction and kinematic coupling. (Section 6.3.3 discusses friction modelling in detail. We will only discuss here how the base motion influences friction torque.)

Coulomb friction torque is a function of the relative azimuth and elevation gimbal rates between the gimbal base and its bearings. These rates are represented by $\dot{\eta}_0$ and $\dot{\epsilon}_0$, respectively and when integrated, are the azimuth and elevation gimbal angles, η_0 and ϵ_0 in the piogram. For example, the azimuth gimbal base is rotated at the rate, ω_k , due to spacecraft yaw angle motion. This

motion induces a friction torque disturbance into the inner CG loop (see Figure 6.3-4.) The servo loop responds to the disturbance by torquing the azimuth and elevation gimbals yielding inertial gimbal rates of $\omega_{0\eta}$ and $\omega_{0\varepsilon}$, respectively.

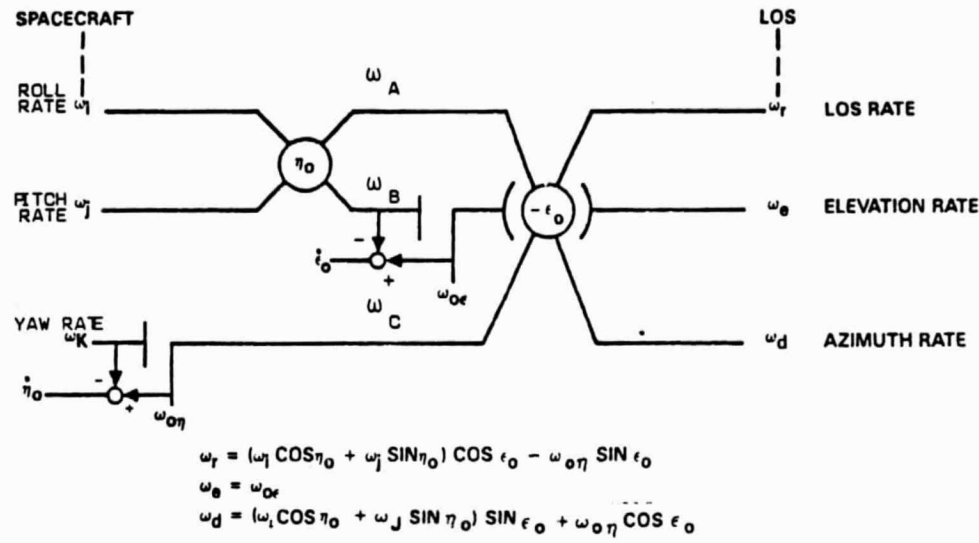


Figure 6.3-4: Two Axis Gimbal Rate Piogram

The gimbal angle rates are computed as follows:

$$\dot{\eta}_0 = \omega_{0\eta} - \omega_k$$

$$\text{and } \dot{\epsilon}_0 = \omega_{0\varepsilon} - \omega_B$$

$$\text{where } \omega_B = \omega_i \cos \eta_0 - \omega_j \sin \eta_0$$

Base motion that couples into the LOS directly, without entering through bearings or flexure pivots is called kinematic coupling. It is very easy to determine the kinematic coupling terms from the rate piogram - it is the only path that is not broken for a gimbal bearing. For our 2-axis gimbal, this path originates from ω_A affecting the LOS and azimuth rates as follows:

$$\omega_d = \omega_A \sin \epsilon_0$$

$$\omega_r = \omega_A \cos \epsilon_0$$

$$\text{or } \omega_d = (\omega_i \cos \eta_0 + \omega_j \sin \eta_0) \sin \epsilon_0$$

$$\text{and } \omega_r = (\omega_i \cos \eta_0 + \omega_j \sin \eta_0) \cos \epsilon_0$$

For $\eta_0 = 0^\circ$ and $\epsilon_0 = 90^\circ$, the azimuth rate, ω_d , equals the spacecraft roll rate, ω_i , and the roll LOS rate equals zero. Since we are tracking a symmetric beam, LOS rate is not servo controlled.

The gyro-stabilized and complementary filter configurations are two gimbal systems. Kinematic coupling is shown to enter the CG loop of the azimuth channel in Figures 6.2-3 and 6.2-5.

The mass-stabilized configuration is a four gimbal system where the two additional angles, n_i and ϵ_i , are the reference platform deflections from the coarse gimbal. Its rate program is more complicated than the two gimbal system, but the same rules and characteristics apply. Figure 6.3-5 reveals four broken lines - two for the azimuth and elevation gimbal bearings and two for the platform deflections.

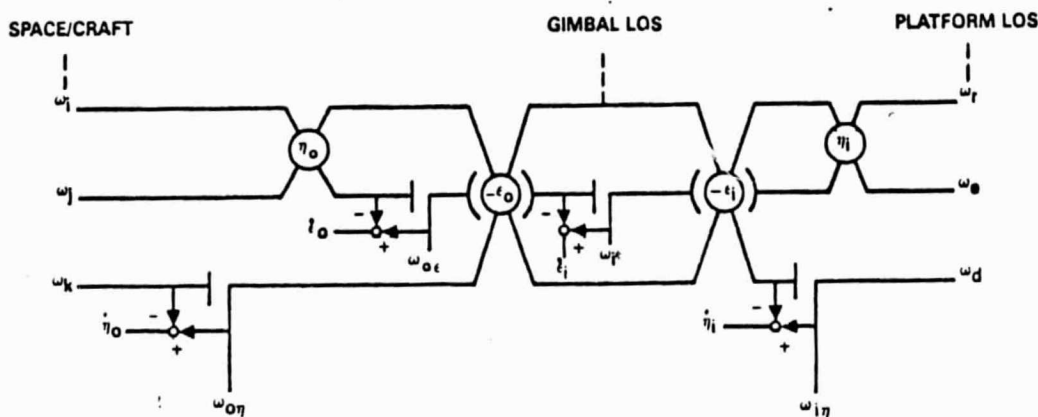


Figure 6.3-5: Four Axis Gimbal Rate Piogram

It is interesting to note that the kinematic coupling for the four gimbal system influences the elevation and azimuth channels. The elevation term is quite small because it is multiplied by the sine of η_j , which is maintained near zero (slave error) by the CG loop. The azimuth term affects the CG loop in the same manner as the two gimbal configurations.

The flexure pivots are represented by the break points in Figure 6.3-5 that generate the angle rates $\dot{\eta}_j$ and $\dot{\epsilon}_j$. The flexure pivots have negligible friction torque loads but do transmit attenuated base motion disturbances to the platform. These disturbances are sensed by the LVDT and enter the track loop through the LVDT error signal (see Figure 6.2-4). This coupling transmits disturbances to the platform that exceed the track loop's bandwidth and degrades LOS pointing accuracy.

A comparison of the servo configuration performances appears in Figure 6.3-6. The left-hand graphs are the Bode plots of the error rejection transfer functions* and the right-hand plots are the LOS error residuals due to base motion disturbance inputs.

The mass-stabilized error rejection curve shows less base motion rejection than the gyrostabilized and complementary filter curve for frequencies less than 10 hertz. The IMC loops in each configuration equally attenuate any errors with frequencies above 10 hertz. This accounts for the identical error rejection curves above the 10 hertz frequency. For the mass-stabilized approach, any error less than 10 hertz couples into the track loop through the flexure and corrupts the reference platform's desired LOS command to the CG loop. The CG loop follows this command thereby causing a LOS error to the system.

The right-hand curves are plots of the RMS LOS error residuals versus frequency. They were generated by a frequency response computer program which applies the base motion PSD (Figure 6.3-3) to the azimuth loops in Figures 6.2-3,

*Error rejection transfer functions show the sensitivity of the LOS to base motion disturbances in the frequency domain.

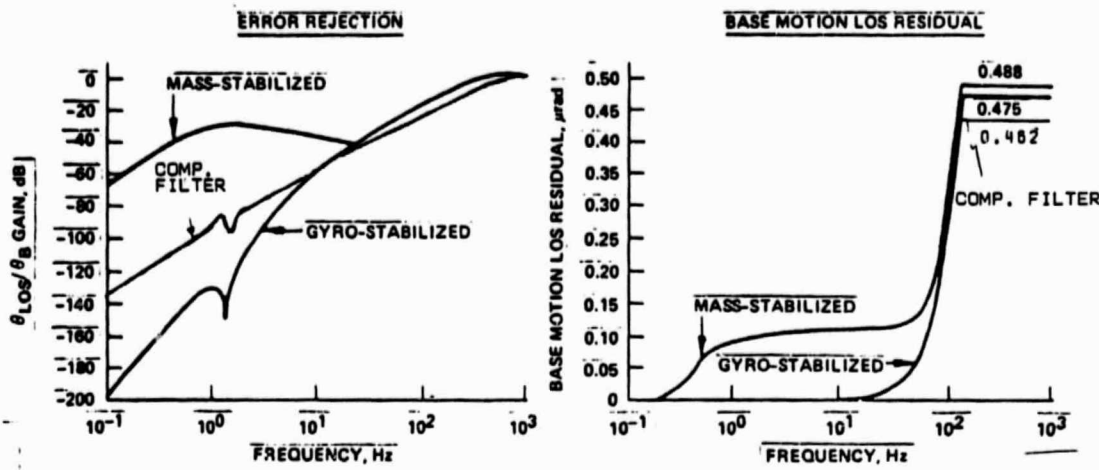


Figure 6.3-6: Servo Configuration Comparisons of Base Motion Error Rejection

through 6.2-5. This generates an output PSD at the LOS which is integrated over frequency to obtain the mean-squared error.

The three configurations show very small differences between their base motion LOS residual errors. At frequencies below 10 hertz, the mass-stabilized RMS LOS error is about .10 urad larger than the other two configurations, but at 125 hertz, it differs by only .013 to .025 urad. This is attributed to the improved mass-stabilized error rejection at the higher frequencies. Although this improvement is small, it acts over a much larger bandwidth (10-125 hertz) than the inferior low frequency error rejection (0-10 hertz).

The desired IMC loop bandwidth was determined by applying the base motion disturbances to the gyro-stabilized servo for various bandwidth values and recording the RMS LOS errors. This was done for 100 to 400 hertz bandwidths with the results plotted in Figure 6.3-7.

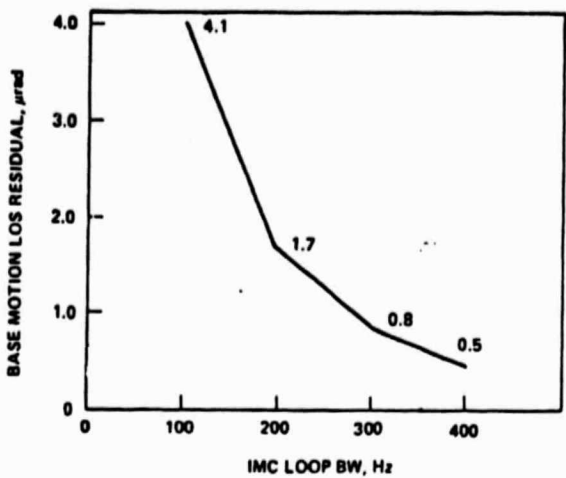


Figure 6.3-7 LOS Error vs. IMC Loop Bandwidth

With a system error budget of 1 urad, the 400 hertz bandwidth was chosen. Its LOS error of 0.5 urad allows enough margin for other error contributions. This bandwidth was also chosen to exceed the base motion bandwidth of 125 hertz to allow for unforeseen high frequency components.

6.3.3 Friction Torque Disturbance

Due to the limited resources and time for this study, the friction disturbance was modeled as a simple Coulomb friction torque acting at the gimbal bearings. Stiction and motor hysteresis were not addressed.

Coulomb friction was modeled as a random process from which a probability density function (pdf) was derived (See Appendix 6.5.3). From the pdf, a PSD was generated to provide us with a frequency domain representation. The PSD from Appendix 6.5.3 is factored to yield,

$$S_{\theta F}(\omega) = \frac{4A^2 u}{\omega^2 + 4u^2} = \left(\frac{2A\sqrt{u}}{j\omega + 2u} \right) \left(\frac{2A\sqrt{u}}{-j\omega + 2u} \right) \quad 6.3.3.1)$$

The factored form provides us with a friction acceleration transfer function that was applied to each of the servo configurations in the manner depicted in Figure 6.3-8.

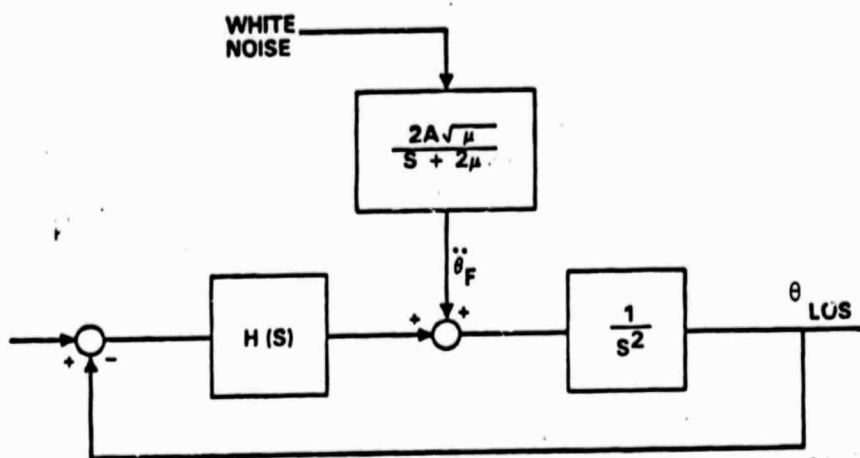


Figure 6.3-8 : Friction Torque Disturbance Input to Servo Loops

A white noise process was input to the friction transfer function. Its output is a random acceleration disturbance that enters the servo loop and causes a residual LOS error. The RMS of the LOS error is generated by a computer program that performs the following linear mathematics.

$$\theta_{RMS} = \left[\frac{1}{2\pi j} \int_0^{\infty} S_{\ddot{\theta}_F}(\omega) |H'(j\omega)H'(-j\omega)| d\omega \right]^{1/2} \quad (6.3.3.2)$$

$H'(S)$ is the servo loop transfer function that relates the LOS angle, θ_{LOS} , to the input friction acceleration, $\ddot{\theta}_F$, for each of the candidate servo configurations. For the simple block diagram in Figure 6.3-8,

$$H'(S) = \frac{\theta_{LOS}}{\ddot{\theta}_F} = \frac{1}{S^2 + H(S)} \quad (6.3.3.3)$$

Substituting equations (6.3.3.3) and (6.3.3.1) into (6.3.3.2) yields,

$$\theta_{RMS} = \left[\frac{1}{2\pi j} \int_0^{\infty} \frac{4A^2 u}{\omega^2 + 4u^2} \left| \frac{1}{-\omega^2 + H(j\omega)} \cdot \frac{1}{\omega^2 + H(-j\omega)} \right| d\omega \right]^{1/2} \quad (6.3.3.4)$$

Simplifying this equation yields θ_{RMS} as a function of u , the average number of zero crossings per second. RMS LOS errors for A equal to unity were generated for each servo configuration and for varying values of u . That data is plotted in Figure 6.3-9 (note that two scales were needed to plot all three curves on the same graph).

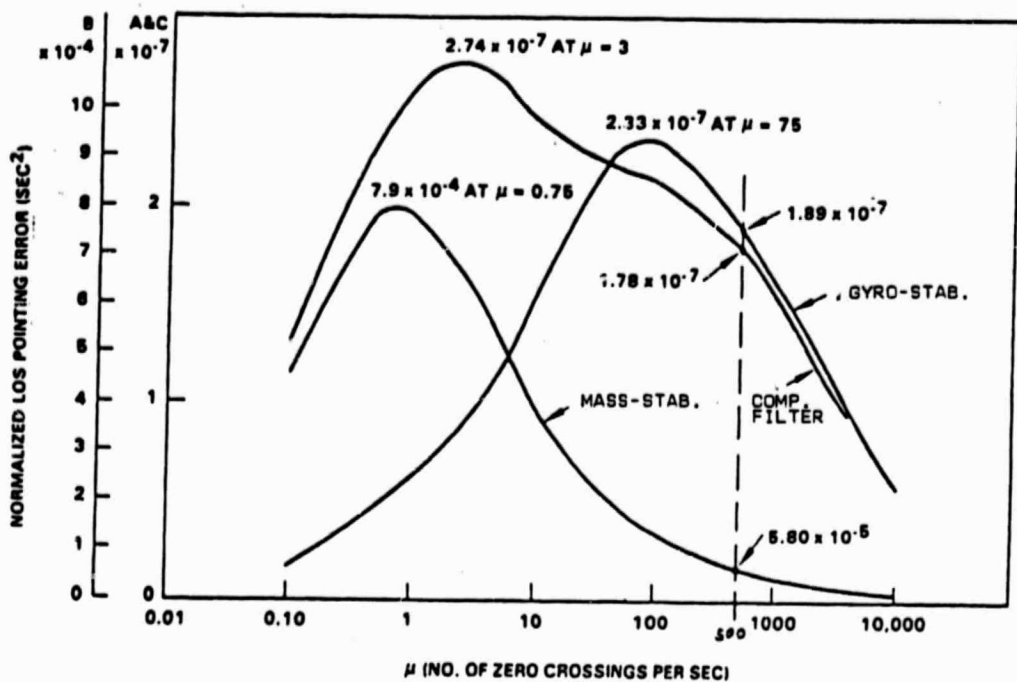


Figure 6.3-9: Friction Acceleration Effects to Servo Configuration LOS Errors
 (See Appendix 6.5.3 for an interpretation of the Coulomb friction modeling and LOS results in Figure 6.3-9).

The data at $\mu = 500$ is highlighted because that is the estimated number of zero crossings per second that is computed from the base motion PSD (Figure 6.3-3). The algorithm estimating μ is derived in Reference 1 to equal

$$\mu = \frac{1}{\pi} \left[\frac{\int_{-\infty}^{\infty} \omega^2 S(\omega) d\omega}{\int_{-\infty}^{\infty} S(\omega) d\omega} \right]^{1/2} \quad (6.3.3.5)$$

where $S(\omega)$ equals the base motion angular rate PSD.

In comparing the three curves, it is apparent that the mass-stabilized configuration performs much more poorly to friction disturbances than the other two configurations. This is true for two reasons.

- 1) In Section 6.3.2, it was pointed out that the mass-stabilized configuration does not reject low frequency disturbances as well as the gyro-stabilized configuration. This fact by itself is not sufficient to cause the extreme performance differences.

2) The shape of the disturbance input in the frequency domain is also an important factor. Figure 6.3-10 shows an asymptotic frequency plot of the friction transfer function.

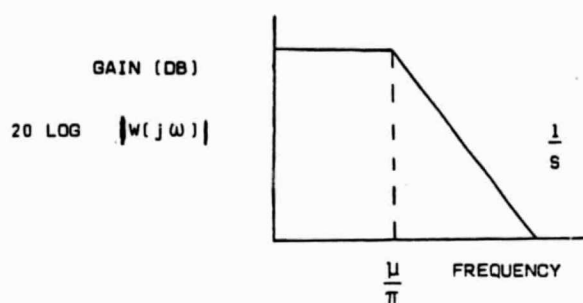


Figure 6.3-10: Friction Disturbance Angular Acceleration Transfer Function

The gain in Figure 6.3-10 represents a random angular acceleration. To compare this disturbance to the base motion disturbance and apply it to the error rejection transfer functions (Figure 6.3-6), it must be converted to an angular displacement through double integration.

$$\text{Therefore, } \frac{1}{s^2} W(s) = \frac{1}{s^2} \frac{2A\sqrt{u}}{s^2 + 2u} \quad (6.3.3.6)$$

and when plotted versus frequency, becomes

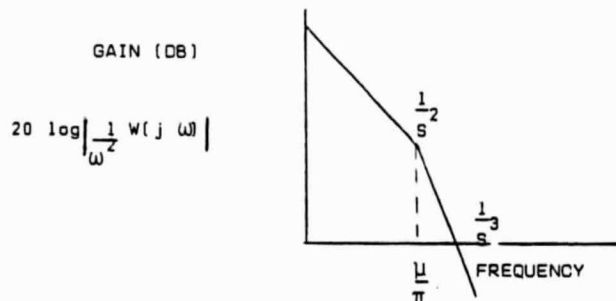


Figure 6.3-11 : Friction Disturbance Angular Displacement Transfer Function

It is quite obvious that this transfer function predominates at the lower frequencies and decreases very rapidly with increasing frequency ($\frac{1}{s^2}$, $\frac{1}{s^3}$).

Therefore, this function shape, together with the inferior mass-stabilized error rejection performance, justifies the relative LOS errors between the mass- and gyro stabilized configurations.

The complementary filter error rejection performance is slightly inferior to the gyro-stabilized results. This again is caused by two factors.

- 1) It was pointed out in Section 6.3.2 that the complementary filter error rejection curve at low frequencies does not perform as well as the gyro-stabilized configuration but performs better at higher frequencies.
- 2) The friction disturbance at $u = 500$ (corner frequency equals 160 hertz) has its predominant energy at low frequencies (Figure 6.5-9).

Since the friction error is essentially at low frequencies where the complementary filter performs less favorably, its LOS error is larger.

The curves in Figure 6.3-9 are normalized LOS errors for a friction-to-inertia ratio of A equal to 1 rad/sec². For our gimbals, the azimuth and elevation values of A were estimated to equal .12 rad/sec² and .16 rad/sec², respectively. At u equal to 500 zero crossings per second, the LOS errors for each configuration are tabulated below.

CONFIGURATION	FRICTION LOS ERRORS (URAD)		TOTAL (URAD)
	AZ	EL	
GYRO-STAB.	.022	.031	.053
MASS-STAB.	6.79	9.45	11.64
COMP. FILTER	.021	.029	.050

Figure 6.3-12: Friction LOS Error Summary

6.3.4 Other Error Sources

This section discusses the less significant error sources that complete the error analysis. The errors consist of

- 1) point ahead
- 2) dynamic following
- 3) LVDT non-linearity
- 4) gyro noise

6.3.4.1 Point Ahead Error

The point ahead error is the angular error in pointing the transmitted beam caused by the time delay it takes the beam to travel from one satellite to the other. The two way transmission time is computed as

$$T = \frac{2R_D}{C} \quad (6.3.4.1.1)$$

where R_D = relative LOS range between satellites

C = speed of light

The point ahead angle equals the change in the LOS angle during the transmission time, T . It is computed from the LOS tangential velocity to be

$$\alpha_D = \frac{V_D}{R_D} T \quad (6.3.4.1.2)$$

which yields,

$$\alpha_D = \frac{2V_D}{C} \quad (6.3.4.1.3)$$

Note that the point ahead angle is only a function of V_D . Therefore, the point ahead error is derived from the uncertainty in estimating V_D .

From previous studies, the tangential velocity error, ΔV_D , was assumed to be less than 1 m/sec for orbits where V_D equals 50 km/sec (for our LEO/GEO orbits, maximum V_D equals 12 km/sec). Using a conservative ΔV_D of 10 m/sec,

$$\Delta \alpha_D = \frac{2\Delta V_D}{C} = \frac{2 \cdot 10}{3 \times 10^8} = .066 \text{ urad} \quad (6.3.4.1.4)$$

for both axes which applies only to the transmitted beam's pointing error.

6.3.4.2 Dynamic Following Error

The dynamic following error is a DC error that is caused by tracking an accelerating target with a Type II track loop. Type II implies that there are two integrators in the track loop (either electronic as in the gyro-stabilized or kinematic as in the mass-stabilized).

The following error is the amount of angular position error that must be output by the track sensor before the track loop responds to an acceleration disturbance.

For example, in Figure 6.3-13 , a Type II track loop is driving a reference platform that is being perturbed by the friction acceleration disturbance, $\ddot{\theta}_F$.

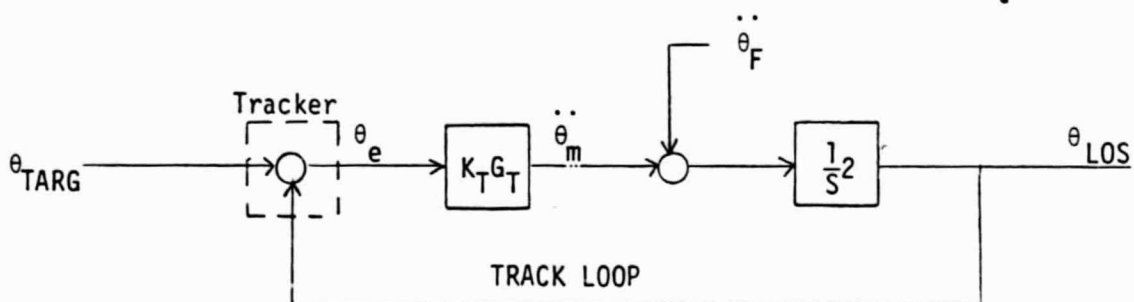


Figure 6.3-13 : Track Loop Block Diagram for Following Error

The reference platform will not move until the motor's acceleration, $\ddot{\theta}_m$, equals or exceeds $\ddot{\theta}_F$. From the figure,

$$\ddot{\theta}_m = K_T G_T \theta_e \quad (6.3.4.2.1)$$

Under steady state conditions, $G_T \approx 1$ yielding

$$\ddot{\theta}_m = K_T \theta_e \quad (6.3.4.2.2)$$

To null the disturbance acceleration $\ddot{\theta}_F$, θ_e must build up to or exceed $\frac{1}{K_T} \ddot{\theta}_F$, the dynamic following error.

Formally, the transfer function relating the track error to $\ddot{\theta}_F$ equals

$$\frac{\ddot{\theta}_e(s)}{\ddot{\theta}_F(s)} = \frac{1}{s^2 + K_T G_T} \quad (6.3.4.2.3)$$

Under steady state conditions,

$$\lim_{s \rightarrow 0} \frac{\ddot{\theta}_e(s)}{\ddot{\theta}_F(s)} = \frac{1}{K_T} \quad (6.3.4.2.4)$$

where $K_T = \frac{(2\pi f c)^2}{R^{1/2}}$ as derived in Appendix 6A.2. Therefore, the steady state error due to an accelerating target is

$$\theta_{e_{ss}} = \frac{\ddot{\theta}_F R^{1/2}}{(2\pi)^2 f_c^2} \quad (6.3.4.2.5)$$

From Appendix 6A.4, it was determined that the maximum total angular LOS acceleration between satellites equals 0.2 urad/sec². Setting the lead ratio R equal to 6, equation 6.3.4.2.5 is evaluated for track loop bandwidths of 1 and 400 hertz to yield

$$\theta_{e_{ss}}(1) = .01 \text{ urad}$$

and $\theta_{e_{ss}}(400) = 0 \text{ urad}$

The dynamic following error can mostly be eliminated by feedforwarding estimates of the LOS angular velocity and acceleration data* to the inner loops of the mass- and gyro-stabilized configurations. The feedforward signals effectively increase the track loop bandwidth by providing anticipation to the system.

6.3.4.3 LVDT Non-Linearity

An accurate approach to measuring small angular displacements is to use an LVDT. The LVDT measures linear displacements that are adjusted by the lever arm distance from the center of rotation to the LVDT, to output an angular displacement.

*It is assumed this data does not contain excessive noise. Otherwise, it is best to not correct the error at all.

A typical LVDT manufactured by Schaevitz has a linear range of $\pm .01$ inches. The maximum IMC mirror linear travel equals $\pm .0075$ inches assuming an angular travel of ± 10 mrad. For these conditions, the LVDT is linear to $\pm .25\%$ of the IMC travel.

The LVDT is being used for two applications.

- 1) It measures the relative angles between the reference platform and the telescope (mass-stabilized configuration only).
- 2) It measures the relative angles between the IMC mirror and the telescope (for all configurations).

Since the reference platform operates about the null during steady state, any LVDT non-linearities will vanish as the angular deviation approaches zero.

For the IMC mirror, the angular deflections are small because the IMC loop only responds to disturbances above 10 hertz. For the worst case, however, lets assume the mirror must remove the entire 12 urad of base motion RMS error.

Therefore, the LVDT non-linearity is computed as

$$\Theta_{LVDT} = (.0025)(12 \text{ urad}) = .03 \text{ urad}$$

for each axis.

6.3.4.4 Gyro Noise

The GI-G6G gas bearing rate-integrating gyro built by Northrop is a strap-down space-qualified device with a life expectancy of years. It has a noise bandwidth of 5 kilohertz with an RMS error of 0.3 urad. The maximum useable bandwidth of 400 hertz results in a gyro noise error of

$$\Theta_{gyro} = [400(\frac{.09}{5000})]^{1/2} = .084 \text{ urad}$$

for each axis.

6.4 Servo Configuration Analysis Summary and Conclusions

This section summarizes the error analysis and spacecraft reaction torque results for each servo configuration. It delineates the receiver and transmitter optical LOS errors and examines the overall system pointing error due to contributions from both sources. Finally, a comparative summary table lists the pros and cons of each configuration to assist in recommending a servo approach.

6.4.1 Error Analysis Results

The error analysis results generated in Section 6.3 are summarized for each configuration in Figure 6.4-1.

Figure 6.4-2 reduces the data from the above table to compare the servo configuration performances. It adds the 1σ LOS tracking error to the point ahead and dynamic following errors to obtain a total LOS pointing error for each optical system.

Configuration	Aperature Diameter (in.)	Mean LOS Error (urad)	1σ LOS LOS Error (urad)	Total LOS Error (urad)
Gyro-Stabilized	6	.078	.63	.71
	20	.078	.49	.57
Mass-Stabilized	6	.078	11.65	11.73
	20	.078	11.65	11.73
Complementary Filter	6	.066	.93	1.0
	20	.066	.52	.59

Figure 6.4-2: Two-Axis Error Analysis Summary

The tabulated data concludes that the mass-stabilized configuration does not satisfy the system LOS error budget requirement of 1 urad. The large LOS

Figure 6.4-1: Two-Axis Error Analysis Results

Error Source	Configuration	Aperture Diameter (in.)	Azimuth LOS Error (urad)	Elevation LOS Error (urad)	Total λ_0 LOS Error (urad)	Mean LOS Error (urad)
Sensor Noise	GS, MS	6 20	.028 .009	.028 .009	.040 .013	---
	CF	6 20	.567 .170	.567 .170	.802 .240	---
Base Motion Disturbance	GS	6 & 20	.475	0	.475	---
	MS	6 & 20	.488	.004	.488	---
	CF	6 & 20	.462	0	.462	---
Gimbal Friction	GS	6 & 20	.022	.031	.038	---
	MS	6 & 20	6.79	9.45	11.64	---
	CF	6 & 20	.021	.029	.036	---
Point Ahead	GS,MS,CF	6 & 20	---	---	---	.066
Dynamic Following	GS,MS	6 & 20	---	---	---	.012
	CF	6 & 20	---	---	---	0
LVDT Non-Linearity	GS,MS,CF	6 & 20	.03	.03	.042	---
Gyro Noise	GS	6 & 20	.08	.08	.113	---

error was shown in Section 6.3.3 to be caused by its poor error rejection performance for low frequency disturbances. In addition, the friction disturbance is predominantly low frequency for u equal to 500 zero crossings per second.

It was suggested that magnetic bearings be used to reduce the friction torque disturbance. In consulting HAC experts, it was pointed out that magnetic bearings are cumbersome to implement because backup roller bearings are required replacements to withstand excessive loading and power failure.

The gyro-stabilized configuration shows the best LOS error performance for both 6 inch and 20 inch receivers. Its shortcomings are reliability, and the limited bandwidth of the gyro. For this study, the highest frequency error that the gyro must sense was base motion that occurred at 125 hertz which approaches its bandwidth limit. For higher frequencies, the gyro must be complemented by a higher bandwidth device such as an ADS, which adds further complexity.

To simplify the design, NASA/GSFC suggested that the gyro be replaced by an ADS. The ADS is a high frequency device operating between 2 and 1000 hertz (Systron Donner). If only the ADS were used to measure inertial LOS position, the track loop bandwidth must be increased to 2 hertz to attenuate all errors below the ADS's 2 hertz limit. This approach improves reliability since the ADC is not a spinning device.

The complementary filter's LOS tracking accuracy is inferior to the gyro-stabilized configuration because it transmits a greater amount of sensor noise to the LOS. This additional LOS noise is due to the wide bandwidth track loop that eliminates the need for inner loops to attenuate base motion disturbances.

However, by doubling laser power to increase the sensor SNR to 10, the complementary filter LOS errors are reduced to

.82 urad 6 in. dia.

.55 urad 20 in. dia.

which is comparable to the gyro-stabilized results.

6.4.2 Reaction Torque Results

The reaction torques to the spacecraft are predominantly caused by torque loads applied to the 2-axis gimbal. These reaction torques were generated for the friction and kinematic coupling disturbances via the computer simulation that generated the LOS errors.

The simulation outputs azimuth and elevation gimbal RMS accelerations which are converted to RMS torques by multiplying them by their respective inertias. This data was generated for each configuration and tabulated in Figure 6.4-3.

CONFIGURATION	RMS FRICTION* (FT-LB)		RMS BASE MOTION (FT-LB)		RMS TOTAL REACTION TORQUE (FT-LB)
	AZ	EL	AZ	EL	
GYRO-STAB.	.058	.038	.107	0	.13
MASS-STAB.	.057	.038	.107	0	.13
COMP. FILTER	.028	.018	.006	0	.03

*RESULTS FOR 500 ZERO CROSSINGS PER SEC

Figure 6.4-3: Reaction Torque Summary

The complementary filter RMS reaction torque is somewhat smaller than the other configurations. Upon observing the transfer functions relating gimbal angle to base motion disturbance, the complementary filter transfer function rolls off at $\frac{1}{s^4}$ (at 10 hertz) verses the other configurations roll off at $\frac{1}{s^2}$ (at 10 hertz). This means that the complementary filter coarse gimbal removes less LOS error than the other configurations resulting in less reaction torque.

Figure 6.4-4 shows the spacecraft reaction acceleration PSD resulting from the base motion disturbance provided by NASA and applied to the gyro-stabilized configuration. The forward sum of this curve times the gimbal inertia results in the RMS value of .107 ft-lb appearing in the above table.

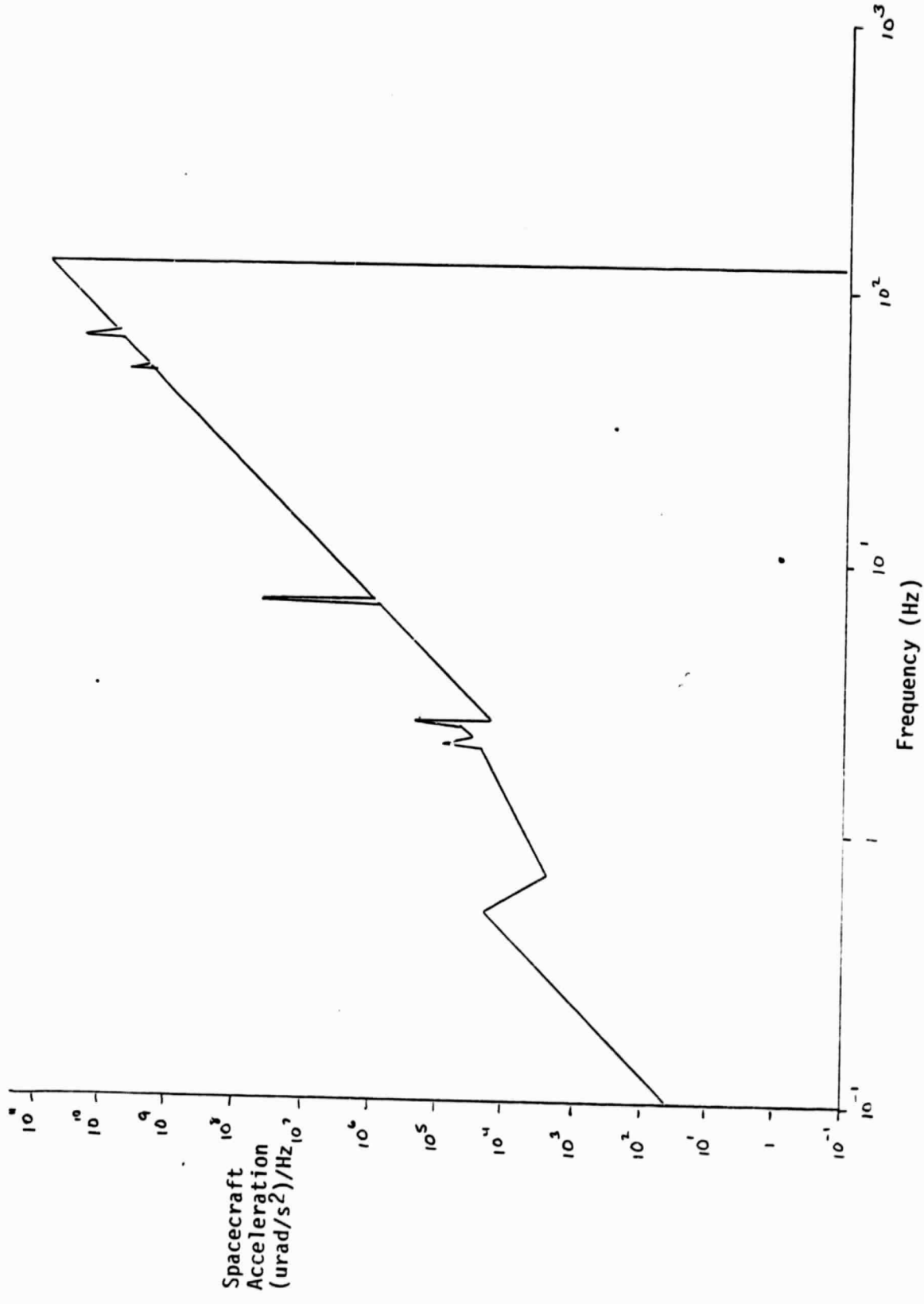


Figure 6.4-4: Spacecraft Reaction Acceleration PSD

6.4.3 Comparative Summary and Recommendations

The table in Figure 6.4-5 summarizes the advantages and disadvantages of each servo configuration. It seems appropriate to review them in light of the three requirements stated in Section 6.1.1

- 1) pointing accuracy
- 2) spacecraft reaction torque
- 3) design simplicity and reliability

For pointing accuracy, the gyro-stabilized approach outperforms each of the other configurations. It is able to satisfy the 1 urad 2-axis LOS pointing error budget with half the required power than the complementary filter approach. The mass-stabilized approach was unable to meet the error budget due to excessive LOS error residuals caused by friction.

The spacecraft reaction torque results are very similar for all configurations. The complementary filter has more flexibility in splitting the LOS error by merely changing the corner frequency of its low-pass filter. This characteristic is advantageous only if the actual base motion disturbances are larger than the predicted values. Under this condition, the IMC mirror travel may be inadequate requiring the corner frequency to be increased. A problem caused by underestimating the base motion is that the complementary filter track loop bandwidth must be increased to attenuate the additional disturbance. This in turn increases the sensor noise perturbing the LOS. For the gyro-stabilized approach, increasing the IMC loop bandwidth has no noise effects on the LOS.

The complementary filter provides the most reliability of all the configurations because of its simple design. However, it was mentioned that the gyro-stabilized reliability could be improved if the gyro were replaced by a more space-qualified sensor such as the ADS. This change decreases complexity by eliminating excitation signal generators and demodulators associated with gyro implementation.

Figure 6.4-5: Servo Configuration Summary Comparison

Configuration	Required Loops Per Axis	Sensors Per Axis	Advantages	Disadvantages	Comments
Gyro-Stabilized	<ul style="list-style-type: none"> o Track o Coarse Gimbal o IMC 	<ul style="list-style-type: none"> o Tracker o RIG and/ or ADS o LVDT 	<ul style="list-style-type: none"> o Low BW track loop o minimizes sensor noise error <p>c requires 20 times less laser power for an SNR equivalent to high BW SNR</p> <ul style="list-style-type: none"> o Satisfies optical LOS pointing error budget of 1 urad 	<ul style="list-style-type: none"> o Complex design o multiple loops o multiple sensors o Reduced reliability o Not flexible in re-apportioning track error between coarse gimbal and IMC mirror 	<ul style="list-style-type: none"> o Replacing the RIG with an ADS o reduces complexity o improves reliability o increases sensor BW o For possible high accelerating targets, ephemeris data can be feedforwarded to provide anticipation to low BW track loop
Mass-Stabilized	<ul style="list-style-type: none"> o Track o Coarse Gimbal o IMC 	<ul style="list-style-type: none"> o Tracker o 2 LVDT's 	<ul style="list-style-type: none"> o Low BW track loop (same as gyro-stabilized) o Platform defines LOS reference o reduces complexity o increases reliability 	<ul style="list-style-type: none"> o Does not satisfy optical LOS pointing error budget o Poor error rejection performance at low frequencies o Friction torque causes excessive optical LOS error 	<ul style="list-style-type: none"> o High BW track loop o amplifies sensor noise error
Complementary Filter	<ul style="list-style-type: none"> o Track 	<ul style="list-style-type: none"> o LVDT 	<ul style="list-style-type: none"> o Simple design o Single servo loop o Minimum number of sensors o Easy to reapportion track error between coarse gimbal and IMC mirror 	<ul style="list-style-type: none"> o Satisfies optical LOS pointing error budget of 1 urad 	<ul style="list-style-type: none"> o Exceeds 1 urad LOS error budget for a sensor SNR = 5 (1.2 urad) o Requires 20 times more laser power for an equivalent high BW SNR o Requires twice as much power to satisfy error budget

The above results indicate that the gyro-stabilized configuration provides the best tracking approach for the laser communication problem. Its reliability was improved by replacing the gyro with an ADS as the inertial LOS reference. Its design has been implemented by HAC on numerous pointing and tracking systems and satisfies all system requirements.

6.5 Appendices

6.5.1 Justification for Soft-Mounted IMC Mirror

Figure 6.1-2 in the text shows the IMC mirror to be soft-mounted to the telescope by means of a single post flexure. This mounting isolates the optical train from any telescope vibrations that may enter the loop. To illustrate its importance, a simple servo block diagram of the IMC loop is presented in Figure 6.5.1-1.

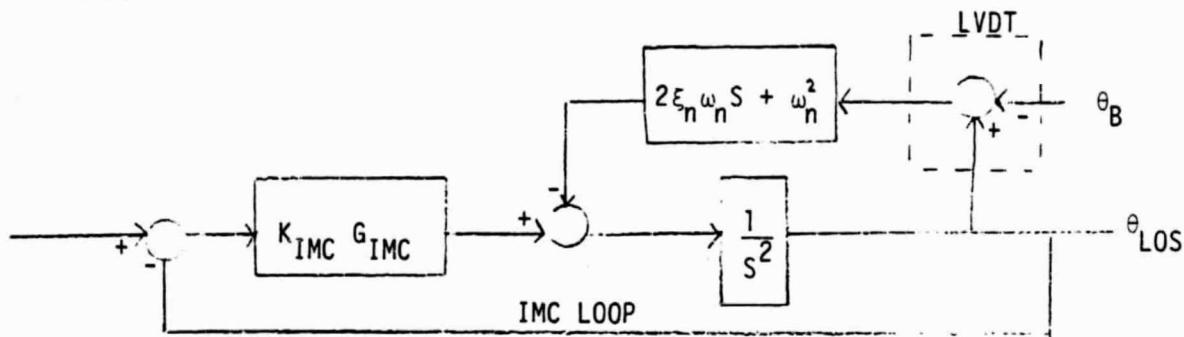


Figure 6.5.1-1: IMC Servo Block Diagram with Soft-Mounting Dynamics

where, K_{IMC} = DC gain

G_{IMC} = IMC loop compensation

ξ_n = flexure damping

ω_n = flexure natural frequency

The closed loop transfer function relating the LOS angle, θ_{LOS} , to the base motion disturbance angle, θ_B , is

$$\frac{\theta_{LOS}}{\theta_B} = \frac{2\xi_n \omega_n s + \omega_n^2}{s^2 + 2\xi_n \omega_n s + \omega_n^2 + K_{IMC} G_{IMC}} \quad (6.5.1.1)$$

The IMC mirror becomes more isolated from the base (telescope) as ω_n becomes small. In the limit,

$$\lim_{\omega_n \rightarrow 0} \frac{\theta_{LOS}}{\theta_B} = 0 \quad (6.5.1.2)$$

and θ_{LOS} decouples from θ_B .

The IMC mirror becomes more rigidly attached to the base as ω_n becomes large. In the limit,

$$\lim_{\omega_n \rightarrow \infty} \frac{\theta_{LOS}}{\theta_B} = 1 \quad (6.5.1.3)$$

and θ_{LOS} couples directly with θ_B .

Hence, we see that isolating the IMC mirror from the telescope isolates the optical train from any disturbances to the mirror base.

6.5.2 Derivation of Servo Control Equations

6.5.2.1 Type II Loop Gain and Compensation

Given a Type II loop, we wish to determine the gain and compensation to provide ample phase margin at the open loop crossover frequency, f_c .

Without compensation, a Type II loop has zero phase margin ($\phi = -180^\circ$ at crossover). It is necessary to add phase lead at f_c in order to improve loop stability. This is done by incorporating a lead/lag network into the loop that is expressed as

$$G_C(s) = \frac{s + 1}{\frac{s}{Ra} + 1} \quad (6.5.2.1.1)$$

with s = Laplacian variable

a = compensating zero

R = lead ratio

We wish to derive the value of 'a' such that the lead angle, ϕ_c is a maximum at f_c . We first express equation 6.5.2.1.1 in the frequency domain.

$$G_C(j\omega_c) = \frac{j\omega_c + 1}{\frac{j\omega_c}{Ra} + 1} \quad (6.5.2.1.2)$$

Multiplying numerator and denominator of 6.5.2.1.2 by the denominator's complex conjugate yields,

$$G_C(j\omega_c) = \frac{\omega_c^2}{1 + \frac{Ra^2}{\omega_c^2} + j(\frac{\omega_c R - \omega_c}{Ra})} \quad (6.5.2.1.3)$$

and solving for the phase angle results in

$$\angle G_c(j\omega_c) = \phi_c = \tan^{-1} \frac{\omega_c(R-1)}{Ra + \omega_c^2/a} \quad (6.5.2.1.4)$$

where ϕ_c = the desired phase margin at f_c .

Taking the tangent of both sides of 6.5.2.1.4 yields

$$\tan \phi_c = \frac{\omega_c(R-1)}{Ra + \omega_c^2/a} \quad (6.5.2.1.5)$$

To solve for the maximum value of ϕ_c requires taking the derivative of ϕ_c with respect to 'a', setting it to zero, and finally solving for 'a'.

Therefore,

$$\frac{d}{da} \tan \phi_c = \frac{1}{\cos^2 \phi_c} \frac{d\phi_c}{da} \quad (6.5.2.1.6)$$

or $\frac{d\phi_c}{da} = \frac{\cos^2 \phi_c}{(Ra^2 + \omega_c^2)^2} [(Ra^2 + \omega_c^2) \omega_c (R-1) - \omega_c (R-1)(2Ra^2)] = 0 \quad (6.5.2.1.7)$

There are two ways for equation 6.5.2.1.7 to equal zero

- 1) $\phi_c = \pm 90$ degrees
- 2) the bracketed expression equals zero

Since we do not wish to limit ϕ_c to ± 90 degrees,

$$(Ra^2 + \omega_c^2) = (2Ra^2) \text{ and } \boxed{a = \frac{\omega_c}{\sqrt{R}}} \quad (6.5.2.1.8)$$

Having solved for the compensating zero, we wish to now solve for the DC gain (K_a) which must satisfy the requirement that the open loop gain at the cross-over frequency equals unity. i.e.,

$$|G(j\omega_c)| = \frac{K_a \left| \frac{j\omega_c}{a} + 1 \right|}{\left| \frac{j\omega_c}{Ra} + 1 \right|} = 1 \quad (6.5.2.1.9)$$

Upon substituting equation 6.5.2.1.8 into 6.5.2.1.9 and simplifying, yields

$$|G(j\omega_c)| = \frac{K_a(R+1)^{1/2}}{\omega_c^2(R-1+1)^{1/2}} = 1 \quad (6.5.2.1.10)$$

Finally, solving for K_a results in,

$$K_a = \frac{2}{R^{1/2}} \frac{\omega_c}{s^2}$$

6.5.2.2 Complementary Filter Compensation

This section derives the compensation networks for the complementary filter configuration. The servo philosophy is to split the track error signal into its high and low frequency components such that the high frequency error is attenuated by the IMC and the low frequency error is attenuated by the coarse gimbal. A servo block diagram depicting this scheme appears in Figure 6.5.2-1

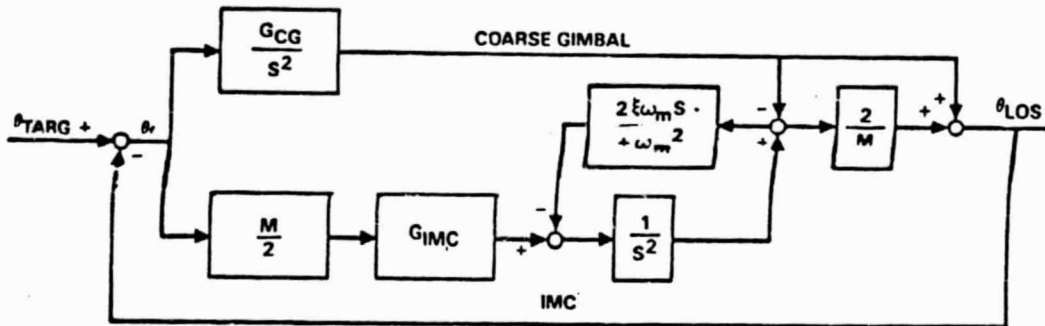


Figure 6.5.2-1: Simplified Complementary Filter Configuration Servo Block Diagram
where G_{CG} = coarse gimbal compensation

G_{IMC} = IMC mirror compensation

M = telescope magnification

ξ = IMC mirror flexure damping ratio

ω_m = effective IMC mirror spring rate

We wish to determine G_{CG} and G_{IMC} such that the open loop transfer function, $\frac{\theta_{LOS}}{\theta_e}$, equals an optimally compensated Type II track loop (Appendix 6.5.2.1), ie.,

$$\frac{\theta_{LOS}}{\theta_e} = \frac{K_a}{s^2} \frac{\frac{s}{a} + 1}{\frac{s}{Ra} + 1} \quad (6.5.2.2.1)$$

The open loop transfer function was computed using Figure 6.5.2-1 to be,

$$\frac{\theta_{LOS}}{\theta_e} = (G_{IMC} - \frac{2}{M} G_{CG}) \frac{1}{s^2 + 2\xi\omega_m s + \omega_m^2} + \frac{G_{CG}}{s^2} \quad (6.5.2.2.2)$$

Since there are two unknowns and one equation, G_{CG} was defined to be the gain K_a times a fourth order low pass filter

$$G_{CG} = \frac{K_a}{\left(\frac{s^2}{\omega_n^2} + 2\xi_n s + 1 \right)^2} \quad (6.5.2.2.3)$$

where $f_n = \frac{\omega_n}{2\pi}$ = corner frequency (10 hertz)

With G_{CG} defined, equation 6.5.2.2.2 is set equal to 6.5.2.2.1 and solved for G_{IMC} to yield,

$$G_{IMC} = K_a \left[\frac{\frac{s^2 + 2\xi_m s + \omega_m^2}{s^2}}{\frac{s}{Ra} + 1} + \frac{1}{(\frac{s^2}{\omega_n^2} + \frac{2\xi_n s}{\omega_n} + 1)^2} \left(\frac{2}{M} - \frac{s^2 + 2\xi_m s + \omega_m^2}{s^2} \right) \right] \quad (6.5.2.2.4)$$

The resulting servo block diagram appears in Figure 6.5.2-2

6.5.3 Interpretation of Statistical Coulomb Friction Model (See reference 1 for derivation of model)

Coulomb friction enters the CG loop as a result of the relative motion between the gimbal base and its bearings. Figure 6.5.3.1 shows this effect in a simple servo block diagram where

ω_T = inertial gimbal angular rate

ω_v = inertial gimbal base angular rate

$\ddot{\theta}_F$ = friction acceleration

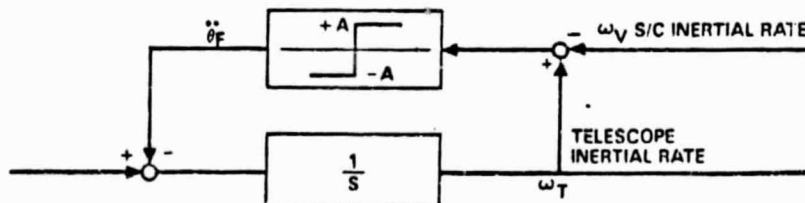


Figure 6A.3-1: Friction Acceleration Model

In this model, it is assumed that the gimbal rate, ω_T , is zero, and the only input is the base motion rate, ω_v . Therefore, the relative motion between the gimbal base and its bearings is ω_v .

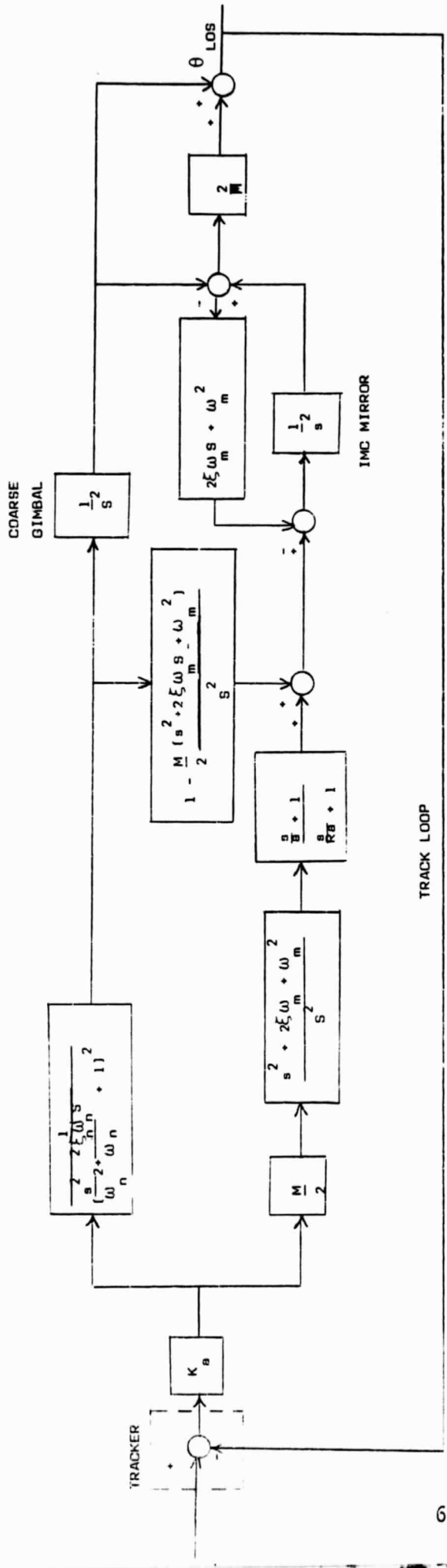


Figure 6.5.2-2: Complementary Filter Configuration Servo Block Diagram

ω_v is a random signal that can be represented by the upper curve in Figure 6.5.3.2. The friction acceleration corresponding to this rate is the constant amplitude A , that has a polarity equal to the polarity of ω_v . The lower curve in Figure 6.5.3-2 represents the applied friction acceleration. This curve, known in

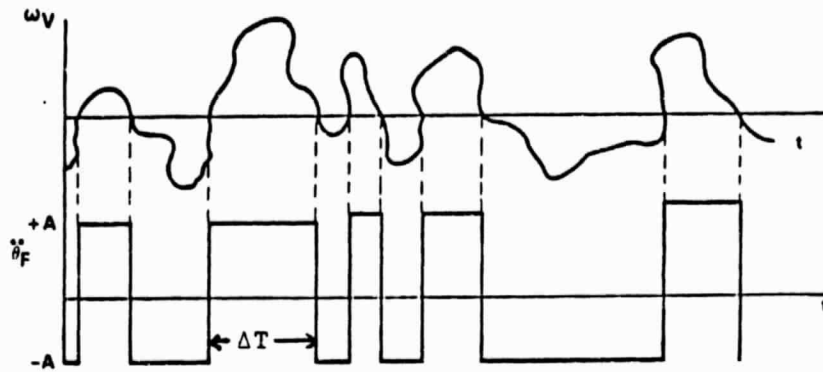


Figure 6.5.3-2: Base Motion Rate and Friction Acceleration vs. Time probability theory as a "random telegraph signal", consists of a sequence of steps of constant amplitude ($\pm A$) that occur at random time intervals, ΔT . The probability that the signal changes sign exactly K times in T seconds is given by the Poisson distribution,

$$P(K) = \frac{(uT)^k e^{-uT}}{k!} \quad (6.5.3.1)$$

where u = average number of zero crossings per second.

The maximum value of $P(k)$ occurs when k equals its expected value, uT (the average number of zero crossings). As uT increases, the probability of uT , $P(uT)$, decreases and the variance about the mean increases. This is illustrated by plotting $P(k)$ for two values of uT equal to 3 and 5 in Figure 6.5.3-3

Increasing the average number of zero crossings implies that the base motion rate has frequency components spread over an increasingly larger portion of the spectrum. The larger frequency spread increases the sample size and decreases the probability of occurrence for a given frequency value.

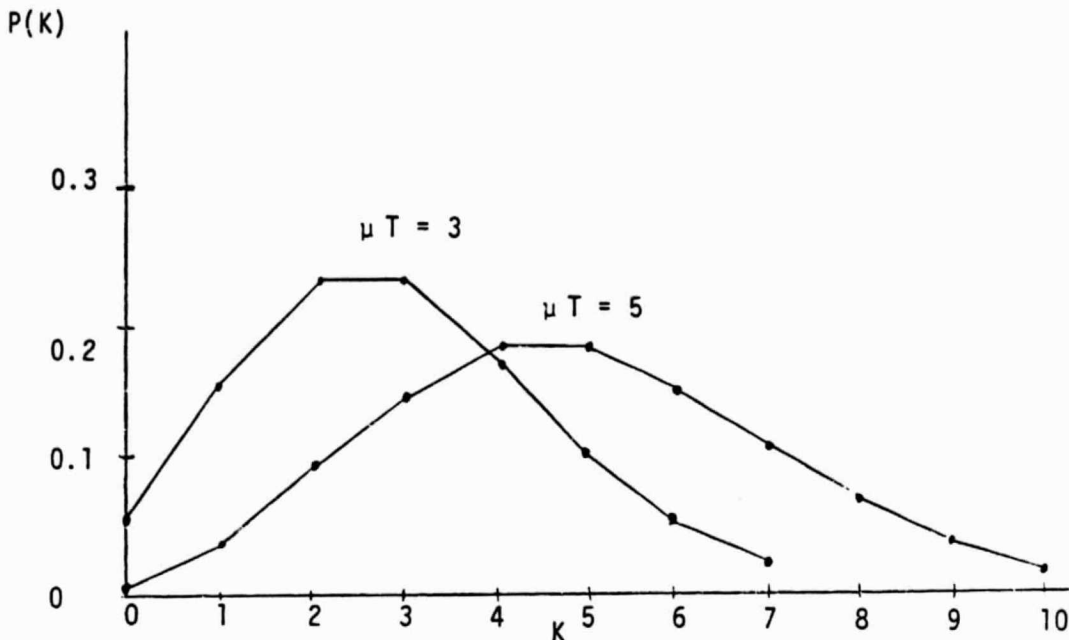


Figure 6.5.3-3: Poisson Distributions for $uT = 3$ and 5

These probability distribution characteristics appear in the autocorrelation function derived in reference 2 to be,

$$R(\tau) = A^2 e^{-2u|\tau|} \quad (6.5.4.2)$$

and is plotted in Figure 6.5.3-4 for two values of u .

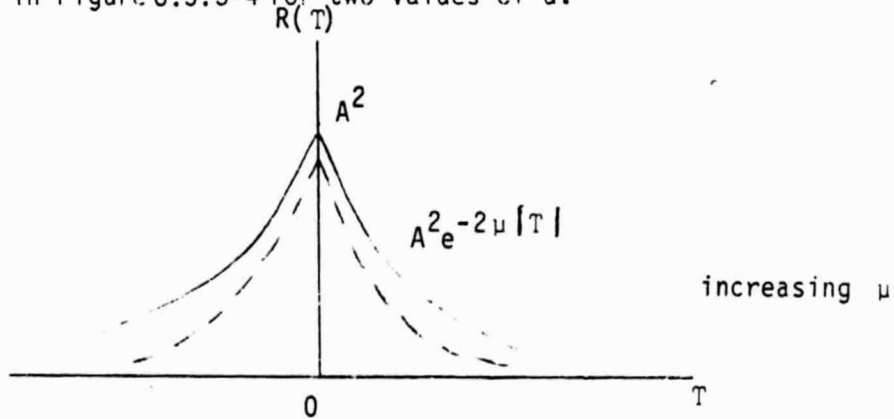


Figure 6.5.3-4: Friction Acceleration Autocorrelation Function

As u increases, the friction acceleration becomes less correlated with time (dotted curve). Increasing u subsequently reduces the PSD amplitudes as displayed in Figure 6.5.3-5. And, in the limit,

$$\lim_{u \rightarrow \infty} S_{\epsilon F}(\omega) = \lim_{u \rightarrow \infty} \frac{A^2}{\frac{\omega^2}{4u^2 + 1}} = 0 \quad (6.5.4.3)$$

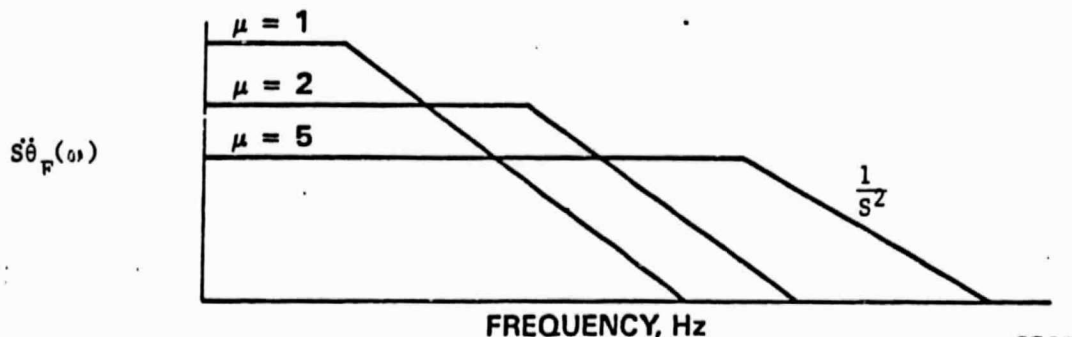


Figure 6.5.3-5: Friction Acceleration PSD Variations with μ

During our final briefing to NASA/GSFC, there was concern that as μ increases, more frequency components of friction would exceed the servo loop bandwidth and cause the LOS error to increase. This statement is correct but is not reflected in the data of Figure 6.3-8. Since this data was generated by a computer, integration limits are required. As μ was increased, that portion of the friction disturbance PSD that exceeded the upper integration limit, was truncated. Since the friction angular displacement PSD ($S_{\theta_F}(\omega)$) rolls off at $\frac{1}{s^6}$ ($\frac{1}{s^4}$ times $S_{\theta_F}(\omega)$ in Figure 6.5.3-5), increasing μ truncates a greater portion of $S_{\theta_F}(\omega)$ resulting in a smaller RMS LOS error.

6.5.4 Orbital Mechanics Equations to Compute Relative LOS Angular Accelerations

This section develops the LOS angular acceleration equations between the two earth-orbiting satellites. One satellite (GEO) is in a geosynchronous orbit in the equatorial plane while the other (LEO) is in a low earth orbit at an inclination of 8.2 degrees from the spin axis. The orbital geometry is illustrated in Figure 6.5.4-1.

An inertial orthogonal coordinate system is defined by the unit vectors (\bar{I} , \bar{J} , \bar{K}) where \bar{I} and \bar{J} are in the equatorial plane and \bar{K} passes through the Earth's spin axis.

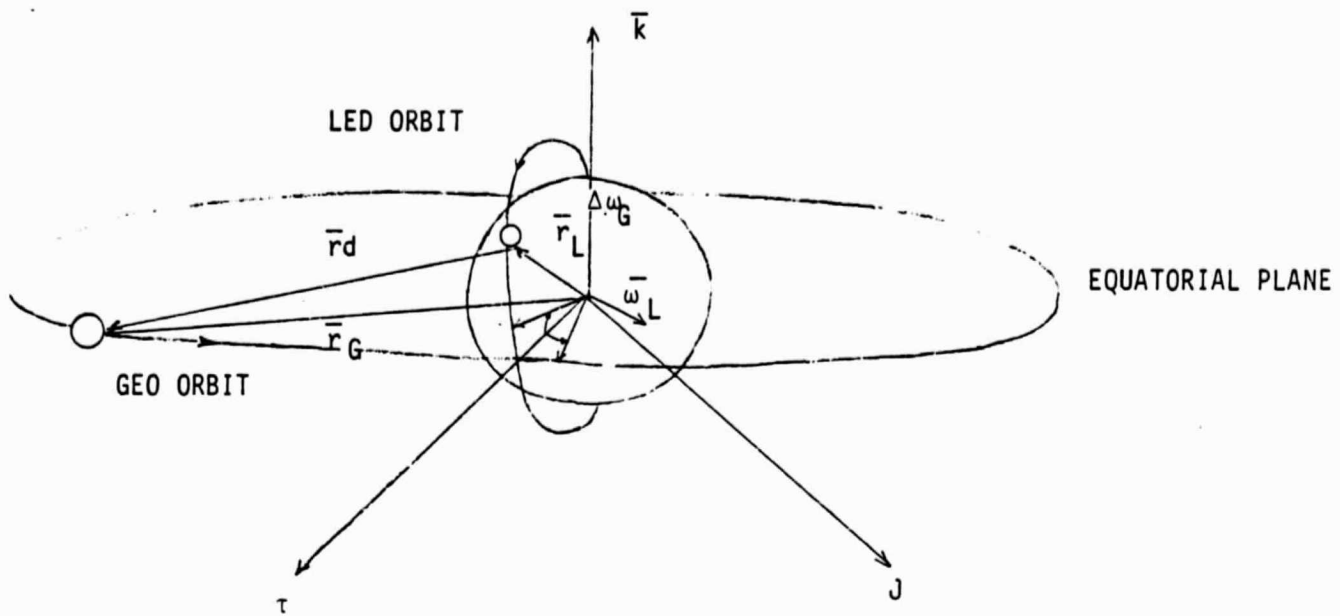


Figure 6.5.4-1: Orbital Geometry

For relative LOS orbital computations, an in-plane polar coordinate system is most desirable where position, velocity and acceleration vectors are resolved into components along (\bar{u}_r) and perpendicular to (\bar{u}_θ) the LOS vector.

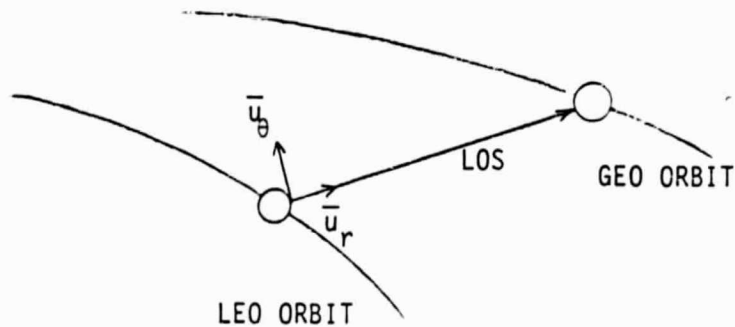


Figure 6.5.4-2: In Plane Polar Coordinate System

The following list defines all parameters used in the derivation.

\bar{r}_L, \bar{r}_G = LEO, GEO position vector in inertial coordinates

\bar{v}_L, \bar{v}_G = LEO, GEO velocity vector in inertial coordinates

$\bar{\omega}_L, \bar{\omega}_G$ = LEO, GEO angular velocity vector in inertial coordinates

The LOS vectors are defined as

$$\bar{r}_D = \bar{r}_G - \bar{r}_L \quad \text{LOS position vector}$$

$$\bar{v}_D = \bar{v}_G - \bar{v}_L \quad \text{LOS velocity vector}$$

$$\dot{\bar{v}}_D = \text{LOS acceleration vector}$$

The LOS position, velocity and acceleration vectors are represented in the polar coordinate system as follows:

$$\begin{aligned}\bar{r}_D &= r_D \bar{u}_r \\ \dot{\bar{v}}_D &= \dot{r}_D \bar{u}_r + \omega_D r_D \bar{u}_\theta \\ \text{and } \dot{\bar{v}}_D &= (\ddot{r}_D - \omega_D^2 r_D) \bar{u}_r + (\omega_D \dot{r}_D + 2\omega_D r_D) \bar{u}_\theta\end{aligned}\quad (6.5.4.1)$$

where $\omega_D = \frac{(v_D^2 - \dot{r}_D^2)^{1/2}}{r_D}$

$$\text{and } u_r = \frac{r_D}{\dot{r}_D} \quad (6.5.4.2A)$$

$$u_\theta = \frac{v_D - \dot{r}_D u_r}{\omega_D r_D} \quad (6.5.4.2B)$$

We wish to solve for ω_D in equation 6A.4.1. By taking the dot product of 6A.4.1 with the unit vector, \bar{u}_θ , results in

$$\dot{\bar{v}}_D \cdot \bar{u}_\theta = \dot{\omega}_D r_D + 2\omega_D \dot{r}_D \quad (6.5.4.3)$$

Substituting equations 6.5.4.2A and B into 6.5.4.3 and solving for ω_D yields the desired expression

$$\boxed{\omega_D = \frac{r_D \dot{\bar{v}}_D \cdot \bar{u}_\theta - \dot{r}_D \dot{\bar{v}}_D \cdot \bar{u}_\theta - 2\omega_D \dot{r}_D}{r_D}}$$

6.5.5 References

- 1) C.E. Kaplow, "The Statistical Analysis of Coulomb Friction Disturbances in Stabilization Systems", Hughes Aircraft Co. NPT Book 2, Section 5.1 Sequence 3, 11/1/73.
- 2) Mischa Schwartz, "Information Transmission, Modulation and Noise", McGraw Hill, 1970.
- 3) Andy Wu, "Analysis of LOS Jitter Due to Track Sensor Noise", HAC reference no. 7214.4/646, November 16, 1982.

7.0 TRACKING AND BEACON LINK

7.1 INTRODUCTION

In the given study scenario of a low earth orbiting (LEO) satellite transmitting a high data rate link to a satellite in geosynchronous (GEO) orbit, the most severe tracking burden is placed on the LEO optical tracking system. The LEO has a 15 cm (5.9 inch) receiving telescope, and must generate the pointing commands to direct the narrow communication beam ($10\mu\text{rad}$, $1/e^2$) to the GEO with about one microradian rms accuracy. By contrast, the GEO optical tracker has a receiving area of 50 cm (19.7 inches), and has more than a factor of two reduction in required pointing accuracy due to the larger beamwidth of the low data rate beacon (GEO to LEO).

This study then focuses on optical tracking at the LEO, since if this can be accomplished, the GEO optical tracking can also be accomplished, due to the greater optical collecting area and reduced pointing requirements.

7.2 NOISE EQUIVALENT ANGLE OF QUAD CELL TRACKING SENSOR

The pointing and tracking servo analysis of section 6.0 requires knowledge of the tracking sensor noise equivalent angle (NEA) in order to determine the relative contribution of the optical sensor to the residual pointing error. The NEA can be considered as the inverse of the rms signal to noise ratio referred to angle space.

For a quad cell with the upper right quadrant designated as quadrant 1, and numbering clockwise, the azimuth and elevation tracking error signals are given by

$$e_z(t) = [x_1(t) + x_2(t)] - [x_3(t) + x_4(t)] \quad \text{Azimuth}$$

$$e_L(t) = [x_1(t) + x_4(t)] - [x_2(t) + x_3(t)] \quad \text{Elevation}$$

where $X_i(t)$ is the electrical output of the i^{th} quadrant. The assumptions made in this analysis are:

- 1) Each quad element has identical statistics, and is statistically independent of the other elements.
- 2) The mean output of a quad element due to signal is $E[X_i] = eG K_S$ where e is the electronic charge, G is the average detector gain, and K_S are the signal photoelectron counts. Since K_S are the signal photoelectron counts per element, K_S must be computed on the basis of one-fourth of the optical signal power incident on the quad array. The noise mean is assumed to be zero (non-zero mean noise is discussed at the end of this section).
- 3) The rms noise per element is given by

$$\sigma_{X_i} = e G \sqrt{F_N K_S + K_N}$$

where F_N is the detector excess noise factor, and K_N are the total noise photoelectrons. For an RCA silicon reach-through avalanche photodiode, the excess noise can be approximated for high gain by

$$F_N \approx 2 + 0.02 G$$

where G is the mean detector gain. The excess noise is a measure of the randomness of the detector gain, and is unity for a detector with no gain.

The noise photoelectrons are given by

$$K_N = F_N (K_B + K_D) + K_{DS} + K_T$$

where K_B are the photoelectrons due to optical background radiation, K_D are the photoelectrons due to gain-dependent dark current, K_{DS} are the photoelectrons due to gain-independent dark current, and K_T are the thermal noise photoelectron counts. Since these photoelectron counts are for a single quad element, K_B must be computed on the basis of one-fourth of the total background power incident on the array.

- 4) The Airy spot on the quad array is approximated by a uniform intensity disc with radius

$$r_0 = 1.22 (\lambda/D_r) f$$

where D_r is the effective diffraction limited receiving telescope diameter and f is the focal length of the focusing lens.

We will analyze the elevation error signal, and the azimuth case is completely analogous. The expected value of the error signal is

$$\begin{aligned} E \{ e_L(t) \} &= E \{ X_1 + X_4 \} - E \{ X_2 + X_3 \} \\ &= eG (\eta/h\nu) I_s \tau (A_1 + A_4 - A_2 - A_3) \end{aligned}$$

where η is the detector quantum efficiency, $h\nu$ is the photon energy, I_s is the signal intensity, τ is the integration time, and A_i is the area intercepted by the spot in the i^{th} quadrant.

Referring to the focal plane geometry of Figure 7.2-1, where ψ_z and ψ_ℓ are the offset angles from null in azimuth and elevation, respectively, we obtain

$$A_2 + A_3 = \frac{1}{2} r_0^2 \theta - f \psi_\ell \sqrt{r_0^2 - f^2 \psi_\ell^2}$$

$$A_1 + A_4 = \pi r_0^2 - \frac{1}{2} r_0^2 \theta + f \psi_\ell \sqrt{r_0^2 - f^2 \psi_\ell^2}$$

where ϕ is defined in the figure. Taking the difference, we have

$$A_1 + A_4 - (A_2 + A_3) = \pi r_0^2 \left[1 - \frac{2}{\pi} \cos^{-1} \left(\frac{f\psi_L}{r_0} \right) \right. \\ \left. + \frac{2 f \psi_L}{\pi r_0} \sqrt{1 - (f\psi_L/r_0)^2} \right]$$

This result agrees with that obtained by Gagliardi and Karp, Optical Communications, page 391. Using the small argument approximation for the inverse cosine (to linearize the loop),

$$\cos^{-1} x \approx \pi/2 - x, \quad x \ll 1$$

the area difference becomes

$$A_1 + A_4 - (A_2 + A_3) \approx (\pi r_0^2) \frac{4}{\pi} \frac{\psi_L}{(1.22 \lambda/D_r)}$$

The expected value of the elevation error signal is then

$$E \left\{ e_L(t) \right\} = eG(n/hv) I_S (\pi r_0^2) \frac{4}{\pi} \frac{\psi_L}{(1.22 \lambda/D_r)} \\ = \frac{16}{\pi} eG K_S \frac{\psi_L}{(1.22 \lambda/D_r)}$$

The second step can be accomplished since $I_S \pi r_0^2$ is the total power in the spot (intensity x area), which generates $4K_S$ signal photoelectrons (K_S in each element).

Now examining the variance of the elevation error signal, due to the assumptions of independence and identical statistics per element we have

$$\text{Var } e_L(t) = \text{Var } X_1 + \text{Var } X_4 + \text{Var } (-X_2) + \text{Var } (-X_3) \\ = 4 \sigma_{X_i}^2 = 4 e^2 G^2 (F_N K_S + K_N)$$

$$r_o = 1.22 (\lambda D_f) f$$

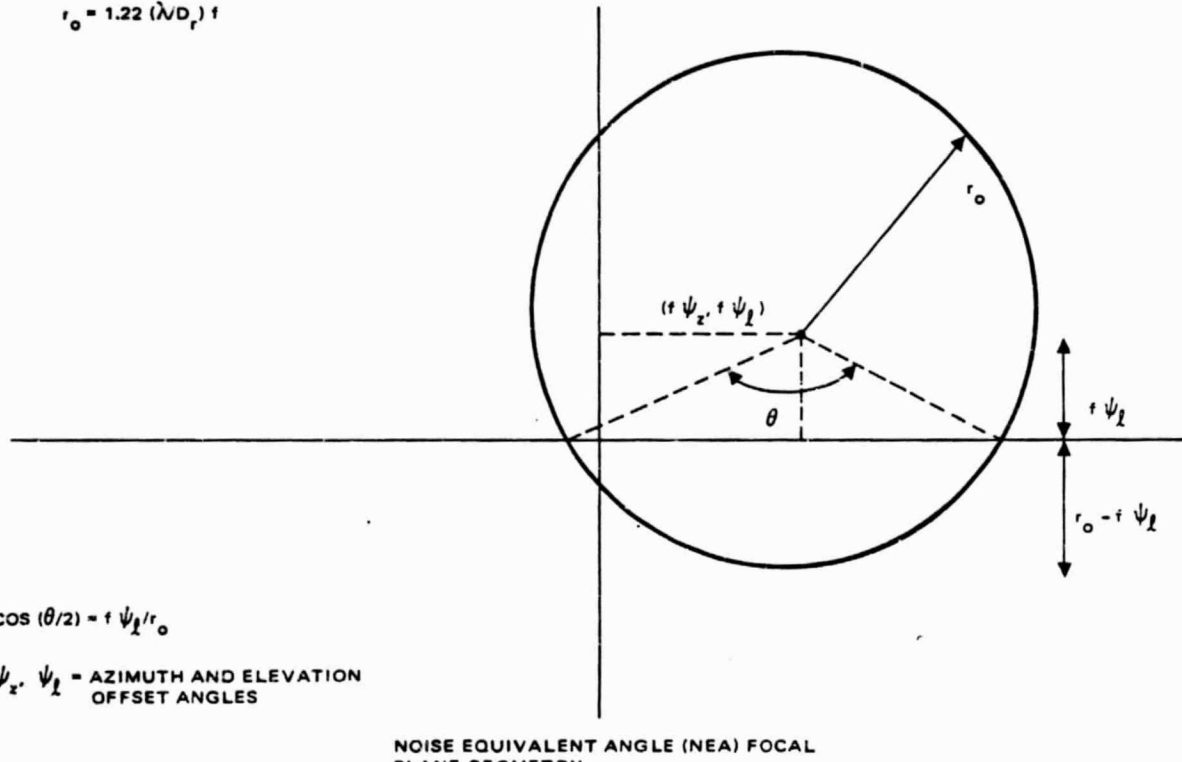


Figure 7.2-1. Noise Equivalent Angle Focal Plane Geometry.

The mean signal to rms noise of the angle measurement is then

$$\frac{E \{e_L(t)\}}{\text{Var } [e_L(t)]} = \frac{8}{\pi} \frac{\psi_l}{(1.22 \lambda/D_r)} \text{SNR}_{\text{rms}}$$

where the rms signal to noise ratio is defined by

$$\text{SNR}_{\text{rms}} = \frac{K_S}{\sqrt{F_N K_S + K_N}}$$

Note that the azimuth offset angle does not appear in the expression for elevation error, so that the azimuth and elevation tracking loops are uncoupled.

The noise equivalent angle (NEA) is thus given by

$$\sigma_{\text{NEA}} = \frac{\pi}{8} \frac{(1.22 \lambda/D_r)}{\text{SNR}_{\text{rms}}}.$$

If the imaging system is not diffraction limited, then the quantity $(1.22 \lambda/D_r)$ can be replaced by the radius of the angular optical blur. Again, it should be emphasized that the SNR is computed on the basis of an element of the quad, which sees on average one fourth of the total optical power incident on the array (signal and background).

Recently, analyses of quad cell tracking have been performed which take into account the Airy intensity distribution of the focal plane spot rather than using a uniform intensity disc. [G. Tyler and D. Fried, J. Opt. Soc. Am., Vol. 72 No. 6, June 1982; R. Gagliardi, et. al., JPL Publication 81-40]. The difference with the present analysis is slight, replacing $1.22\pi/8$ in the previous NEA expression by $3\pi/16$.

It should be noted that if assumption (2) in the derivation for tracking NEA is relaxed to allow an identical noise mean in each quadrant, the NEA expression does not change. The DC currents due to thermal noise, dark current, and uniform background illumination are cancelled in the sum and

difference algorithm [Gagliardi and Karp, Optical Communications]. For this to occur, however, the four detector elements must be matched in terms of gain, responsivity, excess noise, preamp noise, and dark currents.

The noise means therefore affect the tracking algorithm only to the extent they are nonuniform among the quadrants. Assuming the detector-preamp parameters can be matched reasonably well, the noise mean nonuniformity is primarily caused by optical background. An extended source could be offset in the quad FOV, or a star located in a single quadrant. For these cases the noise mean nonuniformity appears identical to the signal mean nonuniformity to be tracked. The only solutions to this are to overwhelm the worst case noise mean nonuniformity with signal, or to track a source with a spectrum shifted away from DC (such as a PPM data waveform) so that AC coupling may be used. In general, the latter approach is suggested, although if a gyro-stabilized tracking servo approach is used, there may be enough SNR available to overcome the noise mean nonuniformity.

It should also be mentioned that shot noise nonuniformity between the quadrants (as in the case of a star in one quadrant) does not bias the tracking error. This is because the error variance of the angular measurement is the sum of the noise variances in the four quadrants. Thus a star of a given irradiance in one quadrant contributes one fourth the angular error contribution of an extended source with the same irradiance level present in all four quadrants.

To compare alternative servo tracking system designs such as gyro-stabilized or complementary filter, it is desirable to know the dependence of the rms SNR on sample rate. Assuming the integrator output is directly sampled, the sample rate (f_s) is given by $f_s = 1/\tau$, where τ is the integration time. If the noise is not dominated by thermal noise (valid for both PIN and APD detectors for $\tau > 1.0 \mu\text{sec}$) the noise photocounts can be written as $K_N = n_N \tau$, where n_N is the noise count rate (e^-/sec) and τ is the integration time. Similarly, the signal counts can be written $K_S = n_S \tau$, where n_S is the signal count rate (e^-/sec). The expression for SNR then becomes

$$\text{SNR}_{\text{rms}} = \frac{n_s \sqrt{\tau}}{\sqrt{F_N n_s + n_N}} = \frac{1}{\sqrt{f_s}} \frac{n_s}{\sqrt{F_N n_s + n_N}}$$

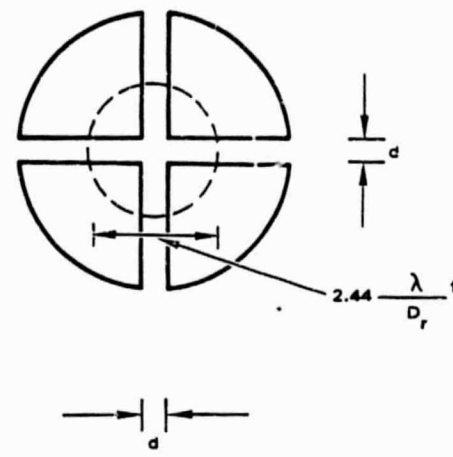
Since n_s is proportional to laser power, we conclude that for a given laser power, the rms SNR is inversely proportional to the square root of the sample rate. This is important for comparing the stabilized approach and the complementary filter approach, since the complementary filter approach requires a much higher sample rate, and therefore more laser power for a given SNR.

7.3 QUAD CELL DEAD ZONE LOSS

The typical quadrant tracking detector has a gap between the quadrants which generates no photoelectrons in response to optical intensity - in effect, a dead zone. (If the detector is reverse-biased, some photoelectron events may occur in the quadrant gap, but for a worst case analysis the gap will be considered as "dead".) When a quadrant detector has the optical spot centered, as in closed loop tracking, the spot has a vertical and horizontal stripe of dead zone obscuration. The fraction of total spot intensity lost due to the dead zone can be approximated as the ratio of area obscured by the dead zone to the total area of the spot. (This assumes a uniform intensity approximation to the Airy spot).

Referring to the geometry of Figure 7.3-1, d is the width of the dead zone, and the diffraction limited optical blur is $2.44 \frac{\lambda}{D_r} f$, where D_r is the receiving optics diameter and f is the focal length. (If not diffraction limited, $2.44 \lambda/D_r$ can be replaced by the angular subtense of the optical blur).

Let η denote the fraction of intensity lost in the dead zone gap. η is given by the ratio of obscured area to total spot area. Then η becomes



GEOMETRY FOR DETERMINATION OF INTENSITY LOSS
DUE TO QUADRANT GAP

Figure 7.3-1. Geometry for Determination of Intensity Loss Due to Quadrant Dead Zone.

$$n = \frac{2 (2.44 \lambda/D_r) f d - d^2}{\frac{\pi}{4} (2.44 \frac{\lambda}{D_r} f)^2}$$

$$= \frac{1}{1.22\pi} (4 \gamma - \gamma^2)$$

where γ is defined by

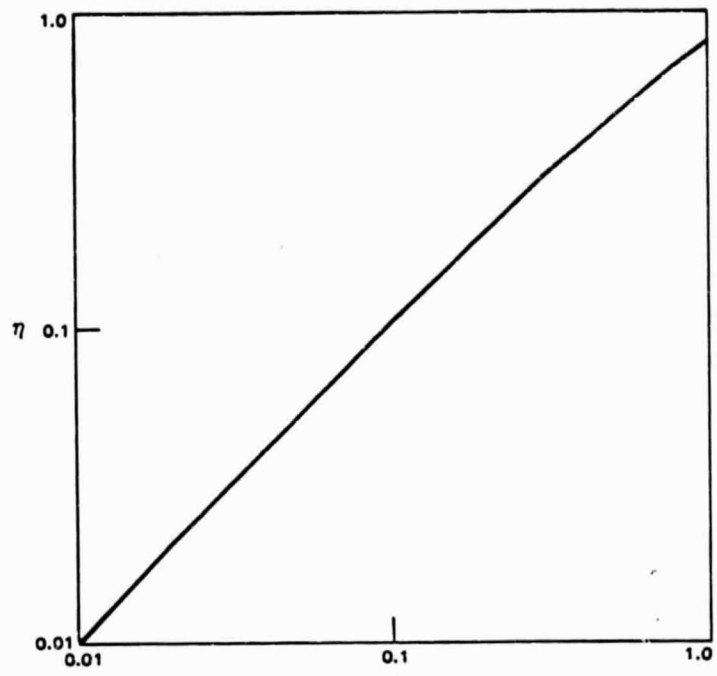
$$\gamma = (d/f) / (\lambda/D_r)$$

γ is proportional to the ratio of the angular subtense of the quadrant gap to the angular blur of the receiving optics. For small γ , $n \sim 1.04 \gamma$. Figure 7.3-2 shows a plot of n versus γ for n from 1 percent to 80 percent.

Until realistic numbers are inserted, it is not apparent that the dead zone loss can pose a serious design constraint. Suppose we choose a quad cell with a 4.4 mil (112 μm) gap (for example the Hughes HP1N 200 Q quadrant detector), $\lambda = 0.85 \mu m$, $D_R = 20$ inches, and decide to allow only 1 percent loss. This would require a focal length of 6.6 km!

Therefore very small quadrant dead zones are desirable, and to obtain practical focal lengths some intensity loss must be tolerated. The RCA quadrant avalanche photodiode (Section 7.5) has a smaller 75 μm dead zone. For $D_R = 6$ inches (15 cm), $\lambda = 0.85 \mu m$, $d = 75 \mu m$, and 50 percent dead zone loss a focal length of 26.5 meters is required. A program is underway at RCA (in Montreal) to reduce the dead zone to 30 μm . This improvement would reduce the required focal length to 10.6 meters, which is approaching a manageable length. Other programs are needed to produce small dead zone quadrant detectors.

It might be suggested that dead zone loss could be decreased by defocusing the spot, making it larger in relation to the quadrant gap. But, as shown in section 7.1, the noise equivalent angle (NEA) of the tracking sensor is proportional to the optical blur size and inversely proportional to SNR. So if the spot were increased due to defocusing, the SNR would have to be increased to get back to the same tracking performance. Either way, the dead zone loss costs laser power.



FRACTION OF INTENSITY LOST DUE TO QUADRANT GAP (η)
VERSUS $\gamma = (d/f)/(\lambda/D_r)$

Figure 7.3-2 Fraction of Intensity Lost Due to Quad Cell Gap (η)
versus $\gamma = \frac{(d/f)}{(\lambda/D_r)}$

7.4 QUAD CELL CLOSED LOOP FIELD OF VIEW

It is of interest to determine the dynamic tracking range over which a quad cell tracker can remain closed loop, since if tracking is lost some form of reacquisition must take place. If the optical spot is centered on the four quadrants, displacement of one spot radius will cause it to no longer overlap one or more quadrants. Unless all four quadrants have at least some intensity, a quantitative error signal cannot be generated for both azimuth and elevation. Thus the maximum radial displacement for which closed loop can be maintained is half of the angular blur. Let D_S denote the optical blur diameter in the focal plane, with angular subtense D_S/f , where f is the lens focal length. Since the closed loop displacement in the focal plane is $\pm D_S/2$, we can consider the closed loop field of view to be

$$\theta_{CL} = D_S/f$$

Rewriting the expression for Noise Equivalent angle (NEA) from Section 7.2 to call $D_S = 2.44 (\lambda/D_r)f$, the expression for the residual rms tracking error becomes

$$\begin{aligned}\sigma_{NEA} &= (\pi/16)(D_S/f)/SNR_{rms} \\ &= (\pi/16)(\theta_{CL}/SNR_{rms})\end{aligned}$$

Since σ_{NEA} is a radial error, if we call $\theta_{NEA} = 2\sigma_{NEA}$ as the residual tracking error field of view, the closed loop tracking dynamic range is given by

$$\frac{\theta_{CL}}{\theta_{NEA}} = (8/\pi) SNR_{rms}$$

Thus the closed loop tracking dynamic range is proportional to the SNR. For SNR above about 50, other practical limitations to the residual tracking error begin to dominate, such as element nonuniformities, amplifier dynamic range, and focal spot asymmetry. The minimum tracking error practical to obtain is about 0.01 (λ/D), so that the maximum closed loop dynamic range for high SNR is about 127.

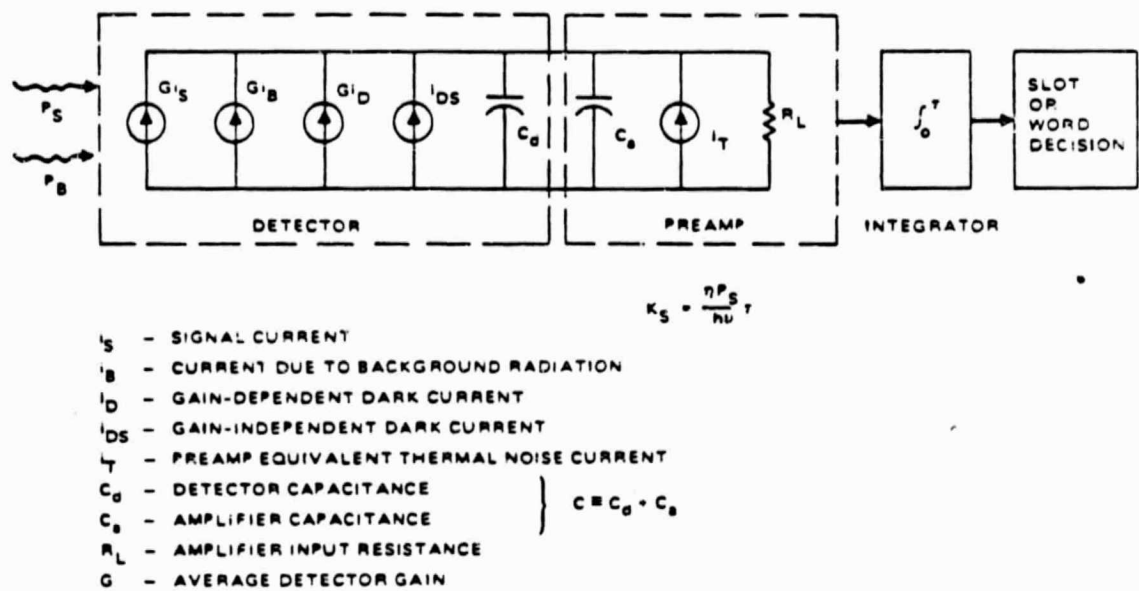
7.5 PHOTODETECTION ANALYSIS

7.5.1 Means and Variances (Gaussian). This section will relate the signal and noise means and variances to the physical parameters of the optical receiver. This preliminary development is required in order to evaluate and compare the various detection strategies.

The simple circuit model is shown in Figure 7.5-1. The receiver model described here is a high impedance (integrating) front end, which is the lowest noise approach. Signal and background optical radiation is incident on the optical detector, and their photocurrents (i_s , i_b) are amplified by the detector's internal gain (mean gain G). Also shown is a dark current which receives detector gain (i_D), as well as a gain-independent dark current (i_{DS}). The preamplifier has an equivalent thermal noise current source (i_T). The detector and preamp each have a capacitance, and the sum capacitance is $C = C_d + C_a$. R_L is the input resistance of the preamp, which is the physical source of the thermal noise. The input resistance can be generalized to an equivalent temperature which includes the other noise sources of the amplifier. This equivalent temperature (T_{eq}) is related to the preamplifier noise figure (F) by

$$T_{eq} = (F-1) 290$$

ORIGINAL PAGE IS
OF POOR QUALITY.



Direct detection receiver model

Figure 7.5-1. Direct Detection Receiver Circuit Model.

To find the equivalent thermal current source, recall that a resistor R_L at a temperature T_{eq} will generate a one-sided voltage spectral density $4kT_{eq}R_L V^2/\text{Hz}$, or a two-sided density $2kT_{eq}R_L V^2/\text{Hz}$ (where k is Boltzmann's constant). The power delivered to R_L by this voltage source is $2kT_{eq} W/\text{Hz}$ (two-sided). The power delivered to R_L by the equivalent thermal current source is $\bar{i}_t^2 R_L$ (where \bar{i}_t^2 is the mean squared current). Equating the expressions for power delivered to R_L yields

$$\bar{i}_t^2 R_L = 2kT_{eq}$$

or

$$\bar{i}_t^2 = 2kT_{eq}/R_L \quad A^2/\text{Hz} \text{ (two-sided)}$$

The total mean-squared current noise level (\bar{i}_{TOT}^2 , two-sided) in a time slot containing the optical pulse is

$$\begin{aligned} \bar{i}_{TOT}^2 &= e \bar{G}^2 i_s + e \bar{G}^2 i_B + e \bar{G}^2 i_D + e i_{DS} \\ &\quad + \frac{2 k T_{eq}}{R_L} \quad A^2/\text{Hz} \end{aligned}$$

where \bar{G}^2 is the mean-squared optical detector gain and e is the electronic charge. (The one-sided spectral density of shot noise due to current source I is well known to be $2eI$.)

Using Parseval's Theorem to take advantage of the simple time domain response of an integrator,

$$h(t) = \begin{cases} 1 & 0 < t < \tau \\ 0 & \text{otherwise} \end{cases}$$

where τ is the integration time, the variance in a pulse slot is given by

$$\sigma_s^2 = e\tau \left[\bar{G^2} i_s + \bar{G^2} i_B + \bar{G^2} i_D + i_{DS} + 2kT_{eq}/eR_L \right]$$

The variance in a slot with no pulse (σ_n^2) is obtained by setting $i_s = 0$ in the expression for σ_s^2 . The mean signal at the integrator output (m_s) is given by

$$m_s = \int_0^\tau G i_s(t) dt = G i_s \tau$$

If we define $K_s = i_s \tau/e$ as the signal photoelectron counts per integration period, then $m_s = eGK_s$. (For Gaussian statistics and fixed noise mean, the mean output for a slot with no pulse can be taken as $m_n = 0$, without loss of generality. For time-varying background sources the noise mean may have to be considered - Sections 7.7, 7.8).

A quality factor, or SNR, can be defined by

$$\text{SNR} = \frac{m_s^2}{\sigma_s^2} = \frac{K_s^2}{F_N K_s + K_N}$$

where K_N includes all the noise photoelectron counts, and F_N is the detector excess noise factor. The total noise counts are given by

$$K_N = F_N (K_B + K_D) + K_{DS} + K_T$$

where by this definition the noise counts depend on the excess noise factor. The noise photocounts due to background radiation, gain-dependent dark current, gain-independent dark current, and thermal noise are given by, respectively,

$$K_B = i_B \tau/e, \quad K_D = i_D \tau/e, \quad K_{DS} = i_{DS} \tau/e G^2,$$

and

$$K_T = 2 kT_{eq} \tau / e^2 G^2 R_L.$$

Rewritten in terms of photoelectron counts, the means and variances become

$$m_s = e G K_S$$

$$m_n = 0$$

(The noise mean will be addressed separately where required.)

$$\sigma_s^2 = e^2 G^2 \left[F_N (K_S + K_B + K_D) + K_{DS} + K_T \right] = e^2 G^2 (F_N K_S + K_N)$$

$$\sigma_n^2 = e^2 G^2 \left[F_N (K_B + K_D) + K_{DS} + K_T \right] = e^2 G^2 K_N$$

The photodetector excess noise factor, F_N , is a measure of the randomness of the detector internal gain. It is defined by the ratio of the mean squared gain to the mean gain squared, i.e.

$$F_N = \frac{\overline{G^2}}{G^2} = 1 + \frac{\text{Var}(G)}{G^2}$$

where $\text{Var}(G)$ is the gain variance. For a reach-through silicon avalanche photodiode, the excess noise factor can be approximated as

$$F_N = k_{\text{eff}} G + (2 - 1/G)(1 - k_{\text{eff}})$$

where k_{eff} is the electron ionization rate ratio. For an experimentally measured $k_{\text{eff}} = 0.02$, and with reasonably high gain ($G \sim 100$), the excess noise becomes

$$F_N = 2 + 0.02 G$$

The photoelectron counts due to background radiation are given by

$$K_B = L_R \frac{\pi}{4} \theta_R^2 A_R N_R \beta N_F \eta \frac{\tau}{h\nu}$$

where L_R is the background radiance, θ_R is the receiver planar field-of-view, A_R is the receiving area, N_R is the efficiency of all the receiver optics, β is the bandwidth of the optical bandpass filter, N_F is the optical filter efficiency, η is the detector quantum efficiency, τ is the slot integration time, and $h\nu$ is the photon energy. If a localized object is entirely within the receiver field-of-view, $L_R [\frac{\pi}{4}\theta_R^2]$ must be replaced by L_I , the irradiance of the object. Care must be taken to properly scale objects which are only partially within the receiver field-of-view.

7.5.2 Minimization of Thermal Noise. As shown in the previous section, the thermal noise photoelectron count (K_T) is given by

$K_T = 2 k T_{\text{eq}} \tau / e^2 G^2 R_L$, where k is Boltzmann's constant, T_{eq} is the equivalent temperature of the preamp, τ is the integration time, e is the electronic charge, G is the mean gain of the optical detector, and R_L is the input resistance of the preamp. As can be easily seen, it is desirable to make R_L as large as possible to reduce the thermal noise photocount. However, the circuit must respond faster than the sample rate ($1/\tau$). Let C represent the total capacitance of the detector-preamp combination. The $R_L C$ product then imposes a bandwidth limitation on the receiver. If the circuit

is modeled as a single pole RC filter, the 3 dB frequency is $f_2 = 1/2\pi R_L C$. Setting the 3dB frequency equal to the sample rate ($1/\tau$), we obtain $f_2 = 1/\tau$, or $\tau/R_L = 2\pi C$. Thus the thermal noise count becomes $K_T = 4\pi kT_{eq} C/e^2 G^2$. Note that the thermal noise is now independent of τ . Thus the receiver has two fundamentally different noise sources, the background radiation and dark current noises which are τ - dependent, and the thermal noise which is τ - independent. It should also be noted that the minimum thermal noise is fixed by the capacitance of the detector - preamp combination.

7.5.3 Optimum APD Gain. Recall from Section 7.4.1 the SNR was defined as

$$SNR = K_S^2 / [F_N (K_S + K_B + K_D) + K_{DS} + K_T]$$

and from Section 7.4.2 the minimized thermal noise term

$$K_T = 4\pi k T_{eq} C / e^2 G^2 = \delta/G^2,$$

where δ is now defined to absorb irrelevant terms. The excess noise factor was shown in Section 7.4.1 to be closely approximated by $F_N = 2 + 0.02G$. Thus it can be seen that as detector gain is increased, thermal noise is reduced, but excess noise is increased. Clearly an optimum value of gain exists to maximize the SNR.

By differentiating the SNR expression with respect to gain, equating to zero, and solving, it is straightforward to show that the gain for maximum SNR is given by

$G = \sqrt[3]{100 \delta / (K_S + K_B + K_D)}$. However, the gain which maximizes the SNR may not, in general, minimize a digital probability of bit error. This is because the expressions for error probability of an optical communication system are not necessarily dependent on SNR as an explicit parameter.

7.6 LINK EQUATION

The relation for propagation of electromagnetic energy to a distant collecting area is applicable to RF and optical frequencies. Antenna gain values will be quite different for RF and optical system because optical apertures are much larger in wavelength units than RF antennas. Also, signal energy loss mechanisms will be quite different for RF and optical systems because the devices employed to implement the systems are completely different. Therefore, although the range equation for RF and optical frequencies is conceptually identical, in practice the values of parameters in the equation are very different.

The detection analysis results in determination of the optical power required at the detector input (P_R). The link equation translates the required P_R into laser source transmitted power (P_T) From this viewpoint, the link equation can be written

$$P_T = P_R \left(\frac{\lambda}{\pi D_T} \right)^2 \left(\frac{\lambda}{\pi D_R} \right)^2 \left(\frac{4\pi R}{\lambda} \right)^2 \frac{1}{N_T N_R L_p N_F T_A T_S}$$

where D_T and D_R are the transmitting and receiving telescope diameters, λ is the wavelength, R is the range, N_T and N_R are the overall transmitting and receiving efficiencies, L_p is mispoint loss, N_F is the optical filter efficiency, T_A is the atmospheric transmission (if applicable), and T_S includes any power splitting.

The reciprocal of the bracketed squared quantities containing D_T and D_R can be considered as the transmitting and receiving antenna gains. Because D_T and D_R are very large in terms of optical wavelengths, the antenna gains will be much larger than for an RF system. However, the large antenna gain (narrow beam divergence) is the cause of additional pointing, tracking, and acquisition complexities for optical systems. Using $\theta_T = 2.44 \lambda/D_t$ allows the link equation to be expressed in terms of transmitting divergence, where θ_T is the full width of the main Airy lobe. (The comparable $1/e^2$ width is about 2/3 of the Airy lobe width.)

The signal photoelectrons required from the detector output are given by

$$K_S = (\eta/h\nu) P_R \tau$$

where η is the detector quantum efficiency, $h\nu$ is the photon energy, and τ is the effective integration time.

Table 7.6-1 summarizes the values of some of the link parameters which are assumed in this report, unless otherwise specified.

TABLE 7.6-1. ASSUMED LINK PARAMETERS

<u>Parameters</u>	<u>Value</u>
Range	$R = 44,500 \text{ km}$
Receiver Diameter	$D_R = 0.15 \text{ m}$
Transmitting Optics Efficiency	$N_T = 0.5$
Receiving Optics Efficiency	$N_R = 0.54$
Mispoint Factor	$L_p = 0.4$
Filter Transmission	$N_F = 0.7$
Filter Bandwidth	$\delta = 50 \text{ \AA}$
Amplifier Noise Figure	$F = 2$ ($T_{eq} = 290$)
Optical Wavelength	$\lambda = 0.85 \mu\text{m}$

7.7 PIN QUADRANT DETECTOR TRACKING

Many companies manufacture silicon PIN quadrant detectors, including Hamamatsu, Silicon Detector Corporation, Applied Solar Energy Corporation, United Detector Technology, and Hughes Industrial Products Division. A summary of commercially available quadrant detectors and their performance is given in Table 8.2-2. The Hughes data sheet is shown in Figure 7.7-1, since its performance meets that of the other manufacturers, and has the most complete data sheet. The key performance parameters for the Hughes HPIN 200Q are:

Dead Zone:	4.4 mils
Element Size:	100 mils
Quantum Efficiency:	83 percent
Capacitance (per element):	4.5 pf
Dark Current (per element):	30 nA

Since the HPIN 200Q is representative of commercially available quadrant detectors, its parameters will be used to calculate a tracking link budget.

As required by the complementary filter tracking servo analysis (Section 6.0), we will assume a sensor sample rate of 4 kHz. This is an effective integration time of $\tau = 250 \mu\text{sec}$. With 4.5 pf capacitance per element of the quad, and assuming the quad element amplifier contributes another 5 pf, the total capacitance of the detector-preamp combination is about 10 pf. Using an amplifier noise figure of 3dB (Table 7.6-1), the amplifier equivalent temperature is $T_{eq} = 290$, and the thermal noise counts are $K_T = 2.0 \times 10^7$ (See Section 7.4). For dark current $I_D = 30 \text{ nA}$, the dark counts are $K_D = 4.7 \times 10^7$.

To determine the photocounts due to background radiation, we must determine the field of view of the entire quad array. Using dead zone loss $\eta = 50$ percent, with quadrant gap $d = 4.4$ mils, and for a 15 cm aperture $\lambda/D = 5.6 \mu\text{rad}$, a focal length of 40 m is required. (A program to reduce the quadrant gap in quad cells is essential.) The quad array field of view is then $\theta_R = D/f$, where D is the diameter of the quad array and f is the focal length. Using $D = 200$ mils and $f = 40$ m gives $\theta_R = 127 \mu\text{rad}$.

PRELIMINARY DATA SHEET

HPIN SERIES PIN PHOTODETECTOR ARRAYS

HUGHES
HUGHES AIRCRAFT COMPANY
INDUSTRIAL PRODUCTS DIVISION
CARMEL, CALIFORNIA

Hughes offers users of high performance photodiode arrays which compete with dual quadrant and linear photodiode arrays are made by the same advanced planar techniques of the single element line, including an implantation process and the use of site on one and nine layers for maximum spectral response and low noise.

Hughes high performance detector arrays are used in many position sensing and motion sensing applications, as well as in optical metrology and simpler pattern recognition. While the widely accepted devices described below are representative of the Hughes capability, a complete line of custom arrays is also available. We will be pleased to provide customer assistance and alternate configurations to fit your particular application.

HPIN MONOLITHIC ARRAYS

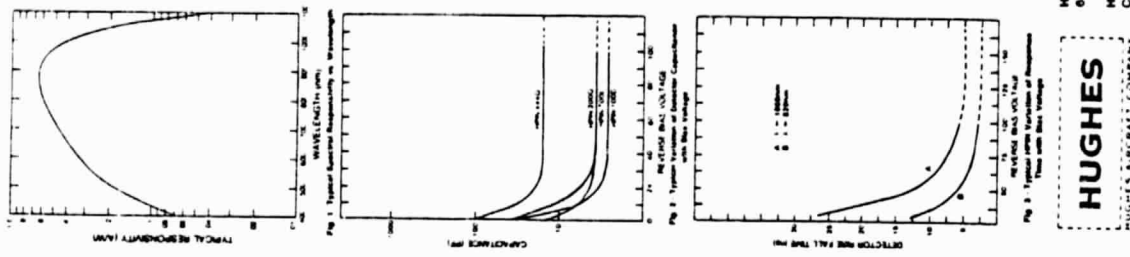
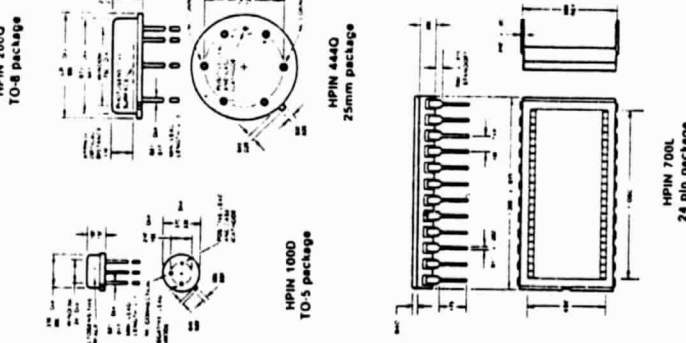
DIMENSIONS

ARRAY	HPIN 2000		HPIN 4440		HPIN 600	
	Case	Quadrant	Case	Quadrant	Case	Quadrant
Type	TO-5	4	TO-5	4	TO-5	16
Number of Elements	2	4	100x130	493x493	75x247	16x44
Circ. Size (mm)	2.87x2.87	2.87x2.87	100x130	22.24x	16x44	4.4x4.4
Element Spacing (mm)	100x130	100x130	100x130	100x130	100x130	100x130
Active Area (mm ²)	0.01	0.0176	0.0176	0.0176	0.0075	0.0075
Current (mA)	3.2	5.1	25.0	25.0	4.4	4.4
Voltage (Volts)	5	4.4	6	6	2.4	2.4

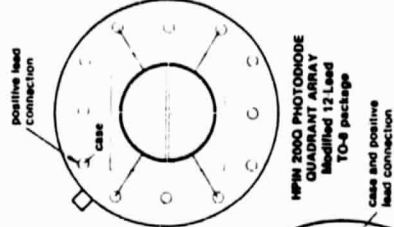
ELECTRICAL SPECIFICATIONS

PARAMETER	HPIN 1900		HPIN 2000		HPIN 4440		HPIN 600	
	100V	500V	100V	500V	100V	500V	100V	500V
Responsivity (A/W)	0.6	0.6	0.6	0.6	0.6	0.6	0.6	0.6
Dark Current (A)	<1	<1	<1	<1	<1	<1	<1	<1
Quantum Efficiency (%)	83	83	83	83	81	81	81	81
Capacitance (fF/pin Element)	4.0	4.5	15.0	15.0	5	5	5	5
Dark Current (mA) at 100V	1.5	30	100	100	10	10	10	10
Dark Current (mA) at 500V	6	6	6	6	6	6	6	6
100V - 1000V Breakdown Voltage (V)	1.2	1.5	3.0	3.0	1.5	1.5	1.5	1.5
Package (1.2mm)	>100	>100	>100	>100	2.4mm	2.4mm	2.4mm	2.4mm

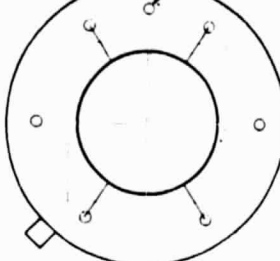
All values are typical and represent at a wavelength of 900nm and at 50°C unless otherwise specified.



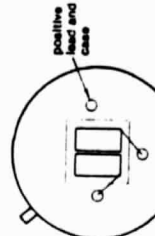
**DETECTOR OUTLINES
(TOP VIEWS)**



**HPIN 2000 PHOTODIODE
QUADRANT ARRAY
Beaded 12 Lead
TO-5 package**



**HPIN 4440 PHOTODIODE
QUADRANT ARRAY
25mm package**



**HPIN 1000 PHOTODIODE
DUAL ELEMENT ARRAY
TO-5 package**

HUGHES
HUGHES AIRCRAFT COMPANY

HUGHES AIRCRAFT COMPANY • Industrial Products Division • Solid State Product Sales
6115 El Camino Real, Camarillo, CA 93008 • Tel (714) 436-9191 Ext 335 • TWX 910-322-1393
HUGHES AIRCRAFT INTERNATIONAL SERVICE COMPANY (HASIC)
Clive House, 1218 Queen's Road, Weybridge, Surrey KT13 0ED, England
Tel (0932) 531860 • TWX 929277
Printed in U.S.A.

24-6-1-3

Figure 7.7-1. Data Sheet for Hughes Industrial Products
Division Quadrant Detectors.

Referring to Table 7.7-1, which lists the astronomical sources of background radiation, the worst case irradiance within 127 μ rad (neglecting the sun) would be due to the moon with $L_I = (\pi/4) L_R \theta_R^2 = 5.7 \times 10^{-11} \text{ WM}^{-2} \text{ A}^{-1}$. For parameters as assumed in Table 7-1, with quantum efficiency $\eta = 0.83$ and integration time $= 250 \mu\text{sec}$, the background counts per quad element are

$$K_B = 4300 T_S$$

where T_S is the fraction of total intensity routed to the tracking detector. (Note that in obtaining K_B for an element the total background power on the array was divided by four.)

The total photoelectron counts due to shot noise are given by

$$K_N = K_B + K_D + K_T = 6.7 \times 10^7$$

Note that the counts due to background radiation are negligible, so the noise counts are not dependent on the tracking split T_S .

A block diagram of a tracking detection circuit is shown in Figure 7-7.2. This circuit can track cw or modulated sources. The output of each detector quadrant is amplified, integrated, thresholded, and then fed into the usual quadrant detector sum and difference circuit. The sum and difference circuit implements the algorithms (Section 7.2) which generate the azimuth and elevation error signals. The detection probability densities are shown in Figure 7.7-3, which illustrates that by incorporating a threshold the noise mean is effectively removed. The signal mean just has to be enough larger than the noise mean to overcome the noise variance, so the detection quality depends only on the signal mean and noise variance (both signal present and signal absent). The threshold has eliminated dependence on the noise DC level (assuming the noise mean is fixed).

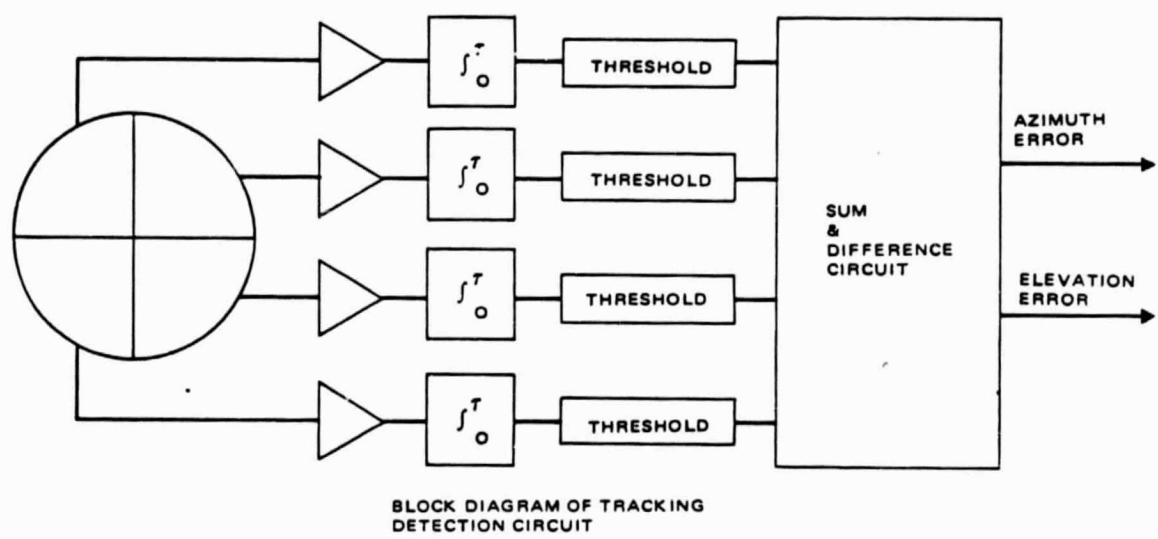
An alternate tracking detection scheme to that in Figure 7-6 for tracking a data waveform is shown in Figure 7.7-4. Each quadrant detector output is AC coupled and lowpass filtered, with the filter being sampled at the rate f_s .

These sample values are then summed and differenced (Section 7.2) to yield the angular error signals. The lowpass filter bandwidth must be greater than the sample frequency. The required sample rate is dependent on the selected tracking servo approach, as for example a 4 kHz rate for a complementary filter servo, and a 10 Hz rate for a gyro-stabilized servo.

Since the detector output is AC coupled, this approach cannot track a cw source, but only a signal with a spectrum shifted away from DC. This is characteristic of a PPM data waveform, for example. The lowest frequency component for PPM is about $1/2 M\tau$, where M is the number of time slots and τ is the time slot width. This is because the longest time period which the voltage baseline held is for a pulse in the first slot of a PPM word and a pulse in the last slot of the following word, a total time of approximately $2M\tau$. The lowpass filter in Figure 7-8 effectively tracks the average power of the data waveform. For cases where the data spectrum is comparable to the sample frequency, a special scheme is required to avoid spectral interference (Section 7.10).

TABLE 7.7-1. ASTRONOMICAL BACKGROUND SOURCES ($\lambda = 0.83 \mu\text{m}$)

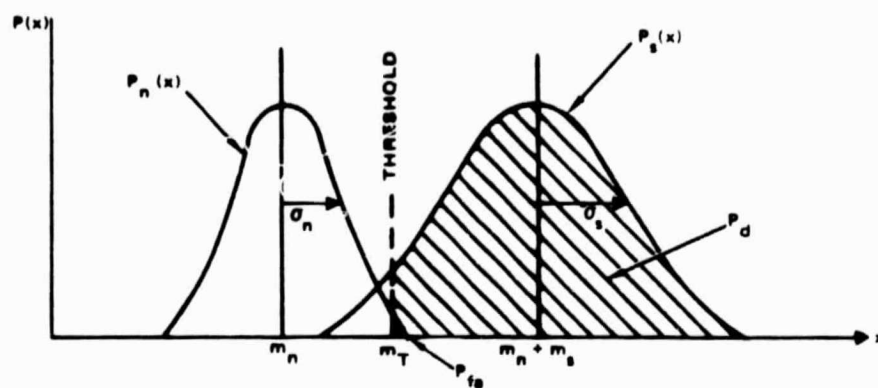
<u>Source</u>	<u>Maximum Size (μrad)</u>	<u>Maximum Radiance ($\text{Wm}^{-2}\text{Sr}^{-1}\text{\AA}^{-1}$)</u>	<u>Maximum Irradiance ($\text{Wm}^{-2}\text{\AA}^{-1}$)</u>
Sun	9300	1800	1.05×10^{-1}
Moon	8960	4.5×10^{-3}	2.7×10^{-7}
Venus	85	1.8×10^{-2}	1.0×10^{-10}
Jupiter	226	4.5×10^{-4}	1.8×10^{-11}
Sirius	2.8×10^{-2}	7600	4.8×10^{-12}
ϵ . Orionis	$\sim 1.1 \times 10^{-3}$	$\sim 1.2 \times 10^5$	1.1×10^{-13}
Mira	~ 0.12	~ 180	2.1×10^{-12}



BLOCK DIAGRAM OF TRACKING
DETECTION CIRCUIT

Figure 7.7-2. Block Diagram of Tracking Detection Circuit.

ORIGINAL PAGE IS
OF POOR QUALITY



$$P_n(x) = \frac{1}{\sqrt{2\pi}\sigma_n} \exp \left[-\frac{(x-m_n)^2}{2\sigma_n^2} \right] \quad (\text{PULSE ABSENT})$$

$$P_s(x) = \frac{1}{\sqrt{2\pi}\sigma_s} \exp \left[-\frac{(x-(m_n+m_s))^2}{2\sigma_s^2} \right] \quad (\text{PULSE PRESENT})$$

$$\sigma_s > \sigma_n$$

Slot probability densities (threshold detection, gaussian statistics)

Figure 7.7-3. Probability Densities for Gaussian Threshold Detection.

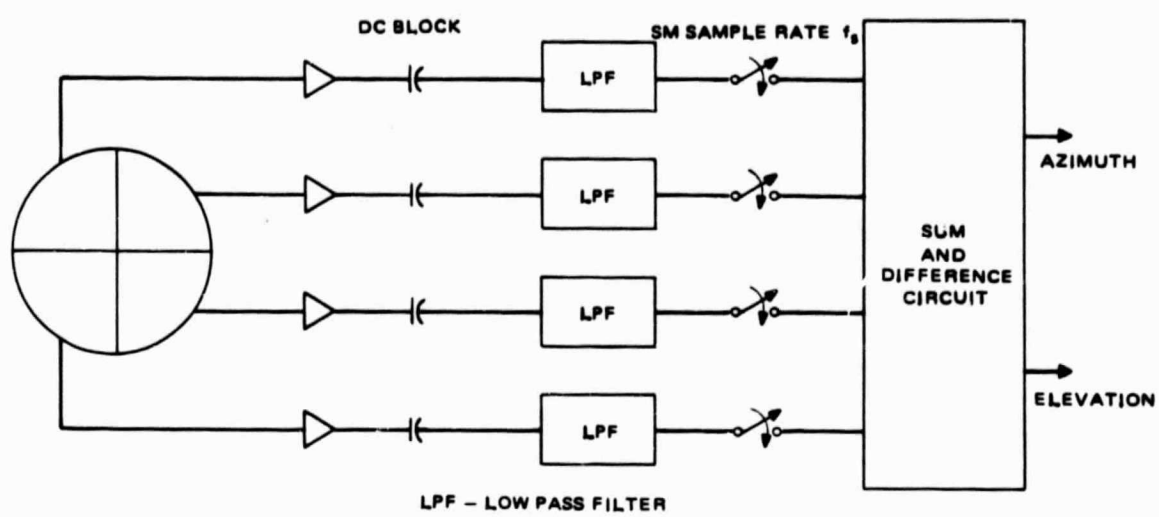


Figure 7.7-4. AC-coupled, low pass filter tracking circuit.

$$\frac{K_S}{\sqrt{K_N}} = 5$$

which gives $K_S = 4.1 \times 10^4$. Note this is three orders of magnitude less than the noise photocounts, justifying the neglecting of signal noise for a PIN detector.

For integration time of $\tau = 250 \mu\text{sec}$ (4 kHz sample rate), quantum efficiency $\eta = 0.83$, and photon energy $h\nu = 2.34 \times 10^{-19}$ joules, the required power per element is $P_R = K_S (h\nu/\eta\tau) = 46.2 \text{ pW}$. The total power required by the quad array is then $P_R = 185 \text{ pW}$.

Using the link parameters of Table 7.6-1, $T_S = 0.1$ (10 percent tracking split), 50 percent dead zone loss, and Airy lobe beamwidth $\theta_T = 14 \mu\text{rad}$, the required average transmitter power is $P_T = 228 \text{ mW}$. Since the noise was not dependent on the tracking power split (background was negligible), by using a 50 percent tracking split the average transmitter power can be reduced to 46 mW. Since commercially available laser diodes have only 20 mW cw power, even with a 50 percent tracking split and a 14 μrad beam the link is not reliably closed with a PIN quadrant detector. To provide a more implementable and reliable link, a quadrant avalanche photodiode detector is evaluated in the following section.

Note that for the PIN quadrant detector tracking analysis, a sample rate of 4 kHz was assumed, which is representative of the complementary filter servo tracking approach. A stabilized servo system approach will require a much slower sampling rate. For example a gyro-stabilized tracking servo with a 1.0 Hz bandwidth, requires only $f_s = 10 \text{ Hz}$ sample rate. It was shown in Section 7.2 that $\text{SNR} \sim P_T/\sqrt{f_s}$ where P_T is the transmitted laser power ($P_T \sim n_S$, the signal count rate). Thus to achieve a given SNR, a sample rate of $f_s = 4 \text{ kHz}$ requires a factor of 20 more laser power than $f_s = 10 \text{ Hz}$. Although the PIN quadrant detector is not sensitive enough for a 4 kHz sample rate, the PIN quadrant detector is more than adequate for the gyro-stabilized servo sample rate. Thus to use a PIN quadrant detector for tracking requires adopting the gyro-stabilized servo approach, or obtaining 6 - 9 dB more laser power.

Note that the optical background counts, even for a 50 percent tracking split, are only $K_B = 2150$ compared to $K_S = 4.1 \times 10^4$. As mentioned before, the background shot noise was negligible when compared with other noise sources. The background DC nonuniformity is also negligible, since the worst possible case is 5 percent of the signal. Thus either tracking circuit in Figure 7.7-2 or 7.7-4 could be used with a PIN quadrant detector.

7.8 AVALANCHE PHOTODIODE QUADRANT DETECTOR TRACKING

7.8.1 Quad APD Detector

The only known commercial vendor of quadrant avalanche photodiode detectors at the present time is RCA Electro-Optics in Quebec, Canada. They have been involved in single element and quad array avalanche photodiodes (APD) for a number of years. Their single element APD is widely recognized as one of the best available. Hughes Industrial Products has recently fabricated some 4×10 APD arrays, but these are not yet commercially available.

Two versions of the quadrant APD have been fabricated by RCA. The old version has a common junction, and isolation between elements is obtained by segmenting. The advantage of this approach is that there is virtually no dead space between the elements (Section 7.3). However this device is very difficult to fabricate, and also difficult to radiation harden. The fabrication difficulties cause RCA to have little or no interest in continued production of this device.

The newer version of the quad APD has 4 separate junctions to form the quad element. This results in a dead space between quadrants of $75 \mu\text{m}$, but there is an ongoing program to reduce this to $25-30 \mu\text{m}$. The entire quad array is the same size as their single element APD (1.5 mm), and if the four elements are tied together they achieve the same performance as their single element APD. A single bias must be used for all four elements. As the detector gain is increased by increasing the bias voltage, the gain nonuniformity between elements increases. For a gain of 100, the gain nonuniformity is $\pm 10 - 15$ percent. For a gain of 50, the nonuniformity will

be only ± 5 percent. In addition, DC levels on the amplifier input to each element can be used to compensate for nonuniformity. Thus nonuniformity does not seem to be a significant problem for gains of 50 or less. The new version of the quad APD will be assumed for performance analysis in this report.

Since the four elements together give the performance of the single element APD, the assumed parameters (per quad element) are:

Quantum efficiency:	$\eta = 0.77$
Capacitance (per element):	$C = 0.5 \text{ pf}$
Gain-dependent dark current (per element):	$I_D = 2.5 \times 10^{-13} \text{ A}$
Gain-independent dark current (per element):	$I_{DS} = 2.5 \times 10^{-9} \text{ A}$

7.8.2 Quad APD Tracking Performance

Assuming capacitance of 1.5 pf per amplifier, and 0.5 pf per quad element, the total capacitance per element is 2.0 pf. The thermal noise then becomes (Section 7.5) $K_T = 3.9 \times 10^6/G^2$. For integration time $\tau = 250 \mu\text{sec}$ (sample rate 4 kHz), the gain-dependent dark photocount is $K_D = 391$ per element. The gain-independent dark photocount is $K_{DS} = 3.9 \times 10^6/G^2$ per element.

Assuming a dead space of 75 μm , $\lambda/D_R = 5.6 \mu\text{rad}$ for $D_R = 15 \text{ cm}$, and 50 percent dead zone loss, a focal length of 26.8 m is required. If the dead zone is reduced to 30 μm , the focal length becomes a more reasonable 10.7 m. The detector array field of view is given by $\theta_R = D/f$, where D is the quad diameter and f is the focal length. Using $D = 1.5 \text{ mm}$, $d = 30 \mu\text{m}$, and $f = 10.7 \text{ m}$, $\theta_R = 140 \mu\text{rad}$. Referring to Table 7-2 for background sources, the worst case irradiance (neglecting the sun) for 140 μrad is for Venus with $L_I = 1.0 \times 10^{-10} \text{ WM}^{-2} \text{ \AA}^{-1}$. The resulting background photocounts are then $K_B = 7600 T_S$, where T_S is the fraction of received intensity sent to the tracking detector.

For $K_D = 391$, 10 percent tracking split so that $K_B = 760$, $\delta = G^2 K_T = 3.9 \times 10^6$, guessing $K_S \sim 400$, the optimum APD gain is $G = 63$ (Section 7.5). Since the optimum gain function is fairly broad, and to reduce gain nonuniformity, we will assume $G = 50$. If the tracking split is increased, so that background noise increases, this will be even closer to the true optimum.

For $G = 50$, the excess noise is $F_N = 3$, and the noise photocounts become $K_T = 1576$, $K_D = 391$, $K_{DS} = 1564$, and $K_B = 760$ (10 percent tracking split).

The total noise count is

$$K_N = F_N (K_B + K_D) + K_{DS} + K_T = 6593$$

For mean signal to rms noise equal to 5 (Section 6.0) we require

$$\text{SNR}_{\text{rms}} = \frac{K_S}{\sqrt{F_N K_S + K_N}} = 5$$

and thus require $K_S = 445$ signal photocounts per element. For $n = 0.77$ and $\tau = 250 \mu\text{sec}$, we require 0.55 pW per element, or total power for the quad array $P_R = 2.2 \text{ pW}$. Note that in the previous section, the PIN quad required total power $P_R = 185 \text{ pW}$, so the quad APD is 19.2 dB more sensitive. Assuming Airy lobe beamwidth $\theta_T = 35 \mu\text{rad}$ (we used $\theta_T = 14 \mu\text{rad}$ for the PIN quad), dead zone loss of 50 percent, 10 percent tracking split, and link parameters of Table 7-1, a transmitted power of 17.1 mW is required, which is less than the 20 mW cw currently available. Note that the 19.2 dB improvement in sensitivity (compared to the PIN quad) has been used to both increase the transmitted beamwidth and reduce the required transmitter power.

For additional tracking link margin with a 20 mW source, we might want to increase the fraction of intensity sent to the tracking detector.

For 25 percent tracking split, $K_B = 1900$, K_N becomes 1.0×10^4 , and for rms SNR = 5, $K_S = 540$ are required. This requires a total power on the array of $P_R = 2.6 \text{ pW}$. For $\theta_T = 35 \mu\text{rad}$, dead zone loss of 50 percent, and 25 percent tracking split a transmitted power of $P_T = 8.2 \text{ mW}$ is required. This would give a 3.9 dB margin with a 20 mW cw source.

If a 50 percent tracking split is used, $K_B = 3800$, K_N becomes 1.57×10^4 , and rms SNR = 5 requires $K_S = 665$. A received power $P_R = 3.3 \text{ pW}$ is then required on the array. For $\theta_T = 35 \mu\text{rad}$ (Airy lobe), 50 percent tracking split, and 50 percent dead zone loss, a transmitted power of $P_T = 5.1 \text{ mW}$ is required. This provides 5.9 dB power margin for the tracking link.

Note that, unlike the PIN quadrant detector case, the optical background counts are larger than the signal counts for the APD quadrant detector with SNR = 5. Although the K_S are adequate to overcome the shot noise due to the background DC current, the mean signal is not sufficient to overcome the DC background current itself. To overcome the DC nonuniformity due to optical background, it is recommended that the AC - coupled tracking approach (Figure 7.7-4) be used with a quadrant APD. Otherwise, much of sensitivity advantage over a PIN would be lost.

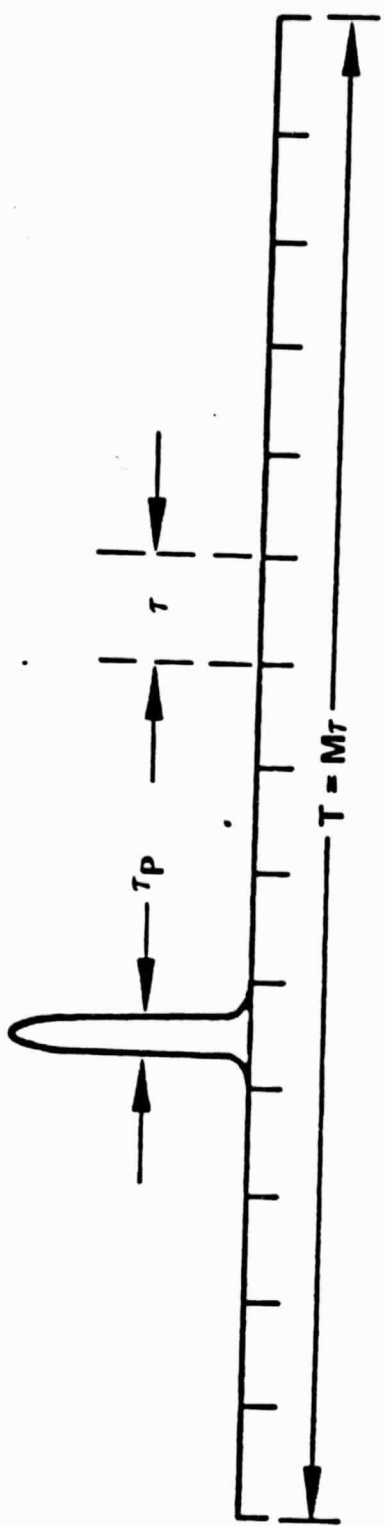
In summary, the vast sensitivity improvement of the quad APD over the PIN quad makes the tracking link viable with a single 20 mW source. Since the beacon link at 10 Kbps will be seen to be compatible with a 20 mW source and 50 percent tracking split (Section 7.9), up to 5.9 dB of margin can be allocated to the tracking link. However, just as in the PIN quad case, a program is needed to reduce the dead zone to 30 μm or less, to keep the required focal lengths reasonable.

7.9 BEACON LINK - TRACKING SPLIT

Although a low data rate beacon link from GEO to LEO is assumed in the SOW for this report, no specific data rate is mentioned. As an example of the typical telemetry beacon link a data rate of 10 Kbps has been assumed, and discussion with NASA representatives has confirmed this is reasonable.

The beacon link communication format will be taken as pulse position modulation (PPM), since it has become recognized as the most efficient modulation scheme for energy detecting optical communications. The PPM format is illustrated in Figure 7.9-1.

MODULATION SCHEME: PULSE POSITION MODULATION (PPM)



NUMBER OF TIME SLOTS PER WORD = $M = 2^K$

NUMBER OF BITS PER WORD = $\log_2 M = K$
TOTAL TIME PER WORD = $M\tau = T$

$$\text{DATA RATE} = \frac{\text{BITS PER WORD}}{\text{TIME PER WORD}} = \frac{\log_2 M}{M\tau} = \frac{\Delta}{R_D}$$

$$\text{DUTY CYCLE} = \frac{\tau_P}{M\tau} \approx \frac{1}{M}$$

Figure 7.9-1. Pulse Position Modulation Format.

Since the peak to average power ratio of commercially available 20 mW laser diodes has been experimentally measured at Hughes to be in the range of 8-16, we will choose the number of time slots to be $M = 8$. Hughes experiments have shown that commercial 20 mW diodes (RCA, Telefunken, Amperex) can maintain their 20 mw average power at least up to $M = 8$, for a peak power of 160 mW. This may be true only for pulses shorter than 1.0 μsec , however.

Since $\log_2 M$ bits are transmitted per pulse, and a pulse occurs every $M\tau$ seconds, where τ is the time slot width, the PPM data rate is

$$R_D = \log_2 M / M\tau$$

For $R_D = 10$ Kbps, and $M = 8$, we have $\tau = 37.5 \mu\text{sec}$.

We will assume a single element APD such as the RCA C30902E, with a total detector-preamp capacitance of 2.0 pf. The thermal noise is then $K_T = 3.9 \times 10^6 / G^2$, where G is the mean detector gain. For gain-dependent dark current $I_D = 10^{-12} \text{ A}$, $K_D = I_D \tau / e = 234$. For gain-independent dark current $I_{DS} = 10 \text{ nA}$, $K_{DS} = 2.3 \times 10^6 / G^2$.

For a detector field of view $\theta_R = 40 \mu\text{rad}$, the worst case background (except the sun) is Venus (Table 7-2), with radiance $L_R = 1.8 \times 10^{-2} \text{ WM}^{-2} \text{ Sr}^{-1} \text{ \AA}^{-1}$. Using the link parameters of Table 7-1, $n = 0.77$, $\tau = 37.5 \mu\text{sec}$, and assuming a 50 percent tracking split, the background photocounts are $K_B = 475$. (A 50 percent tracking split is assumed to give the worst case required transmitter power.)

For $K_B = 475$, $K_D = 234$, $\delta = G^2 K_T = 3.9 \times 10^6$, and using $K_S = 450$ yields an optimum gain around $G = 70$. Since the gain optimum is broad, and tabulated results exist for $G = 100$ ($F_N = 4$) we will analyze the system for $G = 100$. (It should be recognized that $G = 70$ should be used for actual system implementation.)

For $G = 100$, the noise photocounts are $K_T = 393$, $K_B = 475$, $K_D = 234$, and $K_{DS} = 234$, so that the total noise counts are $K_N = F_N(K_B + K_D) + K_{DS} + K_T = 3500$. For error probability $PE = 10^{-6}$, $K_S = 470$ are required, and $P_R = 3.8 \text{ pW}$ is required at the detector. Still assuming a 50 percent (worst case) tracking split, and $\theta_T = 35 \mu\text{rad}$ (Airy lobe), the required peak transmitter power is $P_T = 3.0 \text{ mW}$. If the transmitter peak

power is run at the cw level of 20 mW, the beacon link has 8.2 dB power margin. If the 20 mW average power source has 160 mW peak power at $M = 8$, as experimentally measured by Hughes, the peak power margin becomes 17.3 dB. For the 37.5 μ sec pulses, the laser may be constrained to 20 mW peak with 8.2 dB margin.

In summary, from a power standpoint the beacon link presents no design problems, even with 50 percent of the transmitted power allocated to the tracking system.

7.10 TRACKING ON BEACON PPM

As shown in the previous section, from a power standpoint there is no problem sharing the GEO beacon for both tracking and telemetry data at the LEO. However, there could be a separate problem due to interference of the beacon data modulation with the tracking signal, since for a tracking sample rate of 4 kHz and beacon data rate of 10 Kbps there is significant spectral overlap. In other words, if the tracking system samples at 4 kHz, sometimes it samples while a pulse is present, and sometimes when the pulse is absent. A 4 kHz low pass filter on the 10 kbps modulation will not remove all the signal fluctuation from the tracking system. Ironically, if the data rate were 100 Mbps or more, the tracking system could utilize the average power of the data signal, and would not respond to the high frequency modulation. One approach to avoiding this problem is to use a single quad APD for both tracking and beacon data modulation, rather than power splitting between a quad detector for tracking and another detector for beacon data. This can be accomplished by summing the output from the four quad elements to form the beacon data output, while the quad outputs are simultaneously summed and differenced in the usual way to provide the tracking error signals. A circuit for tracking with PPM would first examine the sum photocount of all four quadrants in each time slot, while storing the individual photocount from each quadrant in each time slot (4M storage registers). At the end of the PPM word the time slot with the maximum sum photocount is chosen as the slot containing the optical pulse, which demodulates the beacon data. Then the quadrant outputs from the time slot which has been determined to contain the pulse are summed and differenced to provide the tracking error signals. Note that the

circuit must first determine which time slot contained the pulse before the tracking signal can be generated, and the tracking error signals are updated at the PPM word rate. If the tracking sample rate is slower than the PPM word rate, the tracking error signals could be loaded into a buffer register at the PPM word rate, and the buffer could then be read out at a slower rate. The PPM word rate should be a multiple of the tracking sample rate, so that readout does not occur while the buffer register is being loaded.

As an example, a system design for a 4 kHz tracking sample rate will be generated. The PPM word rate will be chosen to match the 4 kHz sample rate, so that $1/M\tau = 4$ kHz.

If we then choose $M = 8$, the time slot width is $\tau = 31.25 \mu\text{sec}$. Since the pulses occur at the word rate of 4 kHz, and for $M = 8$ three bits are transmitted per pulse, the beacon data rate is 12 Kbps.

We will assume a quad APD, such as analyzed in section 7.8. The noise photocounts from section 7.8 are $K_T = 1576$, $K_D = 391$, $K_{DS} = 1564$, and $K_B = 2.1 \times 10^4 T_S$, where T_S was the tracking power split. Assuming $T_S = 1.0$, since there is no power split in this approach, and scaling the noise counts for $\tau = 31.25 \mu\text{sec}$ instead of 250 μsec (except K_T - section 7.5.2), the noise counts per element become $K_T = 1576$, $K_D = 49$, $K_{DS} = 196$, and $K_B = 2625$. The total noise counts are $K_N = F_N(K_B + K_D) + K_{DS} + K_T = 9794$. To obtain an rms SNR = 5 as needed for tracking, $K_S = 534$ are required. Thus 5.2 pw are required per element, for a total received power of $P_R = 20.8$ pw. Assuming 50 percent dead zone loss, $\theta_T = 35 \mu\text{rad}$ (Airy lobe), and link parameters as in Table 7-1, the required peak transmitted power is $P_T = 4.0$ mw. Note this is even less required transmitter power than for the 50 percent tracking split case in section 7.8, which required 5.1 mW. However, we still must verify that this is also enough power to demodulate the beacon data.

To determine the communication performance with the summed quad elements as the communication detector, we use the fact that the sum of independent Gaussian random variables is Gaussian, with mean given by the sum of the means and variance given by the sum of the variances. Therefore

$$m_S = 4 eGK_S$$

$$\sigma_S^2 = 4 e^2 G^2 (F_N K_S + K_N)$$

Note that previously derived equations for error probability can be used by considering K_S in the equation to be $4K_S$, and K_N in the equation as $4K_N$. The noise counts per element per integration time are $K_N = 9794$, as computed for tracking. The error probability (PE) is then based on $K_N = 4 K_N = 3.92 \times 10^4$. For $PE = 10^{-6}$, $K_S = 1500$ are required. Since the required $K_S = 1/4 K_N = 375$ per element are less than the $K_S = 534$ required for tracking, $P_T = 4.0$ mw is sufficient peak transmitter power to perform both the tracking and communication functions.

Note that since this system tracks a data waveform, each quadrant detector output can be AC-coupled. This avoids the problems of DC non-uniformity due to optical background.

Thus using a single quad APD detector to perform both tracking and beacon data detection is an appealing alternative to power splitting with separate detectors. This technique assures that the beacon data does not spectrally interfere with the tracking signal.

7.11 TRACKING WITH AN ACQUISITION ARRAY

If an array is used for acquisition, which will be seen in section 8 to have significant advantages quad cell acquisition, this array could also perform the tracking function. The advantage of tracking with an array is to combine two separate acquisition and tracking subsystems into a single subsystem. A separate tracking detector, its optics and electronics are eliminated, as well as a bifurcated mirror and electronics to perform the handover function.

A video tracker examines the video output of the array, and generates the angular error signals to the tracking servo. The array and video tracker must provide angular error samples at a rate compatible with the tracking servo (4 KHz for complementary filter, 10 Hz for gyro-stabilized).

Array tracking is made possible by using a video tracker, which is an existing Hughes product line. The video tracker digitizes the video output of each pixel within a tracking gate, and tracks the desired image in either centroid or correlation mode. In correlation tracking, the digitized image from the previous frame is correlated with the image within the current frame, to deduce the apparent image motion. Centroid tracking establishes a video threshold, and tracks on the centroid of the image intensity that exceeds threshold. For tracking a distant optical communication terminal, centroid tracking would be used, with the threshold set to eliminate unwanted background, but allowing the laser to appear to a bright spot. The tracking system would then align the line of sight with the center of the laser spot.

Existing CCD array and video trackers operate at frame rates up to 60 Hz (interlaced), which is compatible with the requirements of the gyro-stabilized servo. If a CID array were used instead of a CCD array (Section 8.2.1), the x-y addressability of the CID array could be used to define a tracking gate. This tracking gate would consist of a much smaller subgroup of pixels which could then be read out at a much more rapid frame rate. The video tracker already incorporates a similar tracking gate in its processing, so that its tracking algorithm does not have to be applied to the entire video field. A 400×500 array reads out 2×10^5 pixels in 1/30 of a second. At this rate, 1500 pixels could be read out in 250 μ sec (4 KHz rate). Thus a 38×38 pixel track gate could be implemented, which is adequate since the distant receiver is unresolved within a pixel. The CID sacrifices about 3 - 5 dB in low light sensitivity compared to the CCD, but to eliminate star background the CCD performance will be background-limited anyway.

For a 400×500 array, staring into a 0.5° (8.7 mrad) uncertainty cone (see Section 8.0), the pixel field-of-view is $8.7 \times 10^{-3}/400 = 22 \mu\text{rad}$.

Setting the optical blur circle over 2×2 pixels gives the angular blur subtense of $44 \mu\text{rad}$. For reasonably high SNR, the tracking jitter is closely approximated by

$$\sigma \sim 0.685 \Delta / (\text{SNR}-3)$$

where the Δ is the angular subtense of the optical blur, and SNR is the ratio of mean signal to rms noise. For $\Delta = 44 \mu\text{rad}$, an $\text{SNR} = 33$ is required to achieve $\sigma = 1.0 \mu\text{rad}$ rms jitter. If a 1000×1000 array were used, with $\Delta = 18 \mu\text{rad}$, an $\text{SNR} = 15$ is required. (If a complementary filter tracking servo is used, the sensor jitter contribution must be less than $1.0 \mu\text{rad}$.)

Suppose a 400×500 CCD array is used with a gyro-stabilized servo at a 10 Hz frame rate. The DC background due to thermal noise and dark current is fixed, and the other levels ride on top of these, so setting a threshold eliminates them. The DC optical background may or may not be present in a pixel, so that if the optical background is eliminated with a threshold, the signal must be able to exceed this threshold and the shot noise variance even with the DC optical background absent. With these considerations, the SNR can be defined as

$$\text{SNR} = \frac{(\text{mean signal} - \text{DC optical background})}{\text{rms noise}}$$

(This assumes that the array can only output the accumulated charge per pixel, rather than a modulated signal.)

For integration times of $\tau = 100 \text{ msec}$ (10 Hz frame rate) the dark current nonuniformity dominates the noise variance. (The assumed parameters here are discussed in Section 8.5.3). For dark nonuniformity of 1.0 nA/cm^2 (15°C), $12 \mu\text{m} \times 18 \mu\text{m}$ pixel area, and $\tau = 100 \text{ msec}$ integration time, the rms dark non-uniformity count is $K_{DN} = 1350$.

For pixel FOV = $22 \mu\text{rad}$ and Venus background, the optical background DC level is $K_B = 2.5 \times 10^5$. $\text{SNR} = 33$ is required for $1.0 \mu\text{rad}$ gyro-stabilized jitter performance. Thus

$$\frac{K_S - 2.5 \times 10^5}{1350} = 33$$

or $K_S = 3.0 \times 10^5$. For 25 percent quantum efficiency, this is a required power of 27.0 pW. Using the link parameters of Table 7.6-1, with $\theta_T = 35 \mu\text{rad}$ (Airy lobe) and $T_S = 0.5$ (50 percent tracking split), an average power of 21.0 mW is required. (A 12 Kbps beacon link was shown to be compatible with a 50 percent tracking split with an APD detector). Therefore tracking using the acquisition array should be considered as a viable system option.

7.12 SUMMARY - TRACKING AND BEACON LINK

Section 7.0 has examined the problem of tracking a data beacon from the GEO satellite to less than one microradian rms accuracy in order to derive pointing commands for a high data rate LEO transmitter. The noise equivalent angle of a quadrant tracking detector was derived explicitly stating the assumed signal and noise parameters per element. The tracking detector quadrant gap has been identified as an area needing further technology development, but which does not preclude operational systems with currently available devices. The angular dynamic range over which closed loop tracking can be maintained was shown to be proportional to the rms SNR in an element of the quadrant detector.

Photodetection analysis and link equations were presented to allow calculation of tracking (and acquisition) link budgets. It was shown that a PIN quadrant detector was not sensitive enough to close the tracking link budget to 1.0 μrad rms accuracy unless a gyro-stabilized tracking servo is used or laser of 200 mW or greater are available. The quadrant APD detector is about 19 dB more sensitive than the PIN, which allows 1.0 μrad tracking accuracy with the complementary filter servo approach, 35 μrad GEO beamwidth, a commercial 20 mW laser diode, and 6 dB link margin.

For tracking a GEO 10 Kbps beacon data link three different configurations were shown to be viable. A 50-50 optical beamsplit between an APD quadrant tracking detector and single element APD data detector satisfied both functions (with adequate margin) with a commercial 20 mW laser. Or the quadrant APD tracking detector may also provide the data detection by summing the four outputs. This may be necessary if the tracking sample rate has significant spectral overlap with the beacon data, as would be the case with a 4.0 KHz complementary filter sample rate and 10 Kbps beacon data. Finally, it was shown that if an array were selected as the acquisition detector, it could also perform the tracking function. A CCD (or CID) array with standard video frame rates is compatible with the gyro-stabilized tracking servo. A CID array with a circuit to create a 40 x 40 pixel tracking gate could provide updates at the 4.0 KHz complementary filter servo sample rate.

8.0 ACQUISITION

8.1 INTRODUCTION

Acquisition for optical communication systems is the process by which two terminals initially locate each other and progress to mutual fine tracking and two way communication. Each terminal initially knows the location of the other within some angle of uncertainty, which must be reduced to the order of microradians in order to fine track with narrow communication beams over intersatellite distances. This may involve handover between sensors within the acquisition subsystem before eventual handover to the fine tracking system. In one extreme the acquisition sources and sensors may be wholly separate to the acquisition subsystem, or in the other extreme the communication sensors and sources could be utilized for acquisition.

We have performed acquisition analysis with several driving goals:

- a) minimum number of components in addition to those for communication
- b) reliable acquisition times less than 5 - 10 minutes
- c) single stage for reduction of initial uncertainty to fine tracking
- d) avoid mechanical placement or removal of optical elements in the optical train.

Goal (a) is motivated by keeping the system as simple as possible. Goal (b) results since the low earth orbiting (LEO) satellite in our study orbits the earth every two hours. The acquisition time should be small compared to the roughly one hours communication time available per orbit. Since the earth blocks the LEO as seen from geosynchronous (GEO) orbit, acquisition must be performed every LEO orbit, or about twelve times a day. Thus the acquisition sequence should be very reliable, since it must be performed frequently. Goal

(c) again reflects the desire for system simplicity, to minimize sensor handover sequences. Goal (d) is motivated by the difficulty of maintaining microradian optical alignment when mechanically adding or removing lenses or beamsplitters. Thus we have resisted using a lens to spoil the communication beam to serve as an acquisition beacon, but instead recommend that a separate beacon be used.

The acquisition subsystem has received the least attention in past analyses of optical communication systems. Since no communication can occur until acquisition takes place, the overall system availability is ultimately dependent on acquisition performance.

The determination of the acquisition uncertainty angle is a critical first step in designing an acquisition subsystem. Since the acquisition time will be shown to be proportional to θ_{UNC}^2 (θ_{UNC} is the acquisition uncertainty angle), and since background radiation photocounts are proportional to θ_{UNC}^2 , it is desirable to keep θ_{UNC} as small as possible. In general, however, this is not an independent design variable, but depends on the specific spacecraft and its control systems.

In general, the acquisition uncertainty is dependent on the spacecraft's own attitude uncertainty, the orbital ephemeris uncertainties of the position and velocity of the other terminal, relative timing errors, etc. However, using the specific scenario of Landsat for the LEO and TDRS for the GEO, we found that the attitude uncertainties were significant fractions of a degree, while the other errors were of the order of tenths of milliradians, so that attitude uncertainty clearly dominates. In fact, the TDRS yaw axis attitude uncertainty at the ground station is the single dominant influence to the acquisition uncertainty angle.

Based on conversations with Hup Damare (NASA GSFC), simulations reveal maximum attitude uncertainties of 0.08 degrees in the roll and pitch axes, and 0.2 degrees in the yaw axis. These are the maximum magnitudes of error before the next sensor update. The yaw axis sensor update rate is much slower than the other axes, resulting in its larger attitude uncertainty. Gimbal servo analysis reveals that the yaw axis uncertainty may be fully coupled into the line of sight uncertainty.

Assuming the uncertainties of the three axes are independent, the root square sum has magnitude 0.23 degrees, i.e. \pm 0.23 degrees. To be slightly conservative, we have assumed that the uncertainty region is a 0.5 degree diameter cone, and our acquisition analysis is based on this value.

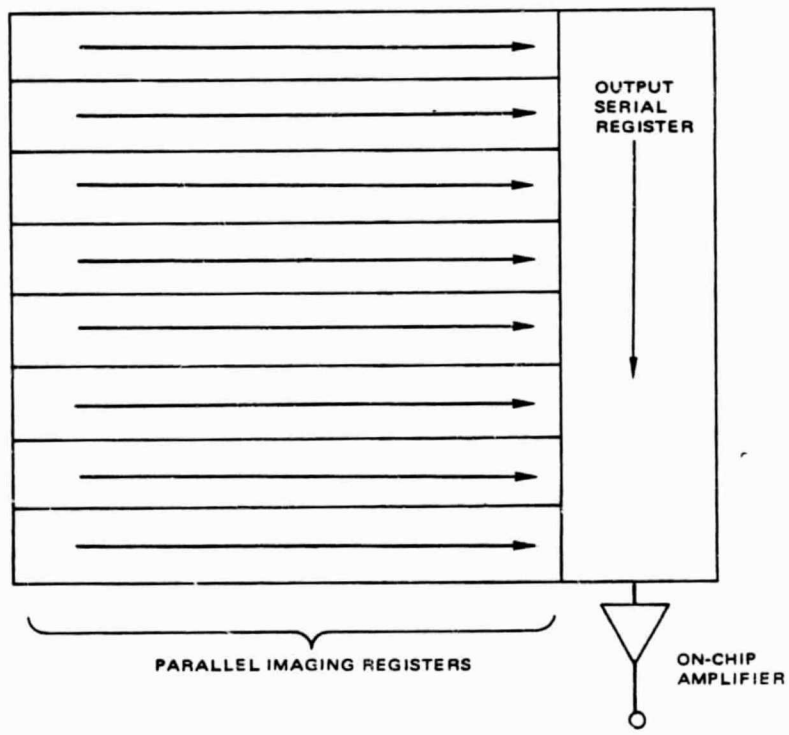
8.2 ACQUISITION SENSORS

8.2.1 Arrays

Sensors for the acquisition subsystem fall into two broad categories - quad cells or arrays. Quad cells will be discussed in the next section. Arrays can be charge - coupled devices (CCD), charge - injection devices (CID), or MOS photodiode arrays which use charge - coupled readout technology. Although a linear array could be scanned across the uncertainty solid angle, we have chosen to avoid mechanical scanning and focus on area arrays.

The area arrays function as any energy detector, since the photocurrent resulting from incident light is integrated to yield a collected charge within each pixel. The various arrays differ in how this charge is stored and ultimately read out. The CCD readout is similar to an analog shift register, in which the charge is transferred from pixel site to pixel site. Voltages which control potential wells are manipulated at the proper time sequences to shift the charge along the row. The endmost vertical column of charge falls into a register which is then serially read out before the next column of charge is clocked in. Figure 8.2-1 schematically depicts the CCD readout process. Early CCD devices were limited by charge loss during charge transfer, such that a point of light could become a horizontal streak. Current devices, however, have transfer efficiencies of 0.9999 - 0.99999, and this is no longer the low light limitation. The CCD readout is serial, and timing information is retained to restore the pixel to its proper location in a video display. Although the CCD readout technique requires readout of the entire array to address any specific pixel, there are two distinct advantages to optical sensitivity which results.

First, since the image sites collect and transfer the charge, no separate charge storage areas are needed. The CCD focal plane filling efficiency is virtually 100 percent, so that no optical intensity is wasted by illuminating non-responsive charge storage sites. Second, since the charge is read out

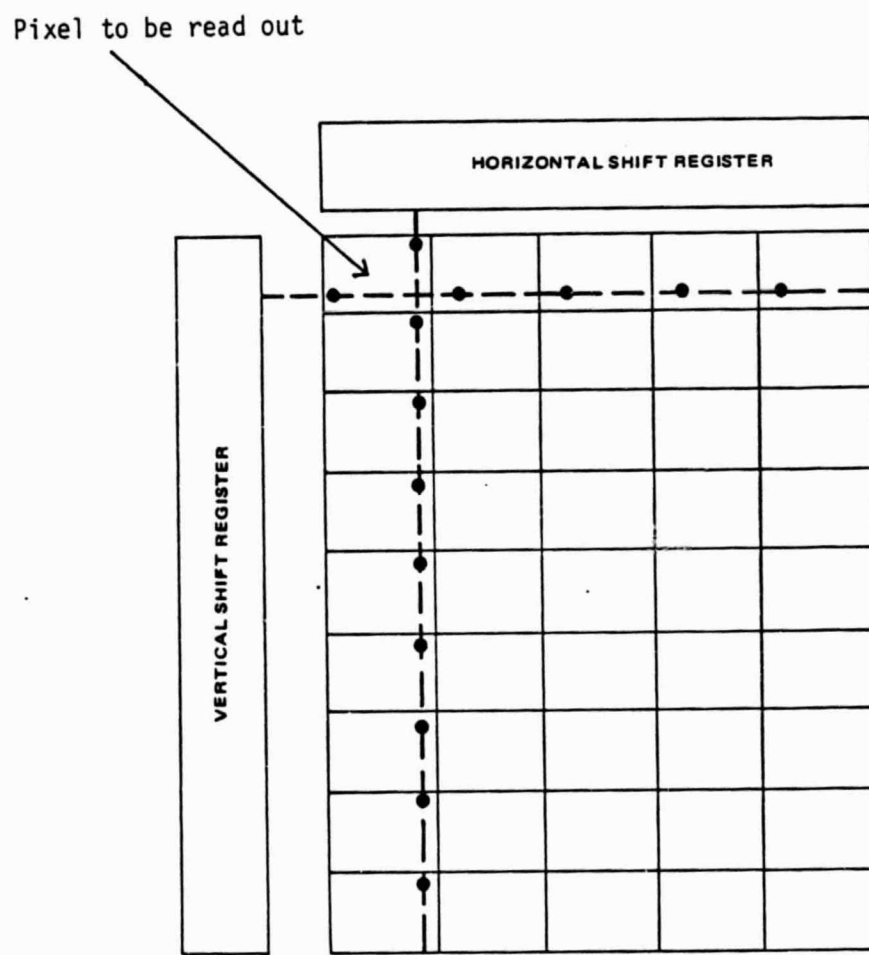


Schematic diagram of CCD readout technique.

Figure 8.2-1. Schematic Diagram of CCD Readout Technique.

along one-dimension, electrical connections and associated capacitance are minimized. The sensitivity is directly reduced as the capacitance is increased. So the combination of low capacitance and 100 percent focal plane light responsivity cause the CCD's to be the most sensitive area array detectors, at the expense of x-y pixel addressability.

The charge-injection device (CID) array uses an x-y coincident voltage readout technique, which allows a particular pixel location to be addressed. The two-dimensional nature of the readout results in more electrical connections and higher capacitance than for a CCD, so the CID sensitivity is poorer than the CCD. In parallel injection CID's it is possible to perform non-destructive readout, i.e. leaving the charge in the pixels by deferring the injection operation. Otherwise, injection is used to empty the charge storage capacitors after line readout. In sequential injection CID's the photon-generated charge is injected into the substrate and the resultant displacement current is sensed. Figure 8.2-2 shows schematically how CID readout is accomplished. Each sensing site consists of two MOS capacitors which are coupled to facilitate charge transfer. A row is selected for readout by setting its vertical scan register. Signal charge at all sites in that row is transferred to the column capacitors. The charge is then injected into the substrate by driving each column voltage to zero, in sequence, using the horizontal scan register and signal line. Charge in unselected rows remains stored in the row capacitors during the column voltage pulses. Thus any row can be selected and read out, but having both vertical and horizontal voltage signal lines connected to each sensing site is the reason CID capacitance is greater than for a CCD. The x-y coincident voltage configuration of the CID is also adaptable to random pixel addressing, in which only the selected pixel receives coincident x-y voltages and injects its charge into the substrate. This is not seen to be a significant advantage over CCD's for acquisition, since frame rates are already fast (10 msec or less), and a relatively small percentage of acquisition time is expended after array illumination. However, if the acquisition array is used for tracking also, the CID pixel addressability allows a pixel tracking gate to be formed with a small group of pixels. These may be then read out at a much higher frame rate as dictated by tracking requirements (Section 7.11).



Schematic diagram of CID and photodiode array readout technique.

Figure 8.2-2. Schematic Diagram of CID and Photodiode Array Readout Technique.

The MOS photodiode image sensor is an array of photodiodes with an MOS transistor scanning circuit embedded into the same monolithic structure. The photodiode array loses some responsivity due to added capacitance from the x-y coincident voltage readout as in the CID. The photodiode array sacrifices additional responsivity due to sharing the focal plane between the MOS scanning transistors, a loss of up to 40 percent. The MOS photodiode array was not initially thought to allow large video arrays, due to difficult fabrication of its complicated focal plane structure, and because the individual cell size can require up to four times the area of a CCD cell. Recently, however, photodiode arrays of about 400 x 500 have become commercially available (Figure 8.2-3), which is comparable to current CCD arrays.

A summary of commercially available imaging arrays is shown in Table 8.2-1. Array sizes of up to about 400 x 500 are available in both CCD and photodiode technology, and up to about 300 x 400 for CID.

Unfortunately, most manufacturers specify the array sensitivity in luminous units, which takes into account the spectral responsivity of the human eye. However, a good idea of the relative sensitivity of the CCD, CID, and photodiode array formats at standard video rates of 30 frames per second can be obtained from the first four entries in Table 8.2-1. The minimum illumination for the Fairchild and Sony CCD's are 5 lux and 3 lux, respectively. The GE CID requires 11 lux, a factor of 2-3 times more illumination than the CCD. The Hitachi photodiode array requires 30 lux, about a factor of three more than the CID, and a factor of ten more than the CCD. The relative radiometric sensitivity follows the same ratios, since less than 1.0 pw sensitivity for CCD and 10.0 pw sensitivity for photodiode arrays has been measured at Hughes.

Fairchild and RCA both have intensified SIT-CCD arrays available. The Fairchild array has a microchannel plate illuminating a phosphor tube, which is then coupled by fiber optics into the CCD. The RCA version is more sensitive, since the intensifier tube launches directly into the CCD, resulting in secondary electron "avalanche gain" of about 1500. The RCA SIT-CCD has the same sensitivity as the well known SIT vidicon, which is 200 - 300 times more sensitive than the unintensified CCD. However, the 10 - 15 kV voltage requirement of the intensifier tube may make it undesirable from some space applications.

- SOLID STATE AREA ARRAY
- 384 X 485 ELEMENTS
- SI - MOS
- VIDEO READOUT
- SENSITIVITY AT $0.9 \mu\text{m}$
 $\approx 10 \text{ PW}$

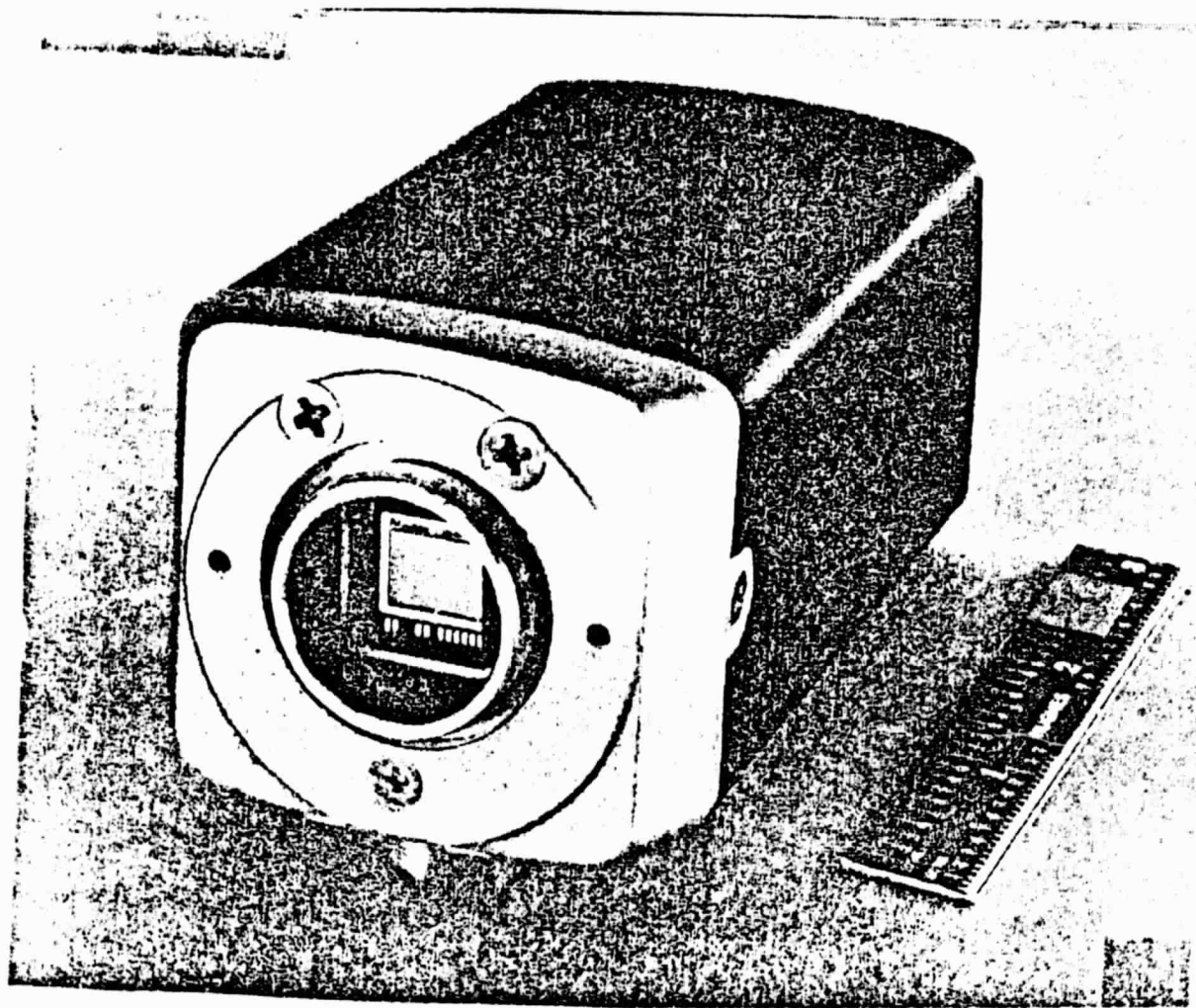


Figure 8.2-3. Hitachi 384 x 485 Element MOS Photodiode Array.

TABLE 8.2-1. COMMERCIALLY AVAILABLE IMAGING ARRAYS

Manufacturer	Type	No. of Pixels	Minimum Illumination
FAIRCHILD	CCD (SIT-CCD)	380 x 488	5 LUX @ F 1.4
SONY	CCD	384 x 491	3 LUX @ F 1.4
GE	CID	290 x 416	11 LUX
HITACHI	MOS P.D.	384 x 485	30 LUX @ F 1.4
RCA	SIT CCD (CCD)	403 x 512	1.1×10^{-2} LUX
EG & G RETICON	CCPD	256 x 256	$10^{-3} \mu\text{J}/\text{cm}^2$
TEXAS INSTR.	CCD	292 x 290 (1024 x 1024 for space telescope)	$\sim 2.0 \times 10^{-3} \mu\text{W}/\text{cm}^2$
HUGHES IPD	CCD (radiation-hardened)	100 x 100 (324 x 324)	< 1.0 pW

Texas Instruments Central Research Laboratory is building two large space-qualified CCD arrays for space programs at the Jet Propulsion Laboratory. An 800 x 800 CCD array is being fabricated for use on the Galileo program, and a 1024 x 1024 CCD array is being built for Space Telescope. The space qualification included the packaging, documentation, and vibration testing aspects, as well as radiation shielding for the Galileo array. Both the arrays read out at frame rates of 1-2 frames per second.

In summary, solid state arrays are commercially available in sizes up to 400 x 500, with sub-picowatt sensitivity for the CCD's. Since CCD arrays with standard video rates will be shown to be compatible with acquisition subsystems for satellite optical communication (Section 8.5), experimental testing by NASA personnel is highly recommended.

8.2.2 Quadrant Detectors

A summary of commercially available quadrant detectors is shown in Table 8.2-2, and the Hughes HPIN quadrant detector data sheet is shown in more detail in Figure 7.7-1. The Hughes quad detectors seem to offer the smallest dark current and capacitance for a given ratio of array diameter to dead zone width, which is important for field of view reduction during acquisition. The RCA quadrant APD is listed with a dead zone of 2.9 mils ($75 \mu\text{m}$), but a program is ongoing to reduce that value to 1.2 mils ($25 \mu\text{m}$). Unless otherwise specified, the Hughes quadrant detectors will be assumed for the PIN quad case, and the RCA for the APD quad case.

Manufacturer	Model	Quantum Efficiency (%)	Responsivity (A/W)	Dark Current (nA-per element)	Capacitance (pf-per element)	Dead Zone (mils)	Array Diameter (mils)
Hughes	HPIN 200Q	83	0.6	30	4.5	4.4	247
Hughes	HPIN 444Q	83	0.6	100	15	6	499
Hamamatsu	S994-13	-	-	0.025*	70*	3.9	118
Applied Solar Energy	45 PQU	-	0.5	5.0	50*	5	105
SDC	118-23	-	0.55	35	4	-	118
SDC	380-23	-	0.55	140	48	3.9	380
UDT	SPOT-4D	-	0.42	6	5	-	105
UDT	SPOT-90	-	0.42	30	40	-	394
RCA-APD	APD-QUAD	77	0.536	10	0.5 pf	2.9	59

*No reverse bias voltage (typical bias is 50 V)

TABLE 8.2-2. COMMERCIALLY AVAILABLE QUADRANT DETECTORS

8.3 ACQUISITION SOURCES

Two basic types of semiconductor laser sources for acquisition are presently commercially available: fundamental transverse mode single laser sources, and multi-transverse mode multi-laser incoherent arrays. Commercially available single transverse mode lasers are summarized in Table 8.3-1. Average power in the 20 - 30 mW range is presently available, and device power improvement has been rapid. Several manufacturers have now reported 100 mW in the laboratory. Probably devices with 50 mW cw will be commercially available in the 1986 - 88 time frame. Perhaps by that time frame some version of the Xerox multiple stripe coherent array will also be available. Although 1.0 watt cw has been reported in the laboratory for the Xerox array, lifetimes have been only several hundred hours. It is difficult to extrapolate the power a reliable coherent array might obtain. In addition, incoherent power combining schemes with diffraction gratings or dichroic mirrors might be used, but practical considerations may prohibit using a power combiner for both the communication and acquisition sources.

The second type of acquisition source is the multiple-laser incoherent array, in which several multi-transverse mode lasers are combined in the image plane of the optical system. Laser Diode Labs (LDL) is the industry leader in this technology, and high peak powers are available. Some devices physically position the lasers as close together as possible, and others use fiber optics to couple the emission from all the lasers into the image plane. Figure 8.3-1 summarizes the characteristics of the LDL LS-410 array. Although 1.0 kW peak power initially seems impressive, a practical problem arises in collimating the array.

The basic problem with the LDL arrays is one of collimating an extended multiple-laser source with the broad angular emission characteristic of a single laser. The efficiency with which the optical system captures the emitted light is given by

TABLE 8.3-1. COMMERCIALLY AVAILABLE SINGLE TRANSVERSE MODE LASER DIODES

<u>MANUFACTURER</u>	<u>DIODE</u>	<u>RATED POWER</u>	<u>STRUCTURE</u>	<u>WAVELENGTHS (NM)</u>	<u>COST</u>	<u>FEATURE</u>
RCA	C86030E	20 MW CW 40 MW @ 50% d.c.	CDH-LOC	810-870	\$ 1980	Large Optical Cavity
Telefunken	TXSF-8500	20 MW CW	DH - V-GROOVE	810-850	\$ 725	V-Groove Mode Filter
Amperex	374 CQY	50 MW @ 10% d.c.	DH - Proton Bombarded Stripe	800-880	\$ 500	Pulsed Operation
General Optronics	GOLS 4000	30 MW CW	DH-CSP-LOC	780-950	\$ 2500	Large Optical Cavity
Mitsubishi	ML5101A	15 MW CW 30 MW @ 50% d.c.	Crank TJS	795-905	\$ 565	"Crank" Non-Absorbing Facet
Hitachi	HLP-1400 (New Version)	30 MW CW	DH-CSP	800-850	\$1500	HR Coat Rear Facet AR Coat Front Facet

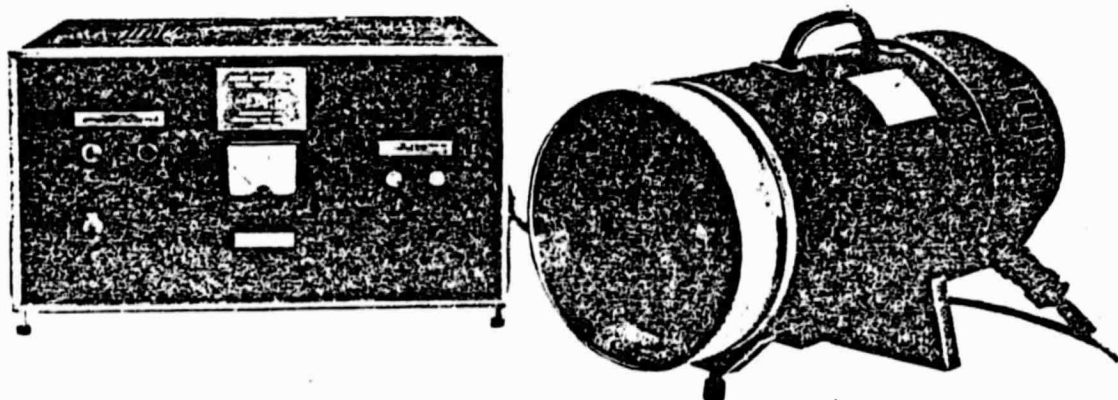
MODELS LS-410 LSA-410

FEATURES

- UP TO 1.2KW PEAK OPTICAL SOURCE POWER.
- UP TO 0.6 AVERAGE SOURCE POWER OUTPUT.
- 1 TO 5 KHZ REPETITION RATE.
- 115 VAC. 60/50 HZ OPERATION.
- 850 OR 904 NM STANDARD PEAK EMISSION WAVELENGTH.
- CUSTOM UNITS AVAILABLE INCLUDING 800 TO 880 NM WAVELENGTH SELECTION, 28 VDC OR 220 VOLTS/50 HZ INPUT POWER.

DESCRIPTION

The LS-410 and LSA-410 are intended as high pulsed power laser illuminators. The unit is capable of emitting over 750 watts peak optical power into the air with an 8 milliradian beam divergence at a 5kHz repetition rate. Up to 0.5 watts average optical power is available. The unit is complete, providing the laser optics, pulse circuitry control and power supply in rugged and functional housings. The pulses may be triggered from an internal or external source. Custom designs are available on special order.



Laser Diode Laboratories high power illuminators are a line operated completely self contained system ideal for applications in Infrared viewing systems, Infrared target designators, etc.

Figure 8.3-1a). Laser Diode Labs High Pulsed Power Array.

ORIGINAL PAGE IS
OF POOR QUALITY

PERFORMANCE CHARACTERISTICS

Peak power output	1000 watts	1000 watts
Peak wavelength emission	904nm	850 nm
Spectral width (50% points)	3.5nm	3.5nm
Average power output at 5KHZ (approx.)	0.6 watts	0.4 watts
Source size	170x190 mils	200x190 mils
Peak current	40 amps	Up to 40 amps
Optical pulse duration	130ns	90ns max
Repetition rate (internal or external trigger)	1 — 5KHZ	1 — 5KHZ
System		
Peak power output (with F1.8 lens)	750 watts	750 watts
Beam divergence	8mr	8mr
Size:	Laser transmitter	= 9.5" OD x 20" 2 long
	Power supply	= 17" x 16" x 8"
	Total weight approx.	= 30 lbs.

Figure 8.3-1b). Laser Diode Labs High Pulsed Power Array Data Sheet.

$$T_{NA} = \frac{\int_{-A}^A \int_{-B}^B \exp(-x^2/2\sigma_x^2) \exp(-y^2/2\sigma_y^2) dx dy}{\int_{-\infty}^{\infty} \int_{-\infty}^{\infty} \exp(-x^2/2\sigma_x^2) \exp(-y^2/2\sigma_y^2) dx dy}$$

$$= \operatorname{erf}(A/\sqrt{2}\sigma_x) \operatorname{erf}(B/\sqrt{2}\sigma_y)$$

where $\operatorname{erf}(x)$ is the error function, A and B are the half angles of acceptance of the numerical aperture of the optical system, and σ_x and σ_y are the $1/e^2$ half angles of the laser Gaussian beam divergence. The optical system must be fast (low f number) to capture a significant fraction of the widely divergent light. To capture 60 percent of the emitted light, F 2.5 optics are required (experimentally measured). The far field beam divergence is then given by

$$\theta_{FF} = D_S/f$$

where D_S is the source diameter in the image plane and f is the lens focal length. To collimate the beam to the 0.5° (8.7 mrad) acquisition uncertainty, with F 2.5 optics for 60 percent collection efficiency and 200 mils array source diameter, a nine inch diameter lens is required. Even if a more complicated collimating optical system is used, the output aperture diameter must be nine inches or greater. Assuming only a six inch transmitting diameter is available on the GEO, and keeping F 2.5 optics, divergence angle is increased a factor of 1.5. The 600 watts peak that was collected delivers 5.0 pW peak to a 15 cm collecting aperture on the LEO. However, this is an average power of only 2.3×10^{-3} pW, since the maximum pulse width is 90 ns and the maximum pulse rate is 5 kHz. The average power is too low to reasonably detect, so a viable detection scheme would have to time gate around the optical pulse, thereby utilizing the laser peak power. This will be discussed in Section 8.4.6.

8.4 QUADRANT DETECTOR ACQUISITION

8.4.1 Field of View Reduction

There are three fields of view associated with a quadrant tracking detector. The field of view (FOV) over which a source can cause a spot to fall on the active area of at least one quadrant is normally considered to be the quadrant detector FOV. This is given by $\theta_{FOV} = D/f$, where D is the diameter of the quad array, and f is the focal length of the optical system. As shown in Section 7.4, the closed loop field of view is the FOV over which a source can cause a spot to overlap all four quadrants, such that both azimuth and elevation error signals can be obtained. The closed loop field of view is given by $\theta_{CL} = D_S/f$, where D_S is the spot diameter in the quadrant detector focal plane. The third field of view for a quadrant detector is the effective FOV determined by the residual tracking jitter. For a quadrant detector used for acquisition, the residual tracking error is associated with the quadrant detector noise equivalent angle (NEA), which was discussed in Section 7.2.

Analogous to defining θ_{CL}/θ_{NEA} ($\theta_{NEA} = 2 \sigma_{NEA}$) as the closed loop tracking dynamic range in Section 7.4, we can define $\theta_{FOV}/\theta_{NEA}$ as the dynamic range of FOV reduction for a quadrant detector used for acquisition. Since from Section 7.4 we have

$$\theta_{NEA} = (\pi/8) (D_S/f) / SNR_{rms}$$

the acquisition FOV reduction ratio (R) is given by

$$R = \theta_{FOV} / \theta_{NEA} = (8/\pi) (D/D_S) SNR_{rms}$$

Thus the obtainable FOV reduction is proportional to the rms SNR in a quad element, and also proportional to the ratio of quadrant array diameter (D) to optical spot diameter (D_S).

The obtainable FOV reduction compared with the ratio of uncertainty angle to tracking detector field of view determines the number of acquisition stages required to handover to fine tracking. If the quadrant acquisition array is configured so that $\theta_{FOV} = \theta_{UNC}$, where θ_{UNC} is the angular uncertainty in location of the opposite terminal, then the following stage must have a field of view greater than or equal to θ_{NEA} of the preceding stage. The FOV reduction ratio (R) then determines the field of view ratio between successive stages

$$(\theta_{FOV-1} / \theta_{FOV-2}), \text{ since } \theta_{NEA-1} = \theta_{FOV-2}.$$

We have attempted to use single stage acquisition to keep the subsystem as simple as possible. This suggests that the single stage acquisition sensor must have FOV reduction capability such that $R \geq (\theta_{UNC} / \theta_{FOV-T})$, where θ_{UNC} is the acquisition angular uncertainty and θ_{FOV-T} is the field of view of the tracking detector. Although it would be desirable to handover to the closed loop field of view of the tracking detector (θ_{CL-T}), this is not necessary since a multi-step angular reduction can move the spot from the quadrant array field of view (θ_{FOV-T}) to the closed loop tracking FOV (θ_{CL-T}) (Section 8.4.2).

8.4.2 Servo Angular Step Reduction

When a quadrant detector is used for acquisition, one approach would be to set the closed loop field of view equal to the acquisition angular uncertainty. The FOV reduction would then be given by the expression for tracking dynamic range (Section 7.4).

$$\theta_{CL} / \theta_{NEA} = (8/\pi) SNR_{rms}$$

From Section 8.4.1, if the total quadrant array field of view (θ_{FOV}) is set equal to the acquisition angular uncertainty, the FOV reduction is given by

$$R = \theta_{FOV} / \theta_{NEA} = (8/\pi) (D/D_s) SNR_{rms} .$$

The FOV reduction is increased by the ratio of the quad array diameter (D) to the optical spot diameter (D_S). For single stage acquisition the extra factor of D/D_S is required, and we set $\theta_{UNC} = \theta_{FOV}$.

Then it becomes necessary to adopt an algorithm to transfer the optical spot from being within a single quadrant in θ_{FOV} to being within θ_{CL} , where the spot overlaps all four quadrants. This is the same problem that occurs when the acquisition sensor hands over to a single quadrant in the tracking quad array. The servo system knows only that the spot is within one quadrant, but not how far in angle the spot is from being centered. A linear angular step could be used, in which the servo steps x microradians toward the illuminated quadrant, checks to see if an error signal exists, then steps x microradians again, until eventually the spot falls within θ_{CL} and an error signal occurs.

An angular reduction scheme which is faster than the linear step reduction is to use a log step reduction. The first step will be half of the quadrant FOV, the second step one-fourth of the quadrant FOV, etc., until the spot falls within θ_{CL} . If the spot changes quadrants, then the next step is in the opposite direction, but still half of the previous angular step.

We need to provide an estimate of the number of steps required for the log angular reduction to transfer the spot from θ_{FOV} to θ_{CL} . Define the ratio of the quad array diameter (D) to the dead zone (d) as $\delta = D/d$. For small dead zone loss (Section 7.3), the loss is given by $n \approx \gamma = (d/f)/(\lambda/D)$. Rewriting the expression with the spot diameter given by $D_S = 2.44 \lambda f/D$ gives $n = 2.44 d/D_S$.

The number of servo increments (N) is given by

$$\theta_{FOV} / \theta_{CL} = 2^N$$

or

$$D/D_S = 2^N$$

Rewriting D_S in terms of d and n , and using $\delta = D/d$, we obtain

$$N = \log_2 (n\delta/2.44)$$

For 50 percent dead zone loss ($n = 0.5$), and using $\delta = 83.2$ for the Hughes HPIN 444Q quadrant detector, $(n\delta/2.44) = 17$, so that $N = 5$ is required. Although sometimes fewer steps will be needed, in general $N = 5$ will be required for the HPIN 444Q and $n = 0.5$.

8.4.3 Detection and False Alarm Probabilities

For a quadrant detector acquisition sensor, the transmitter dwell time must be sufficient for the quadrant detector to perform N angular reduction steps which transfer the spot into the closed loop tracking field of view (Section 8.4.2). Since during that time the spot is located in a single quadrant, the probability that a single servo step is accomplished correctly is $P_d (1 - P_{fa})^3$, where P_d is the detection probability in the quadrant with the signal present, and P_{fa} is the false alarm probability in a quadrant with no signal. The probability that N servo steps are accomplished correctly is $P_d^N (1 - P_{fa})^{3N}$. This is the probability that the acquisition quadrant detector achieves closed loop tracking when it is illuminated by the transmitter.

The overall acquisition sequence also requires that no false alarms occur from the quadrant detector during the time it is not illuminated by the transmitter. Since we have required N servo steps to occur within a dwell time, we have set $t_d = N\tau$, where t_d is the dwell time and τ is the effective integration time of the quad detector. During a dwell in which the quadrant detector is not illuminated, there are four quad elements, each with N chances for false alarm, so the probability that no false alarms occur is $(1 - P_{fa})^{4N}$. If the transmitter addresses a total of M acquisition cells, then we require no false alarms to occur in the $M-1$ dwell times during which the quadrant detector is not illuminated. The probability that no false alarms occur during the $M-1$ non-illuminated dwell times is then $(1 - P_{fa})^{4N(M-1)}$.

The probability of a completely successful acquisition sequence (P_{ACQ}) is the probability of N successful servo steps during the dwell in which the quadrant detector was illuminated, and no false alarms during the other dwells, and is given by

$$P_{ACQ} = P_d^N (1 - P_{fa})^{3N} (1 - P_{fa})^{4N(M-1)}$$

$$= P_d^N (1 - P_{fa})^{4NM-N}$$

If we then require equal contributions from missed detection and all the chances for false alarm, we set the threshold such that

$$P_d = (1 - P_{fa})^{4M-1}$$

Using the binomial expansion this becomes

$$P_d = 1 - (4M-1) P_{fa}$$

For a given detection probability with equal contributions from missed detection and all chances for false alarm, the resulting false alarm probability is then given by

$$P_{fa} = (1 - P_d)/(4M-1).$$

8.4.4 CW Integrating Approach

There are three basic modulation/detection alternatives for quadrant detector acquisition. The first is the cw integrating approach, in which the acquisition transmitter is a cw laser, the detector integrates the signal photoelectrons, and then thresholds out most of the noise. The second alternative is to intensity modulate the laser transmitter with an audio sinusoid (tone). The optical quadrant detector is followed by a narrow bandpass filter around the audio tone, envelope detected, and thresholded. This approach is discussed in Section 8.4.5. The final alternative is to time-gate the receiver to the laser pulse width. This approach is discussed in Section 8.4.6 in the context of the high peak power, low duty cycle, Laser Diode Labs laser array, as well as a single mode laser source.

In the cw integrating approach, the quadrant acquisition detector receives cw illumination from the transmitter during the dwell time. The dwell time (t_d) allows N angular steps to occur, so $t_d = N\tau$, where τ is the integration time per servo step. The servo sample rate ($1/\tau$) then determines the required detector bandwidth. Setting $(1/\tau)$ equal to the bandwidth determined by the RC product of amplifier input resistance and total detector-preamp capacitance gives the minimum thermal noise (Section 7.5). For the Hughes HPIN 444Q quadrant detector the capacitance is 15 pf per element. For a preamp noise figure of 3 dB ($T_{eq} = 290$), the thermal noise photoelectron counts are $K_T = 3.0 \times 10^7$ (independent of τ). For the HPIN 444Q dark current of $I_D = 100$ nA per element, the dark photoelectron count rate is given by

$$n_D = I_D/e = 6.3 \times 10^{11} e^-/\text{sec}$$

For the 15 cm LEO collecting aperture, worst case irradiance in the 8.7 mrad (0.5°) field of view due to the moon ($L_I = 2.7 \times 10^{-7} \text{ Wm}^{-2} \text{ \AA}^{-1}$ - Table 7.7-1), quantum efficiency $\eta = 0.83$, and other parameters as in Table 7.6-1, the background count rate per element is $n_B = 8.15 \times 10^{10} e^-/\text{sec}$. (Note the background flux splits into four detectors.) For optical signal power at the detector (P_r), the signal count rate is $n_S = (\eta/h\nu)P_r$. Defining the rms SNR as the square root of the power SNR in Section 7.5, we have for a PIN quadrant detector

$$\begin{aligned} \text{SNR}_{\text{rms}} &= \frac{K_S}{\sqrt{K_S + K_B + K_D + K_T}} \\ &= \frac{n_S \sqrt{\tau}}{\sqrt{n_S + n_B + n_D + K_T/\tau}} \end{aligned}$$

The count rates and counts are related by $K_i = n_i \tau$, except that the minimum K_T is independent of τ as shown in Section 7.5. From Section 8.4.3, the probability of successful acquisition is

$$P_{ACQ} = P_d^N (1 - P_{fa})^{4NM-N},$$

where the threshold is set such that $P_{fa} = (1 - P_d)/(4M-1)$. For overall acquisition probability of $P_{ACQ} = 0.99$, and with $N = 5$ servo steps to achieve closed loop, we require $P_d = 0.999$. The false alarm probability then depends on M , the number of acquisition cells addressed by the transmitter. However, for a given P_d , the required SNR is not extremely sensitive to P_{fa} . Thus we will assume a nominal $P_{fa} = 10^{-9}$, and adjust it later for the M for each specific case.

For $P_d = 0.999$ and $P_{fa} = 10^{-9}$, an rms SNR = 9.3 is required. [Kingston, Detection of Optical and Infrared Radiation]. The required signal count rate versus integration time is

<u>n_s</u>	<u>τ (msec)</u>
9.3×10^8	0.1
2.5×10^8	1.0
7.9×10^7	10.0
2.5×10^7	100.0
7.8×10^6	1000

Note that the signal count rate is less than $n_s = 10^9 e^-/\text{sec}$, which is a negligible shot noise source compared to $n_B = 8.2 \times 10^{10} e^-/\text{sec}$ and $n_D = 6.3 \times 10^{11} e^-/\text{sec}$.

For $\tau \geq 1.0 \text{ msec}$, the dark current dominates the noise contributions, so that the signal count rate is $n_s \sim 1/\sqrt{\tau}$ for $\tau \geq 1.0 \text{ msec}$. Rewriting the signal count rate using $P_R = n_s (hv/n)$, the required power versus integration time is given by

P_r (pW)	τ (msec)
258	0.1
69.3	1.0
21.9	10.0
6.9	100
2.2	1000

Again, $P_R \sim 1/\sqrt{\tau}$ for $\tau \geq 1.0$ msec, due to dark current dominated noise.

Note that the large dark current is due to requiring a physically large detector to get a high diameter to dead zone ratio (δ). If the dead zone were physically smaller, for a fixed δ the array diameter could be smaller, which decreases both the capacitance and dark current in proportion to the reduction in detector area. Since we were required to assume worst case background (except the sun) the best detector performance will be background noise limited. A quadrant APD would not help in this respect since the background noise is multiplied by the APD excess noise ($F_N = 3$ for $G = 50$). However, a PIN quad with a small dead zone and dark current less than 10 nA per element could be background noise dominated.

For the ideal background - dominated performance case, the required power versus integration time is given below, with the power savings relative to the dark-limited HPIN 444Q.

P_R (pW)	τ (msec)	Power savings (dB)
158	0.1	2.1
27.2	1.0	4.1
7.5	10	4.7
2.3	100	4.7
0.75	1000	4.6

The required power goes as $P_R \sim 1/\sqrt{\tau}$ for $\tau \geq 10$ msec. Thus a small dead zone PIN quadrant detector which could achieve a given δ with smaller array diameter (and correspondingly less dark current) could save 4.7 dB in laser power.

The parametric evaluation of the HPIN 444Q quadrant detector performance is summarized in Table 8.4-1, where the initial assumption of $P_{fa} = 10^{-9}$ has been corrected to the true value for the number of acquisition cells (M) for that case. Note that $t_d = N\tau$, and $N = 5$ angular reduction steps are assumed.

Several features of Table 8.4-1 are noteworthy. First, even though integrating longer reduces the required power at the detector, since the dwell time is also increased, the number of acquisition cells must be reduced for a given acquisition time. Reducing the number of acquisition cells requires increasing the transmitted beamwidth, which in turn increases the required transmitter power. Thus integrating longer actually increases the required transmitter power for a given acquisition time.

Second, the cases for $\tau < 10$ msec would be difficult to implement, since the angular step reduction would require very large accelerations and torque, as well as greater than 100 Hz bandwidths. Third, to use an acquisition beamwidth $\theta_T < 30 \mu\text{rad}$ is probably impractical. This is because the spacecraft rms two axis attitude jitter is about $17 \mu\text{rad}$, and some fraction of that jitter is coupled by gimbal friction into line of sight pointing error, reducing control of beam overlap for a narrow beam. Then if cases of $\theta_T < 30 \mu\text{rad}$ and $\tau < 10$ msec are ignored, the most viable case from the standpoint of laser power is $T_{ACQ} = 2500$ seconds, $\theta_T = 58 \mu\text{rad}$ (Airy lobe) and $P_T = 22 \text{ mW}$. Since present single transverse mode sources have 20 - 30 mW power, there would be essentially no margin. If a new PIN quadrant detector were developed, such that it could be background limited instead of dark current limited, a power savings of 4.7 dB would result for $\tau = 10$ msec. This would in effect provide the power margin of 4.7 dB with an acquisition time of $T_{ACQ} = 2500$ seconds (42 minutes) and $P_T = 22 \text{ mW}$ transmitter. Note that by restricting laser power to current commercially available levels, an unrealistic acquisition time of $T_{ACQ} = 42$ minutes is required. In fact, to obtain any power margin a developmental quadrant detector had to be postulated.

TABLE 8.4-1. HPIN 4440 QUADRANT DETECTOR ACQUISITION PERFORMANCE

a) $T_{ACQ} = 2500$ sec

τ (msec)	M	θ_T (μ rad)	P_T (mW)
0.1	5×10^6	6.0	3.1
1.0	5×10^5	18	7.3
10	5×10^4	58	22
100	5000	184	70
1000	500	581	210

b) $T_{ACQ} = 1000$ sec

τ (msec)	M	θ_T (μ rad)	P_T (mW)
0.1	2×10^6	9.2	7.2
1.0	2×10^5	29	18
10	2×10^4	92	56
100	2000	291	169
1000	200	919	513

c) $T_{ACQ} = 500$ sec

τ (msec)	M	θ_T (μ rad)	P_T (mW)
0.1	10^6	13	14
1.0	10^5	41	37
10	10^4	130	111
100	10^3	411	334
1000	100	1300	1015

d) $T_{ACQ} = 250$ sec

τ (msec)	M	θ_T (μ rad)	P_T (mW)
0.1	5×10^5	18.4	28
1.0	5×10^4	58	72
10	5×10^3	184	220
100	500	581	659
1000	50	1840	2000

If the burden were shifted to the transmitter laser, assuming that 100 mW cw were available, an acquisition time of 1000 seconds (17 minutes) could be obtained, with 2.5 dB margin ($P_T = 56$ mW required). If a 100 mW transmitter and a developmental quadrant detector (background limited) were assumed, $T_{ACQ} = 500$ seconds (8.3 minutes) could be obtained with about 4.3 dB power margin (4.7 dB less than 111 mW required). However, this is probably the upper bound on cw integrating quadrant detector performance for acquisition, and the minimum acquisition time is 8.3 minutes (100 mW transmitter, developmental background - limited quadrant detector).

The results in Table 8.4-1 can be described (to first order) in compact form. The acquisition time is given by $T_{ACQ} = M t_d$, where M is the number of acquisition cells and t_d is the dwell time. Since $t_d = N\tau$, where N is the required number of angular reduction steps and τ is the integration time, we can write $T_{ACQ} = MN\tau$. The number of acquisition cells (M) is given by $M = (\theta_{UNC}/\theta_T)^2$, where θ_{UNC} is the acquisition angular uncertainty, and θ_T is the acquisition transmitter beamwidth. Thus the acquisition time can be written

$$T_{ACQ} = N\tau \theta_{UNC}^2 / \theta_T^2$$

At this point it can be seen that the acquisition time is proportional to the square of the uncertainty angle, i.e. the uncertainty solid angle.

Using the link equation (Section 7.5), it can be seen that the required transmitter power is proportional to the required detector power, and proportional to the transmitted beamwidth squared, $P_T \sim \theta_T^2$. Since we showed $P_R \sim 1/\sqrt{\tau}$, for $\tau \geq 10$ msec whether background or dark limited, we can write $P_T \sim \theta_T^2/\sqrt{\tau}$, or $\theta_T^2 \sim P_T \sqrt{\tau}$. Replacing θ_T^2 in the expression for T_{ACQ} we obtain

$$T_{ACQ} \sim N \theta_{UNC}^2 \sqrt{\tau} / P_T \quad (1)$$

Thus the acquisition time varies inversely with laser power (since broader beamwidths can be used), is directly proportional to the uncertainty solid angle, and increases as the square root of the integration time. This relationship is modified slightly when the dependence of P_{fa} on M is taken into account.

The data from Table 8.4-1 is plotted in Figures 8.4-1 through 8.4-7. Figures 8.4-1 through 8.4-5 plot required power (P_T) versus the inverse of acquisition time ($1/T_{ACQ}$) for fixed integration times (τ) from 0.1 through 1000 msec. As can be easily seen, the deviation from inverse proportionality due to the dependence of P_{fa} on M is slight. Figures 8.4-6 and 8.4-7 plot P_T versus τ for fixed acquisition times of $T_{ACQ} = 250$ and 2500 seconds, respectively. The linearity of the log-log plots in Figures 8.4-6 and 8.4-7 indicates that the deviation from $P_T \sim \sqrt{\tau}$ in equation (1) is small.

The analysis of the cw integrating approach thus far has considered only the shot noise generated by the thermal, dark current, and optical background noise sources, and not the DC currents themselves. This implicitly assumes that the DC currents do not vary in time, and can therefore be thresholded out (see Figure 7.7-2). While a threshold can indeed eliminate the DC currents due to thermal noise and dark current (since this can be calibrated into the receiver design), the DC current due to optical background changes as background sources move in and out of the receiver field of view. Star sources will be present in one quadrant, but not the others. Therefore the DC current due to optical background must be considered for the cw integrating approach.

On the basis of shot-noise limited performance, the cw integrating approach will be seen to be about 4.5 dB superior to the sinusoidal intensity modulation approach, and could be considered an upper bound to performance. However, the sinusoidal intensity modulation approach is not affected by optical background DC, and for practical systems will be superior to cw integration for this reason.

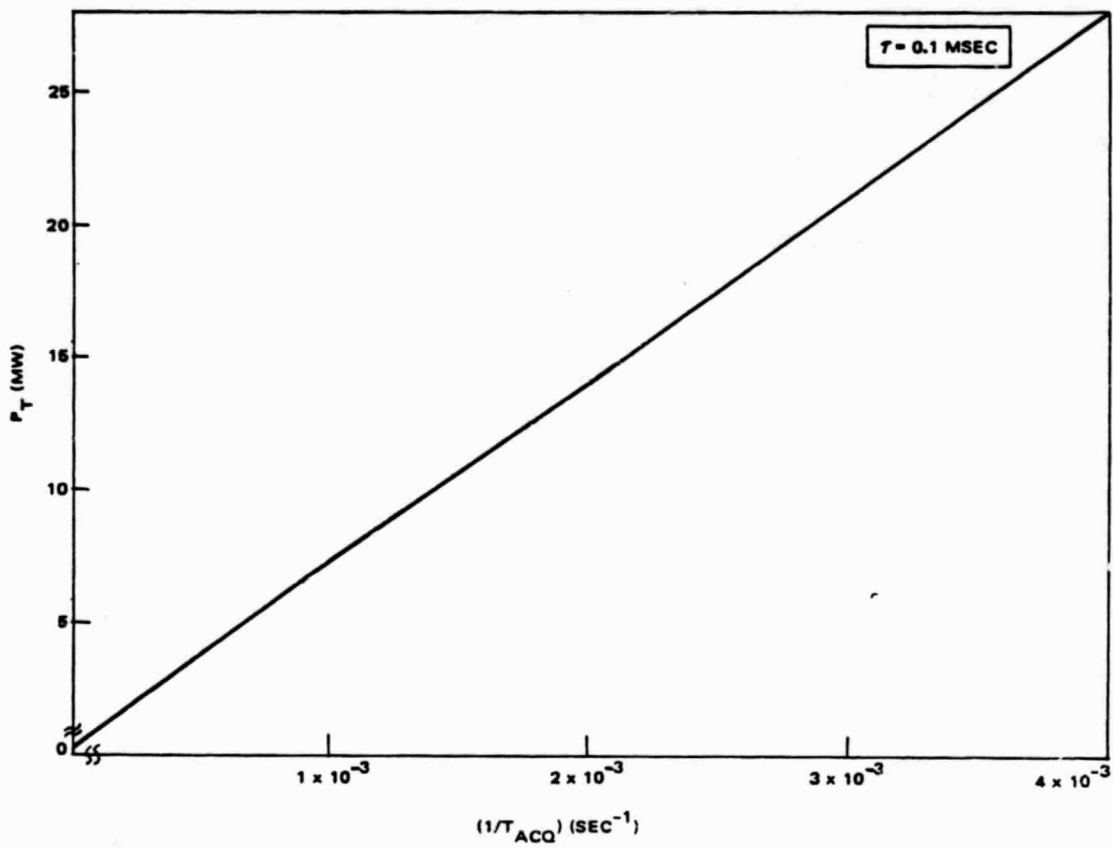


Figure 8.4-1. Required Power (P_T) versus the Inverse of Acquisition Time ($1/T_{ACQ}$) for Integration Time $\tau = 0.1 \text{ msec}$.

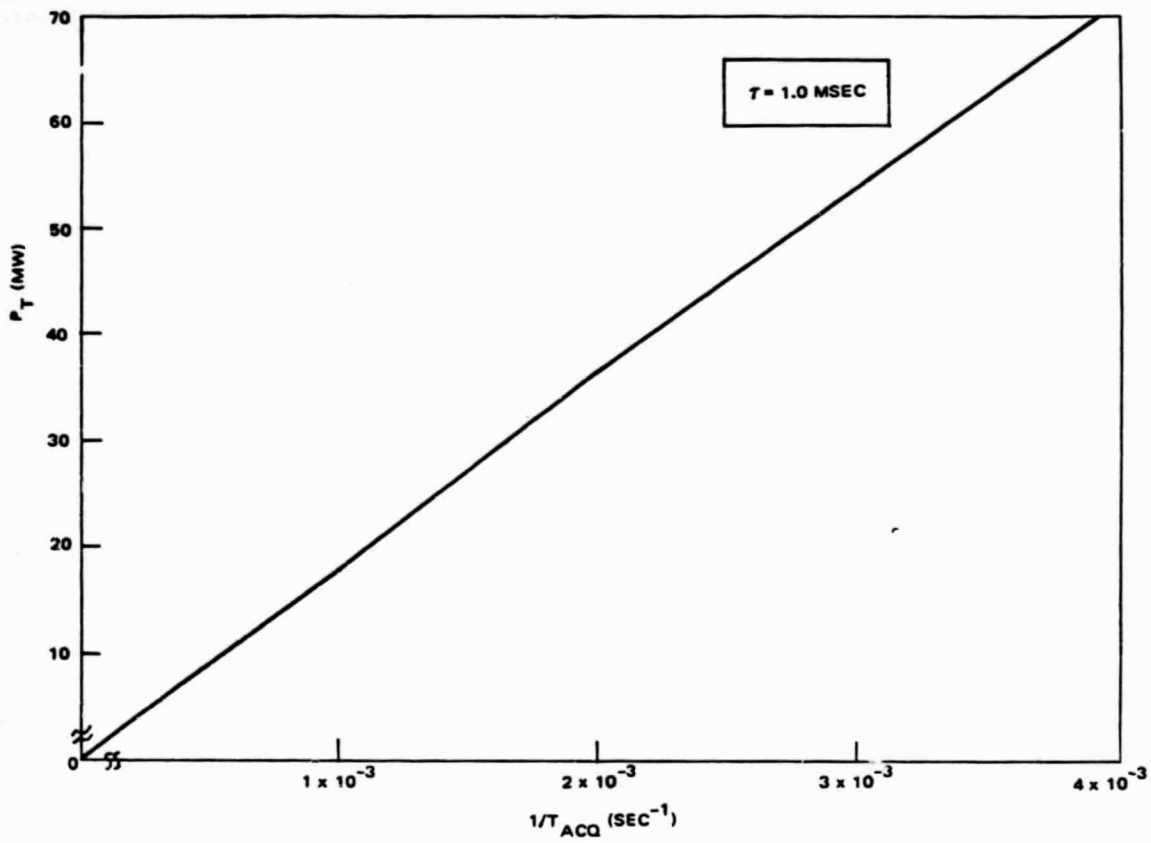


Figure 8.4-2. Required Power (P_T) versus the Inverse of Acquisition Time ($1/T_{ACQ}$) for Integration Time $\tau = 1.0 \text{ msec}$.

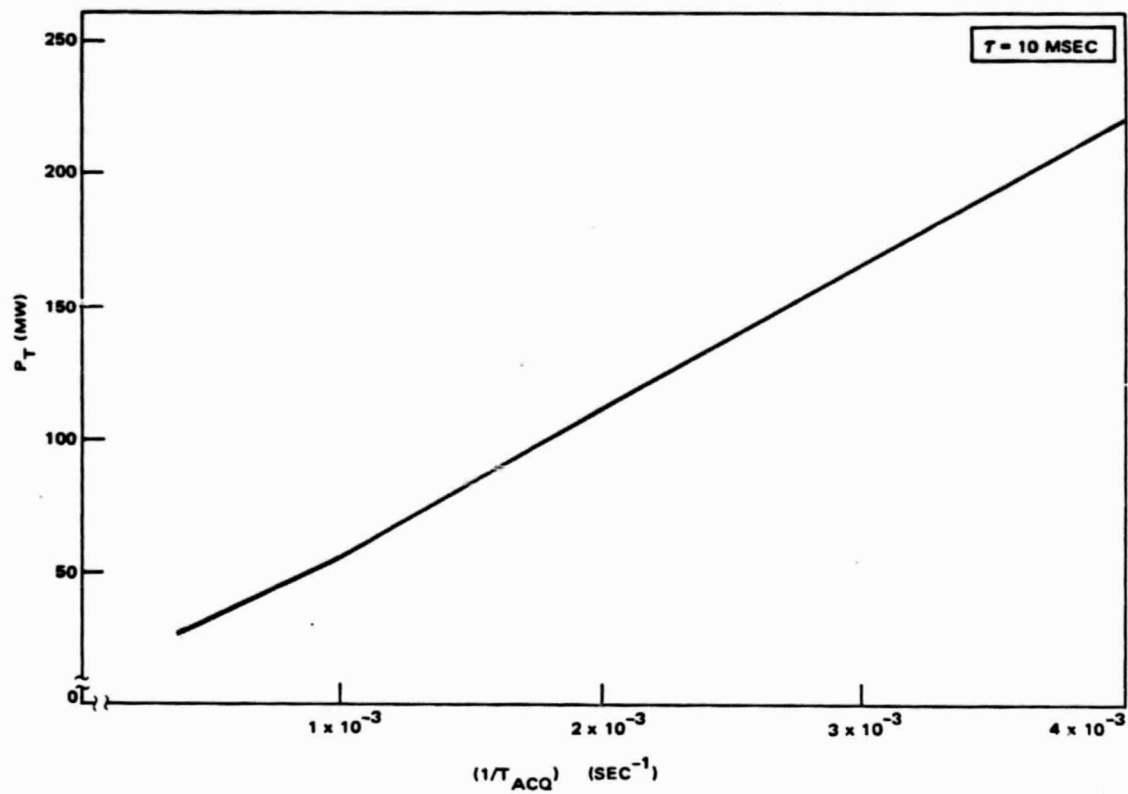


Figure 8.4-3. Required Power (P_T) versus the Inverse of Acquisition Time ($1/T_{ACQ}$) for Integration Time $\tau = 10 \text{ msec}$.

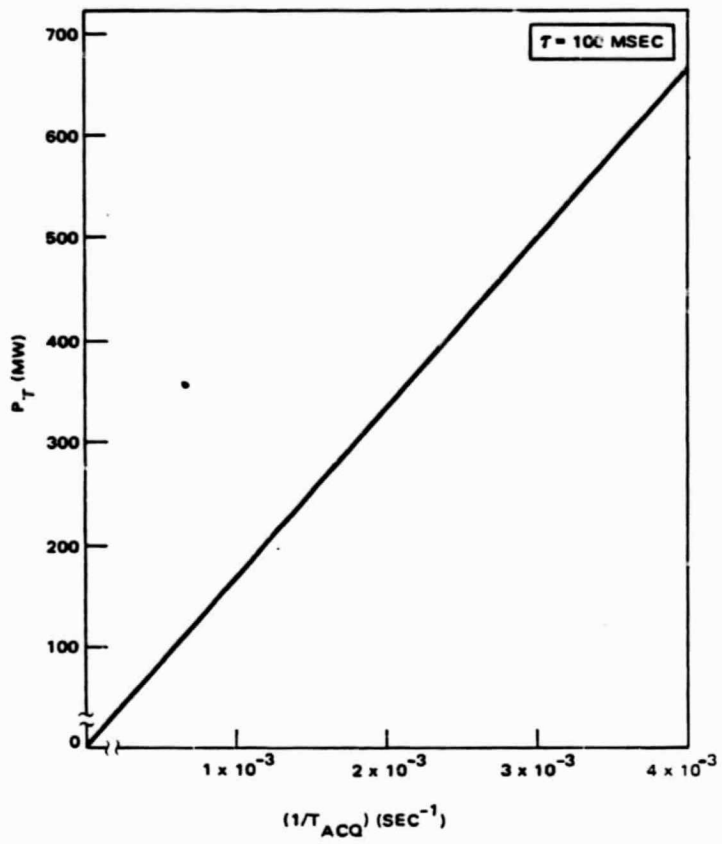


Figure 8.4-4. Required Power (P_T) versus the Inverse of Acquisition Time ($1/T_{ACQ}$) for Integration Time $\tau = 100 \text{ msec.}$

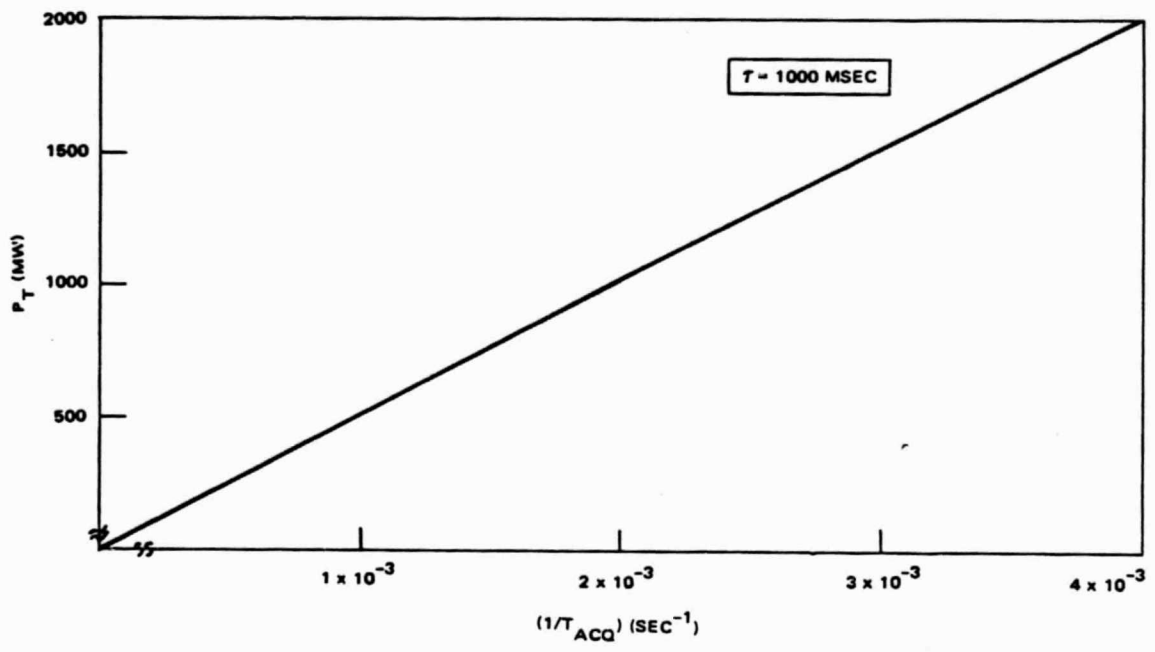


Figure 8.4-5. Required Power (P_T) versus the Inverse of Acquisition Time ($1/T_{ACQ}$) for Integration Time $\tau = 1000$ msec.

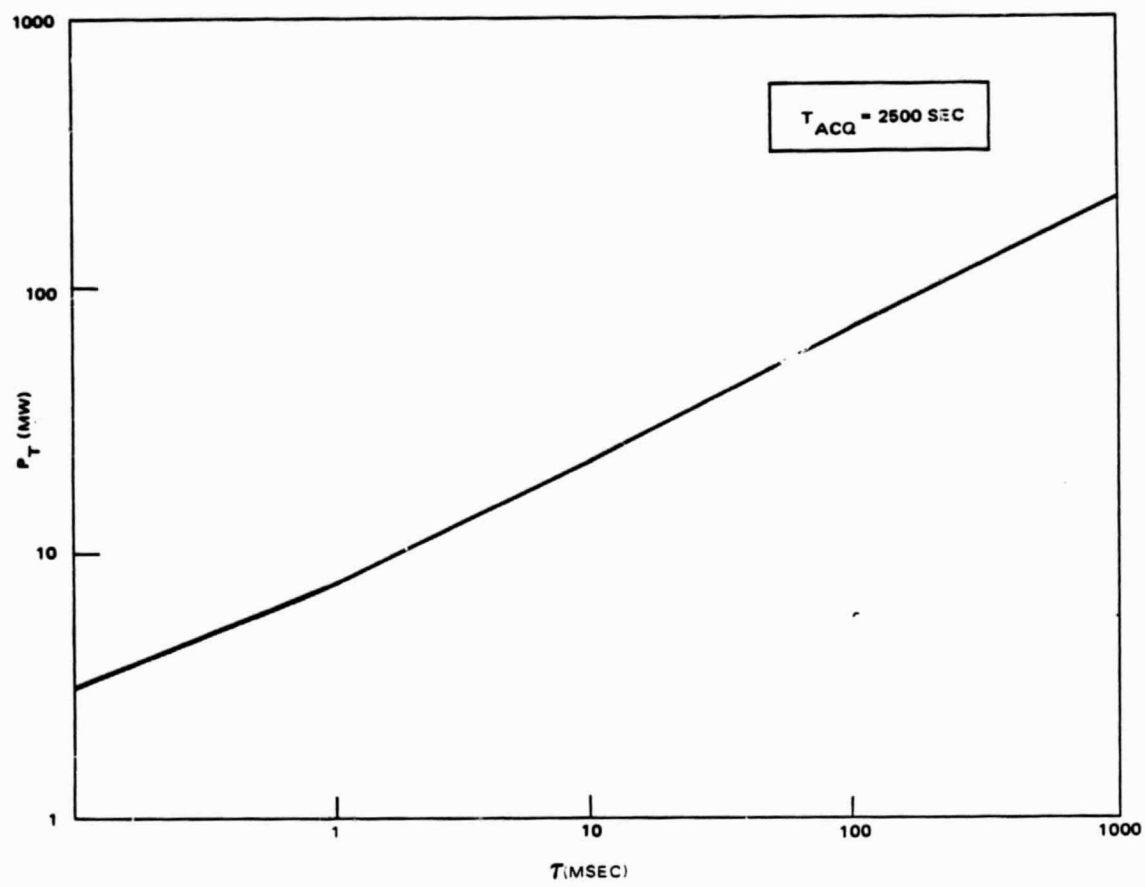


Figure 8.4-6. Required Power (P_T) versus Integration Time (τ) for Acquisition Time $T_{ACQ} = 2500$ Seconds.

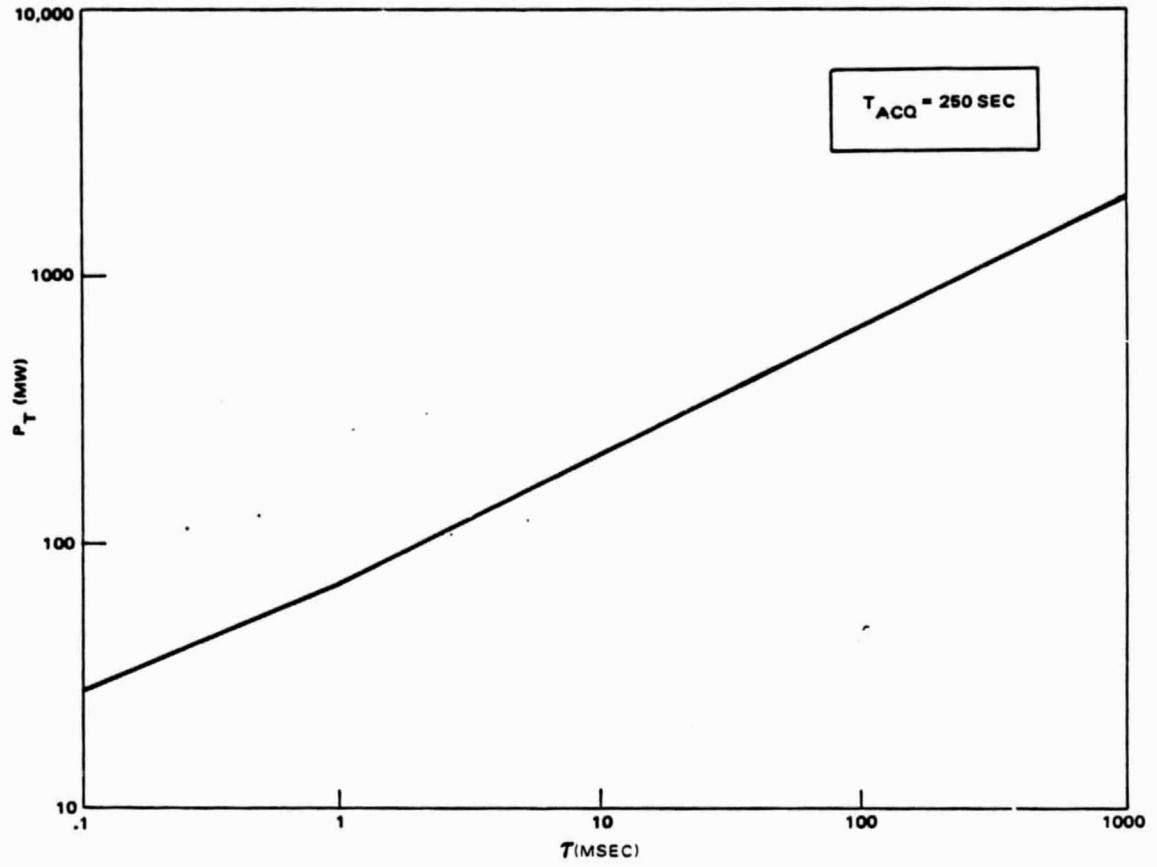


Figure 8.4-7. Required Power (P_T) versus Integration Time (τ) for Acquisition Time $T_{ACQ} = 250$ Seconds.

It is useful to consider an example of the impact of optical background DC on the cw integrating approach. As in the tracking case, a uniform DC background cancels out in the sum and difference circuit, so the DC non-uniformity between quadrants is the real issue. However, the nonuniformity can be as large as the worst case background, since even an extended source could illuminate only one of the four quadrants.

When background DC is considered, the SNR must be redefined as mean signal minus DC background divided by rms noise, i.e.

$$\text{SNR}_{\text{rms}} = \frac{K_S - K_B}{\sqrt{K_S + K_B + K_D + K_T}}$$

Again defining count rates (n_i) by $K_i = n_i \tau$, where τ is the integration time, the SNR becomes

$$\text{SNR}_{\text{rms}} = \frac{(n_S - n_B)\sqrt{\tau}}{\sqrt{n_S + n_B + n_D + K_T/\tau}}$$

Taking the same count rates for the HPIN 444Q as before ($n_D = 6.3 \times 10^{11} \text{ e}^-/\text{sec}$, $n_B = 8.15 \times 10^{10} \text{ e}^-/\text{sec}$, and $K_T = 3.0 \times 10^7 \text{ e}^-$), requiring $\text{SNR} = 9.3$ and $\tau = 0.1 \text{ msec}$, the required signal is $n_S = 8.25 \times 10^{10}$, a 19.5 dB increase compared to the case for shot noise only. (For longer τ , the dB increase is even larger). If the optical filter bandwidth were reduced from 50 to 10 angstroms (note that $\theta_R = \theta_{UNC} = 0.5^\circ$ and cannot be reduced), reducing the background count rate to $n_B = 1.63 \times 10^{10} \text{ e}^-/\text{sec}$, $n_S = 1.72 \times 10^{10} \text{ e}^-/\text{sec}$ are required ($\text{SNR} = 9.3$, $\tau = 0.1 \text{ msec}$), a 12.7 dB increase over shot noise alone.

For the LEO to GEO uplink in this study, with a large 0.5° diameter uncertainty angle, and acquisition required about twelve times daily, it is probably not practical to wait for intense background sources to exit the field of view.

Therefore a modulation scheme which eliminates the optical background DC is necessary for quadrant detector acquisition. Although about 4.5 dB worse than cw integration in shot noise performance, the sinusoidal intensity modulation approach will be seen to eliminate the optical background DC problem. The performance in Table 8.4-1 (Figures 8.4-1 through 8.4-7) can be considered as the upper bound on shot-noise limited PIN quadrant detector acquisition, for cases where severe background sources can be avoided.

8.4.5 Sinusoidal Intensity Modulation Approach

This method of quadrant detector acquisition requires biasing the transmitter laser at its half power level, and intensity modulating the laser with an audio sinusoid. For detection, the optical detector is followed by a narrow bandpass filter around the audio tone, and an envelope detector then determine the amplitude of the sinusoid (Figure 8.4-8). A threshold then removes most of the noise. We need to determine the performance of the modulation/detection scheme.

The transmitter laser is biased at half power (P_S) and sinusoidally intensity modulated, so that the power waveform is described by $P(t) = P_S(1+\cos \omega_s t)$. Note that the laser must have a cw power capability $P_{CW} = 2P_S$. Although it might be argued that since sinusoid modulation is 50 percent duty cycle, the diode average power could be set equal to the cw power, this is valid only for frequencies above about 1.0 MHz. Audio frequencies appear to be cw to the diode.

The photon induced current at the optical detector is $i_s(t) = (\eta eG P_r/h\nu) (1 + \cos \omega_s t)$ where P_r is the received power (related to P_S by the link equation - Section 7.6) and the other parameters are defined in Section 7.5. The average value is $\bar{i}_s = \eta eG P_r/h\nu$, and this is also the amplitude of the sinusoid term.

The two-sided mean-squared current noise level (per element) is given by (from Section 7.5)

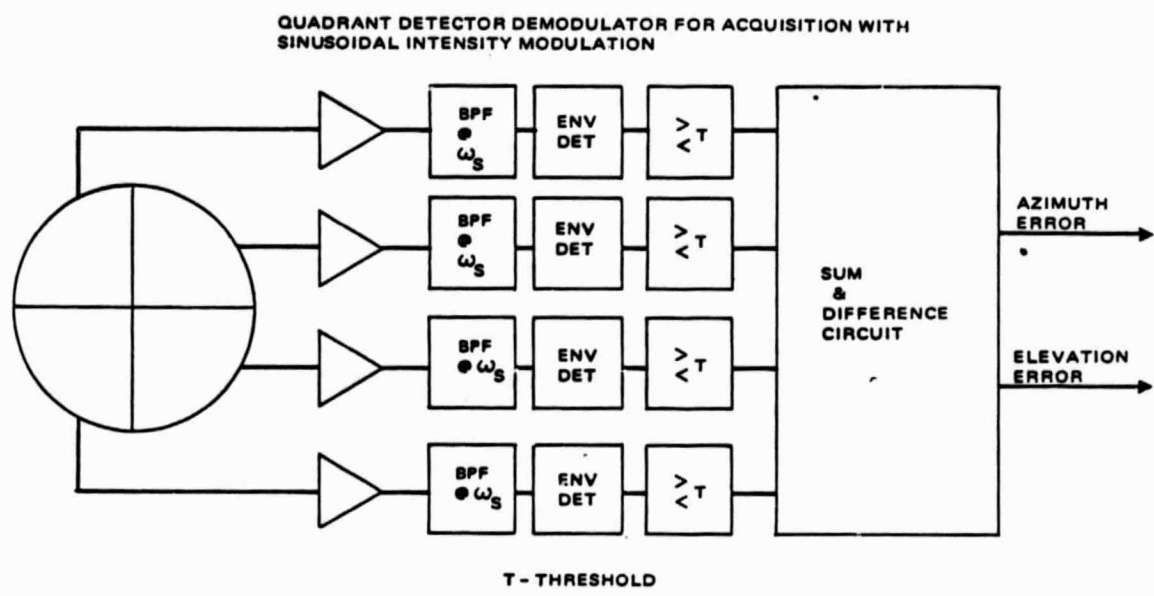


Figure 8.4-8. Quadrant Detector Demodulator for Acquisition with Sinusoidal Intensity Modulation.

$$\overline{i_{TOT}^2} = e \overline{G^2} i_s + e \overline{G^2} i_B + e \overline{G^2} i_D \\ + e i_{DS} + 2 k T_{eq} / R_L \quad (\text{A}^2/\text{Hz})$$

The noise spectral density following the bandpass filter of transfer function $H_{BPF}(f)$ is

$$S_n(f) = \overline{i_{TOT}^2} |H_{BPF}(f)|^2$$

Using a quadrature expansion of the noise we can write $n(t) = n_c(t) \cos(\omega_s t + \psi) - n_s(t) \sin(\omega_s t + \psi)$. The spectra of n_c and n_s are obtained by shifting the one-sided bandpass spectrum to baseband,

$$S_{nc}(f) = S_{ns}(f) = 2 \overline{i_{TOT}^2} |\tilde{H}_{BPF}(f)|^2 ,$$

where $\tilde{H}_{BPF}(f)$ is the bandpass filter function shifted to baseband. For a bandpass bandwidth from $f_c - B/2$ to $f_c + B/2$, the noise power after the bandpass filter is given by

$$\sigma_n^2 = \int_{-B/2}^{B/2} 2 \overline{i_{TOT}^2} |\tilde{H}_{BPF}(f)|^2 df \\ = 2 \overline{i_{TOT}^2} B$$

The envelope detector is a nonlinear element, and alters the Gaussian probability distribution of the noise. When no signal is present, the envelope is given by

$$a(t) = \sqrt{n_c^2 + n_s^2}, \text{ and the envelope obeys Rayleigh statistics.}$$

The Rayleigh density for the envelope a is given by

$$P_a(x) = (x/\sigma_n^2) \exp(-x^2/2\sigma_n^2)$$

When the signal is present, the statistics become Rician. The envelope of a sinusoid of amplitude \bar{i}_s added to Gaussian noise is

$$a(t) = \left\{ [\bar{i}_s + n_c(t)]^2 + n_s^2(t) \right\}^{1/2}$$

and the Rician density for the envelope is

$$P_a(a) = (x/\sigma_n^2) \exp[-(x^2 + \bar{i}_s^2)/2\sigma_n^2] I_0(Ax/\sigma_n^2)$$

which is valid for $x \geq 0$, and I_0 is the modified Bessel function.

False alarm and detection probabilities for Rayleigh and Rician statistics are tabulated in Introduction to Radar Systems by M. Skolnik (McGraw-Hill 1962) as well as many radar texts.

Since the power in the signal sinusoid is $P_s = (1/2) \bar{i}_s^2$, Skolnik defines the signal to noise ratio S/N as

$$S/N = (1/2) \bar{i}_s^2 / \sigma_n^2$$

Inserting the expressions for \bar{i}_s , σ_n^2 and i_{TOT}^2 , and rearranging, gives

$$S/N = \frac{1/2 (n P_R / h\nu)^2}{(\bar{i}_s + i_B + i_D) 2F_N B/e + \frac{2 i_{DS} B}{e G^2} + \frac{4 k T_{eq} B}{e^2 G^2 R_L}}$$

Using the acquisition probability expression from Section 8.4.3, for acquisition probability of $P_{ACQ} = 0.99$, equal contributions from missed detections and all chances for false alarms, and $N = 5$ servo steps, we require $P_d = 0.999$ and $P_{fa} = (1 - P_d)/(4M - 1)$, where M is the number of acquisition cells.

Since the required S/N is not extremely sensitive to P_{fa} , we will use a nominal $P_{fa} = 10^{-12}$, and later revise the S/N for the exact M and P_{fa} for that case. For $P_d = 0.999$ and $P_{fa} = 10^{-12}$, $S/N = 17.5$ dB is required (Skolnik).

Again we assume parameters for the Hughes HPIN 444Q quadrant detector, and worst case background illumination due to the moon with $L_I = 2.7 \times 10^{-7} \text{ Wm}^{-2} \text{ \AA}^{-1}$. We will also assume that the bandpass filter has a bandwidth of 100 Hz. Note, however, that the detector bandwidth has to respond to the sinusoid modulation frequency f_s , and minimum thermal noise is computed on the basis of detector bandwidth f_s (section 7.5.2). Therefore f_s should be as low in frequency as possible, yet must be high enough to get outside the detector $1/f$ noise. We will assume $f_s = 10$ kHz, which is a low enough frequency that thermal noise is not the dominant noise source for the HPIN 444Q. (The relative contributions of background, dark current, and thermal noise are in the ratios 1.6, 12.5 and 6.3, respectively).

Note that if a modulating frequency such as $f_s = 1.0$ MHz were chosen, so that the diode average power could be set equal to its cw power (instead of $P_{cw} = 2P_s$), the thermal noise would be increased a factor of 100 (compared to $f_s = 10$ kHz.) For fixed capacitance, R_L must be reduced to increase the bandwidth, and the thermal noise spectral level is $2 K T_{eq}/R_L$.

Signal induced noise is negligible due to the high contributions of the other noise sources. For $S/N = 17.5$ dB ($P_d = 0.999$, $P_{fa} = 10^{-12}$), $P_R = 42$ pW is required.

Table 8.4-2 summarizes the acquisition performance of the Hughes HPIN 444Q with sinusoidal intensity modulation. P_{cw} is the cw power requirement of the laser transmitter, given by $P_{cw} = 2 P_s$, where P_s is the amplitude of the sinusoid in the power waveform. Table 8.4-2 was calculated with a fixed dwell time $t_d = N/B$, where N is the number of servo steps for angular reduction, and the servo response time is $1/B$, where B is the bandwidth of the bandpass filter. For $N = 5$ and $B = 100$ Hz, $t_d = 0.05$ seconds.

TABLE 8.4-2. ACQUISITION WITH SINSUSOIDAL INTENSITY MODULATION
(HUGHES HPIN 444Q)

T_{ACQ} (sec)	θ_T (μ rad)	M	P_{cw}
2.1×10^4	20	4.2×10^5	9.2
1.0×10^4	29	2.0×10^5	17.9
5027	41	1.0×10^5	35.3
2000	65	4.0×10^4	87.4
956	94	1.9×10^4	171
471	134	9412	338
188	212	3760	835
93	302	1853	1650

Note that the sinusoidal intensity modulation (SIM) approach (Table 8.4-2) has poorer performance than the shot noise limited cw integrating (CWI) approach (Table 8.4-1, for $\tau = 10$ msec). $T_{ACQ} = 1000$ seconds requires about

164 mW (interpolating by $T_{ACQ} \sim 1/P_{CW}$), while for CWI $T_{ACQ} = 1000$ seconds is achieved with 56 mW, a savings of 4.7 dB. Similarly, $T_{ACQ} = 500$ seconds requires about 318 mW for SIM, and 111 mW for CWI, a 4.6 dB savings. CWI would be a superior approach to SIM if optical background DC were fixed and could merely be thresholded out. However, as described in the previous section, the CWI approach pays a 12.7 dB or greater penalty for optical background moving in and out of the receiver field of view, as would occur for practical satellite receivers. Therefore, by eliminating the background DC current, SIM is seen to be the superior approach for quadrant detector acquisition.

Figure 8.4-9 plots required power P_{CW} versus the inverse of acquisition time ($1/T_{ACQ}$) from Table 8-4 for the HPIN 444Q. Since the log-log plot deviates only slightly from a slope of unity, the inverse proportionality is only slightly modified by the dependence of P_{fa} on M.

A savings of 2.0 dB in laser power from Table 8.4-2 is obtained if a developmental quadrant detector is assumed, which has a smaller area (for a given δ) so that dark current is negligible. (This is less than the 4.7 dB savings which results by removing dark current from the shot noise limited CWI case, since SIM has additional thermal noise from the requirement that the detector bandwidth accomodate the 10 kHz tone.)

It is interesting to qualitatively compare the shot noise limited cw integrating approach (CWI) with the sinusoidal intensity modulation (SIM) approach. SIM requires biasing the laser at half power, so that the sinusoid amplitude is given by half the laser's cw power capability - effectively a 3 dB loss. The receiver pays an additional 3 dB penalty, since the power in a sinusoid of amplitude A is $1/2 A^2$. However, the Rayliegh/Rician statistics give the same detection and false alarm probability performance at about 1.5 dB less in rms SNR than for Gaussian statistics. The net effect is that shot noise limited CWI could achieve the same acquisition time with about 4.5 dB less laser power. However as previously mentioned, the optical background DC current CWI problem eliminates this advantage.

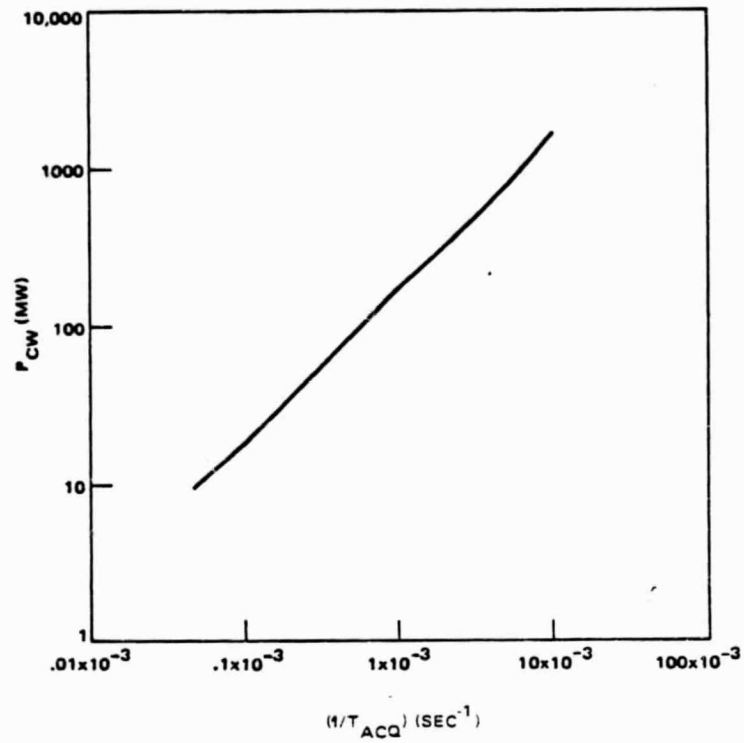


Figure 8.4-9. Required Power (P_{CW}) versus the Inverse of the Acquisition Time ($1/T_{ACQ}$) for the HPIN 444Q Quadrant Detector with Sinusoidal Intensity Modulation.

Since for the SIM approach if dark current is removed thermal noise becomes important (unlike shot noise limited CWI, which was background limited with dark current removed) it is of interest to see if a quad APD could improve the SIM approach.

Assuming the developmental RCA quadrant APD with dead zone reduced from $d = 75 \mu\text{m}$ to $d = 25 \mu\text{m}$, $\delta = 60$. The number of servo angular steps required are $N = \log_2 (\eta \delta / 2.44)$, which gives $N = 4$ for 50 percent dead zone loss. For $P_{ACQ} = 0.99$, using the detection and false alarm expressions from Section 8.4.3, we require $P_d = 0.999$, and assuming a nominal $P_{fa} = 10^{-9}$, $S/N = 16.5 \text{ dB}$ is required (Skolnik).

Again assuming moon background, and gain $G = 50$ ($F_N = 3$), performance is background limited as might be expected for an APD. Note it is desirable to become background limited with a PIN detector if possible, because the background is multiplied by F_N for an APD, which is a factor of $\sqrt{F_N}$ additional laser power required. In a 100 Hz bandwidth, for $G = 50$, 19.7 pW are required for $S/N = 16.5 \text{ dB}$, but reducing the gain to $G = 25$ ($F_N = 2.5$) reduces the required power to $P_R = 18 \text{ pW}$.

Table 8.4-3 summarizes the acquisition performance of SIM with a quadrant APD. The dwell time is $t_d = N/B = 0.04$ seconds. Comparing Table 8.4-3 to Table 8.4-4 (HPIN 444Q), at $T_{ACQ} = 180$ seconds the APD quad requires 374 mW, while the PIN quad requires about 872 mW (using $P_{CW} \sim 1/T_{ACQ}$ to interpolate), a difference of 3.7 dB. $T_{ACQ} = 500$ seconds requires about 136 mW with the quad APD and 318 mW for the PIN quad, also a 3.7 dB difference.

Figure 8.4-10 plots required power (P_{CW}) versus the inverse of acquisition time ($1/T_{ACQ}$). Again the log-log plot has nearly unity slope, for a near linear relationship between P_{CW} and $(1/T_{ACQ})$.

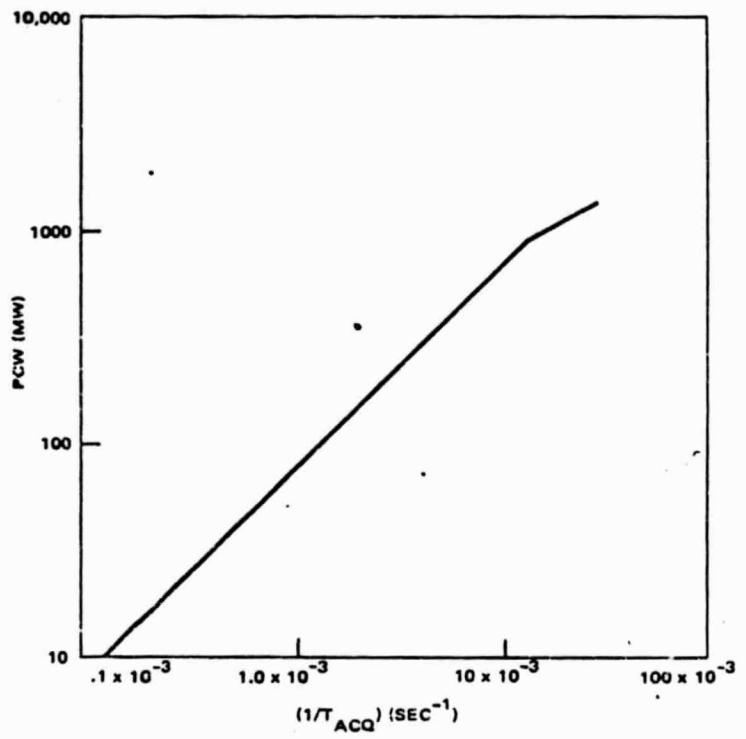


Figure 8.4-10. Required Power (P_{CW}) versus the Inverse of Acquisition Time ($1/T_{ACQ}$) for an RCA Quadrant APD with Sinusoidal Intensity Modulation.

TABLE 8.4-3. ACQUISITION WITH SINSUSOIDAL INTENSITY MODULATION
(RCA QUADRANT APD)

T_{ACQ} (sec)	$\theta_T(\mu\text{rad})$	M	P_{CW}
7660	30	1.9×10^5	10
3830	42	9.6×10^4	20
1878	60	4.7×10^4	39
734	96	1.8×10^4	96
360	137	9000	189
180	194	4500	374
70	311	1750	914
34	445	850	1785

Let us also derive a compact (first order) expression for acquisition time with sinusoidal intensity modulation. As for the shot noise limited cw integrating case, $T_{ACQ} = M t_d$, where M is the number of acquisition cells and t_d is the dwell time. The dwell time is given by $t_d = N/B$, where B is the servo bandwidth, but we will consider t_d fixed at its shortest value (0.05 seconds for the HPIN 444Q) to avoid the dependence of required power on noise bandwidth. Again $M = (\theta_{UNC}/\theta_T)^2$, where θ_{UNC} is the angular acquisition uncertainty and θ_T is the transmitted beamwidth. Since the required transmitter power is proportional to θ_T^2 (link equation - section 7.6) we can write $P_t = \gamma \theta_T^2$, with the result

$$T_{ACQ} = \gamma \theta_{UNC}^2 t_d / P_t.$$

Again the acquisition time is proportional to the uncertainty solid angle, and inversely proportional to laser power. This relationship is slightly modified when the dependence of P_{fa} on M is taken into account.

8.4.6 Time-Gated Acquisition

For this detection scheme the acquisition laser source is operated pulsed, and the acquisition receiver establishes time slots equal to the pulse width. The receiver integrates over each time slot, and compares to a threshold to determine if a pulse was present in that time slot. Since the transmitter and receiver do not share time synchronization during acquisition, the desired detection performance must be achieved in the worst case for which the pulse energy is shared equally between adjacent time slots (i.e. can only utilize half the pulse energy). This scheme thus utilizes a higher bandwidth, more complex acquisition receiver than the cw integration (CWI) or sinusoidal intensity modulation (S/M) approaches. Since the lowest frequency component of the pulsed waveform is approximately $(1/T_{rep})$, where T_{rep} is the pulse repetition period, the detector output can be AC-coupled to avoid the problem of the optical background DC component.

The detection and false alarm probabilities for the time-gated acquisition (TGA) scheme are somewhat different than for CWI or SIM (Section 8.4.3). As before, there are N servo steps which must be correctly performed to center up the illuminated spot on the quadrant detector. The dwell time (t_d) is then given by $t_d = N \tau$, where τ is the servo integration time. Now assume there are R laser pulses per servo integration time, where $R = \tau / T_{rep}$. The probability that at least one of the R pulses is correctly detected is given by $[1 - (1 - P_d)^R]$, where P_d is the detection probability within a time slot. (This is one minus the probability that none of the R pulses were detected.)

The total number of time slots per servo integration time is given by τ / τ_p , where τ_p is the laser pulse width (same as time slot width.) Since there are 4 detectors in the array, the number of chances for false alarm is $4 \tau / \tau_p$. Since N successful servo steps are required, the probability of a successful event during the illuminated dwell time is

$$[1 - (1 - P_d)^R]^N (1 - P_{fa})^{4N \tau / \tau_p}$$

The probability that there are no false alarms during the $(M-1)$ non-illuminated dwell times (M is the number of acquisition cells) is

$$(1-P_{fa})^{4N(\tau/\tau_p)(M-1)}.$$

Thus the probability of successful acquisition is

$$P_{ACQ} = [1-(1-P_d)^R]^N (1-P_{fa})^{4NM\tau/\tau_p}$$

Since the acquisition transmitter and receiver do not share time synchronization, the desired acquisition probability must be obtained with only half the pulse energy within the time slot.

For equal contributions from missed detection and false alarm, we set

$$1-(1-P_d)^R = (1-P_{fa})^{4M\tau/\tau_p}$$

Using the binomial expansion, this becomes

$$1-(1-P_d)^R = 1-(4M\tau/\tau_p)P_{fa}$$

$$P_{fa} = \frac{(1-P_d)^R}{(4M\tau/\tau_p)}$$

First we examine the case using the Laser Diode Labs (LDL) LS-410 incoherent laser array (Section 8.3). The maximum repetition rate is 5 kHz ($T_{rep} = 200 \mu\text{sec}$) and the maximum pulse width is 130 nsec.

For a 99 percent acquisition probability, and equal contributions from missed detection and false alarm, we require

$$[1-(1-P_d)^R]^N = \sqrt{0.99}$$

For $N = 5$ servo steps (Section 8.4.2), servo integration time $\tau = 0.01$ seconds ($B = 100$ Hz), and $T_{rep} = 200 \mu\text{sec}$ ($R = \tau / T_{rep} = 50$ pulses), the required detection probability is $P_d = 0.13$. This illustrates that the detection probability requirement is low since we only need detect one out of 50 pulses. Assuming a maximum $M = 2.0 \times 10^5$ acquisition cells ($M = (13.7 \times 10^{-3}/30 \times 10^{-6})^2$), $\tau = 0.01$ sec, and $\tau_p = 130$ nsec, the required false alarm probability is $P_{fa} = 10^{-14}$. For $P_d = 0.2$ and $P_{fa} = 10^{-14}$, an rms SNR = 7 is required.

For an RCA quadrant APD, with values as in Section 7.8.1, $G = 50$ ($F_N = 3$), moon background (Table 7.7-1), $\theta_R = 0.5^\circ$, $\tau_p = 130$ nsec, 2.0 pf per detector-preamp element, and parameters as in Table 7.7-1, the noise counts are $K_D = 0.2$, $K_{DS} = 0.8$, $K_B = 38,600$ and $K_T = 1576$. For rms SNR = 7 we require

$$\frac{K_S}{\sqrt{F_N(K_S + K_B + K_D) + K_{DS} + K_T}} = 7$$

which then requires $K_S = 2500$. Since up to half the pulse energy is wasted due to lack of time synchronization, the pulse rate generate $K_S = 5000$. The required power is $P_R = K_S(hv/n \tau_p) = 11.5$ nW. Since in Section 8.3 we found that the LDL array can be collimated to deliver only about 5.0 pW peak power to the detector, the array has about 33.6 dB less power than required.

Now let us consider a single mode laser with 20 mW average power, such as the RCA C86030E. We will assume the same pulse width ($\tau_p = 130$ nsec), but for duty cycles of 12 percent or less the RCA can deliver up to 160 mW peak power. The false alarm requirement is the same, but since now $T_{rep} = 1.0 \mu\text{sec}$, there are 10^4 pulses per servo integration time. The required detection probability is only $P_d = 6.9 \times 10^{-4}$, with $P_{fa} = 10^{-14}$ as before. Using $P_d = 0.01$ and $P_{fa} = 10^{-14}$, an rms SNR = 5.5 is required. With the same noise counts as just evaluated, and SNR = 5.5, $K_S = 2000$ are required. Thus the total photoelectrons per pulse are $K_S = 4000$, due to lack of time synchronization. This corresponds to a required power of $P_R = 9.2$ nW.

For $P_R = 9.2 \text{ nW}$, $\theta_T = 30 \mu\text{rad}$ (airy lobe), and other parameters as in Table 7.7-1, a transmitted power of $P_T = 2.6 \text{ W}$ is required. This is about 12 dB more than the 160 mW peak power capability of the RCA diode. However, it can be seen that the LDL array, in spite of its 1.0 kW peak power, is about 20 dB inferior to a single mode laser. This is because the large source size of the LDL array makes the output difficult to collect and collimate.

8.4.7 Quadrant Detector Acquisition Sequence

To avoid the earth as a background source, the geosynchronous (GEO) satellite is designated the acquisition transmitter, and the low earth orbiting (LEO) satellite is the acquisition receiver. Initially, the GEO scans its transmitted beam over the 0.5° uncertainty cone, while the LEO acquisition quadrant receiver stares at the entire 0.5° uncertainty cone of the GEO. Although the GEO scan is continuous, the time to complete the scan can be estimated by $T_{ACQ} = M t_d$, where M is the number of acquisition cells and t_d is the dwell time. M is given by $M = (\theta_{UNC}/\theta_T)^2$, where θ_{UNC} is the acquisition uncertainty angle and θ_T is the transmitted beamwidth. This scan time can be loosely called the acquisition time, since it is by far the dominant contribution.

When the LEO quadrant detector senses that one quadrant has been illuminated, the servo angular step reduction sequence (Section 8.4.2) is initiated. Once closed loop tracking is obtained the field of view is then reduced to θ_{NEA} (Section 8.4.1). The (worst case) time for the acquisition sequence to this point is $M t_d$.

It should be noted that the SNR which determines θ_{NEA} is different than the SNR on which the false alarm and detection probabilities are calculated. This is because prior to angular step reduction, the light spot is in a single quadrant (typically), but once closed loop tracking begins, the spot becomes divided between four quadrants and additionally sees dead zone loss. For 50 percent dead zone loss, this represents a factor of eight reduction in power per quadrant for closed loop tracking. This corresponds to a factor of 8 (9 dB) reduction in rms SNR, and a factor of 64 (18 dB) reduction in power

SNR. The rms SNR per quadrant for acquisition (cw integration approach) was about 9.3 for $P_d = 0.999$ and $P_{fa} = 10^{-9}$. After a factor of eight loss, the rms SNR is only 1.2, which is used to compute σ_{NEA} . For $SNR = 1.2$ the field of view reduction ratio is $R = 3.1$ $D/D_S = 1.27 \approx 6$. For 50 percent dead zone loss, $R = 0.64 \approx 6$. Thus the quadrant detector diameter to dead zone ratio is the critical parameter for FOV reduction. For the Hughes HPIN 444Q $\delta = 83.2$, so that $R = 53.2$. Reducing the 0.5° (8.7 mrad) by $R = 53.2$ gives a GEO uncertainty FOV at the LEO of $\sigma_{NEA} = 164 \mu\text{rad}$.

From the point of having achieved a closed loop σ_{NEA} estimate at the LEO, the acquisition sequence proceeds as follows. By the time the servo angular step reduction is completed at the LEO, the GEO transmitter has essentially moved to address the next acquisition cell. The GEO acquisition quadrant detector must have a field of view at least three or four acquisition cells wide, so that the transmitter can move on to the next acquisition cell, without having to include more time for the return beam within each dwell time.

The LEO now knows that the GEO is located within $\sigma_{NEA} = 164 \mu\text{rad}$, and directs its $10 \mu\text{rad}$ ($1/e^2$) communication beam to scan σ_{NEA} . With a dwell time of $t_d = 0.05$ seconds, the GEO can perform angular step reduction with its acquisition quadrant detector. This scan time will take approximately $T_{SCAN} = 300 (0.05) = 15$ seconds.

As soon as the GEO quadrant detector is satisfied that it has been illuminated (e.g. two successive quadrant hits) the GEO acquisition transmitter is directed to stop scanning, and is gradually directed toward σ_{NEA} during the dwell time, as determined by the GEO quadrant detector. (σ_{NEA} is about four acquisition cells reduced by $R = 53.2$). At this time the $35 \mu\text{rad}$ beacon transmitter is turned on, which shares the aperture with the acquisition transmitter by orthogonal polarizations. If σ_{NEA} (GEO) is large, a small scan may take place, otherwise σ_{NEA} is illuminated continuously. Using the beacon laser allows the LEO acquisition quad to get a boosted rms SNR by the ratio of the acquisition transmitter beamwidth to beacon beamwidth ratio squared. The LEO acquisition quad obtains additional FOV reduction due to higher SNR, so that the spot falls through a bifurcated mirror onto the LEO tracking quad. The tracking quad performs an angular step reduction, which

then results in closed loop tracking. The 10 μ rad LEO communication beam then continuously illuminates the LEO. Both the acquisition quadrant FOV reduction and tracking quadrant angular step reductions on the LEO require a total of about 0.1 seconds. The GEO then performs FOV and angular step reduction on its quadrant detectors, requiring another 0.1 seconds, resulting in mutual tracking and communication.

The amount of time which should be added to the times in Tables 8.4-1, 8.4-2, and 8.4-3 is 15 seconds plus 0.1 seconds plus 0.1 seconds plus 0.6 seconds, where the last term represents four d/c time of flight delays. Thus about 16 seconds should be added to the acquisition times in Tables 8.4-1, 8.4-2, and 8.4-3.

8.5 ARRAY ACQUISITION

8.5.1 Field of View Reduction

For array acquisition, the linear field of view (FOV) reduction is given by \sqrt{N} , where N is the number of pixels in the array. With a 400 x 500 array, the FOV can be reduced by a factor of 400, from an uncertainty angle of 0.5° (8.7 mrad), to 22 μrad. This is nearly eight times greater than the FOV reduction of 53 which is practical for a quad cell with low SNR.

If the array is being used with a video tracker, additional FOV reduction can take place. If the optical blur is set to subtend two by two pixels (for good tracking performance) the angular tracking jitter (for high rms SNR) is given by

$$\sigma_j = \frac{0.685 \Delta}{SNR - 3}$$

where Δ is the angular subtense of the optical blur. We define $\epsilon_{NEA} = 2\sigma_j$ similar to the quad cell case. Since the blur angle is twice the single pixel angle, the uncertainty is $\epsilon_{UNC} = \sqrt{N} \Delta/2$, where \sqrt{N} is the one dimensional number of pixels in the array. Defining the FOV reduction ratio as $R = \epsilon_{UNC}/\epsilon_{NEA}$, the FOV reduction is $R = 0.365 \sqrt{N} / (SNR - 3)$.

8.5.2 Detection and False Alarm Probabilities

All CCD-type imaging arrays effectively integrate the photocurrent in each pixel - they vary only in how the collected charge is stored and read out. The choice of detection scheme is to threshold the collected charge in each pixel, removing much of the noise. A simple circuit on the video output of the array electronics can accomplish the thresholding (a greatly simplified

version of current Hughes video trackers, for example.) This is similar to the integration and threshold scheme used for tracking (Sections 7.4, 7.8) and to the cw integration scheme for quad cell acquisition (Section 8.4.4). The detection performance can be characterized by the probabilities of detection and false alarm, as for the quad cell acquisition schemes.

Let the array consist of N pixels ($\sqrt{N} \times \sqrt{N}$), and the acquisition uncertainty consist of M acquisition cells ($\sqrt{M} \times \sqrt{M}$), where M is given by $M = (\epsilon_{UNC}/\epsilon_T)^2$ as for the quadrant detector cases. The array stares into the entire uncertainty field of view, where in the worst case, it must wait $(M-1)$ seconds before it is illuminated (τ is the integration time). Note that the integration time is equal to the dwell time, since no step angular reduction is required as for the quad cell. Since there are $M-1$ chances for all N pixels to incur a false alarm, and one chance for $N-1$ false alarms, there are a total of $MN-1$ chances for pixel false alarm, but a single chance for detection.

The probability of a successful acquisition is $P_{ACQ} = P_d (1 - P_{fa})^{MN-1}$ where P_d is the detection probability and P_{fa} is the false alarm probability. The expression for P_{ACQ} results since we require a single correct detection, and no false alarms. For equal contributions to error by missed detection and all chances for false alarm, the threshold is set such that

$$P_d = (1 - P_{fa})^{MN-1}$$

Using the binomial expansion, this is equivalent to setting

$$P_{fa} = (1 - P_d) / (MN-1)$$

An upper bound can be obtained on MN as follows. For a 400×500 array $N = 2.0 \times 10^5$. Since $\epsilon_T = 30 \mu\text{rad}$ is about the minimum beamwidth desirable to use for acquisition, and the uncertainty angle is 0.5° (8.7 mrad), an upper bound on M is obtained by $M = (\epsilon_{UNC}/\epsilon_T)^2 = 1.9 \times 10^5$. An upper bound on MN is then about 4×10^{10} .

For $P_{ACQ} = 0.99$, we require $P_D = 0.995$, and then $P_{fa} = 10^{-13}$ based on the upper bound of MN. Since the required SNR is not extremely sensitive to P_{fa} , we will use the nominal $P_{fa} = 10^{-13}$ and later correct the SNR for the exact case. For $P_d = 0.999$ (better than required) and $P_{fa} = 10^{-13}$, an rms SNR = 10.6 is needed.

8.5.3 Array Acquisition Performance

As mentioned in Section 8.5.2, nominal detection and false alarm probability of $P_D = 0.999$ and $P_{fa} = 10^{-13}$ will be assumed, which results in better than $P_{ACQ} = 0.99$ overall acquisition probability. The false alarm probability will later be adjusted for the number of acquisition cells in the specific case, according to the P_{FA} expression in Section 8.5.2.

We will assume an array size typical of currently available commercial CCD arrays (Section 8.2.1), and use 400×500 pixels, so that $N = 2.0 \times 10^5$. Since the overall acquisition uncertainty is $\sigma_{UNC} = 8.7$ mrad (0.5°), the single pixel FOV is $(8.7$ mrad / $400) = 22$ μ rad. Note that the planet background sources (Table 7-2) subtend at least 4×4 pixels, and a simple image processing circuit could discriminate against planets since they are extended sources. Note that stars are unresolved sources, and could not be discriminated. However, we will assume that there is no extended source discrimination, so that the array must detect with the worst case background irradiance (except the sun) in the 22 μ rad FOV.

Using $\sigma_R = 22$ μ rad, the extended sources have the following irradiances in $\text{Wm}^{-2}\text{\AA}^{-1}$: sun, $L_I = 6.8 \times 10^{-7}$; moon, $L_I = 1.7 \times 10^{-12}$; Venus, $L_I = 6.8 \times 10^{-12}$; Jupiter, $L_I = 1.7 \times 10^{-13}$. These can be compared to $L_I = 4.8 \times 10^{-12}$ for Sirius and $L_I = 2.1 \times 10^{-12}$ for Mira. Note that the extended sources and the stars have very comparable irradiances for this 22 μ rad FOV. If the acquisition uncertainty were larger, or there were fewer pixel elements in the array, the pixel FOV would be larger, and the extended sources would clearly dominate the irradiance. Even at the pixel FOV of only 22 μ rad, Venus is the strongest irradiance. For the parameters (Table 7.6-1) $D_R = 15$ cm, $N_R = 0.54$, $\beta = 50\text{\AA}$, $N_F = 0.7$, $n = 0.25$, $h\nu = 2.3 \times 10^{-19}$

joules, $L_I = 6.8 \times 10^{-12} \text{ Wm}^{-2}\text{A}^{-1}$ and $\tau = 10 \text{ msec}$. the background photocounts are $K_B = 2.5 \times 10^4$. Note that the assumed quantum efficiency of 25 percent is somewhat conservative, since some CCD arrays approach 50 to 60 percent for the $0.8 - 0.9 \mu\text{m}$ region.

The maximum number of thermal electrons are $K_T = 300$, which is both a commercial manufacturer's specification and value obtained from the Hughes CCD group. The thermal electrons are independent of integration time (τ).

The typical CCD array has a dark current (at 15°C) given by $I_D = 20 \text{ nA/cm}^2$. (This could be lowered by cooling.) For typical pixel array $12 \mu\text{m} \times 18 \mu\text{m}$, and $\tau = 10 \text{ msec}$, the photocounts due to dark current shot noise are $K_D = 2.7 \times 10^3$. However, an array has an additional dark current problem that single photodetectors do not have - dark current nonuniformity. That is, the variation in dark current from pixel to pixel will cause a "fixed pattern noise" for long integration, given uniform illumination. The typical CCD array dark nonuniformity is 1.0 nA/cm^2 (15°C), which for $12 \mu\text{m} \times 18 \mu\text{m}$ pixel area and $\tau = 10 \text{ msec}$ integration time, results in $K_{DN} = 135 \text{ rms}$ photocount variation.

The rms photocount variation due to shot noise is

$$(K_S + K_B + K_D + K_T)^{1/2} = (3 \times 10^4)^{1/2} = 174.$$

Root-square-summing the shot noise and dark current photocount variation gives $\sigma = [(174)^2 + (135)^2]^{1/2} = 220$.

The CCD array has an additional noise problem with the DC current due to optical background. The DC components due to dark current and thermal noise can be removed with a fixed threshold. Optical background sources move in and out of the array field of view, however. The standard approach to removing background is to establish a threshold above the worst case background level. Since background would not always be present in every pixel, the signal is required to have enough signal to exceed the threshold without the noise mean added to it. From this viewpoint, the rms SNR is given by

$$\text{SNR}_{\text{rms}} = \frac{K_S - K_B}{\sigma}$$

where σ is the combined rms variation due to shot noise and dark current nonuniformity.

For $\tau = 10$ msec, $\sigma = 220$ and $K_B = 2.5 \times 10^4$. To achieve rms SNR = 10.6, $K_S = 2.7 \times 10^4$ are required, corresponding to a received power $P_R = K_S(hv/n\tau) = 2.4$ pW.

Using the link parameters of Table 7.7-1, with $\theta_T = 130$ μ rad (Airy lobe), and $T_S = 1.0$ (no split), a transmitted power of $P_T = 12.9$ mW is required. A laser source with $P_T = 51$ mW would satisfy the acquisition requirement with 6.0 dB power margin.

For $\theta_T = 130$ μ rad there are $M = (13$ mrad/130 μ rad) $^2 = 10^4$ acquisition cells. (Note a transmitter needs $\theta_T = 13$ mrad Airy lobe width to adequately cover the 8.7 mrad uncertainty - see Section 8.6.1). The dwell time could be set equal to the integration time if the GEO acquisition quadrant detector had a field of view several acquisition cells wide, so that it could see a response after moving on to address the next cell. Alternatively the servo time to address the illuminated pixel could be included in the dwell time. Since the former approach provides faster acquisition, we set the dwell time equal to the array integration time.

For $\theta_T = 130$ μ rad, there are 10^4 acquisition cells, and $t_d = \tau = 10$ msec dwell time, so that the acquisition time (neglecting handover) is $T_{ACQ} = M t_d = 100$ seconds, with $P_{ACQ} = 0.99$ and 6.0 dB power margin with a 50 mW source. For comparison, acquisition with an APD quadrant detector was $T_{ACQ} = 734$ seconds with no power margin (SIM approach), and assuming a 96 mW cw source (see Table 8.4-3). The array has a factor of 7 shorter acquisition time with a simultaneous 9.0 dB power advantage. Using the tremendous advantage of the array over the quadrant detector is the only way to achieve acquisition times below two minutes, for currently available laser power. Table 8.5-1 shows some alternate parameters for array acquisition performance.

If the dwell time is set equal to the integration time, and integration time considered fixed, the acquisition time with an array is given by

$$T_{ACQ} = (\theta_{UNC} / \theta_T)^2$$

TABLE 8.5-1. CCD ARRAY - ACQUISITION PERFORMANCE

• $\tau = 10 \text{ msec}$

• $P_{\text{acq}} = 0.99$

$P_T (\text{mW})$	$\theta_T (\mu\text{rad})$	$T_{\text{acq}} (\text{sec})$	Margin (dB)
50	260	25	0.0
100	260	25	3.0
50	130	100	6.0
100	184	50	6.0

Defining $P_T = \gamma \theta_T^2$, where γ absorbs the other link equation parameters, the acquisition time becomes

$$T_{ACQ} = \gamma \theta_{UNC}^2 \frac{\tau}{P_T}$$

The acquisition time is proportional to the uncertainty solid angle, and inversely proportional to laser power, just as in the quadrant detector case. Thus the factor of 7 shorter time and 9.0 dB power advantage of the array over APD quadrant detector acquisition (SIM) can be considered a 17.5 power advantage.

It is also of interest to know the effect of varying the integration time. Since thermal noise was not a dominant noise source, the shot noise variance (counts squared) is proportional to τ . The dark current non-uniformity variance is proportional to τ^2 . The rms SNR can be rewritten as

$$\text{SNR}_{rms} = \frac{K_S - K_B}{\sqrt{\sigma_{DN}^2 + \sigma_N^2}}$$

where σ_{DN}^2 is the variance due to dark nonuniformity and σ_N^2 is the variance due to shot noise. Since the shot noise variance is equal to the number of counts, $\sigma_N^2 = K_N$. The dark current variance is $\sigma_{DN}^2 = K_{DN}^2$. Defining $K_i = n_i \tau$, where n is the count rate, the SNR becomes

$$\text{SNR}_{rms} = \frac{(n_S - n_B) \tau}{(n_N \tau + n_{DN}^2 \tau^2)^{1/2}} = \frac{n_S - n_b}{(n_{DN}^2 + n_N / \tau)^{1/2}}$$

Thus the dark nonuniformity is the dominant noise source for long integration times, and negligible background, as has been experimentally observed.

(Note: $\tau < 1.0$ second to avoid charge saturation.) Note that the signal count rate must exceed the DC background count rate without dependence on integration time. For 1 nA/cm^2 dark current nonuniformity, and $12 \mu\text{m} \times 18 \mu\text{m}$ pixel area, the dark nonuniformity count rate is $n_{DN} = 13500 \text{ e}^-/\text{sec}$. The thermal noise ($K_T = 300$) is negligible compared to the background and dark current shot noise. The noise count rate can then be set as $n_N = n_B + n_D = 2.8 \times 10^6 \text{ e}^-/\text{sec}$ ($n_B = 2.5 \times 10^6$, $n_D = 2.7 \times 10^5$). For $\text{SNR} = 10.6$, the required power versus integration time is ($n = 0.25$)

<u>P_R (pW)</u>	<u>τ (msec)</u>
2.8	1.0
2.5	10.0
2.4	100.0
2.4	1000.0

The effect of integration time is slight because the required signal count rate is dominated by the fixed DC background rate.

In summary, the array acquisition performance was seen to be superior to the APD quadrant detector with SIM by a 17.5 dB laser power advantage, which could also be considered a factor of 56 shorter acquisition time. Since the CCD array is required to allow intersatellite laser communication acquisition times less than two minutes, it is highly advisable to begin space qualifying currently available CCD arrays.

8.5.4 Array Acquisition Sequence

The acquisition sequence with an array is somewhat simpler than with a quadrant detector. Initially, the GEO acquisition transmitter scans a 130 - 260 μrad (Airy lobe) beam over the 0.5° uncertainty cone, which requires $M = 2500 - 5000$ acquisition cells to be addressed. (Again, although the scan

is continuous, "addressing acquisition cells" is a convenient description.) The 400 x 500 CCD array acquisition receiver on the LEO stares into the 0.5° uncertainty cone. When a pixel is illuminated on the LEO array, the gimbal is directed to point the 10 μrad ($1/e^2$) communication beam to the 22 μrad FOV location of the illuminated pixel. Since the APD quadrant tracking detector on the LEO has a 140 μrad FOV, subsequent illumination from the GEO will fall through the central hole of a bifurcated mirror onto the tracking detector.

Although the GEO transmitter has by now moved on to address the next acquisition cell, the GEO acquisition quadrant detector has an FOV which includes several acquisition cells. Thus it is able to see the communication beam from the LEO even though the scan has continued. The 10 μrad beam from the LEO does a small spiral scan in the 22 μrad pixel FOV to illuminate the GEO.

When the GEO quadrant detector recognizes that it has been illuminated, the GEO acquisition transmitter is directed to stop the scan, and the 35 μrad (Airy lobe) beacon transmitter is turned on. Due to the high power and low divergence of the communication beam, even though the signal is intermittent during the spiral scan, the GEO quadrant detector should be able to perform angular step reduction and locate the LEO to less than the 35 μrad beacon beamwidth.

Once illuminated by the beacon, the LEO tracking quadrant detector performs an angular step reduction to obtain closed loop fine tracking. The communication beam then illuminates the GEO acquisition quadrant detector continuously, so that closed loop tracking is obtained, and the spot falls through the central hole of a bifurcated mirror onto the tracking quadrant detector. Once the angular step reduction is performed at the GEO tracking quadrant detector, both terminals have established fine tracking, and communication can take place.

The total acquisition time is given by the expression $T_{ACQ} = M t_d$ from Section 8.5.3, plus the handover time. The time to achieve five steps of angular reduction at the GEO acquisition quadrant detector is determined by a small scan time. Since the 10 μrad LEO communication beam is illuminating a 22 μrad uncertainty, there are about 3 x 3 cells to address. For a dwell time of 0.05 seconds the total time to scan 9 cells is about 0.5 seconds.

When the 35 μ rad GEO beacon is returned to the LEO, the LEO tracking quadrant detector performs an angular step reduction requiring about 0.05 seconds. LEO fine tracking allows continuous illumination of the GEO, where another 0.05 seconds is required for GEO tracking detector angular step reduction.

The total handover time to be added to $T_{ACQ} = M t_d$ from Section 8.5.3 is then $0.5 + 0.05 + 0.05 + 0.6 = 1.2$ seconds, where the last 0.6 second term accounts for four time of flight delays (4 R/c).

8.6 ISSUES FOR ACQUISITION BEAM SCANNING

8.6.1 Beamwidth

The beamwidth for laser communication systems is defined as the width of the commonly observed far field Airy profile. The Airy profile has an angular intensity dependence given by

$$I(\gamma) = I_0 \left[\frac{2J_1(2.44\pi\gamma/\alpha)}{2.44\pi\gamma/\alpha} \right]^2 \quad (1)$$

where I_0 is the on axis intensity, α is the full angle beamwidth to the first null of the Airy pattern and γ is the radial angular variable.

The full beam divergence to the first null of the Airy disk is given as

$$\alpha = 2.44 \lambda/D \quad (2)$$

where λ is the wavelength and D is the diameter of the antenna (primary mirror).

Optimization of the size of the Airy beam profile superimposed upon the basic pointing uncertainty area is needed to provide sufficient power at its boundary while also minimizing the necessary transmitter power. We will use $\frac{\pi}{4} \theta_{UNC}^2$ as the uncertainty area to example a staring acquisition routine. It is clear, for example, that the first dark ring of the Airy profile cannot be even nearly coincident with the edges of θ_{UNC} since little power would be available there. We have chosen to maximize the power received by a collector at the edges of the pointing uncertainty region relative to the transmitted beamwidth, since the least intensity is available at the edge.

The optimization proceeds by using the range equation and the Airy profile. The range equation yields the power collected by the receiver and can be used to deduce an appropriate relation between α and ϵ_{UNC} . The range equation is effectively given by

$$P = \frac{C_0 I(\gamma)}{\alpha^2} \quad (3)$$

where P is the power collected by the receiver, and C_0 represents the appropriate multiplicative factors, such as, receiving antenna diameter, system optical losses and reciprocal range squared.

The optimization may be determined by setting $dP(x)/d\alpha = 0$ with $x = 2.44\pi\alpha/\alpha$, then setting γ coincident with the edge of the pointing uncertainty region. Thus, the optimized beamwidth α_A is,

$$\alpha_A = 2.08 \epsilon_{UNC} \quad (4)$$

which places ϵ_{UNC} close to the 1/e intensity point on the Airy profile as can be determined from Equation 1 and Equation 2.

8.6.2 Beam Overlap

We assume for simplicity and ease of implementation a line by line raster scan of the pointing uncertainty area. Other scan geometries are certainly possible; such as, a spiral scan or a circular scan. However, gimbal and electronic requirements are simpler with a raster scan. A line width of the raster scan is defined by with the beamwidth of the Airy profile at its 1/e intensity points (α_A). The beam overlap from one line to the next is the fraction of the beam relative to the 1/e intensity point which must be caused to traverse a portion of the previously scanned area. This is necessary to provide sufficient coverage of all points within the area of pointing uncertainty for the pulsed operation. The general linear beam overlap is denoted as ϵ with $0 \leq \epsilon \leq 1$ and is defined here for the absence of residual, uncompensated, or unknown drift rates.

The required beam overlap is dependent upon whether the acquisition laser is operated CW or pulsed. A laser operated CW would provide continuous emission along its scan path so that $\epsilon_x(\text{cw}) = \epsilon_y(\text{cw}) = 0$. The situation is different when the laser is operated pulsed as continuous coverage is not provided as the scan proceeds. The beam positions must be placed in such a way to preclude missed coverage. The required overlap is determined by the geometry of the situation, and in general, with pulsed operation, $\epsilon_x(p) = \epsilon_y(p) \geq 1/2 (1 - \sqrt{2/2}) \approx 0.15$.

A single pulse into an element of the area of uncertainty may not be sufficient for acquisition detection. An evaluation of the signal detection probability must be made to establish whether more than one laser pulse per area element is necessary. The operation and the signal to noise ratio (S/N) required for the servo system must also be considered. The angular scan rate is associated with the laser pulse rate (r), and assuming m laser pulses per area element,

$$\dot{\alpha} = \alpha_A (1 - \epsilon_x) \cdot r/m \quad (5)$$

The number of dwell points (n) within the area of initial pointing uncertainty is greater than the geometrical factor $(\theta_{\text{UNC}} / \alpha_A)^2$ by the inverse of the beam overlap, and

$$n = (\theta_{\text{UNC}} / \alpha_A)^2 (1/(1 - \epsilon_x)) (1 - \epsilon_y) \quad (6)$$

8.6.3 Beam Scan

The time required for the acquisition beam to fully scan the pointing uncertainty is given by the number of scan elements within the area of pointing uncertainty, and the dwell time at each scan element. The number of scan elements was given by Equation 6, and the dwell time can be considered as $t_d = N_s/B$, where N_s are the angular servo step reductions (quadrant detector) and B is the servo bandwidth. The scan time is then given by

$$T_o = (\epsilon_{UNC}/\alpha_A)^2 \left(\frac{1}{1-\epsilon_x}\right) \left(\frac{1}{1-\epsilon_y}\right) N_f/B \quad (7)$$

The values of the overlap factor when the laser is operated CW or pulsed were noted earlier.

The angular rate along a raster scan line is associated with the beam divergence and the dwell time, so that

$$\dot{\theta} = \alpha_A / t_d \quad (8)$$

The laser pulse rate required during the scan is dependent upon the S/N required for acquisition. Once the S/N is defined for the acquisition sensor integration period (usually $\tau = 1/B$) the number of pulses required per scan element may be determined. Equation 8 may then be set equal to Equation 5 to define the required laser pulse rate, so that,

$$r = \frac{m}{(1-\epsilon_x) t_d} \quad (9)$$

8.6.4 Spacecraft Induced Angular Errors

The pointing angular uncertainty area and the scan time may be modified by the relative angular motion between spacecraft terminals after correction by the spacecraft attitude and pointing control systems. This residual angular motion is the uncompensated drift rate, $\dot{\theta}_u$. This error is due to fluctuations and uncertainties in spacecraft attitude, ephemeris and electronic controls. Since the vector direction of the angular changes caused by $\dot{\theta}_u$ is unknown, the impact of its presence during the scan time may be interpreted as an increase in ϵ_{UNC} by an additional term ϵ_m . The angular change is given by the product of the uncompensated drift and the scan time to that element. The maximum value over a complete scan is given by

$$\epsilon_m = T_o \dot{\theta}_u$$

The uncompensated drift rate $\dot{\theta}_u$ may also be viewed as causing an increase in the time necessary to scan the original uncertainty area with a beamwidth reduced by a factor $(1-\epsilon)$, where ϵ is related to $\dot{\theta}_u$. The additional beam angular overlap is thus $a_A (1-\epsilon_x)(1-\epsilon_y)$. The change θ_m in the angular uncertainty area may be oriented along the y -dimension without loss of generality and used to define the additional overlap needed per scan line. The additional beam angular overlap is also equal to the ratio of the angular change θ_m (along y) and the number of scan lines along y , $N_y = \theta_{UNC} / a_A (1-\epsilon_x)(1-\epsilon_y)$, so that

$$\epsilon = \frac{1}{1 + (\theta_{UNC}/T_0 \dot{\theta}_u)} \quad (10)$$

and $0 \leq \epsilon \leq 1$.

The scan time T_0 determined earlier will be increased to a larger value (T_S) due to the overlap factor ϵ needed to account for the uncompensated drift rate $\dot{\theta}_u$. We may find the modified scan time by equating T_S to $T_0/(1-\epsilon)$, and

$$T_S = T_0(1 + T_0 \dot{\theta}_u / \theta_{UNC}) \quad (11)$$

T_S is equal to T_0 as defined in Equation 7 when $\dot{\theta}_u = 0$. We recognize that T_S as defined would be different if the probability distribution of finding the distant satellite within θ_{UNC} were non-uniform.

8.7 RECOMMENDED ACQUISITION/TRACKING CONFIGURATION

As described in Section 7.0, the quadrant avalanche photodiode detector provided about 19 dB more sensitivity than the PIN quadrant, and the APD quad is the recommended choice for tracking detector for that reason. The APD bias for each quadrant must be controlled more accurately than for the PIN quadrant, but this is not a serious electronic burden.

As described in Section 8.0, the APD quadrant detector cannot provide reasonable acquisition times, even for 100 mW laser power and no power margin. The CCD array has a 17.5 dB power advantage over the APD quad. Some form of array is needed as the acquisition detector on the LEO, and since the CCD is most sensitive it is the recommended choice. Although adequate CCD technology for video cameras is currently available, and the acquisition requirements are compatible with video frame rates, a development program is necessary to space qualify a 400 x 500 CCD array. Since CCD's are being space qualified for Galileo and Space Telescope, the 400 x 500 video CCD array should pose no special problems.

A summary of the recommended acquisition/tracking configuration is given in Table 8.7-1. It is also suggested that NASA personnel seriously investigate using the acquisition array for tracking. This could be a CCD array with a gyro-stabilized servo sample rate, or a CID with a pixel tracking gate to meet the complementary filter servo sample rate requirements.

TABLE 8.7-1. RECOMMENDED ACQUISITION/TRACKING CONFIGURATION

GEO - Acquisition transmitter
 LEO - Acquisition receiver

GEO	LEO
<u>20 Inch Receive Telescope</u> <ol style="list-style-type: none"> 1) Acquisition Quad Cell 2) Communication Detector 3) Tracking quad APD <p style="text-align: center;">↓</p> <div style="text-align: center; border: 1px solid black; padding: 2px; margin-left: auto; margin-right: auto;"> Bifurcated Mirror </div> <p style="text-align: center;">↓</p> <p style="text-align: right; margin-right: 10%;">5-10% power split</p>	<u>6 Inch Receive Telescope</u> <ol style="list-style-type: none"> 1) Acquisition 400 x 500 CCD Array 2) Quadrant APD for tracking and beacon data demodulation <p style="text-align: center;">↓</p> <div style="text-align: center; border: 1px solid black; padding: 2px; margin-left: auto; margin-right: auto;"> Bifurcated Mirror </div> <p style="text-align: center;">↓</p>
<u>2.5 Inch Transmit Telescope</u> <ol style="list-style-type: none"> 1) 130 μrad (Airy lobe) acquisition beam 2) 35 μrad (Airy lobe) beacon beam (share aperture by polarization) 	<u>6 Inch Transmit Telescope</u> <ol style="list-style-type: none"> 1) 15 μrad (Airy lobe) communication beam

8.8 SUMMARY - ACQUISITION

The acquisition uncertainty angle was found to be dominated by attitude uncertainties on the TDRS spacecraft, especially due to the yaw axis. The resulting uncertainty was approximated by a 0.5° diameter cone.

Acquisition sensors were investigated, including CCD, CID and photodiode arrays, as well as PIN and APD quadrant detectors. Commercially available arrays seem to be compatible with acquisition requirements, while quadrant detectors may require development in the areas of smaller quadrant gap, and smaller device size to reduce capacitance and dark current.

Acquisition sources were evaluated, including the single mode cw lasers and the high peak power Laser Diode Labs incoherent array. Although the 1.0 kW peak power of the LDL array was appealing, it was found that its large source size and divergence made it difficult to collect and collimate its emission. Single mode cw lasers (or coherent multi-stripe arrays, if they become available) are recommended as the choice for acquisition source.

Issues for quadrant detector acquisition were examined, including field of view reduction and servo angular step reduction. The probability of successful acquisition was derived based on detection probability when illuminated by the transmitter, and false alarm probabilities while not illuminated. The cw integrating (CWI) approach was found to yield the best shot noise performance for quadrant detector acquisition, but is seriously limited by the DC component of optical background in a practical system. Sinusoidal intensity modulation (SIM) avoids the DC background problem, but is about 4.5 dB worse in shot noise performance than CWI. Acquisition times for SIM exceed ten minutes with a quadrant APD detector and a 100 mW source, with no power margin. A time-gated acquisition scheme was found to have no advantage over SIM. The quadrant detector acquisition sequence was identified.

The field of view reduction for array acquisition was derived, as well as the probability of a successful acquisition. Commercially available CCD arrays were found to allow acquisition times under two minutes, with a 50 mW source and 6.0 dB power margin. The acquisition sequence using an array was described.

Acquisition times were found to be directly proportional to the uncertainty solid angle, and inversely proportional to laser power, for both array and quadrant detector acquisition.

Issues for scanning the acquisition transmitter beam were identified, including optimum beamwidth, beam overlap, scanning with a pulsed laser, and spacecraft uncompensated drift.

A recommended acquisition/tracking configuration was proposed, which used an acquisition array on the LEO, and a quadrant APD for both tracking and beacon data demodulation on the LEO. Further investigation is recommended to evaluate performing the tracking function with the acquisition array and a video tracker.

9.0 SYSTEM WEIGHT AND POWER

9.1 ESTIMATE RATIONALE

The weight and power estimate was made following the baseline concept of a two axis gimballed optical assembly with support electronics off-gimbal. The configuration approach was described in Section 4.0. Most component weight estimates are based upon earlier engineering work in this area or upon existing hardware developed for similar space electro-optical applications. The baseline concept is noted in Figure 9.1-1. The basic optical layout is reviewed in Figure 9.1-2. The terminal concept design parameters are summarized in Table 9.1-1.

The estimate rationale is based on the use of beryllium for the material for the main optical elements. Both light-weight cervit and beryllium optics were considered. The weight of the optical elements scales with the diameter (D) of the elements as measured in inches. The weight of Light-weighted cervit optics scales as $0.0279 D^{2.7}$ and the weight of beryllium optics scales as $0.006 D^{2.7}$. The weight scaling of the light weighted cervit and beryllium optics is shown in Figure 9.1-3. It is clear that beryllium optics offer substantial weight savings, especially for diameters greater than about 10 inches.

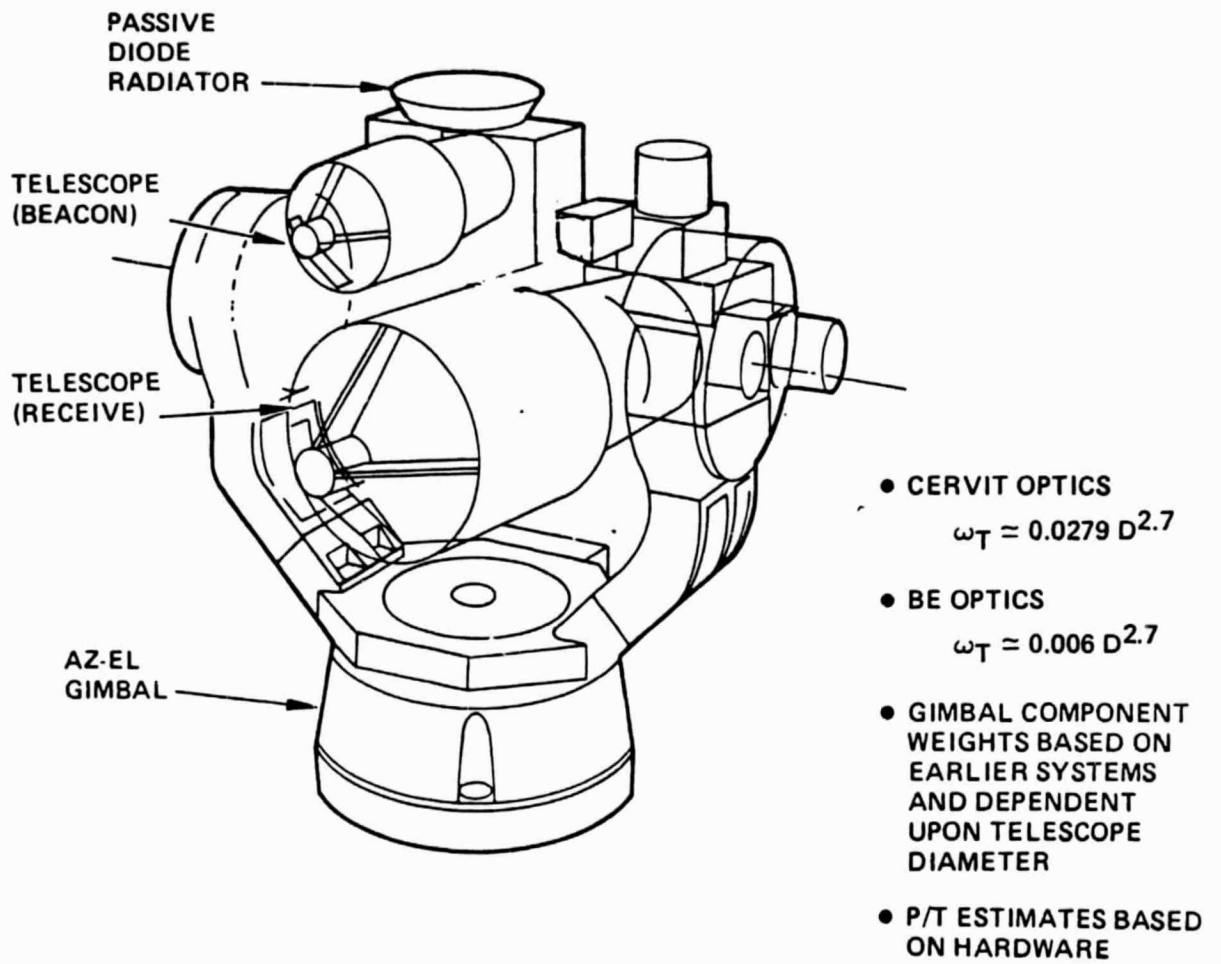


Figure 9.1-1. Baseline Configuration and Rationale for Weight Estimate.

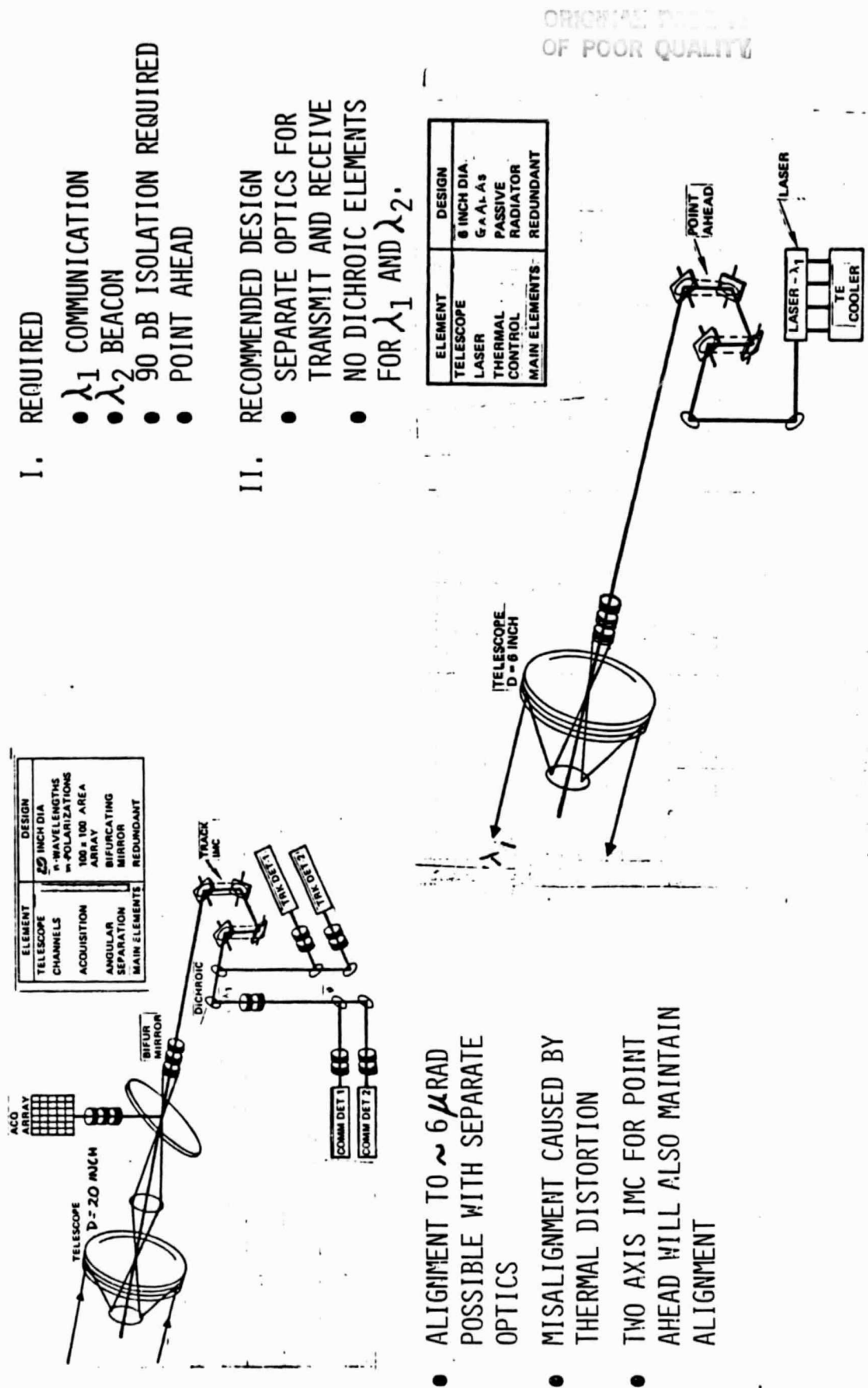


Figure 9.1-2. Basic Optical Layout.

TABLE 9.1-1. TERMINAL CONCEPT DESIGN PARAMETERS

Property	GEO	LEO
• Concept	• Separate Transmit and Receive Optics	• Separate Transmit and Receive Optics
• Transmit Optics	• 2.3 Inch Diameter	• 6 Inch Diameter
• Receive Optics	• 20 Inch Diameter	• 6 Inch Diameter
• Primary Material	• Beryllium	• Beryllium
• Acq Sensor	• Si-Quad	• Si-Array
• Track Sensor	• Si-Quad (APD)	• Si-Quad (APD)
• Comm Sensor	• Si-APD	• SI-APD
• Laser Source	• GaAlAs	• GaAlAS
• Transmit Wavelength	• Beacon (LDR) = 0.85 μm	• Comm (HDR) = 0.83 μm
• Receive Wavelength	• Comm (HDR) = 0.83 μm	• Beacon (LDR) = 0.85 μm
• Gimbal	• Two Axis-Optics on Gimbal	• Two Axis - Optics on Gimbal
• Az Range	• $\pm 20^\circ$	• $\pm 175^\circ$
• El Range	• $\pm 20^\circ$	• $\pm 140^\circ$
• Weight (with redundancy)	211.5 lb	175.2 lb
• Power	• 143.1 watt	• 137.8 watt

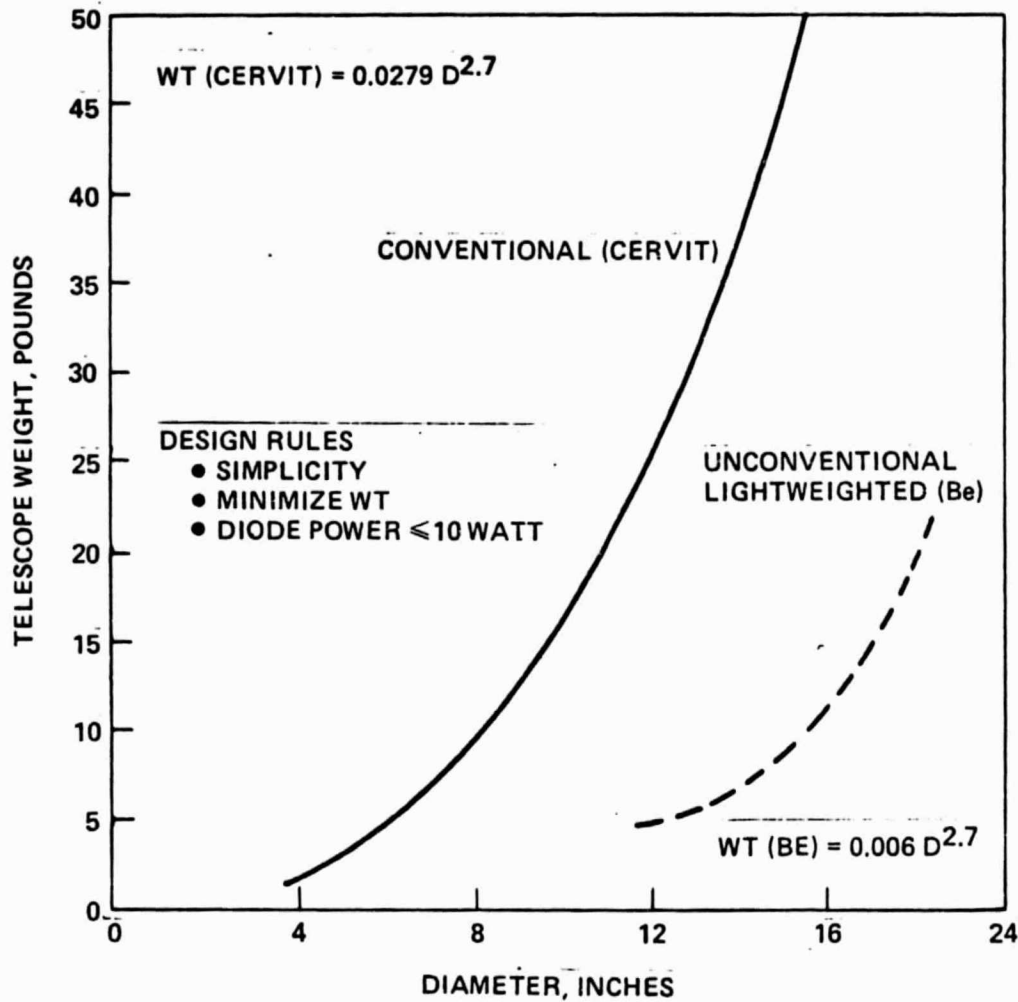


Figure 9.1-3. Telescope Weight Scaling with Size for Be and Cervit Material.

9.2 WEIGHT AND POWER

The weight estimates for the LEO and GEO terminals are noted in Table 9.2-1 and 9.2-2. The estimate is divided into two columns; one without redundancy, one with redundancy. The LEO weight without redundancy is 118.1 lb while that with redundancy is 175.2 lb. The GEO weight without redundancy is 155.5 lb and that with redundancy is 211.5 lb. The primary difference between a system without redundancy and one with redundancy is reliability, life on orbit and risk. Since a space system is normally desired to be long lived, reliable and of low risk, the higher weight estimates are more reasonable. Some additional weight may be expected when the system details regarding the spacecraft interface are more well defined. We consider these weight estimates to be conservative.

The associate power estimates for the LEO and GEO terminals are noted in Table 9.2-3 and 9.2-4. The estimated power for the LEO spacecraft is 137.8 watt and the estimated power for the GEO spacecraft is 143.1 watts. We caution the reader that our weight estimate for data electronics may be somewhat low as a result of the uncertainty regarding the modulation and data formatting scheme to be implemented on the (as yet) unspecified satellite. Additionally, redundant electronics weights, including power supplies, are often optimistic early in a program development as spacecraft interfaces and support are not known.

Weight and power estimates were based upon existing Hughes spacecraft communications systems. These included the Ku-band terminal, the shuttle microprocessor, the DMSP SSM/I μ wave radiometer and other systems currently under development. The data electronics was sized by assuming that the 500 Mbps data originated as the LEO satellite or single channel baseband digital unformatted form. This data was transmitted from the LEO to GEO satellite. It was assumed that the 500 Mbps digital data stream was fully recovered in baseband form on the GEO satellite. This is somewhat more complex and more massive than is required for an rf system where the baseband data is not recovered.

TABLE 9.2-1. LEO WEIGHT ESTIMATE

Area	Component	No Redundancy (Pounds)	Redundancy	With Redundancy (Pounds)
OPTICS	6 Inch Dia Be telescope Coupling optics Tracking sensor 6 inch dia Be telescope Coupling optics Laser transmitter	2.5 1.5 0.5 2.5 1.0 3.0		+3.5
POINT AND TRACKING	Acquisition/tracking array Tracking IMC (2 axis) IMC drive Point ahead IMC (2 axis) IMC drive Acquisition/tracking electronic Servo control electronics Two axis Be gimbal Torquers/resolvers (Az, El)	0.7 0.85 0.5 0.85 0.5 7.0 8.0 7.0 4.0	• • • • • •	+0.7 +0.85 +0.5 +0.85 +0.5 +3.5 +6.0 +4.0
STRUCTURE	Terminal packaging Spacecraft interface Radiation shielding	6.0 4.0 4.0		+2.0
SUPPORT ELECTRONICS	Communication electronics Beacon data electronics Microprocessor Spacecraft CMD and TLM Power conditioning Cabling Torquer power supply	6.0 2.0 8.0 3.0 15.0 6.0 4.0	• • • • •	+4.0 +1.0 +6.0 +2.5 +5.0 +2.0 +4.0
THERMAL	Passive radiator Ducting Active control Thermal blankets	3.0 2.0 2.0 2.0		+1.0
	Subtotal Contingency (10 percent)	107.4 10.7		159.3 15.9
	Total	118.1		175.2

TABLE 9.2-2. GEOSYNC WEIGHT ESTIMATE

Area	Component	No Redundancy (Pounds)	Redundancy	With Redundancy (Pounds)
OPTICS	20 inch dia Be telescope	19.5		
	Coupling optics	2.5		
	Communication sensor	0.5		
	2.3 inch dia Be telescope	1.5		
	Coupling optics	1.0		
	Acquisition/beacon sources	2.0	+2.0	
POINTING AND TRACKING	Acquisition/tracking array	0.7	+0.7	
	Tracking IMC (2 axis)	0.85	+0.85	
	IMC drive	0.5	+0.5	
	Point ahead IMC (2 axis)	0.85	+0.85	
	IMC drive	0.5	+0.5	
	Acquisition/tracking electronics	7.0	+3.5	
	Servo control electronics	8.0	+6.0	
	Two axis Be gimbal	12.0	+4.0	
	Torquers/resolvers (Az, El)	4.0		
STRUCTURE	Thermal packaging	8.0	+2.5	
	Spacecraft interface	10.0	+2.0	
	Radiation shielding	5.0	+2.0	
SUPPORT ELECTRONICS	Communication electronics	6.0	+4.0	
	Beacon data electronics	2.0	+1.0	
	Microprocessor	8.0	+6.0	
	Spacecraft CMD and TLM	3.0	+2.5	
	Power conditioning	15.0	+5.0	
	Cabling	6.0	+2.0	
	Torquer power supply	6.0	+4.0	
THERMAL	Passive radiator	3.0		
	Ducting	2.0		
	Active control	3.0		
	Thermal blankets	3.0	+1.0	
	Subtotal	141.4	192.3	
	Contingency (10 percent)	14.1	19.2	
	Total	155.5	211.5	

TABLE 9.2-3. LEO POWER ESTIMATE

Area	Component	No Redundancy (Pounds)	Redundancy
OPTICS	<ul style="list-style-type: none"> ● 6 Inch dia Be telescope ● Coupling optics ● Tracking sensor ● 6 inch dia Be telescope ● Coupling optics ● Laser transmitter 	0.2 2.0	● ●
POINT AND TRACKING	<ul style="list-style-type: none"> ● Acquisition/tracking array ● Tracking IMC (2 axis) ● iMC drive ● Point ahead IMC (2 axis) ● IMC drive ● Acquisition/tracking electronic ● Servo control electronics ● Two axis Be gimbal ● Torquers/resolvers (Az, El) 	0.3 6.0 6.0 15.0 20.0 12.0	● ● ●
STRUCTURE	<ul style="list-style-type: none"> ● Terminal packaging ● Spacecraft interface ● Radiation shielding 		
SUPPORT ELECTRONICS	<ul style="list-style-type: none"> ● Communication electronics ● Beacon data electronics ● Microprocessor ● Spacecraft T and C ● Power conditioning (83 percent) ● Cabling ● Torquer power supply 	24.0 4.0 10.0 3.0 22.1 2.5	● ●
THERMAL	<ul style="list-style-type: none"> ● Passive radiator ● Ducting ● Active control ● Thermal blankets 	3.0	
	Subtotal	130.1	
	Contingency (10 percent)	13.0	
	Total	143.1	

TABLE 9.2-4. LEO POWER ESTIMATE

Area	Component	No Redundancy (Pounds)	Redundancy
OPTICS	<ul style="list-style-type: none"> ● 20 Inch dia Be telescope ● Coupling optics ● Communication sensor ● 2.3 inch dia Be telescope ● Coupling optics ● Acquisition/beacon sources 	0.2 2.0	● ●
POINTING AND TRACKING	<ul style="list-style-type: none"> ● Acquisition/tracking array ● Tracking IMC (2 axis) ● IMC drive ● Point ahead IMC (2 axis) ● IMC drive ● Acquisition/tracking electronics ● Servo control electronics ● Two axis Be gimbal ● Torquers/resolvers (Az, El) 	0.3 6.0 6.0 15.0 20.0 12.0	● ● ●
STRUCTURE	<ul style="list-style-type: none"> ● Terminal packaging ● Spacecraft interface ● Radiation shielding 		
SUPPORT ELECTRONICS	<ul style="list-style-type: none"> ● Communication electronics ● Beacon data electronics ● Microprocessor ● Spacecraft CMD and TLM ● Power conditioning (83 percent) ● Cabling ● Torquer power supply (83 percent) 	20.0 4.0 10.0 3.0 21.3 2.5	● ● ●
THERMAL	<ul style="list-style-type: none"> ● Passive radiator ● Ducting ● Active control ● Thermal blankets 	3.0	
	Subtotal	125.3	
	Contingency (10 percent)	12.5	
	Total	137.8	

EDSG - 75/41 - JDB and GSM